VOLTAGE AND FREQUENCY CONTROL OF SELF EXCITED INDUCTION GENERATOR INTEGRATED WITH SOLAR PV SYSTEM AND BATTERY ENERGY STORAGE

A Thesis Submitted in Partial Fulfillment of the Requirements for the Award of the Degree of

DOCTOR OF PHILOSOPHY

Submitted by

SOMBIR
(Enrollment No. 2k18/PHDEE/18)

Under the Supervision of

Prof. Madhusudan Singh, EED, DTU
&
Dr. Ashutosh K. Giri, EED, GEC, Bharuch

DEPARTMENT OF ELECTRICAL ENGINEERING
DELHI TECHNOLOGICAL UNIVERSITY
Bawana Road, Delhi-110042, India
November-2023

DECLARATION

I hereby certify that the work presented in this thesis entitled "**Voltage and Frequency Control of Self Excited Induction Generator Integrated with Solar PV System and Battery Energy Storage**" which is submitted in partial fulfillment of the requirements for the award of the degree of Doctor of Philosophy to the Department of Electrical Engineering, Delhi Technological University, Delhi is an authentic record of my own work carried out under the supervision of Prof. Madhusudan Singh and Dr. Ashutosh K. Giri. The matter presented in this thesis has not been submitted elsewhere for the award of a degree

Sombir
(2k18/PHDEE/18)

Place: Delhi

Date: __/__/____

CERTIFICATE

Based on the candidates' declaration, I hereby certify that the work which is presented in this thesis entitled "**Voltage and Frequency Control of Self Excited Induction Generator Integrated with Solar PV System and Battery Energy Storage**" submitted to the Department of Electrical Engineering, Delhi Technological University, Delhi in partial fulfillment of the requirements for the award of the degree of Doctor of Philosophy, is an original contribution with the existing knowledge and faithful record of the research work carried out by him under our guidance and supervision.

To the best of my knowledge, this work has not been submitted in part or full for the award of any degree elsewhere

Prof. Madhusudan Singh	**Dr. Ashutosh K. Giri**
Department of Electrical Engineering	Department of Electrical Engineering
DTU, Delhi	GEC, Bharuch

The PhD viva-voce of **Mr. Sombir**, research scholar has been held on _____

Signature of	Signature of	Signature of
Supervisors		**Head, Dept. of Electrical Engg.**

Acknowledgements

I want to express my deep and sincere gratitude to my supervisor, **Prof. Madhusudan Singh** and **Dr. Ashutosh K. Giri**, for their valuable guidance and continuous monitoring of my research work. It was a great honor to pursue my research work under their supervision. **Prof. Madhusudan Singh** has been the motivating and inspiring factor behind my research work. His vigor and hunger to perform in an adverse situation have inspired me to strive for excellence. Continuous monitoring by Dr. Ashutosh K. Giri, valuable guidance and input has always been a driving force to complete my research work. It is a lifetime experience to work under both of my supervisors and humbly acknowledge lifetime gratitude to them.

I would like to express my thanks to **Prof. Rachana Garg, HOD (EE),** for her kind support.

I would also like to convey my sincere gratitude to **Prof. Suman Bhowmik**, Professor DTU, who has taught me the relevant coursework. I want to thank the SRC members, mainly **Prof. Prerna Gaur, NSUT, Delhi** who has given me valuable guidance and advice to improve the quality of my research work. I am extremely grateful to Prof. Mini Sreejeth, Prof. Neeta Pandey and Dr. Prakash Chittora for their valuable assistance and support. I am highly thankful to Mr. Mukesh Gupta staff member in Project Research Lab for providing me facility and assistance to carry out my research. I want to thank other office staff, central library and computer centre staff members for their valuable cooperation and support. I would like my sincere thanks to Dr. Hemant Saxena, and Dr. Suryakant Shukla who guided me to develop hardware at an initial level of my research work.

I am incredibly grateful to my research group and friends **Arvind Goswami, Divyansh Shailly, Pardeep Parashar, Dharamvir Dixit, Pardeep Sharma, Sukhbir Singh, Rajesh**

Jamdagni, Hitanshu Saluja, Anuj Sinha and **Brijendra Singh** for their valuable assistance, cooperation, and an excellent source of learning.

If I get any success today for my research work, the entire credit should go to my mother, **Smt. Omi Devi**, father **Sh. Rajender Kundu**, my elder sister **Ms. Suman**. I sincerely convey my gratitude to my wife, **Sangeeta Rani,** daughter **Manak Kundu**, and son **Abhay Kundu** who has encouraged me to carry out my research work. I want to thank other family members who directly or indirectly support my research work.

Lastly, I thank Mother Nature and Almighty God for allowing me to pursue doctoral studies.

Place: Delhi

Date: : __/___/_____

<div align="right">

Sombir
Research Scholar
(2k18/PHDEE/18)

</div>

ABSTRACT

Renewable energy mainly wind and solar-based electricity generating systems are becoming increasingly popular for managing energy consumption of remote and isolated communities. Wind and solar are the most promising renewable energy sources (RESs) due to their clean and unbounded supply, low maintenance requirements, lesser mechanical components, no green house gas emission, and ability to be put in remote regions for standalone power generation.

The major challenge in wind and solar energy is their unpredictability. The solar system can generate energy during the day time and wind turbine can generate power when the wind speed is high. Therefore, a wind-solar hybrid system is a more reliable power system with battery energy storage (BES). However, due to the intermittent nature of renewable energy, there are power quality issues in the system such as voltage and frequency fluctuations, harmonics distortions, low power factor, and unbalances in the power supply.

This thesis work presents power electronics (PE) based solutions to control the voltage & frequency of a wind turbine-driven Self-Excited Induction Generator (SEIG) integrated with a PV system for standalone applications. A voltage source converter (VSC) in the system provides power compensation (active and reactive), harmonics elimination, load leveling, and enhancement in the overall power quality of the standalone generation unit. The proposed system is implemented for both three-phase three-wire (3P3W) and three-phase four-wire (3P4W) isolated supply systems. Maximum Power Point Tracking (MPPT) techniques such as Incremental Conductance (IC) and Perturb & Observe (P&O) have been designed to harvest maximal power from the PV system in both the 3P3W & 3P4W isolated system. The performance parameters of the proposed standalone system have been estimated, and a prototype of the proposed system has been developed and demonstrated in the laboratory to validate the effectiveness of control technologies used in the system.

An appropriate control algorithm is needed for the proper operation of PE converters in a wind-solar-based standalone generation system. The control techniques ensure synchronization of different voltages, estimate fundamental components of voltages and

currents, regulation of DC-link voltage of converters, and charging/discharging of BES..
Different conventional approaches for estimating synchronizing signals have been described,
and novel advanced techniques for standalone systems have been proposed.

Frequency Locked Loops (FLLs) and Phase Locked Loops (PLLs) are being extensively
employed to estimate synchronization signals and can compute the phase, amplitude, and
frequency of the load current. These approaches have been implemented under a variety of
operating situations, including fluctuations in wind speed, solar intensity and harmonics in the
loads for standalone operation of wind-solar hybrid system.

Conventional algorithms such as Modified Least Mean Square (MLMS), and Second-
Order Generalized Integrator (SOGI) based FLL have been used for the proposed standalone
system. Furthermore, a novel technique using Second-Order Sequence Filter based FLL has
also been proposed, which demonstrate improved performance under unbalanced load
conditions.

A fast and robust technique based on Delayed Signal Cancellation has been developed,
demonstrating accurate frequency estimate and faster dynamic response for the isolated
system. The conventional Enhanced Phase Locked Loop (EPLL) and Reduced Order
Generalized Integrator (ROGI)-FLL have also been demonstrated, and their performance
degradation under dynamic conditions of renewable sources and loads is discussed. Further
advanced techniques like a Variable Gain Controller (VGC) and Three-Phase All-Pass Filter-
PLL based control techniques have been presented, which are adaptive and provide fast
dynamic response without compromising steady-state performance. A dual SOGI-based PLL
and dual-TOGI PLL for smooth estimation of grid parameters and distortion-free
synchronization signals has been also presented.

In the present work, the PV system and battery energy storage (BES) are connected at the
DC-link of the Voltage Source Converter (VSC) to supply real and reactive power to wind
turbine-driven SEIG for standalone applications. A bi-directional dc-dc controller (BDC) is
utilized to control the charging/draining modes of BES. The BES is employed to absorb
unused power during intermittent conditions and maintain the power equilibrium between the
energy sources and load. The dSPACE-1104 controller is being employed for analyzing

system parameters generating switching pulses for VSC and BDC. The proposed system and algorithms have been simulated and examined in the MATLAB/Simulink environment. The experimental results validate the effectiveness of the proposed control schemes in a standalone system.

Table of Contents

5. Control Techniques for Three-Phase Four-Wire (3P4W) Islanded Wind-Solar-BES-based Hybrid System

LIST OF FIGURES

and ω_g (b) I_m, u_{da}, u_{qa}, V_t and i_{smq} (c) i_{Lfd}, i_{Lfq}, i_{pf}, i_{Lp}^* and i_{Lq}^*.

under Unbalanced Load

TOGI-FLL and LMS algorithms after introducing load dynamics

LIST OF TABLES

LIST OF ABBREVIATIONS

v_{gabc} — Three-phase source voltage

i_{gabc} — Three-phase source current

i_{gabc}^{*} — Reference source current

i_{cabc} — Three-phase compensator current

i_{Labc} — Load current of all phases

i_{Ln} — Neutral load current

$v_{dc\text{-}ref}$ — Reference DC-link voltage

V_{dc} — DC link voltage

c_{dc} — DC-link Capacitor

f_s — Switching Frequency

v_b — Battery Voltage

i_b — Battery Current

V_t — Voltage Amplitude

v_{pv} — PV Voltage

i_{pv} — PV Current

p_{pv} — PV Power

k_p — Proportional Gain

k_i — Integral Gain

I_p — Fundamental Component of Load Current

u_{pabc} — In-phase Unit Vector Templates

u_{qabc} — Quadrature Unit Vector Templates

v_w Wind Velocity

L_f Interfacing Inductors

Ω estimated frequency

Δf Difference between estimated and actual frequency

LIST OF SYMBOLS

PQ	Power Quality
CPI	Common Point of Inter-section
VSC	Voltage Source Converters
BES	Battery Energy Storage
DSTATCOMs	Distribution Static Compensators
RESs	Renewable Energy Sources
DG	Distributed Generation
SPV	Solar Photovoltaic
MPPT	Maximum Power Point Tracking
CCF	Complex Coefficient Filter
ECCF	Enhanced Complex Coefficient Filter
SOSF	Second Order Sequence Filter
SOGI	Second Order Generalized Integrator
IRPT	Instantaneous Reactive Power Theory
PWM	Pulse Width Modulation
LMMN	Lease-Mean Mixed Norm
APF	All Pass Filter
VGC	Variable Gain Controller
DTOGI	Dual Third Order Generalized Integrator
THD	Total Harmonic Distortion
LMS	Least Mean Sqaure

MLMS	Modified Least Mean Square
SRFT	Synchronous Reference Frame Theory
PLL	Phase Lock Loops
FLL	Frequency Locked Loop
3P3W	Three-Phase Three-Wire
3P4W	Three-Phase Four-Wire

Chapter 1

Introduction

1.1   General

Electrical power is an indispensable requirement of modern society, and its significance in sustainable development and improving people's quality of life cannot be overstated. However, it's unfortunate that a large section of the global population still lacks access to reliable and secure power. Despite being considered electrified, many remote or rural locations only have access to electricity for a short period because of scheduled and unexpected blackouts [1]. Distribution companies make out organized disruptions in power supply to protect their business interests. Unorganized outages occur owing to both natural and man-made causes, such as overload, cracking, and the short circuit of wire. Even though the power supply is available, it is often found that supply voltage is poor and unbalanced among all the phases due to the non-uniform distribution of load.

A significant portion of the generated power worldwide comes from non-renewable sources that utilize fossil fuels and are transmitted through a transmission network to load centers [2]. Global energy consumption is constantly rising and increased generation results in massive carbon emissions and a terrible greenhouse effect. Further, fossil fuels are continuously depleting and their increasing prices are imposing several challenges on power producers [3]. Distributed generation (DG) employs regionally available renewable energy sources (RESs) and has invited major attraction of scientists and researchers for electricity generation due to its and availability in abundance and no cost [4]. Major renewable sources are wind, solar, hydro, tidal power, etc. Wind energy conversion system (WECS) using induction generators are becoming popular due to its robust brushless structure, inbuilt protection against short circuits, minimal commutation difficulties, and low maintenance. The wind energy extraction using SEIG has significant potential for standalone applications. However, in large-scale applications, SEIG's poor voltage regulation is a significant bottleneck because it requires variable reactive power support with increasing in load [5], [6]. Wind & solar energies are two rapidly developing RESs

now a day's [7]. Small wind energy systems (WESs) have not achieved attraction for off-grid applications for a variety of reasons, including site constraints, the dynamic conditions of wind, and generator capacity utilization [8]. Prior to development of grid-interactive solar photovoltaic (SPV), solar power via was popular for small off-grid applications [9]. The RESs have major drawbacks, such as its volatility and intermittent nature. To address the continuously increasing energy demand, renewable energy-based standalone systems are gaining popularity. Renewable-based energy systems are gaining popularity as standalone power generation for supplying electric power to isolated locations [10], [11].

1.2 Renewable Energy based Sources

Government support, improving economic conditions and significant advancements in renewable energy technologies are major factors to shift towards usages of renewable energy. The following are few common sources of renewable energy systems.

1.2.1 Solar: The solar photovoltaic effect established the basis for solar energy in 1839. Solar has developed into one of the RESs with the fastest rate of growth over the last two decades. Solar technology is classified into two types:

- Solar thermal

- Solar PV array

Solar thermal systems focus sun energy and convert it to heat using a network of reflecting collectors. Solar photovoltaic systems use a panel of connected solar cells to directly convert sunlight into electrical energy.

1.2.2 Wind: Wind energy is a valuable source of nonconventional energy, playing an essential role in transitioning to a more sustainable and low-carbon energy system. Ongoing technical advancements and encouraging policies are further enhancing the efficiency, reliability, and cost-effectiveness of wind turbines, making them an increasingly vital component of the global energy mix. The offshore and onshore wind energy technologies have evolved over the last few years to maximize the electricity production with large size turbines.

1.2.3 Hydro: The force or energy of moving water generates hydropower. Small power plants rely on naturally flowing water sources, whereas larger hydro plants

require dams to hold the required water head to produce hydropower for running hydro turbines attached to generator shafts. Hydro power relies on rain fall pattern and can be impacted by climate change which causes less rain.

1.2.4 Biomass: Biomass fuel is made from organic materials including, manure, forest trash, crops, and sugar cane residue. Biomass energy may be transformed into electricity. The process of extracting energy from biomass varies based on the substance used. Most biomass is used in rural areas for cooking, lighting and heating in developing countries.

1.2.5 Geothermal: Geothermal energy is a form of nonconventional energy that utilizes the Earth's internal heat to produce electricity and provide heating or cooling for different applications. It takes advantage of the natural heat reservoirs found underground, which are a result of geological processes and the planet's residual heat from its formation. The oil and gas sector typically uses techniques like digging wells below the earth's surface and moving water through them to extract energy from hot rocks. The water is then heated and pushed to the surface, where it powers a turbine and generator to generate electricity. The process is then repeated with recycled water [12], [13].

1.3 State of Art in Wind and Solar Energy Generation for Small and Isolated Applications

A substantial literature has been reported on the control of renewable energy-based isolated systems to enhance PQ while accommodating the variability in wind speed or solar intensity and meeting the demands of balanced/unbalanced nonlinear loads. Wind & Solar energy are omnipresent, abundant, and environmentally favorable. Wind power generation may not be feasible at all locations due to intermittency in wind speeds and are less reliable than solar generation. However, a wind & solar-based standalone system, incorporating multiple energy sources such as a wind-driven SEIG, a PV array, a suitable controller, a BES, and a consumer load, yields an effective solution for efficiently utilizing non-conventional energy sources [14], [15].

The MPPT technique is required because PV has inherent non-linear properties. Different techniques had been utilized by the researchers like as Perturb and Observe

(P&O), Incremental Conductance (IC), neural network & fuzzy based MPPT techniques [16]. An IC and P&O are the most straightforward and effective of these strategies, and as a result, were developed in the thesis work. The proposed thesis work revolves around the development of appropriate controllers to address several PQ issues [17]. The control algorithms need to achieve several tasks viz. estimation of fundamental component & phase angle, synchronizing signal estimation, and DC-link voltage controller [18]. Control techniques commonly employed focus on PLL and FLL circuits [19], [20]. The PLL circuit is developed using a loop filter, a phase detector, and a voltage-driven oscillator to constantly match the frequency of the system to the input signal. All FLLs & PLLs are developed to determine the frequency, amplitude and phase angle of the incoming signals from nonlinear load current. SRFT-PLL is a well-known and frequently used synchronisation method in hybrid systems for standalone applications. It is found to function very well under typical working circumstances, but its performance suffers greatly when subjected to harmonics in generated voltage [21]. As a result, there is a need to build, research, and evaluate the behavior of novel synchronisation techniques. Some improved PLLs and FLLs are reported such as SOGI-PLL, EPLL [22], CCF-PLL, ECCF-PLL [23], DSOGI-PLL [24], SOGI-FLL, SOSF-FLL, DROGI-FLL, DSC-FLL [25], and others have been studied and investigated for wind-solar based standalone hybrid system. In the literature, a few publications comparing the functionality of single-phase PLLs have been reported [26]. The focus of control algorithms for computing the fundamental load current component in wind & solar-based isolated systems is to ensure stable, accurate, and reliable operation under unavoidable intermittency of wind & solar energy. These algorithms are robust and aim to address uncertainties, provide fast response times, minimize oscillations, and maintain PQ standards in the presence of various uncertain conditions [27]. Different algorithms were employed to improve the PQ in three-phase wind-solar islanded hybrid systems. Some conventional algorithms that have been discussed in the literature which include IRPT [28], Power Balance Theory (PBT) [29], SRFT [30], SOGI controller and its different variants have been also implemented in single & three-phase systems [31]. Adaptive control algorithms have made significant improvements in the mitigation of PQ problems with Adaline [32], Least Means Forth (LMF), and various versions of Least Mean Square (LMS) based techniques [33].

Renewable energy-based standalone systems are gaining popularity for power generation in remote and hilly places, particularly where grid supply is insufficient.

Advances in the field of renewable energy as well as a sharp rise in the cost of petroleum-based products are primarily responsible for this. Innovation and advancement activities in renewable energy (solar & wind) based technologies must continue to improve their performance, develop methodologies for properly estimating their output, and amalgamate them reliably with other existing generating sources [34].

Innovation and advancement in the field of wind solar based standalone systems has progressed substantially over the last few decades. To enhance the PQ in RESs based generation, advanced power electronics systems with innovative control strategies are being introduced. A CSMC is intended for a remote solar-wind based isolated system supported by BSS [35]. Adaptive filtering techniques, including MLMS management, are employed to improve PQ and compensate for effect of nonlinear loads. A MPPT employing the P&O control in wind power extraction and variable step size perturbation adaptive P&O in solar PV tracking are used to extract maximum power and overcome environmental disturbances [36]. It employs hierarchical distributed model predictive control (HDMPC). The upper layer in this HDMPC employs an iterative distributed control method to achieve power dispatch coordination. The lower layer enables predictive control, allowing both the economic and tracking properties to be realized [37]. To provide PWM switching pulses for VSC, an RZALMS-based control approach is employed. By harmonic suppression, voltage management during load imbalance, and reactive power correction at CPI, the VSC improves PQ [38] in standalone applications. The use of an LMMN control system is a technique employed for fundamental load component extraction and harmonics mitigation in power systems. This control system aims to mitigate harmonics in the system and extract the fundamental component accurately [39].

1.4   Scope of the Present Work

Some major research gaps in the literature on voltage & frequency regulation of SEIG integrated with PV systems have been identified based on a thorough review of the literature. These issues deal with synchronization methods and adequate compensation for improving PQ. The estimation of synchronization techniques from the unbalanced load current under various operating conditions together with estimating the fundamental component from the unbalanced load current is equally important.

Appropriate synchronization techniques and control algorithms need to be designed and selected. The performance of the selected techniques should be fast under dynamic conditions, having the least steady-state error, minimum oscillations, and robust performance without increasing the complexity of the algorithm.

The proposed research aims to design, simulate, and develop a standalone microgrid system powered by solar and wind energy, with a primary focus on addressing PQ problems to ensure a reliable and stable electricity supply. Such PQ issues include power support (active & reactive), harmonic mitigation, load balancing, and voltage & frequency regulation.

A brief description of the present work for standalone microgrid systems is given below:

1.4.1 Design and Development of a Standalone Hybrid System

The system configuration of the standalone wind solar hybrid system has been developed in Simulink/MATLAB. A hardware prototype is developed in the laboratory to authenticate the Simulink results. The IGBT-based VSC, voltage & current sensors, dc drive to emulate wind turbine, interfacing inductors, optocoupler, dSPACE-1104 and linear/non-linear load has been employed to develop hardware setup.

1.4.2 Developments of Control and Synchronization Techniques

Both conventional and proposed synchronization techniques have been developed throughout this study. These synchronisation approaches have been evaluated under a variety of operational circumstances. Unit-template, SRF-PLL, CCF-PLL, ICCF-PLL, DTOGI-PLL, SOSF-FLL, ADF-FLL, VGC-IPLL, 3Ø-APF-PLL, SOGI-FLL, and DROGI-FLL based synchronization techniques have been designed, developed and tested for a standalone system. Simulation and experimental validation of the developed techniques are presented in the research work.

1.4.3 Application of Control Techniques

Application of some three-phase control techniques has been proposed for achieving the fundamental component from distorted load current. As SOSF-FLL, VGC-IPLL, DSC-FLL, DSOGI-PLL, DTOGI-PLL, DROGI-FLL, 3Ø-APF-PLL control approaches have

been employed for the control and synchronization of the standalone system. The developed techniques have been employed for harmonics abatement, and reducing PQ problems.

1.4.4 SolarPV-Wind-based Standalone System Operation and Control

The integration of the SPV system at the DC-link side of an isolated microgrid system, along with reactive power compensation and MPPT techniques, offers a comprehensive solution for harnessing solar energy and improving the performance of standalone systems. The combination of simulation and experimental studies validates the effectiveness and viability of these methods specially in standalone applications.

1.5 Thesis Organisation

Entire thesis is organized in seven chapters describing the proposed work in a comprehensive way as follows

Chapter-1: This chapter presents an introduction and background for renewable energy-based autonomous power generation, causes of voltage & frequency variation, PQ causes, issues, and possible solutions.

Chapter-2: A literature review on system description and control for wind-solar-based standalone hybrid systems, MPPT & synchronization techniques and fundamental component estimation techniques are incorporated in this chapter.

Chapter-3: This chapter discusses the designing of wind turbine and PV array for the islanded microgrid system. The development of a hardware prototype using dSPACE 1104, VSC, optocoupler, voltage & current sensors is also presented.

Chapter-4: This chapter presents the control techniques utilized for three-phase three-wire (3P3W) wind-solar-BES-based isolated hybrid system under the intermittent condition of wind solar feeding an unbalanced load. The control algorithms have been designed to enhance the overall PQ of the isolated system.

Chapter-5: This chapter addresses the execution of control algorithms utilized for three-phase four-wire (3P4W) wind-solar-BES-based islanded hybrid system. The control

algorithms have been investigated to improve the PQ under intermittent conditions with wind & solar feeding the nonlinear unbalanced load.

Chapter-6: This chapter describes the performance comparison of various control algorithms used in chapter 4 and chapter 5 under different operating conditions of the proposed system.

Chapter-7: This chapter summarizes the major benefits of different control approaches and their comparison in the operation of a standalone hybrid system. The future scope of the proposed work in this field is also presented in this chapter.

Chapter 2

Literature Survey

2.1 General

In the previous chapter, an introduction to the requirement of wind driven SEIG, PV array, BES, PQ problems, effects and solutions in a wind solar based islanded hybrid system have been presented. The state of the art, scope of work and the layout of the thesis work have been discussed. Examining the properties of wind turbines & SPV and extracting the power from the RESs requires precise modeling which matches the characteristics of practical wind turbine & solarPV. The modern distribution system has been interfaced with the various forms of loads which impact the quality of power and has been reviewed. In this chapter, a comprehensive literature study for the synchronization and control techniques is presented which further enables the robust working of the isolated system under intermittent conditions of wind, solar and different loading. An MPPT algorithm-based SPV is connected at the DC-link of the VSC to provide the required power compensation of the isolated system. Further, a bi-directional dc to dc converter based BES is employed for the absorption/supply of extra power during intermittency. A detailed review of the Wind & Solar energy based standalone system under different operating modes on 3P3W & 3P4W is presented.

2.2 Literature Survey on Design of Wind Driven SEIG and their Modeling

Wind energy production capacity in India has increased significantly in recent years. The total installed wind power output as of 31 January 2023 was 41.983 GW, ranked 4th among all the countries. The increased use of RESs for electricity generation has indeed led to a greater emphasis on developing low-cost, low-maintenance, and robust generator units for isolated locations. These standalone applications typically involve generating electricity in remote areas or off-grid locations where connection to a centralized power grid is not feasible or economical. Many countries have abundant RESs, such as wind and micro/mini hydro, but face challenges in exploiting these resources due to their remote availability. In small WECS induction generators (IGs) have been increasingly used as a

low cost solution for electricity generation from wind energy. The benefits of employing an induction generator (IG) over a synchronous generator (SG) are well understood. Reduced size, rugged and, brushless construction, no need of DC-source, less maintenance, self-protection against severe overloads & short circuits, and so on are some of the advantages [40], [41]. In the islanded places where the typical grid supply is not easily available, alternative energy solutions are often employed to meet the community's energy needs. Biogas engines and small hydro or wind turbines can serve as independent prime mover to SEIG generating electrical supply to residential and agricultural loads. The SEIG has emerged as a viable substitute for the conventional synchronous generator for these application [42]. The operational principle of the SEIG has been demonstrated using the well-known phenomenon of self-excitation in IG with capacitor bank at their stator terminals as shown in Fig. 2.1.
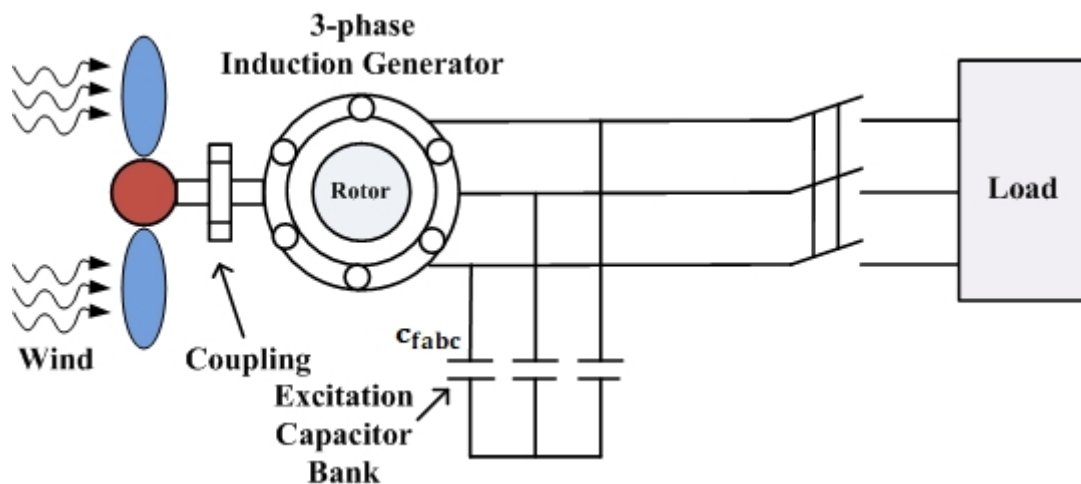
Fig. 2.1 Schematic diagram of wind driven SEIG system for isolated load

[43]. Extensive research has already been conducted on 1) performance evaluation in steady-state conditions [44], 2) choosing an excitation capacitor [45], and 3) the Transient response of SEIG [46]. One of the primary disadvantages of the SEIG is its poor voltage & frequency regulation, which limits its field applications. Several strategies for enhancing voltage regulation exist, including the following: 1) Switched capacitor strategy; 2) Electronic load controllers; 3) Dynamic VAR controllers; and 4) Other solid-state based controllers topology have been discussed in the literature [47], By utilizing a fixed shunt excitation capacitor bank in a SEIG, maintaining a constant terminal voltage under different loads can be challenging. These limitations arise due to the reactive power

requirements of the SEIG, which can change with different load conditions. To manage the SEIG's terminal voltage, one approach is to use a switched capacitor method, which provides voltage control in discrete steps [48]. As an alternative, the prime mover speed can be altered to control the terminal voltage, but this mechanical method of turbine control is more difficult and expensive. Changes in primary mover speed also cause changes in frequency. Further, to control the SEIG terminal voltages & frequency various types of control schemes are also utilized to enhance the performance in standalone applications and depicted in Fig. 2.2 [49].
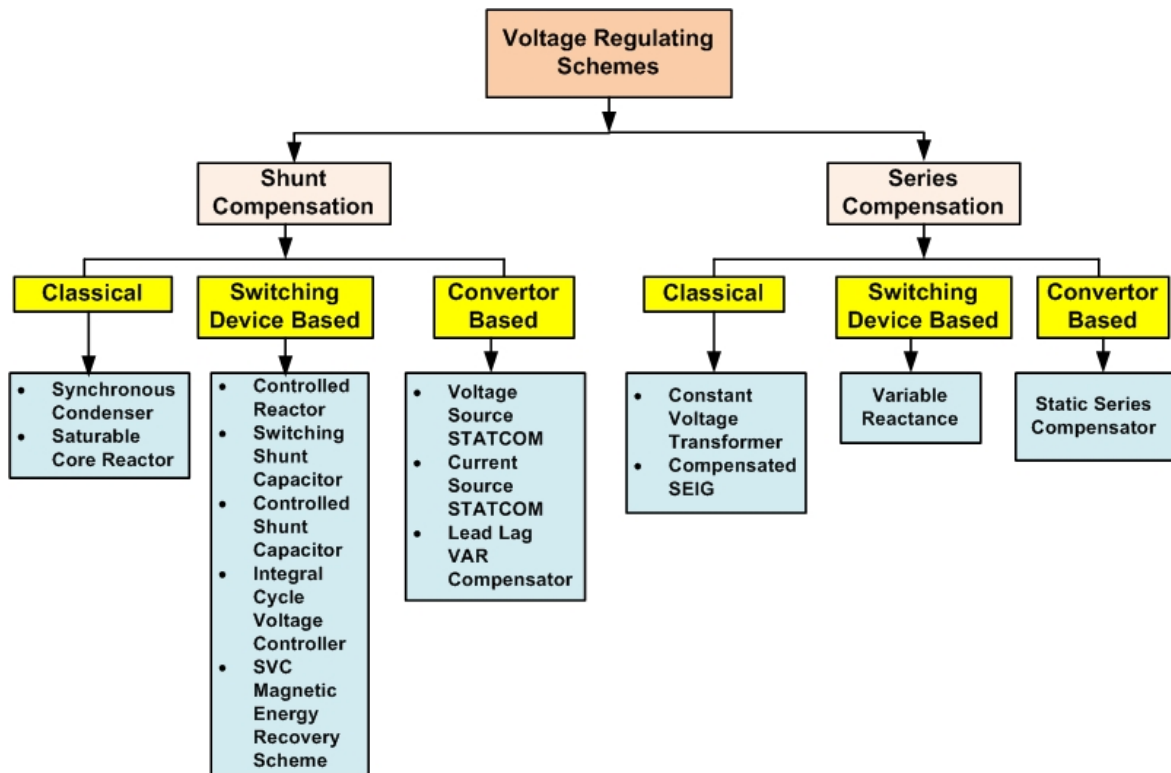
Fig. 2.2 Voltage regulation schemes of SEIG

In the electric load governing (ELG) strategy for a SEIG, the terminals of the SEIG are interfaced with an impedance controller. This approach maintains constant voltage and frequency without the need for turbine speed control or management of the generator excitation capacitors. In this technique, a programmable load resistor is connected over the SEIG terminals to ensure that the generator consistently provides full-load power while maintaining the rated value of the excitation capacitor bank. The load resistor in the constant power load method is indeed adjustable and controlled to produce the desired amount of power [50], [51]. Despite being suitable for small micro-hydro units, the ELG is not a financially viable choice for managing the voltage/frequency of a SEIG [52]. It is

very inefficient, especially for inductive loads. The usage of static VAR compensators (SVC) can provide smooth regulation of the SEIG voltage during intermittency in the load of the system [53]. By actively injecting or absorbing reactive power, the STATCOM helps to regulate the voltage at the SEIG's terminals and ensures a stable and constant voltage output, which is critical for reliable and efficient operation of the SEIG. The STATCOM has also improved system stability and reduced harmonic distortion [54]. A STATCOM can absorb or supply the needed reactive power to control the voltage of SEIG at CPI with the variation in loads. The SEIG may have a lagging power factor, which can affect the overall PQ of the system. The STATCOM can adjust the output of reactive power to improve the power factor and bring it closer to unity, improving the system's power factor [55]. A STATCOM-based regulator, on the other hand, is incapable of adjusting the frequency of SEIG under different load requirements. A STATCOM with a BES on its DC-bus serves as a source or sink of real power, allowing SEIG to manage the voltage & frequency in the desired limit under fluctuating load environments. The STATCOM can also compensate for the reactive power required of the SEIG, thereby reducing the burden on the grid and enhancing overall system efficiency [56].

The STATCOM improves the overall performance of isolated hybrid energy systems by effectively managing reactive power, correcting the power factor, and participating in voltage regulation schemes. It contributes to improved PQ, increased system efficiency, and reliable and stable operation of energy system under varying load conditions. Because of its capability to respond quickly to variations in reactive power demand, the STATCOM is a valuable asset for islanded operation of energy systems that use wind & solar [57], [58]. The challenges associated with tuning PI controllers in a specific scheme involving an ELC (Electric Load Controller) and a STATCOM (Static Synchronous Compensator) are also discussed. While the STATCOM remains a valuable option for precise and dynamic reactive power control, these alternative techniques offer simpler, more cost-effective solutions for providing the necessary reactive power to SEIGs and improving power factor and voltage regulation. According to the literature, one such technique involves using combinations of series and shunt capacitors to provide changeable power support to the SEIG. The appropriate selection of shunt & series excitation capacitors is crucial in ensuring the efficient and reliable operation of a SEIG when used in various applications. The choice of capacitors depends on several factors, including the SEIG's rating, load characteristics, and the desired level of power factor

correction and voltage regulation [59], [60]. The transient and steady-state performance analysis, the selection of excitation capacitor banks for the series-compensated short-shunt SEIG, especially when operating with unbalanced nonlinear loads, are also available in literature [61]. Nonlinear loads introduce harmonics and unbalanced currents, which can adversely affect the generator's performance. However, the steady-state analysis considering these factors is less prevalent in the literature. Transient analysis involves studying the generator's behavior during sudden changes in load or other system parameters. Transients can have a significant impact on the generator's stability, voltage regulation, and overall performance. However, detailed investigations specifically considering unbalanced nonlinear loads may be scarce [62].

Transient behavior refers to the response of the SEIG to sudden variations in load conditions, such as the starting or stopping of a wheat mill or water pump. Variations in load can cause changes in the speed and torque requirements, affecting the SEIG's performance [63]. The optimal arrangement of shunt & series excitation capacitors depends on the specific characteristics of the SEIG and the IM being used. It is determined through system analysis and calculations, taking into account factors such as the IM's power rating, starting current, and desired voltage dip limits. The engineers and experts typically perform these calculations using appropriate formulas and modeling techniques to find the most suitable capacitor values for a given setup [64], [65]. The phenomenon described involving series capacitors connected to the SEIG and Induction Motor (IM), leading to low-frequency oscillations and resonance is also reported [66]. To maintain synchronization with the isolated system and ensure efficient power transfer to grid, the frequency of the generator's output voltage should match the grid frequency. If there is a frequency mismatch, it can cause issues such as PQ problems, poor voltage regulation, or even instability in the electrical network [67].

2.3 Literature Survey on PV System Modeling and MPPT Control Algorithms

Power semiconductor technology has advanced significantly during the last few decades. The cost of PV cells has also decreased extensively; solar energy has become one of the most forms of energy solutions. Furthermore, using direct sunlight is inexpensive and has no impact on the environment [68]. As of December 2013, India's total solar

energy installed capacity was 2180MW, with the potential to contribute a solar installed capacity of 63.303 GWAC by December 31, 2022. However, due to significant advancements in solar technology over the years to improve efficiency and reduce costs are reported. Innovation and advancement efforts are focused on enhancing the response of solar cells and modules, increasing their efficiency, and making them more affordable [69]. The choice between series/shunt connections of solar PV cells depends on the specific needs of the system and the load being served. For medium power demands, a series connection can provide a higher output voltage, but the current will be limited to that of each module. If higher power demands are expected, a combination of series and shunt connections, such as using multiple series-connected strings in parallel used to generate the desired amount of power [70].

The same is true for shunt connections, where the system voltage is constrained to the voltage of a single module and the system current is equivalent to the addition of the currents of each module. As a result, for solar PV modules, a range of inter-connection patterns such as series-parallel (combination of series & shunt connection scheme), Total Cross Tied, Bridge linked, and Honey Comb are offered [71]. The most common topologies are series-parallel connections, which are commonly used to meet load power requirements. However, the output power may be drastically decreased if any of the PV system are shaded. Partial shadowing can be caused by large trees, hoardings, poles, and towers, among other things [72]. As a result, partial shadowing distributes the shadow over the solarPV array unevenly. Partial shadowing is a critical consideration in PV system design and installation, and addressing its effects is essential for maximizing power generation and ensuring the long-term reliability of the system.

The perturbing effects of partial shade are numerous peaks in the PV characteristics and steps in the characteristics [73], [74]. Multiple MPPT control approaches have been investigated in the literature [75]. As classical MPPT methods, P&O [76], hill climbing (HC) [77], and IC [78] are discussed. Despite being easier to implement in hardware, the HC and P&O approaches exhibit considerable oscillations that are closer to the MPP, which causes power losses. An IC approach is accurate and adaptable in changing atmospheric conditions [79]. P&O & IC are conventional algorithms that are easy to implement, less complex and works effectively under varying solar insolation and temperature condition [80].

2.4 Literature Survey on Causes of Voltage & Frequency Variation, Power Compensation, PQ Problems and their Solution

A STATCOM is employed to provide current compensation for reactive power support to the SEIG. It helps to maintain a consistent frequency & voltage in the isolated system, thereby improving voltage regulation of SEIG. Additionally, the STATCOM manages the system's active power by storing excess power in a Battery Storage System (BSS) and supplying it when needed, such as during heavy load demand or at night when the SEIG output may be insufficient [81]. In a microgrid system with 3P4W loads, a generalized filter-based control approach provides an effective solution for voltage & frequency regulation, harmonic suppression, and compensation of neutral current. It improves the microgrids overall performance and reliability by providing added control and stability [82]. By integrating the PV array, BSS, and STATCOM, the microgrid system can benefit from enhanced stability and reliability, improved PQ, and better control over voltage and frequency variations. The combination of PV array, BSS and power conditioning (STATCOM) allows for a reliable and efficient operation of the microgrid [83].

Modern distribution networks are quite complicated and are linked to several sorts of loads. Different PQ difficulties can emerge owing to varying loading situations and natural disturbances. Voltage flicker, Transients, short and long-duration voltage transients, voltage imbalance, and waveform distortion are the most common PQ concerns. Lightning strikes, capacitor switching, single line to ground faults, switching on/off loads, 1-phase loads connected to 3-phase supply, adjustable speed drives, power electronic converters, half-wave rectification, arc furnaces, and other non-linear loads are the primary causes of poor PQ [84], [85]. These PQ difficulties induce failure, improper operation of electrical equipment, and energy loss, all of which result in direct or indirect economic loss [86]. Power experts are deeply concerned about the introduction of harmonics at the CPI in current distribution systems. The primary cause is the advancement of power electronics equipment interfaced with the distribution system, which introduces harmonics into the system [87]. The integration of large-scale PV and fast-charging EV batteries connected to the distribution system also had a negative influence, particularly on voltage magnitude and harmonics [88]. These harmonic currents cause higher losses and heating in a variety

of electromagnetic equipment. When reactive power compensation capacitors are used to improve power factor in electrical systems, there can be a risk of resonant conditions occurring. Resonance can happen when the capacitance of the power factor correction capacitors matches the inductance of the system or specific components within it, such as transformers or cables. PQ standards have been proposed by the IEEE and the International Electrochemical Commission (IEC) [89]. IEEE 1159:2019 (revision of IEEE Std 1159-2019) [90] The prescribed standards are focused on the characterization, measurement, quantification, and interpretation of electromagnetic disturbances in power systems. Its purpose is to provide guidelines for understanding and addressing variations that may arise from internal factors within the power supply or load machinery [91].

IEEE 519:1992 [92] discusses the IEEE recommended practice and standards for harmonic mitigation in electrical-based systems. The IEEE 1547-2018 standard (a version of IEEE 1547-2003) provides standard for interconnecting distributed resources with electric power systems. Their each DER shall meet at point of common coupling (PCC) [93] The integration of wind & solar based energy resources with Electric Power Systems (EPSs) requires the establishment of criteria and standards to ensure safe, reliable, and efficient operation. These criteria and standards address various aspects of DER integration, including technical requirements, communication protocols, operational procedures, and safety guidelines [94]. To address the PQ difficulties, various strategies have been employed. Active power filters (APFs) are one of the most common, and they are classified into three types: shunt, series and hybrid [95]. A series active compensator is linked in series at the load end and is employed to alleviate voltage-based PQ issues like voltage sag/swell, flickers, voltage perturbations, voltage imbalance, and harmonics. Solid State Static Series Compensators (SSSCs) [96], [97] and DVRs are examples of series APFs [98]. DSTATCOM is a term used to describe shunt APFs used in distribution systems. In a shunt-connected state, it can be used as a VSC or Current Source Inverter (CSI) to the CPI. DSTATCOM has been used to solve current PQ issues like harmonic mitigation, reactive power support, balancing of load, and voltage regulation [99]. Because of advancements in switching devices, DSTATCOM is currently rather common for mitigating PQ difficulties [100]. Previously, MOSFET and GTO were used as switching devices, but now it employs IGBT for easy operation and improved performance [101]. The hybrid APF configuration offers a more comprehensive solution for PQ problems by combining the advantages of both series & shunt APFs [102]. The hybrid APF i.e. unified

power quality conditioner (UPQC) is an example [103]. There is a technology or solution that can improve PQ in both voltage and current-related PQ problems. However, this technology has some drawbacks, including complex control, requiring more switches, and therefore being more expensive [104]

2.5 Literature Survey on Synchronization and Control Algorithm for Operation of Standalone System

Control algorithms necessitate the computation of synchronizing signals and the extract fundamental component from the distorted load current. The unit template approach is the easiest method for generating the synchronizing signal, but it only works in the ideal state of an isolated system [105], [34]. However, if the isolated system has multiple PQ difficulties, such as distortion, noise, and DC-offset, novel and enhanced techniques for estimating synchronizing signals are necessary. Furthermore, researchers have developed many PLL approaches, some of which do not perform well under non-ideal or intermittent situations. Researchers employed SRF-PLL as a typical PLL for phase and frequency computation, and it was realized for the production of synchronizing signals [106]. EPLL is capable of reducing dual-frequency oscillations and mitigating harmonics [107]. The ROGI-PLL technique is frequently employed in standalone systems for synchronisation because of its simplicity and efficacy [108]. The ROGI-PLL's performance is shown to be unsatisfactory under unbalanced load and DC-offset conditions. ROGI-FLL has been employed for effective ROGI operation under variable frequency conditions [109]. The block of FLL is implemented to evaluate the frequency of the input signal. When the grid voltage has DC-offset, ROGI-FLL's poor filtering capacity prevents it from producing satisfactory results. CC-ROGI-FLL has been offered as a solution for the eradication of the DC-offset in grid voltage [110]. Under steady-state conditions on a heavily deformed grid, the frequency measured by the FLL exhibits varying degrees of oscillation. In a 3-phase system, a PLL based on the CDSC has been examined. This necessitates the use of transform equations as well as an extra Proportional Integral (PI) controller [111]. Under intermittent RESs and distorted load current, a robust frequency estimate technique has been presented [112]. Furthermore, an Affine Projection Like (APL) approach for estimating synchronizing signals in isolated microgrids has been proposed [113]. These techniques were used under variations in frequency and distorted conditions, but the DC-offset condition was not covered. Except under DC-offset

conditions, these algorithms produce the least steady-state error in frequency computation. The function of Artificial Neural Networks (ANN) in estimating power system parameters is unsurpassed. They have been used to detect phase and symmetry components, harmonics, and so on [114], [115]. Particle Swarm Optimization [116] and recurrent training of neurons for proper weight estimate [117] were two of the earliest ANN approaches. Furthermore, if real-time implementation algorithms based on ANN methodologies are to replace conventional PLLs, they must be quick, precise, and converge within a few cycles. By using the per-phase model and the multi-loop control system, the four-leg converter can effectively handle unbalanced load conditions and provide better orthogonal signals. This improves the converter's performance, enhances the quality of the output power, and ensures reliable operation in practical applications. By removing the requirement to deal with symmetrical components, the suggested control technique can deliver balanced output voltages under varying load demands [118].

The PQ enhancement technique necessitates the use of proper control algorithms. In literature wide range of control algorithms, such as IRPT [119]–[121], SRFT [122], [123], LMS [124] and MLMS [125], have been used for both 3P3W and 3P4W standalone systems. The control approach is designed to extract or estimate the fundamental component. The unpredictable and non-linear nature of load current, however, necessitates that the developed algorithms produce accurate and timely results under all circumstances. Although several methods have been developed for shunt compensation, it is still required to carefully examine changes in convergence time, mathematical level of complexity, quick dynamic response with fewer oscillations, and steady-state response. The most efficient method to develop a control algorithm for improving PQ in isolated 3P3W and 3P4W wind-solar hybrid systems, according to recent literature on FLL-based control techniques, is to use a filter that is both effective and efficient [126], [127]. Various PLL variants have been reported in the literature [128]–[130] as well as recent advances in the study of PLLs [131]. Reduced-order generalized integrators (ROGIs) were developed [132] and are thought to be less difficult than SOGIs, however, they require a fundamental component from the load current [31]. In research articles, FLL-based control approaches are used for harmonics evaluation and suppression in a standalone system. EPLL-based algorithms have also been described in the literature for various applications [133], and they can also be employed as SAPF control algorithms.

2.6 Literature Survey on Bi-directional Power Control and Battery Energy Storage System

Recent advancements in SolarPV materials and technology have made solar based power generation very cost-effective and provide better power options for distant rural locations [134]. Electricity generated by wind & solar is inherently unbalanced, which has a negative impact on the utility grid. With an emphasis on electric vehicles or fuel cell applications and other, Energy storage device interface in RESs usages of bi-directional converters have increased. A large number of dc/dc converters that have been demonstrated to match dc buses with voltages that are significantly different from one another, ranging from tens to hundreds of volts [135]. It has two symmetrical full-bridge converters fed by single-phase electrical power. Furthermore, the first-generation IGBTs had relatively slow switching speeds, leading to longer switching times and higher power losses during the transition between on and off states. This further reduced the efficiency of the converter. But during the past ten years, improvements in power device technology have allowed the converter to operate with up to 97% efficiency [136]. AC microgrids enable greater resilience, efficiency, and integration of RESs into the power distribution system, while also providing localized power supply and reducing dependence on the utility grid [137]. RESs and BES offer pollution-free and cost-effective alternatives to conventional power generation. They promote sustainability, enable distributed generation, enhance energy independence, and contribute to grid stability. The integration of RESs and BES is a major advancement toward a more clean and sustainable energy future [138]. The combination of electrochemical storage systems like batteries with solar PV systems has proven to be a powerful solution for integrating renewable energy into various distribution systems, providing both efficiency and sustainability [139]. A BES typically consists of a two-stage bidirectional converter, an intermediary filter, and a set of control approaches. The BES purposely inserts the battery SOC as a control variable in the control section because its retardation impacts the system's other control parameters [140]. The converter topology of the PV system is identical to that of the BES, but it contains a DC-DC unidirectional boost converter. However, during PV power uncertainty, its control system interacts with the MPPT algorithm to start control action. However, the PV system's performance in islanded mode is suboptimal, particularly in terms of voltage/frequency regulation [141], [142]. A hybrid energy storage system that combines a

bulk battery energy storage (BES) and an ultra-capacitor (UC) is described. The system incorporates a BDC controller with a minimum power rating. The objective is to develop a control strategy that optimizes the operation of the hybrid system while ensuring smooth mode switching and adherence to power limits. The suggested hybrid system operates in four different working modes, each with its characteristics and advantages. The control strategy is intended to select the appropriate mode following the operating circumstances and system requirements. Additionally, the control system manages the power distribution between the BES and the UC, determining how much energy is stored or discharged by each component [143]. The new system described in the study differs from previous systems in that the grid-side converter does not regulate the DC-link. Typically, in energy storage systems, the DC-link voltage or current is managed by the grid-side converter to maintain stable operation [144], by actively controlling the charging and draining cycles of the BES through the bidirectional controller, the system can manage the DC-link voltage at the desired level and manage the power flow according to the system's needs.

This control mechanism ensures a successful and effective operation of the BES while maximizing the utilization of the battery's stored energy. The integration of utility-scale SPV generation and a BES into the existing off-grid community has the potential to reduce operating costs, minimize environmental impact, enhance energy independence & quality and reliability of the power supply. It is a promising step toward a cleaner, more sustainable, and economically viable energy solution for remote off-grid communities. High operating costs, environmental concerns, and fuel handling issues with diesel-powered remote off-grid systems have spurred the use of alternate energy sources and energy storage systems. Operators of isolated microgrids have been looking for these alternatives based on these motivations. In response, a Canadian utility is looking into using utility-scale SPV generation and BES to supplement existing DGs in an off-grid community [145].

2.7 Literature Survey on Wind-Solar-BES based Hybrid Standalone System

There are plenty of rural locations without access to energy throughout the world. The lack of access to electricity for extended periods, as long as 10 to 12 hours each day, can indeed have significant adverse effects on the daily economic operations of the locals in

the affected areas. Reliable access to electricity is crucial for various economic activities, productivity, and overall quality of life. Many of these locations are abundant in RESs such as wind, solar, and bio-mass [146]. Reliance on grid electricity, which is primarily dependent on fossil fuels, can be considerably reduced by an island generation system based on local RESs. Because biomass-based systems are sensitive to supply chain concerns, solar and wind energy sources are favored. RESs (wind and solar) suffer from a large level of variation in power, and an intermittent nature. These problems make it impossible to guarantee stable electricity for standalone applications [147], [148]. While the BES can help reduce fluctuations in power, and enhance predictability, maximizing the utilization factor of energy sources is essential to improve the effectiveness and efficiency of the isolated systems. Operating each energy source at its optimal operating value can contribute to achieving this goal [149]. Implementing effective MPPT algorithms and control systems in wind and solar power systems is crucial for efficient energy conversion and utilization. It maximizes the power output, improves system performance, and enhances the overall efficiency of renewable energy systems [150].

A hybrid system based on renewable energy, which is a combination of two or more two types of generation sources, has the potential to minimize BES requirements while increasing reliability. Both (wind & solar) are complementary to one another in both daily and yearly patterns of behavior. Many researchers have presented Wind/Solar based hybrid systems [151]–[153] in recognition of the benefits of this combination. Because of its durable and brushless structure, low maintenance costs, and inherent short-circuit protection capability, the authors used a hybrid system with a SEIG [154]. Wind turbines also use permanent magnet synchronous generators. Gearless design is conceivable with PMSG, but it necessitates a 100% rated converter as well as a more expensive machine [155]. Furthermore, if speed regulation is performed, a full power-rated converter is required. By combining solar PV with a DFIG-based generator and employing appropriate control strategies, it is possible to achieve an autonomous system that operates as a microgrid. This system can provide a reliable and high-quality power supply, meeting the IEEE-519 standards for voltage balance, THD, and efficiency [117], [156], [157]. A DSOGI-PLL approach is designed to handle real-time signal processing requirements in power systems. This algorithm's enhanced filtering capabilities, harmonic attenuation, DC offset reduction, and sequence component calculation make it a valuable tool for power system analysis, control, and protection applications [24]. Isolated microgrids are

susceptible to instability difficulties during heavy penetration of fluctuating loads such as induction motors, resulting in continuous voltage & frequency oscillations that disrupt the standalone microgrid. By incorporating the MMSOGI-FLL control algorithm, the microgrid system can achieve stable and reliable operation, fast voltage/frequency response, dynamic reactive power control, management of CPI voltage, harmonics abatement, removal of DC-offset, and reactive power compensation. To ensure overall performance, stability, and PQ in an islanded power system, where a local area or microgrid operates independently from the main utility grid, several features are essential. These features are intended to make it possible for the islanded system to operate dependably and effectively [158].

2.8   Identified Research Gap

1) The concept of dump load (R_d) is being explored for the consumption of surplus power and regulating voltage/frequency of SEIG in standalone applications. However, the power consumed in dump load is many times not useful. Therefore, the usage of a PV system along with SEIG may create a scope of battery energy storage and also electrical vehicle battery charging at a DC link with a suitable controller.

2) Researchers have indeed been exploring the use of advanced control algorithms and hybrid algorithms for improving PQ in various power systems, including the control of Distribution Static Compensators (DSTATCOMs) in Self-Excited Induction Generator (SEIG) systems. These control algorithms offer enhanced capabilities for voltage and frequency control, leading to more effective and efficient system operation.

3) Synchronization techniques considering intermittent conditions of wind & solar and different loading conditions are to be addressed. Also, a fair comparison of these synchronization algorithms is required in both simulation and experimental environments.

2.9   Authors Contribution in the Proposed Work

The main contributions in this work are given as follows:

1) Design, modeling, and analysis of the 3P3W and 3P4W standalone system based on solar & wind energy in MATLAB/Simulink and design validation through the development of prototype hardware.

2) Implementation of various control algorithms for the synchronization and control of the proposed system under numerous operating scenarios like as fluctuation in wind speed and solar intensity while satisfying the dynamics of connected unbalanced non-linear load.

3) Design and implementation of MPPT techniques such as IC and modified P&O to extract maximal power from an SPV under dynamic circumstances.

4) Design and implementation of a BDC to manage the charging/discharging of BES during the variation in an isolated system.

5) The combined operation of the VSC and the BES provides a flexible and efficient way to manage fluctuations in load and power generation, enhancing the stability and reliability of the power system.

6) The developed control algorithms enhance system stability, provide a fast dynamic response, and reduced the steady state error during the extraction of fundamental load current component.

7) Further, the control algorithms with VSC maintain all the parameters of the standalone system and provides harmonics abatement, load leveling, power compensation, and enhancement in the overall PQ of the isolated system.

8) Moreover, a comparison is carried out between the proposed and existing control algorithms under different operating circumstances. The work regards the IEEE-519 standard norms of harmonics level and keeps the THD level below 5% under nonlinear load.

2.10 Objectives of the Proposed Research Work

The proposed research work shall mainly focus on the following aspects of SEIG.

1. Voltage & Frequency Control of Self Excited Induction Generator integrated with PV system and scope of using battery energy storage for voltage & frequency regulations in isolated applications.

2. Applications of advanced control algorithms for effective control of DSTATCOM and voltage and frequency control of SEIG and hybrid energy

systems.

3.   Use of evolutionary adaptive techniques for improvement of the dynamic performance of SEIG-DSTATCOM system in wind-solar energy applications.

2.11 Summary

A comprehensive review of the literature has been addressed in this section based on the voltage & frequency regulation of SEIG, design of wind turbine, PV modeling, MPPT techniques, synchronization techniques, control algorithms, configuration and power management for Solar-Wind-BSS-based 3P3W & 3P4W standalone hybrid system. The research gap and objectives have been recognized based on the literature review and the motivation for using an isolated hybrid system.

Chapter 3

Design and Development of 3P3W & 3P4W Wind-Solar-BES-based Islanded Hybrid System

3.1 General

This chapter discusses the development and design of a 3P3W & 3P4W solar wind-based standalone system. A detail mathematical calculation of design parameters have been carried out various elements for simulation and real-time experimental validation. It also discusses the design of wind turbine, modeling of the PV module, and the design of SPV array for the 3P3W & 3P4W renewable energy-based standalone system. The design of different elements of its system for simulation study is shown as per the standards required for the isolated system. The rating of the selected components for experimental work is determined by the accessibility of laboratory equipment.

3.2 Design and Development of 3P3W & 3P4W Wind-Solar-BES based Islanded Hybrid System

The major components of the 3P3W & 3P4W wind solar-based standalone system are a 3-phase SEIG, wind turbine, solar PV array, IGBT-based VSI, and BSS as shown in Fig 3.1 and Fig. 3.2 respectively. The capacitor bank is being utilized to provide the desired reactive power to SEIG generating rated voltage. The capacitor bank serves dual functions: first, it filters out the high frequency noise generated by the controllers, and second, it provides reactive power support to the SEIG. All other device ratings are selected with proper design considerations. The wind turbine acts as a prime mover for the proposed SEIG, which in turn helps the rotor of induction machine to turn faster than synchronous speed thus acting as an induction generator. The generated energy is supplied to the three-phase nonlinear load. Further, IC, P&O and MP&O MPPT techniques are being used to extract maximal power from an SPV. Further, a BES is interfaced at the DC-link with a BDC controller to consume the excess electricity and supply power during

intermittency and increase in consumer load. The standalone system is design & developed for providing electricity with enhanced PQ, reduced harmonics, power compensation, and load balancing.
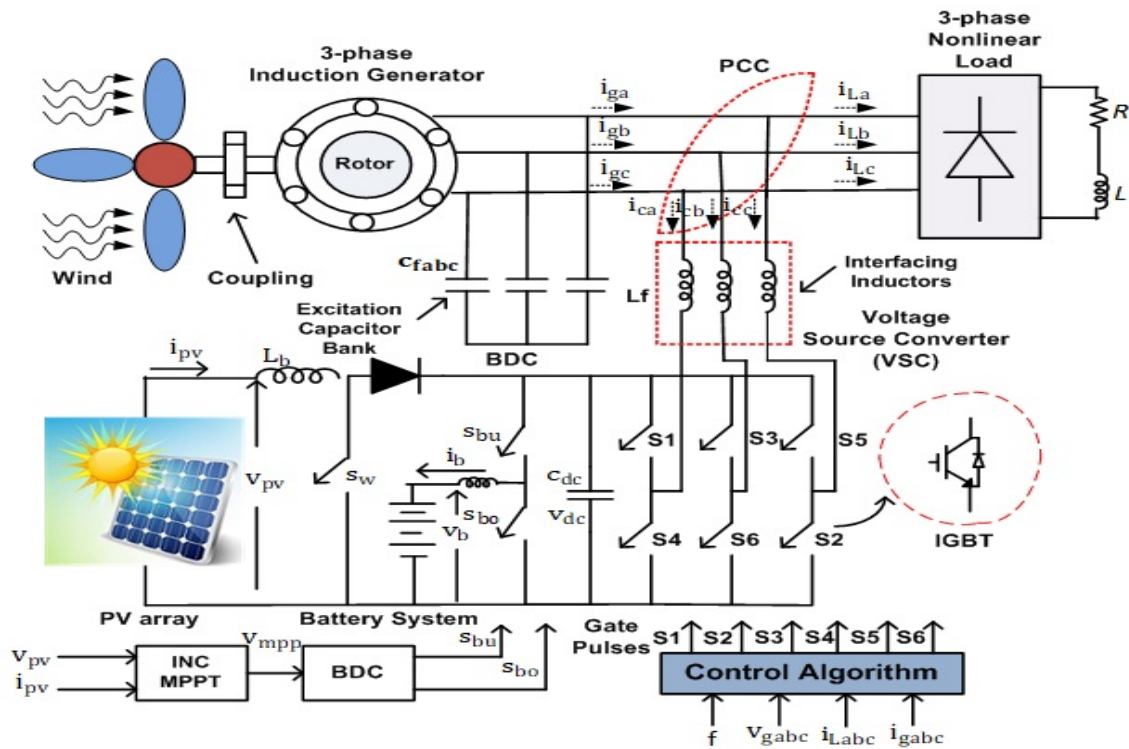
Fig. 3.1 System topology of 3P3W wind-solar based standalone hybrid system
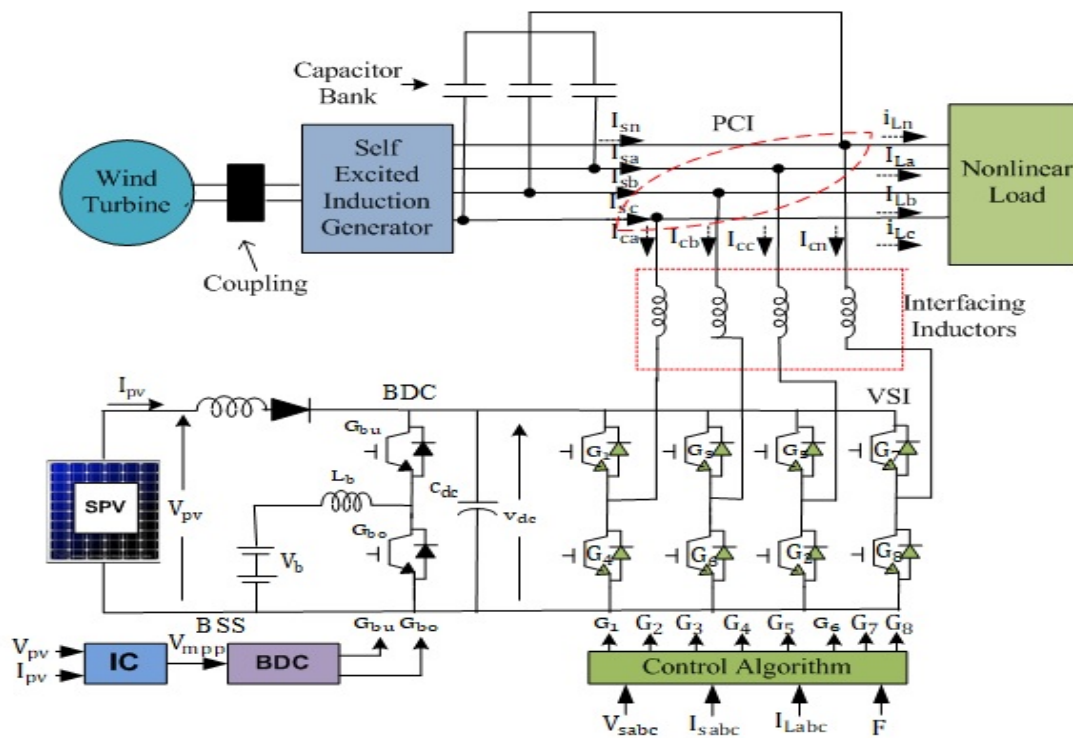
Fig. 3.2 System topology of 3P4W wind-solar standalone system

3.3 Calculation of Excitation Capacitance for SEIG

A SEIG is an induction machine used as a generator for standalone generation using wind energy. A SEIG requires an excitation capacitance to provide the necessary reactive power for self-excitation. Calculating the excitation capacitance for a SEIG entails calculating the generator's reactive power requirements and choosing an appropriate capacitor value to satisfy those requirements. The reactive power requirement is described as a percentage of the rated power output of the generator, and this percentage is essentially the generator's power factor [159]–[162].

Let, the KVAR required to SEIG is 4 KVAR.

$$V = I_C X_C \tag{3.1}$$

Where, $X_C = 1/2\pi FC$

$$I_C = V \times 2\pi FC = 400 \times 2 \times 3.14 \times 50 \times C \tag{3.2}$$

$$I_C = 124600 \times C \tag{3.3}$$

$$KVAR = V \times I_C / 1000 \tag{3.4}$$

$$KVAR = 400 \times 125600 \times C / 1000 \tag{3.5}$$

$$4 = 50240 \times C \tag{3.6}$$

$$C = 79.61 \mu F \tag{3.7}$$

Moreover, a synchronous speed test is performed in the laboratory to compute the values of voltages and currents is depicted in Table-3.1 and the graph is plotted between voltage & current to represent the saturation level or no load characterstics of SEIG.

Table-3.1 Voltage & current values at different speeds

Voltage(V)	Current (A)
80	0.25
100	0.3
120	0.5
140	0.7
160	1
180	1.1
200	1.2
220	1.35
240	1.5
260	1.65
280	1.75
300	1.95
320	2.1
340	2.3
360	2.5
380	2.7
400	2.95
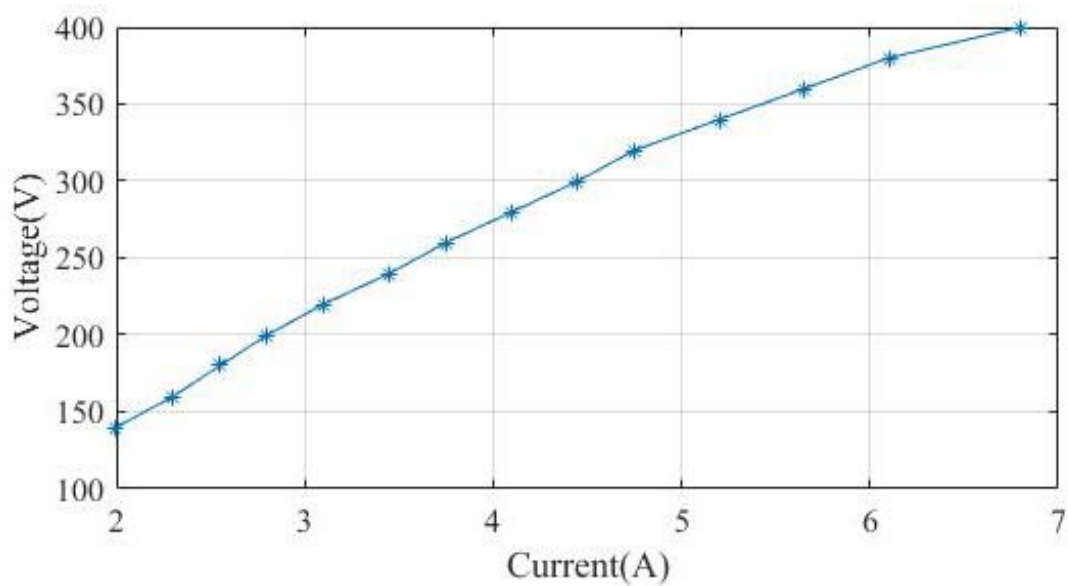
Fig.3.3 Saturation level of SEIG in simulation

The calculated value of the excitation capacitance obtained from the synchronous speed test can be used to optimize the SEIG's self-excitation capability and ensure stable operation.

3.4   Design of Wind Turbine

Selecting the correct rating of wind turbine is indeed crucial for the proper operation and performance of a SEIG in a standalone system. The wind turbine rating determines the power output of the turbine and affects various aspects of the system design and performance. The following relation is used for determining mechanical power.

c_p=power coefficient, v_W=wind velocity, α=area of blade
The output power equation for turbine is:

$$p = \frac{1}{2}c_p(\eta, \beta)\pi r^2 v_w^3 \tag{3.8}$$

Where, r=radius of blade (m), β=air density (kg/m^3)

The tip speed ratio (TSR) and the pitch angle (θ) are crucial parameters in wind turbine performance, and they directly influence the coefficient of performance (c_p) of the turbine. Wind turbine design and operation often involve optimizing these parameters to achieve the best possible energy conversion efficiency under varying wind conditions. The TSR is represented by (η) & computed as:

$$\eta = \omega_R r/v_W \tag{3.9}$$

Where, ω_R= angular velocity in rad/s [163]–[167].

3.5   Design of PV System

A solar cell can be modeled in different ways considering different parameters. A single-diode model with series & parallel resistance is considered nearer to a practical diode and easier to model [168]. The practical single-diode model with series & shunt resistance has been depicted in Fig. 3.4.
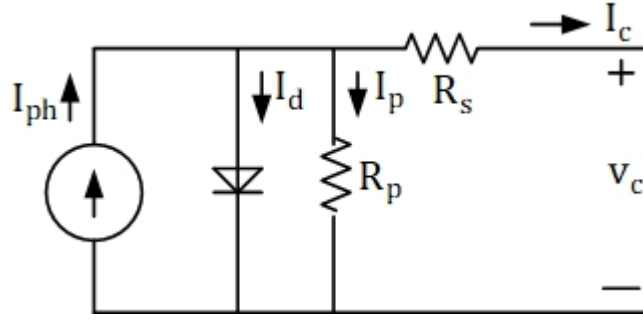
Fig.3.4 Practical single diode model of PV cell [169]

The output current (I_c) of PV cells is evaluated by using Kirchhoff's current law;

$$I_c = I_{ph} - I_d - I_p \tag{3.10}$$

$$I_c = I_{ph} - I_o \left[\exp\left(\frac{V_c + I_{Ra}}{\alpha}\right) - 1 \right] - \frac{V_c + I R_s}{R_p} \tag{3.11}$$

Where, (I_{ph}), (I_d), (I_p) and (α) is the photon current, diode current, leakage current and modified ideality factor in the parallel resistor [170]. Equation for α is given as

$$\alpha = \frac{N_s A k T_c}{q} \tag{3.12}$$

Where, N_s= no. of series cells in PV panel, k = Boltzmann's constant $(1.381 \times 10^{-23} \ m^2 kg - s^{-2} k^{-1})$, q = electron charge $(1.6 \times 10^{-19}$ coulombs), A is the ideality factor.

Ideality factor of different PV technology has different values as shown in Table 3.2. Here, the value if the ideality factor is 1.3 as the considered module is silicon polycrystalline.

The photo current (I_{ph}) is affected by the two variables solar insolation and temperature (T_c), as shown in the equation below.

Table 3.2: Ideality factor (A)

Technology	Si-Mono	Si-ploy	a-Si-H	a-Si-H tandem	a-si-H triple	CdTe	AsGa
Ideality factor	1.2	1.3	1.8	3.3	1.5	1.5	1.3

$$I_{ph} = \frac{G}{G_{ref}} (I_{phref} + \mu_{sc} \Delta T) \tag{3.13}$$

Ideally, $I_{phref} \approx I_{scref}$ and $\Delta T = T_c - T_{cref}$. Here, G_{ref} denotes the solar insolation at standard test conditions (STC) $=1000\omega/m^2$, T_{cref} is the PV cell temperature at STC (298K). $\boldsymbol{\mu}_{sc}$ is the temperature coefficient of short circuit current and is given by the manufacturer. I_{scref} is the short circuit current at STC and I_{phref} denotes photon current at STC. The diode current (I_d) is computed as

$$I_d = I_o \left[\exp\left(\frac{V_c + IR_s}{\alpha} \right) - 1 \right] \tag{3.14}$$

The reverse saturation current of a diode can be determined using the equation as follows.

$$I_o = \frac{I_{scref}}{\exp\frac{V_{ocref}}{\alpha} - 1} \left(\frac{T_c}{T_{cref}} \right)^3 \exp\left[\left(\frac{q\varepsilon_g}{Ak} \right) \left(\frac{1}{T_{cref}} - \frac{1}{T_c} \right) \right] \tag{3.15}$$

Where, V_{ocref} is the open circuit voltage of the PV module at STC and ε_g is the energy band gap of 1.12eV for silicon-based solar cells. A single PV module gives a very small amount of power. Hence, to extract significant power, we require a PV string or PV array which consists of several modules connected in series (N_{ss}) and in parallel (N_{pp}). So, the PV cell equation is modified to make an array of PV and is represented using the below equation. Now, the output voltage & current of the PV array is termed as V_{pv} and I_{pv}.

$$I_{pv} = N_{pp}I_{ph} - I_o \left[\exp\left(\frac{V_{pv} + IR_s \left(\frac{N_{ss}}{N_{pp}} \right)}{\alpha} \right) - 1 \right] - \frac{V_{pv} + IR_s \left(\frac{N_{ss}}{N_{pp}} \right)}{R_p \left(\frac{N_{ss}}{N_{pp}} \right)} \tag{3.16}$$

As the environmental condition varies, the output voltage & current varies according to the P-V and I-V curve. The P-V and I-V curve of the considered module is shown in Fig. 3.5(a) and (b). Fig. 3.5(a) shows the P-V and I-V curves of a module at various temperatures such as 0°, 25°, & 50° and fixed solar insolation $1000w/m^2$.

In this situations, output power and current increase as the temperature of the PV module decreases. This curve shows the non-linear behavior of PV modules as the environmental condition changes. In these curves, there is a point that shows the maximum power of the PV module and it is called the MPP of the PV module. Figure 3.5(b) shows the P-V and I-V curves of a module for difference solar insolation ($200w/m^2$, $450w/m^2$, and $900w/m^2$) and fixed temperature (25^oC) and it shows the as

the temperature increases the PV output current and power increases. MPPT has been employed to achieve the maximum power from the PV module or string or array. MPPT technique forces the PV module to work at the MPP of the PV curve. In the single-stage grid-tied PV system MPPT technique gives the reference voltage for the DC-link and in the double-stage grid-tied PV system it generates a duty cycle to the DC-DC converter to impose the module to work at MPP [171]–[173].
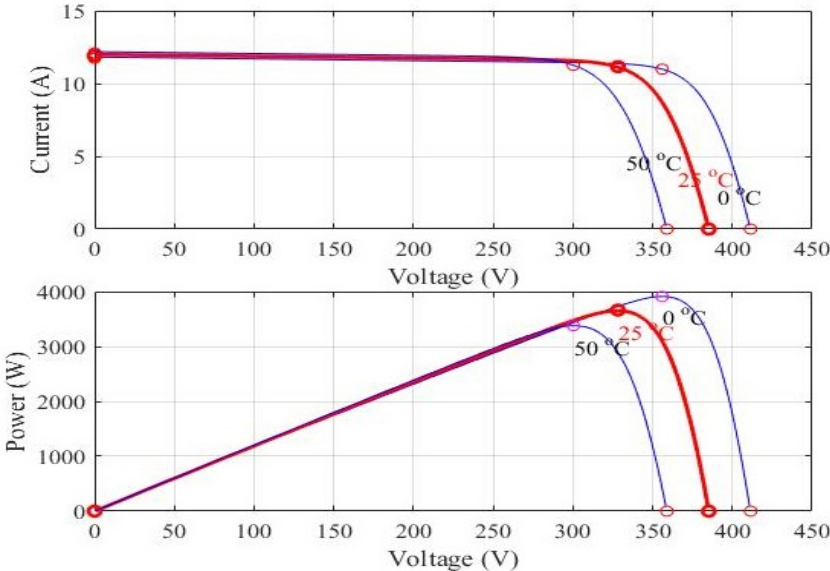
(a)
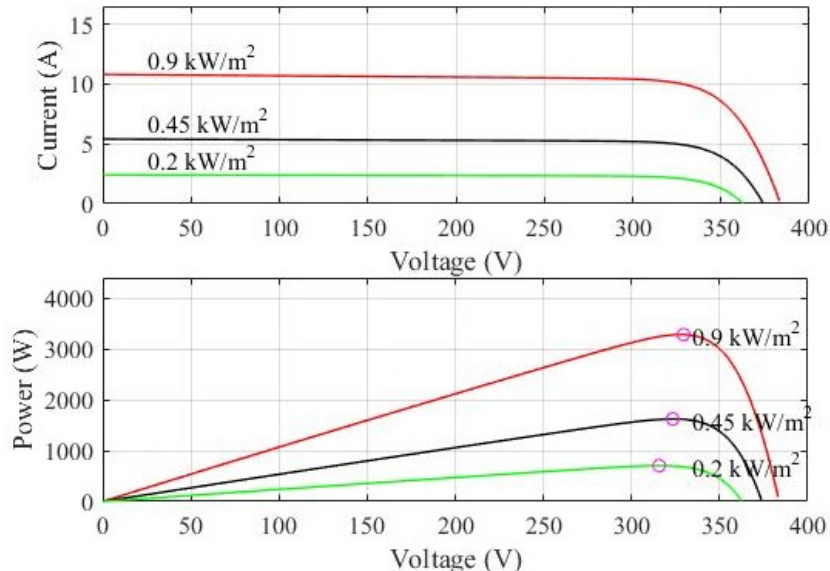
(b)

Fig. 3.5(a) P-V and I-V curve at different temperatures and fixed solar insolation (b) P-V and I-V curve at different solar insolation and fixed temperature

3.6 Design of Boost Converter for SPV

Interconnecting solar modules in series & parallel is a common approach to achieve the desired voltage & current levels for a given application in an SPV system. This configuration allows for better management of voltage & current to improve overall performance, efficiency, and power output. The solar PV array rating of 2.9kW mentioned here suggests that the total power capacity of the SPV array is 2.9kW. An SPV array rating of 2.9kW is explored in MATLAB/Simulink.

The input voltage of a boost converter is the PV array's MPP, which is 250 V. The boost converter's inductor (L_b) is built for a duty cycle calculated as

$$D = (V_{dc} - V_{pv})/V_{dc} == (400 - 250)/400 = 0.375 \qquad (3.17)$$

A boost inductor's designed value is expressed as

$$L_b = \frac{V_{mpp} \times D}{\Delta I_{rp} \times f_s} = \frac{250 \times 0.375}{0.1 \times 11 \times 20 \times 10^3} = 4.26 \text{mH} \qquad (3.18)$$

Where ripple current equals 10% of SPV current at MPP and (f_s) is the switching freq., which is 20 kHz in present analysis [14], [174], [175].

3.7 Design of DC-DC Bidirectional Controller

In the proposed standalone solar-wind energy system, the imbalance in active power is caused by variations in solar insolation levels and dynamic load. To solve this problem, a bi-directional controller (BDC) is employed at the DC-side of the VSC to regulate the DC link voltage and perform buck/boost operations for BES charging or draining. The major function of the BDC control is to maintain synchronization between power generation from the SPV and dynamic load. When there is excess power generation compared to the load demand, the BDC control allows the unused power to be supplied in the BES for later use. Conversely, if the power generation is inadequate to meet the load demand, the BDC control enables the BES to supply the required power. To achieve this control, two Proportional-Integral (PI) controllers are utilized in the BDC control scheme. The DC-link voltage must be regulated by the PI controllers to maintain the desired value under a variety of circumstances. The first PI controller monitors the DC-link voltage and generates a control signal to adjust the duty cycle of the VSC, allowing the buck or boost

operation to manage the BES charging or draining. The control signal is based on the difference between the observed DC-link voltage and the reference value. The second PI controller operates on the power error, which is the difference between the power generated by the energy sources and the power demanded by the load. By utilizing the BDC control with two PI controllers, the system can maintain the desired DC link voltage, ensuring proper regulation and synchronization between power generation and load demand. The control scheme enables the BES to absorb or supply the surplus or deficit power, respectively, thereby balancing the real power in the islanded hybrid system.

The equation for the regulation of DC link voltage in a proportional-integral (PI) controller can be represented as follows:

$$i_b^*(s) = i_b^*(s-1) + k_{dp}\{V_{dce}(s) - V_{dce}(s-1)\} + k_{di}V_{dce}(s) \tag{3.19}$$

Where, k_{dp} and k_{di} are the gains of the PI controller respectively.

$$\text{Where, } V_{dce}(s) = V_{mpp}(s-1) - V_{dc}(s) \tag{3.20}$$

The duty cycle of the BDC control, which determines the operation of the bi-directional converter for BES charging or draining, can be computed using a BES current Proportional-Integral (PI) controller. The duty cycle is typically calculated based on the following equation:

$$D_{dc}(s) = D_{dc}(s-1) + k_{bp}\{i_{ber}(s) - i_{ber}(s-1)\} + k_{bi}i_{ber}(s) \tag{3.21}$$

Where, k_{bp} and k_{bi} are the gains of BES's current PI controller.
The BES current error (i_{ber}) is evaluated by comparing the sensed BES current with the reference BES current.

$$i_{ber}(s) = i_b^*(s-1) - i_b(s) \tag{3.22}$$

The converter's Pulse Width Modulation (PWM) pulses are typically generated by comparing the duty cycle to a saw-tooth signal. The saw-tooth signal serves as a reference waveform for generating the PWM pulses [176]–[180].

3.8 Development of Sensors and Amplifier Circuit

Sensors are an integral part of the islanded system. They are utilized to sense the different parameters (V & I) and gives to ADC channels of dSPACE 1104. The circuit diagram for the voltage (V) & current (I) sensors has been shown in Fig. 3.6(a) & (b). Fig. 3.6(c) & (d) depicts the practical voltage & current circuits.

(a)
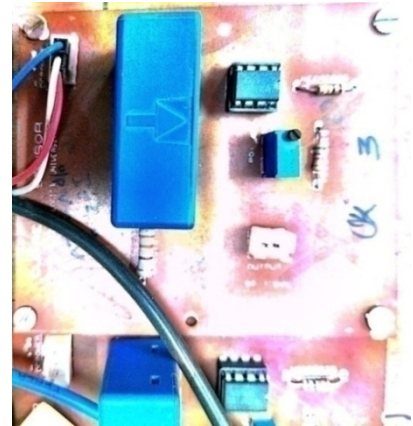
(b)
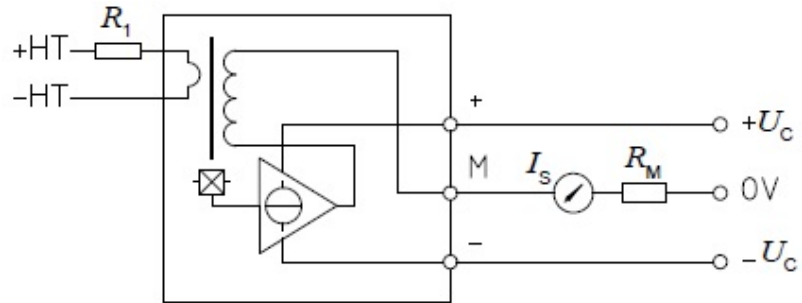
(c)
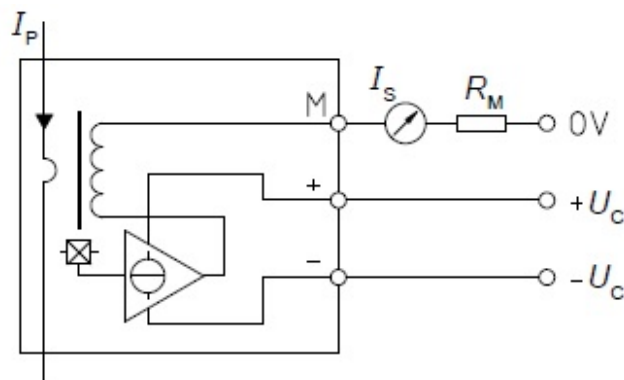
(d)
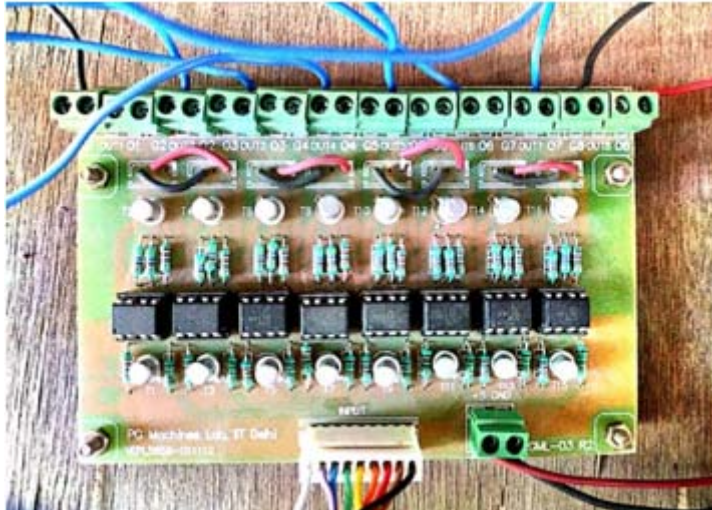
(e)

Fig. 3.6(a)-(e) Development of sensors and amplifier circuit

For sensing the voltage parameters LEM makes Hall-effect based LV25-P/sp2 model is used. Its maximum input voltage range is 1500V. The maximum current of 14mA is limited in the input terminal. To reduce the input current a high resistance of 47kΩ has been used with the power rting of 2W. In the output of the sensor OP07 IC has been used to change the gain ratio of the current sensor such that the output of the voltage sensor should not exceed 5V. For sensing the current parameters LEM make Hall-effect-based LA25-NP model is used and its conversion ratio is 1:1000. In the output of the sensor OP07 IC has been used to change the gain ratio of the voltage sensor such that the output voltage of the sensor should not exceed 5V. The operational amplifier circuit is the same for both the voltage and current circuits [181], [182].

3.9   Development of Experimental Prototype

A hardware prototype of an islanded system has been developed in the laboratory, as demonstrated in Fig. 3.7. The major component of the standalone system is a prime mover DC motor, SEIG, capacitor bank, sensors, opto-coupler, dSPACE-1104, digital storage oscilloscope (DSO), DC supply, multi-meter, auto-transformer, connecting cables, monitor and power analyzer. The voltages & currents of the isolated system are measured using the Hall-effect sensors circuit. The use of two Hall-effect sensors, such as LEM LA-25, indicates that the standalone system is designed to measure the source currents of phases

'a' and 'b' in a balanced 3P3W & 3P4W system. Hall-effect sensors are commonly employed for non-intrusive current sensing as they can detect the magnetic field formed by the current flowing through a conductor. These current sensors are powered by a 15V DC supply. The voltage sensor used in the standalone system captures the voltage signal that needs to be further processed or utilized for measurement, control, or analysis purposes. To ensure accurate and reliable signal transmission, the sensed voltage signal is typically fed to a buffer circuitry. A buffer typically has unity gain and low output impedance while maintaining high input impedance. Using the four channels of the KEYSIGHT INFINII VISION DSO-X 2024A, the dynamic behavior of the standalone system's signals, like voltages, currents, and other relevant parameters, can be observed and analyzed in real-time. This facilitates the evaluation of system performance, identification of abnormalities or transient behavior, and optimization of the system's operation or control strategies. The PQ analyzer (HIOKI PQ3100) was employed to examine the results in the system's steady state.
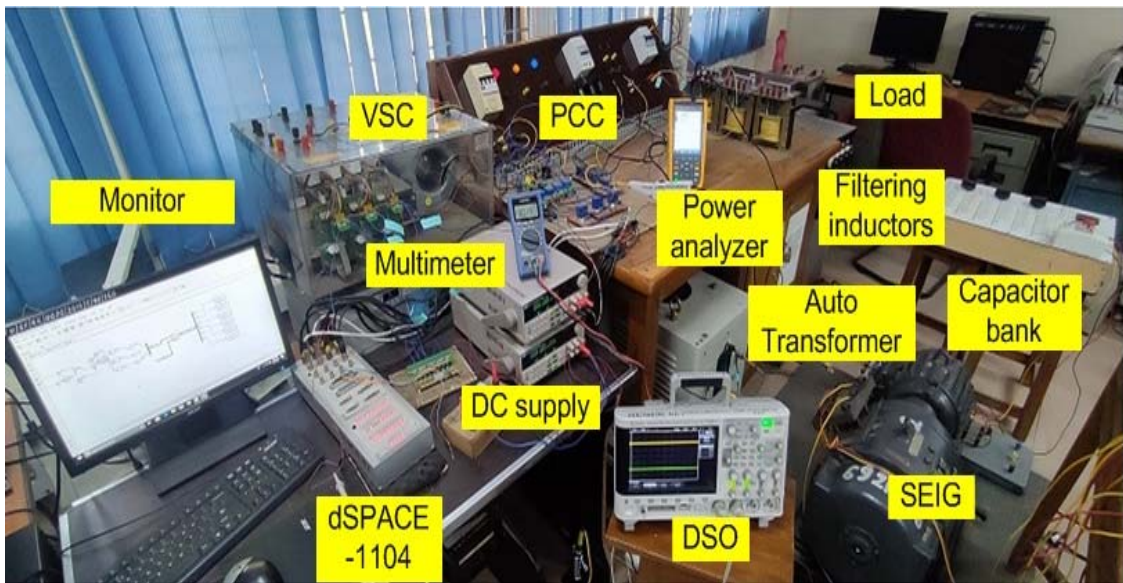
Fig. 3.7 Hardware prototype of a standalone system

3.10 Summary

This chapter addresses the design & development of a wind solar-BES-based islanded hybrid system for standalone applications. Design equations, system configurations for 3P3W & 3P4W, and experimental prototype setup have also been presented. The PV system and BES are interfaced at the DC-link of the VSC for active and reactive power

injection to the hybrid system under dynamic conditions. These system configurations have been considered for simulations & experimental study on the proposed schemes to improve the PQ, provide power compensation (active & reactive) and load leveling in hybrid energy system for standalone applications.

Chapter 4

Implementation of Advance Control Algorithms for Three-Phase Three-Wire (3P3W) Wind-Solar-BES-based Islanded Hybrid System

4.1 General

A precise and accurate estimation of phase & frequency is crucial for the control and synchronization of the islanded hybrid energy system. Hence, the use of advance control algorithms and synchronization techniques is mandatory. Out of several synchronization techniques discussed in literature PLLs and FLLs based synchronization are make popular. Some conventional and advanced control techniques for three-phase PLLs & FLLs are discussed in this chapter for computation of phase, frequency, amplitude and the synchronizing signals under uncertain conditions of RESs and unbalanced load. The designed PLLs & FLLs are further applied for the PQ improvement and compensation of reactive power in the 3P3W standalone system.

Various three-phase control techniques are examined under the intermittent condition of wind, solar and unbalanced load in this chapter. These include Unit Template Estimation, DSC-FLL, SOSF-FLL, VGC-IPLL, 3Ø-APF-FLL and ICCF-PLL. Their individual simulation results and experimental performances are examined under various operating scenarios.

4.2 Unit Template Estimation

This is the simplest method to estimate unit templates of the voltage signal of each phase. This method is largely used by researchers under normal conditions of the standalone system [183], [184]. Three-phase voltages have been measured at CPI and depicted as v_{sa}, v_{sb}, and v_{sc}. Unit templates are obtained by simply dividing the individual phase voltages by the magnitude of the three-phase voltage at the CPI of an isolated system (V_m).

If, V_m is the voltage amplitude of the terminal voltage, which is expressed as

$$V_m = \left(\tfrac{2}{3}\right)^{1/2} \left(v_{sa}^2 + v_{sb}^2 + v_{sc}^2\right)^{1/2} \tag{4.1}$$

Here, phase voltages are evaluated as

$$v_{sa} = \tfrac{1}{3}(2v_{sab} + v_{sbc}),\ v_{sb} = \tfrac{1}{3}(-v_{sab} + v_{sbc}),\ \text{and}\ v_{sc} = \tfrac{1}{3}(-v_{sab} + 2v_{sbc}) \tag{4.2}$$

Thus, by using equation (4.1, 4.2), the unit templates (in-phase & quadrature) are evaluated as

$$u_{ad} = {}^{v_{sa}}\!/_{V_m},\ u_{bd} = {}^{v_{sb}}\!/_{V_m},\ u_{cd} = {}^{v_{sc}}\!/_{V_m} \tag{4.3}$$

$$u_{aq} = -\frac{u_{ad}}{\sqrt{3}} + \frac{u_{cd}}{\sqrt{3}},\ u_{bq} = -\frac{3u_{cd}}{2\sqrt{3}} - \frac{u_{cd}}{2\sqrt{3}} + \frac{u_{bd}}{2\sqrt{3}},\ \text{and}\ u_{cq} = -\frac{3u_{ad}}{2\sqrt{3}} + \frac{u_{bd}}{2\sqrt{3}} - \frac{u_{cd}}{2\sqrt{3}} \tag{4.4}$$

4.2.1 Simulation Results

The model of the proposed controller for SEIG with/without STATCOM feeding unbalanced load is simulated and results of the hybrid system are examined under various operational circumstances. Different parameters of the hybrid system were analyzed to justify the effectiveness of the proposed system. The proposed system is designed using 3.7kW of SEIG, 2.9kW of PV system, 400V of BES, and 400V of DC link voltage.

4.2.1.1 Transient Performance of SEIG at No load and On Load

Fig.4.1 likely represents a graphical representation or waveform depicting the transient behavior of the SEIG during the voltage buildup process. It shows how the voltage across the SEIG terminals changes over time until it reaches the desired value of 600V (peak) when no load is connected.
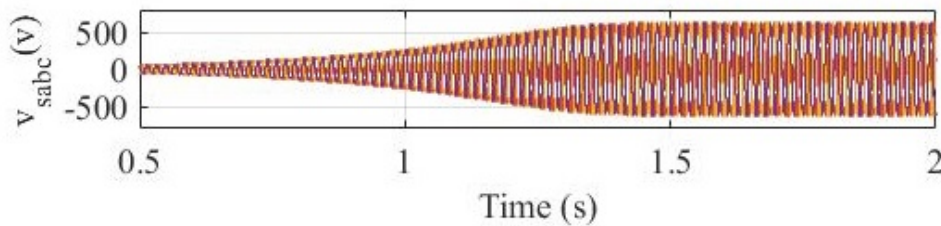
Fig.4.1 Voltage buildup of SEIG at no load

Fig. 4.2 shows the transient performance of SEIG under load perturbation in the absence of STATCOM. At t=1.7 sec, a balanced load is switched to the hybrid system and the generator voltage (v_{sabc}) and capacitive current (i_{cc}) start decreasing and at t=1.8 sec, an additional balanced nonlinear load is switched. The generator voltage (v_{sabc}) and capacitive current (i_{cc}) decreased and finally voltage are collapsed at zero load.
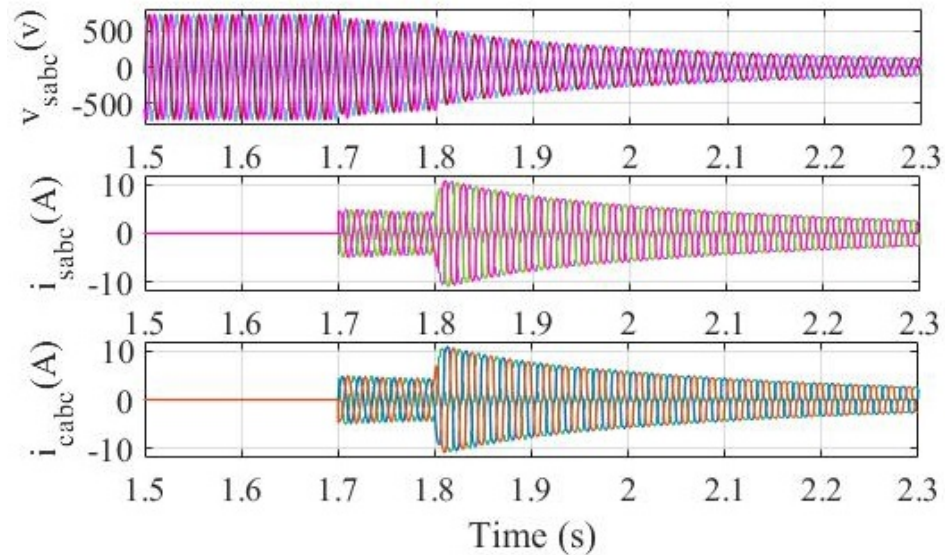
Fig.4.2 Transient performance of SEIG on load

4.2.1.2 SEIG Performance with Linear/Nonlinear Load using STATCOM

Fig.4.3 depicts the response of SEIG with linear/non-linear load using STATCOM for the 3P3W system. At t= 1.7 sec, a balanced load is injected, after this v_{sabc}, v_L, i_c, v_{dc} and freq., are remains constant. A balanced nonlinear load is inserted at t=1.8 sec, After this a sudden change in nonlinear load at t=1.8 sec, v_{sabc}, v_L, i_c, v_{dc} and freq., are decreased

4.2.1.3 Performance of SEIG under Fluctuating Wind Speed

Fig. 4.4 shows the response of SEIG with STATCOM under changing wind speed at t=1.7sec. During the duration of fluctuation in wind speed, the compensator current is increased and provides required power support to SEIG. The controller maintains the other parameters of the isolated system are consistent. Moreover, the source current (i_{cabc}) of the proposed speed is maintained sinusoidal under dynamic conditions of wind speed and distorted load.
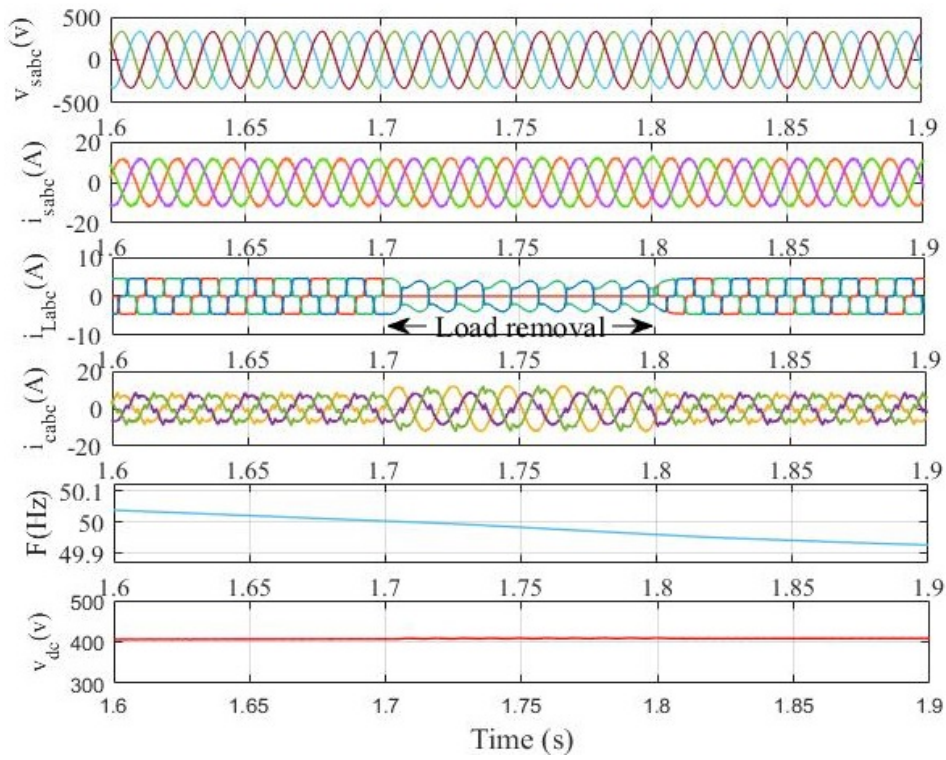
Fig.4.3 Performance of SEIG with STATCOM under balanced load
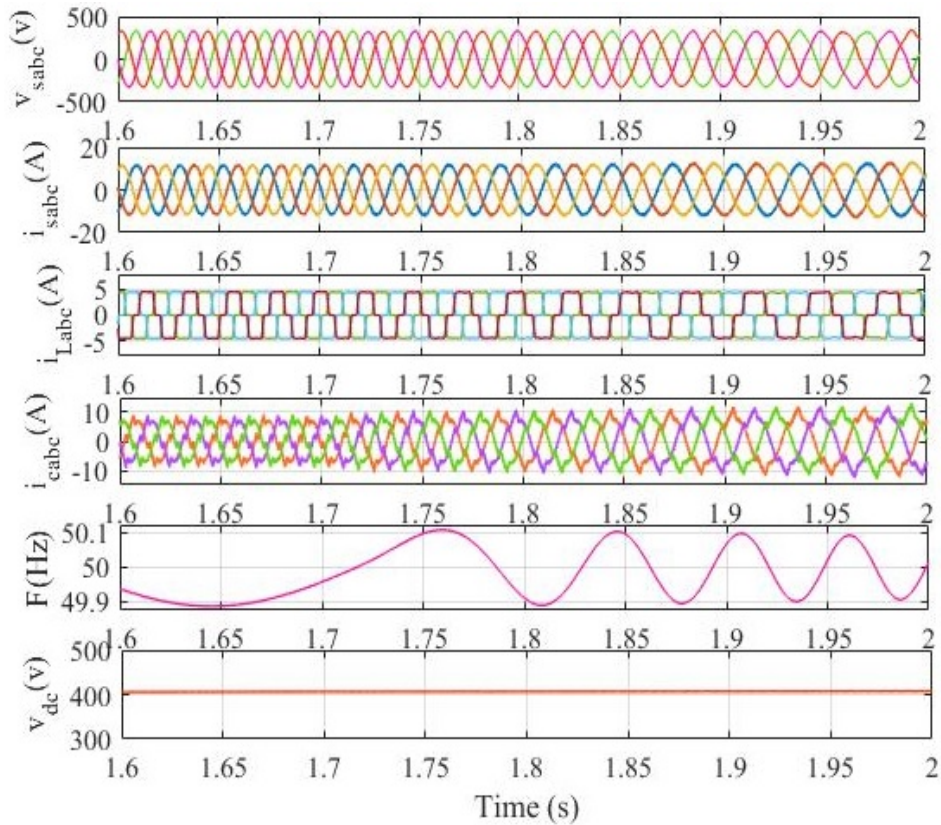
Fig.4.4. Performance under fluctuating wind speed

4.2.1.4 Performance of SEIG with Linear/Nonlinear Load under Change in Solar Insolation

Fig. 4.5(a) & (b) depicts the response of SEIG under a change in solar insolation from $1000w/m^2$ to $700w/m^2$. The output power of a PV system is decreased when the irradiance decreases. A 3kW resistive balanced linear load is supplied at time t=1.7sec. When, a balanced nonlinear load is injected at t=1.8 sec, a declination in PV system output power has an impact on SEIG performance. The performance of hybrid system under varying irradiance is shown in Fig. 4.5(b) for SEIG voltage (v_{sabc}), load voltage (v_L) dc link voltage (v_{dc}) and freq. (f).
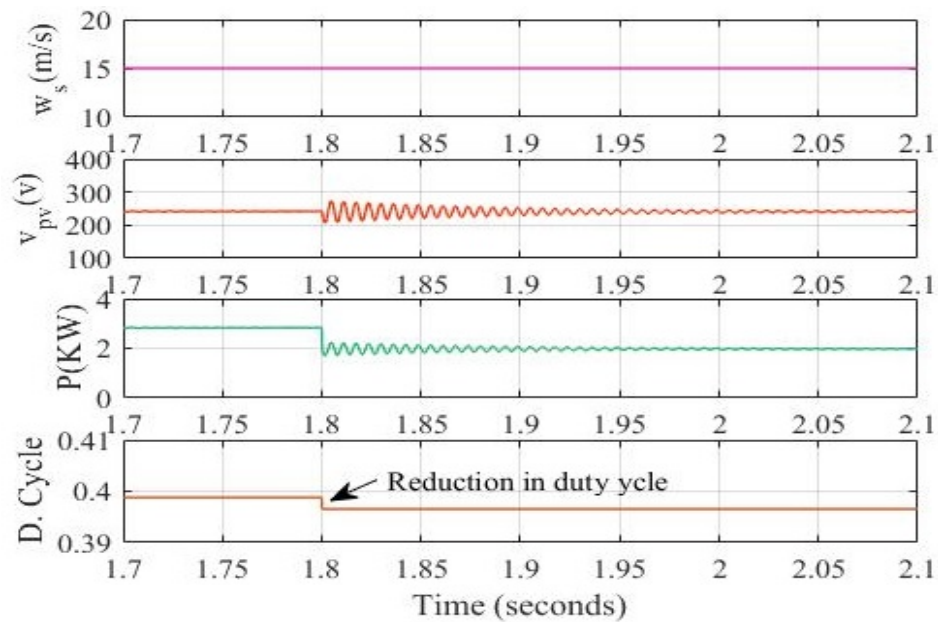
(a)
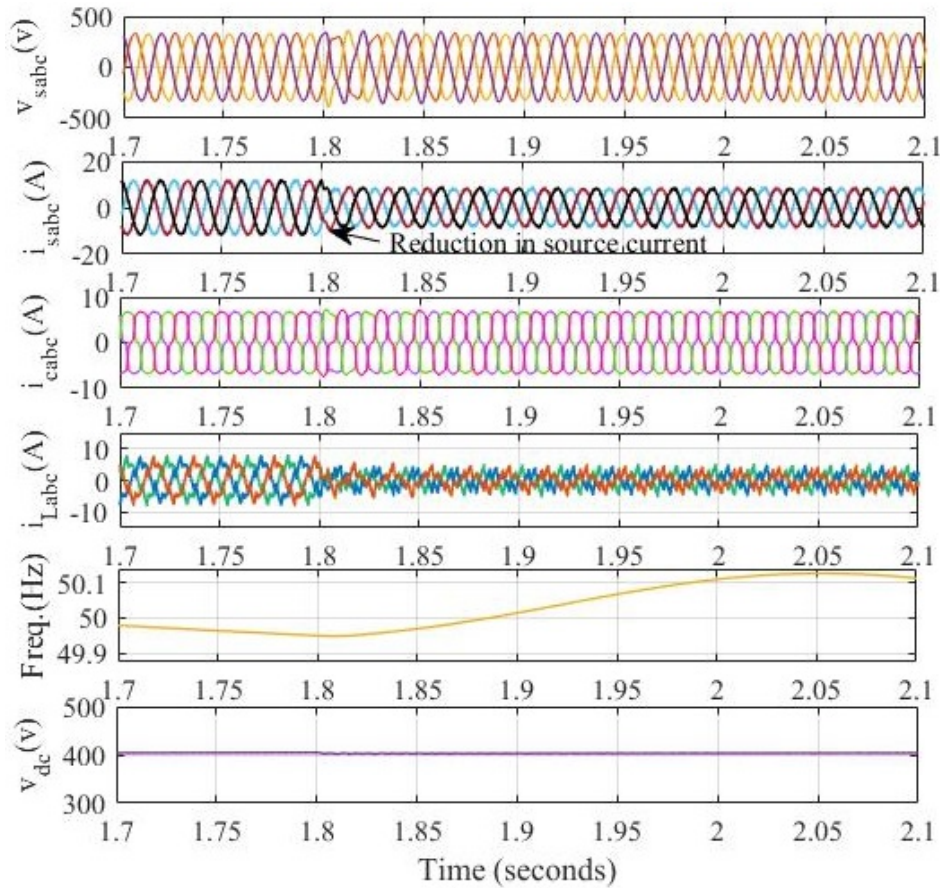
(b)

4.5(a) and (b) Performance under the change in solar insolation feeding a constant load

4.3   DSC-FLL Control Approach

A DSC-FLL control approach is implemented to control the VSC in the isolated mode of operation. The DSC-FLL control utilizes an FLL to regulate the output frequency of the VSC and achieve accurate synchronization with the grid or the reference frequency. One of the advantages of using the DSC-FLL control is its improved disturbance rejection ability. This means that the control system is better equipped to handle external disturbances or variations in the system, such as changes in load conditions or fluctuations in wind & solar. The in-loop filter in the DSC-FLL control plays an essential role in enhancing the disturbance rejection capability. The computed frequency (ω_g) is considered to be constant when describing the concept of in-loop filters in FLLs.
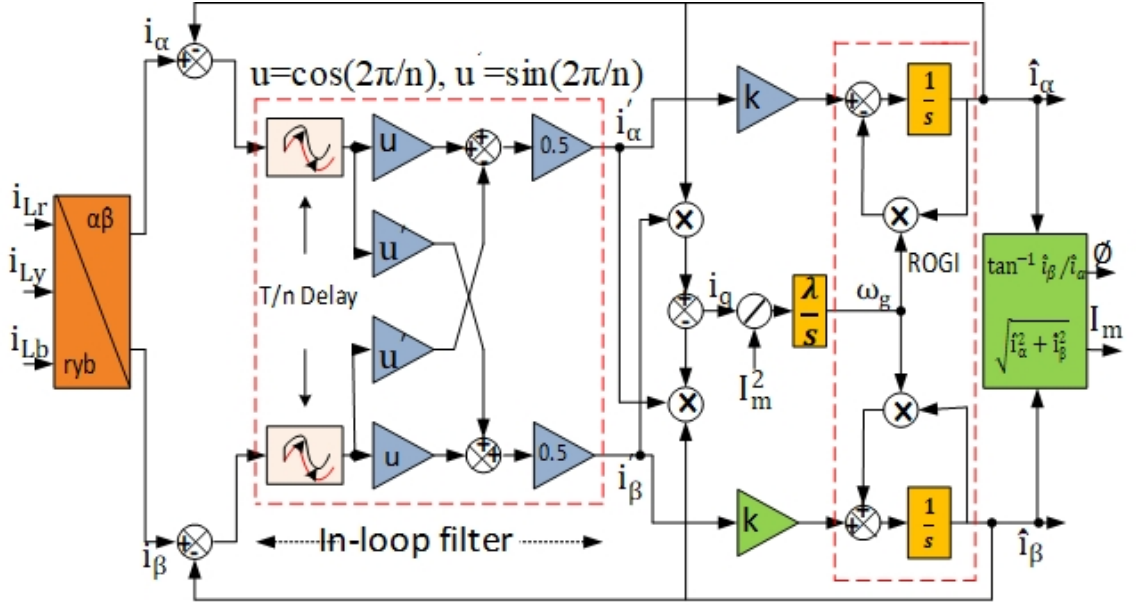
Fig. 4.6 DSC-FLL control approach

The ROGI implementation in space vector notation is shown in Fig. 4.6 expressed as

$$\hat{i}_\alpha(s) + j\hat{i}_\beta(s) = \frac{k}{s - j\omega_g + k}\left(i_\alpha(s) + ji_\beta(s)\right) \tag{4.5}$$

The proposed control technique utilizes a filter that allows the Fundamental Frequency Positive Sequence (FFPS) component to pass while blocking other frequency components. This approach is beneficial for extracting the FFPS component and mitigating disturbances such as harmonics and voltage imbalance. The equation as described as

$$DSC_n = \frac{1 + e^{\frac{j2\pi}{n}} e^{-\frac{T_s}{n}}}{2} \tag{4.6}$$

The fundamental period and operator delay factor, respectively, are represented by the components (T & n). The ability of filtering is primarily dependent on its delay factor (n). A single operator might not be able to eliminate all disturbances, as noted in the literature, so the operators are used in a cascade form with a variable delay factor, as illustrated in Fig. 4.6. It is possible to define the equation for the open loop transfer function in the DSC-FLL as

$$G^\theta = \frac{\theta_1(s)}{\theta_1(s) - \hat{\theta}_1(s)} = \frac{1 + e^{\frac{-T_s}{2}}}{2} \frac{1 + e^{\frac{-T_s}{12}}}{2} \frac{ks + \lambda}{s^2} \tag{4.7}$$

The constant parameters k and λ are calculated as follows:

$$k = \frac{1}{gT_d} \text{ and } \lambda = \frac{1}{g^3 T_d^2} \qquad (4.8)$$

Where k=160, λ=12791 and, g is the phase margin evaluation factor [25].

4.3.1 Estimation of Fundamental Load Current Component and Reference Source Current

The DSC-FLL based control technique is well-suited for accurately estimating the fundamental component and phase angle of load current, enabling effective control and operation of standalone systems, even in the presence of dynamic conditions and disturbances.

$$I_m = \sqrt{\hat{\imath}_\alpha^2 + \hat{\imath}_\beta^2} \qquad (4.9)$$

$$\emptyset = \tan^{-1}(\hat{\imath}_\beta / \hat{\imath}_\alpha) \qquad (4.10)$$

By utilizing the S&H module, the load currents' instantaneous values are captured at a high frequency, providing a precise representation of the current waveforms. The ZCD module detects zero crossings, enabling accurate phase angle determination. The quadrature unit templates employ these sampled values and zero crossing information to compute the magnitude of the fundamental active and quadrature components as represented in Fig. 4.7.
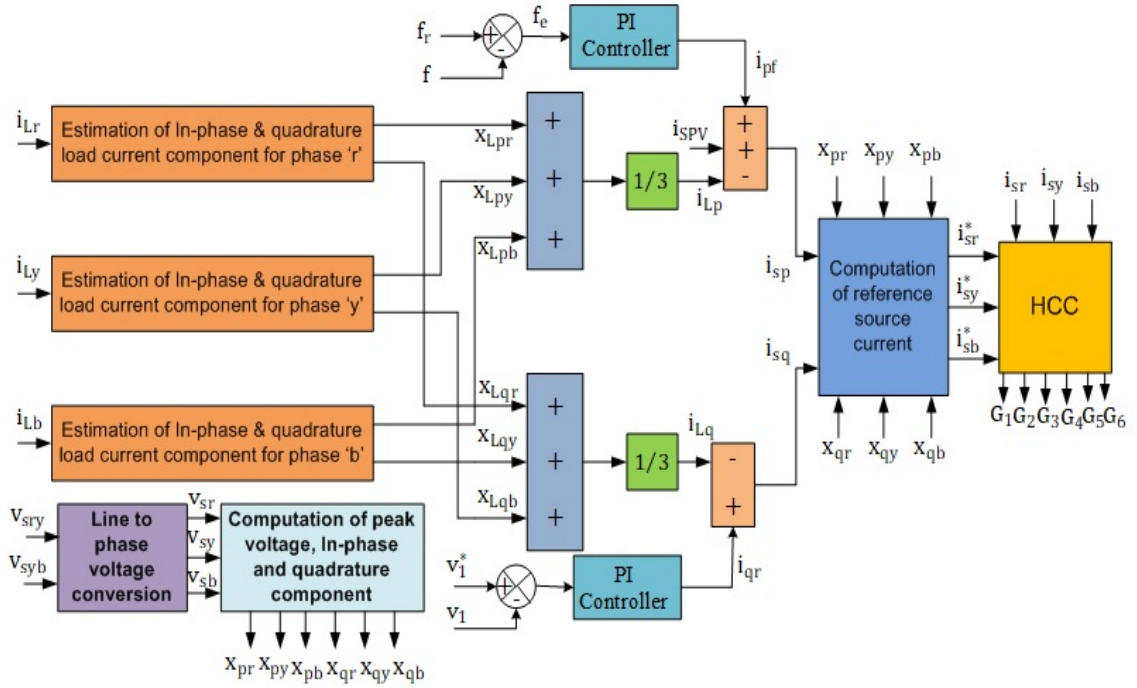
Fig. 4.7 Estimation of fundamental load current component and reference source current

After computing the fundamental component from the load current using the pattern described earlier, the active and quadrature components of the remaining two phases can be computed using a similar approach. Two PI controllers are employed to regulate voltage/frequency. The current of the fundamental components of the load are then minus from the outputs of the PI controllers to achieve voltage & frequency regulation [128]. The control equations for estimating the PI controller's current are.

$$i_{fp}(q) = i_{fp}(q-1) + k_{fp}\{f_e(q) - f_e(q-1)\} + k_{fi}f_e(q) \tag{4.11}$$

$$i_{qr}(q) = i_{qr}(q-1) + k_{vp}\{v_e(q) - v_e(q-1)\} + k_{vi}v_e(q) \tag{4.12}$$

Where the predicted values for the voltage and frequency errors are

$$f_e(q) = f_r(q) - f(q) \text{ and } v_e(q) = v_1^*(q) - v_1(q) \tag{4.13}$$

The peak value of source voltage (v_1) from the CCP is computed as

$$v_1 = \sqrt{\left(\frac{2}{3}\right)} \times \sqrt{\left(v_{sr}^2 + v_{sy}^2 + v_{sb}^2\right)} \tag{4.14}$$

$$v_{sr} = \frac{1}{3}(2v_{sry} + v_{syb}), v_{sy} = \frac{1}{3}(-v_{sry} + v_{syb}), \text{ and } v_{sb} = \frac{1}{3}(-v_{sry} - 2v_{syb}) \tag{4.15}$$

Where, v_{sry} and v_{syb} are the line voltages of the source at CCP and v_{sr}, v_{sy} and v_{sb} are the computed phase voltages. The both active (i_{sp}) and reactive (i_{sq}) reference source currents are evaluated as

$$i_{sp} = i_{fp} + i_{SPV} - i_{Lp} \tag{4.16}$$

$$i_{sq} = i_{Lq} - i_{qr} \tag{4.17}$$

The active/reactive components of load current are analyzed using a three-component average.

$$i_{Lp} = \frac{x_{Lpr} + x_{Lpy} + x_{Lpb}}{3} \text{ and } i_{Lq} = \frac{x_{Lqr} + x_{Lqy} + x_{Lqb}}{3} \tag{4.18}$$

The sinusoidal reference currents derived from the load current are approximated using an in-loop filter-based DSC-FLL, as shown below.

$$i_{sra}^* = i_{sp} \times x_{pr}, \; i_{syb}^* = i_{sp} \times x_{py}, \; i_{sbc}^* = i_{sp} \times x_{pb} \tag{4.19}$$

$$i_{qra}^* = i_{sq} \times x_{qr}, \; i_{qyb}^* = i_{sq} \times x_{qy}, \; i_{qbc}^* = i_{sq} \times x_{qb} \tag{4.20}$$

Where, x_{pr}, x_{py}, x_{pb}, x_{qr}, x_{qy} and x_{qb} are the computed active/reactive unit templates. The process of evaluating unit templates is stated as follows:

$$x_{pr} = {V_{sr}}/{V_1}, \; x_{py} = {V_{sy}}/{V_1}, \; x_{pb} = {V_{sb}}/{V_1} \tag{4.21}$$

$$x_{qr} = -\frac{x_{pr}}{\sqrt{3}} + \frac{x_{pb}}{\sqrt{3}}, \; x_{qy} = \frac{\sqrt{3}x_{pr}}{2} + \frac{(x_{py} - x_{pb})}{2\sqrt{3}}, \text{ and } x_{qb} = -\frac{\sqrt{3}x_{pr}}{2} + \frac{(x_{py} - x_{pb})}{2\sqrt{3}} \tag{4.22}$$

The reference source currents are the addition of extracted active/reactive currents and are stated as

$$i_{sr}^* = i_{sra}^* + i_{qra}^*$$

$$i_{sy}^* = i_{syb}^* + i_{qyb}^* \tag{4.23}$$

$$i_{sb}^* = i_{sbc}^* + i_{qbc}^*$$

The hysteresis controller generates switching pulses based on the difference between the computed reference current and the observed source current [5].

4.3.2 Simulation results

A DSC-FLL control approach is designed to reduce the PQ problems of an isolated microgrid (MG) under wind/solar intermittency and nonlinear load perturbation. The proposed control successfully extracts the unit vectors and generates the appropriate gating pulses for VSC.

4.3.2.1 Dynamic Response of MG with Changes in Wind Velocity

Fig. 4.8 represents the dynamic response of an isolated MG to changes in wind velocity and constant solar intensity. The wind speed is changed from 14m/s to11 m/s at t=3.2s, the solar intensity and temp. (T) are fixed at $1000w/m^2$ and 35°C. The SEIG based source power is decreased from 5.65kW to 5.49kW due to the fluctuation in wind speed. The DSC-FLL with VSC stabilizes and maintains source voltage (v_{sryb}) and current (i_{sryb}). At t=3.2s, the compensator current marginally increases and compensates at CCP through VSC.
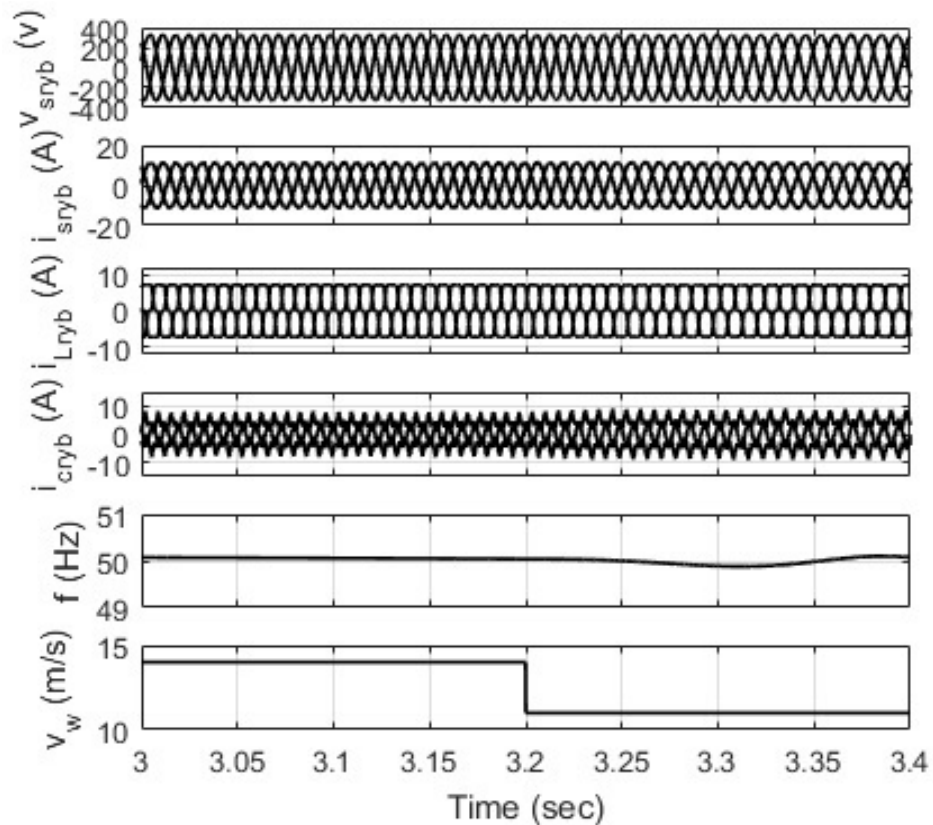
Fig. 4.8 Dynamic response of an isolated MG to changes in wind velocity

4.3.2.2 Dynamic Response under Change in Solar Intensity

Fig. 4.9(a) and (b) depict the dynamic response of an isolated MG to changes in solar insolation and constant wind speed while feeding a nonlinear load. Fig. 4.9(a) depicts the variation in solar intensity and temperature. At t=3.2 s, (T) ranges from $1000w/m^2$ to $600w/m^2$ and 35°C to 24°C. The SPV current and duty cycle (α) declined when the solar level changes. The solar power is cut from 3kW to 1.8kW. At t=3.2s, the source current and compensator current decreased as displayed in Fig 4.9(b). Under dynamic circumstances, the DSC-FLL-based controller stabilizes the isolated MG's frequency and source voltage. During the change at t=3.2s, the source power is diminished from 5.7kW to 3.2kW.
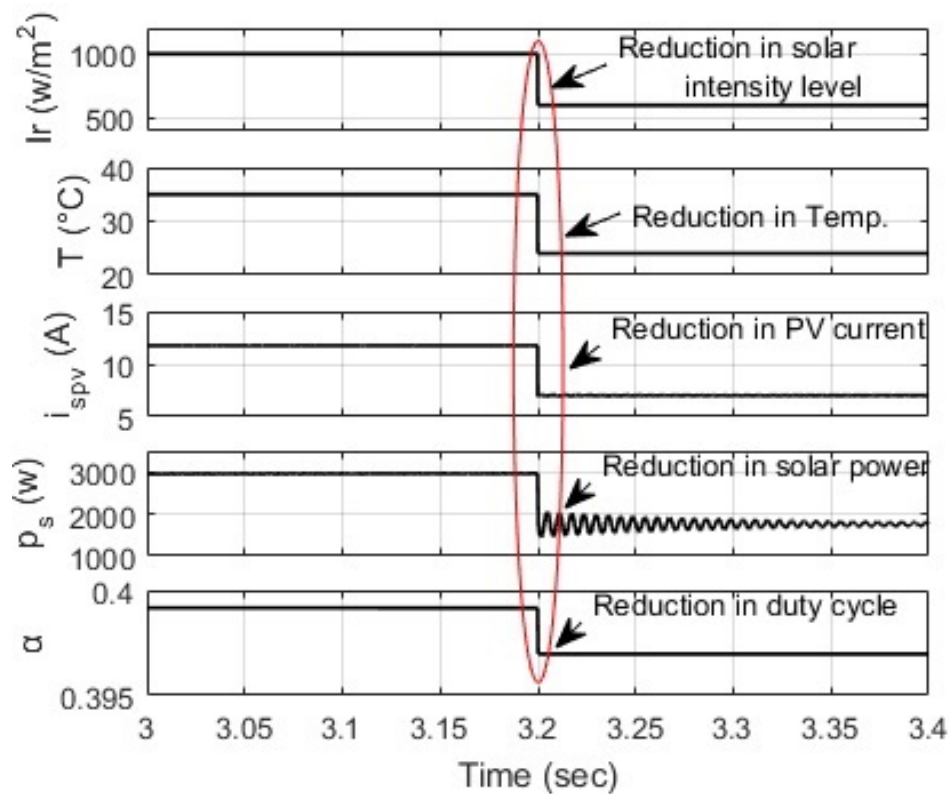
(a)
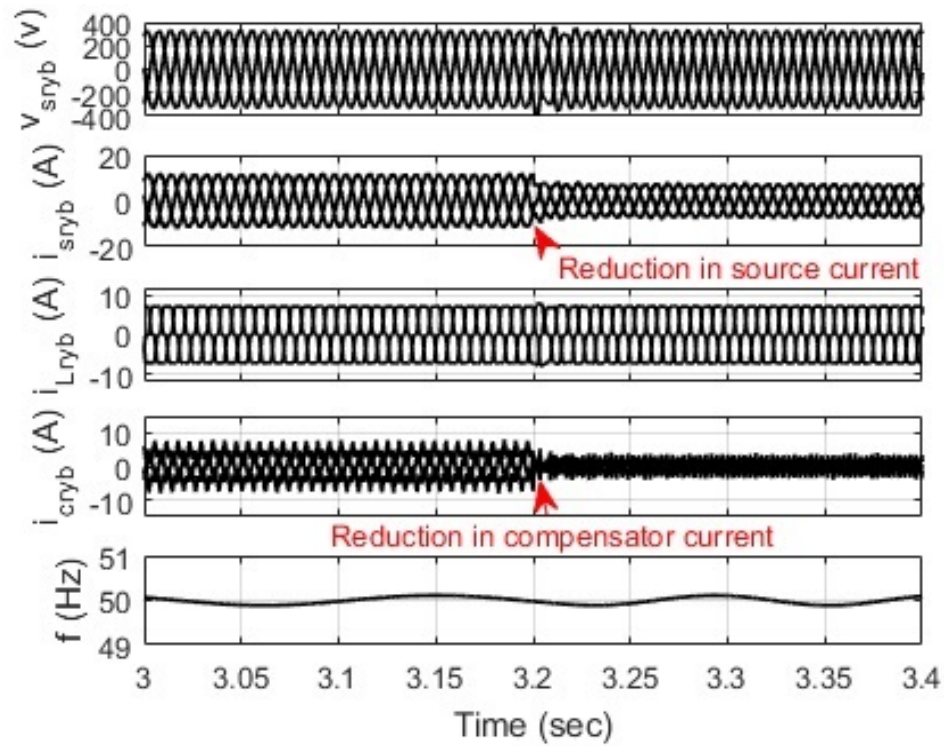
(b)

Fig. 4.9(a) and (b) Dynamic response under the change in solar intensity

4.3.2.3 Dynamic Response of MG with an Unbalanced Load

The dynamic response of an isolated MG under fixed wind velocity and sun intensity feeding an unbalanced nonlinear load is shown in Fig. 4.10. At t=3.1s to 3.3s, the load for phase 'r' is detached. The load current is reduced while the frequency and source voltage of the isolated MG remains unchanged. The excess power generating by SEIG is supplied to BSS during the load disconnection. Because of the load disconnect, the source power increases from 5.6kW to 6.4kW.
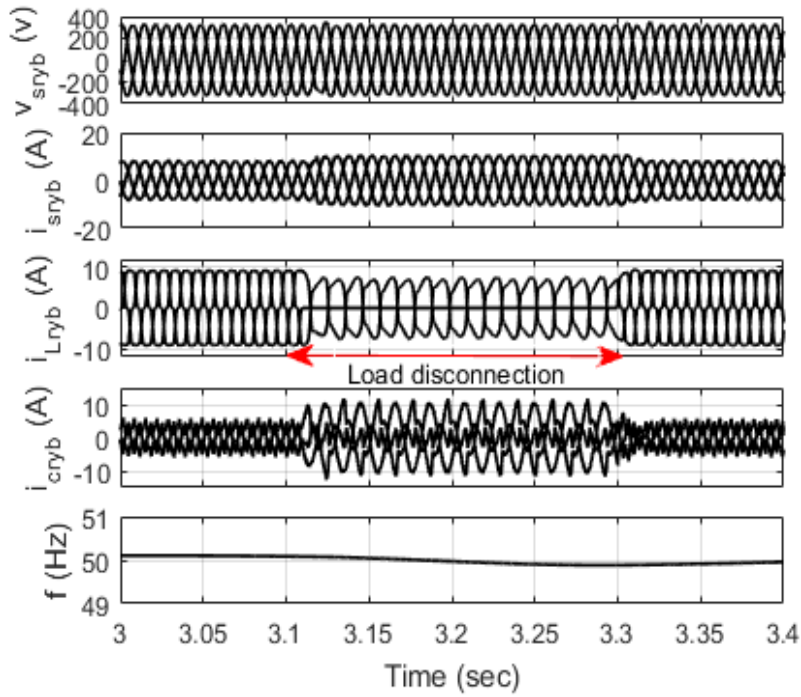
Fig. 4.10 Dynamic response of MG with an unbalanced load

4.3.2.4 Battery Current under Different Operating Conditions

Fig. 4.11 depicts the battery current under various operating conditions. During a reduction in RESs power generation, such as wind and solar, the battery current is supplied to the common coupling point (CCP) through a VSC. This means that when there is a decrease in power generation from RESs, the BSS utilizes its stored energy to compensate for the shortfall by injecting current into the CCP.
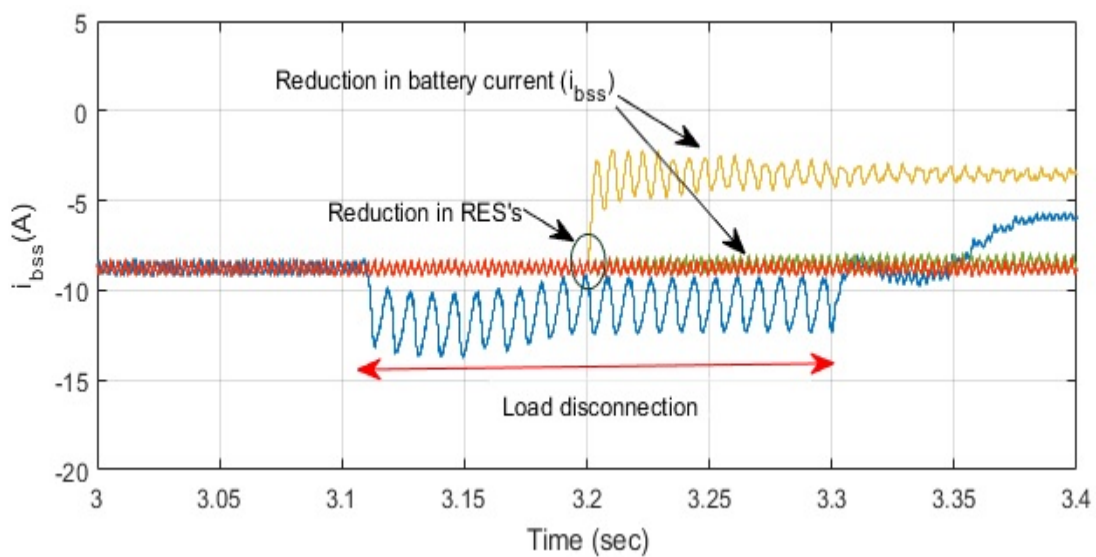
Fig.4.11 Battery current response under different operating conditions

4.3.2.5 Harmonic Spectrum

Fig. 4.12(a) and (b) display the harmonic spectrum of the source and load currents in an isolated MG under nonlinear load conditions. The Total Harmonic Distortion (THD) values of the source and load current at the CCP satisfy the limits specified by the IEEE 1547.4 standard. Additionally, the controller in the MG delivers the necessary reactive power to support the system under different dynamic circumstances.

(a)   (b)
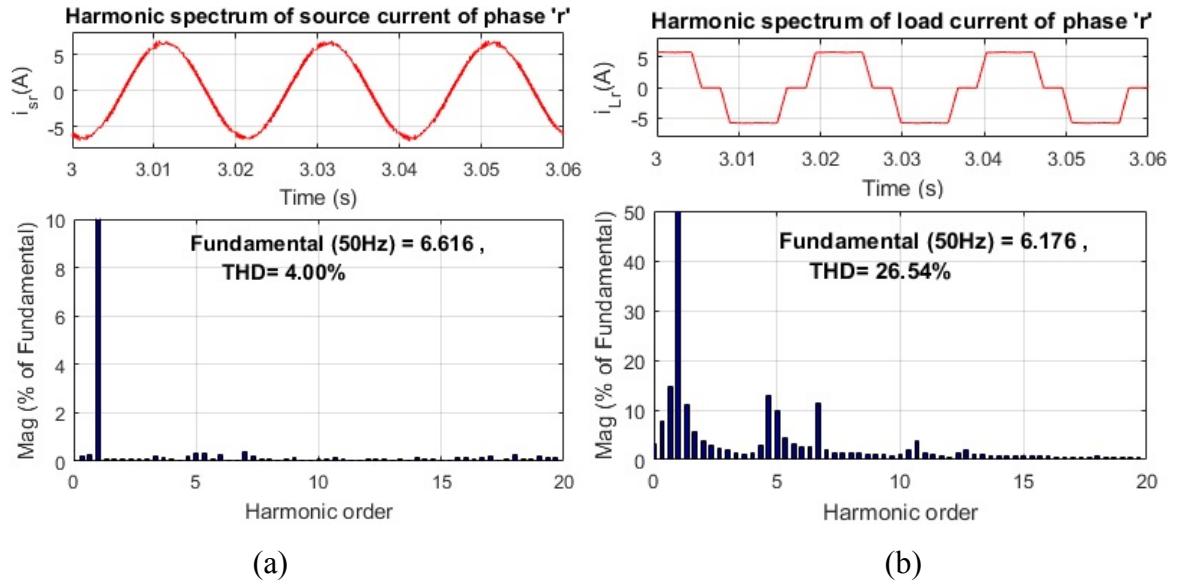
Fig. 4.12 Harmonic spectrum (a) source current and (b) nonlinear load current

4.4   SOSF-FLL Control Approach

A SOSF-FLL control scheme is employed in the proposed islanded system, as shown in Fig. 4.13, and is designed to extract and evaluate the maximum value of the fundamental load current component. It incorporates complex gain constants to enhance the performance of the control system. The SOSF-FLL is a robust control method that ensures that system operates within predefined bounds. This control technique helps to mitigate uncertainties and disturbances in the system, leading to improved performance and stability. By extracting and evaluating the maximum value of the fundamental load current component using the SOSF-FLL control scheme, the system can accurately regulate and control the fundamental component, which is essential for achieving high PQ and efficient operation.
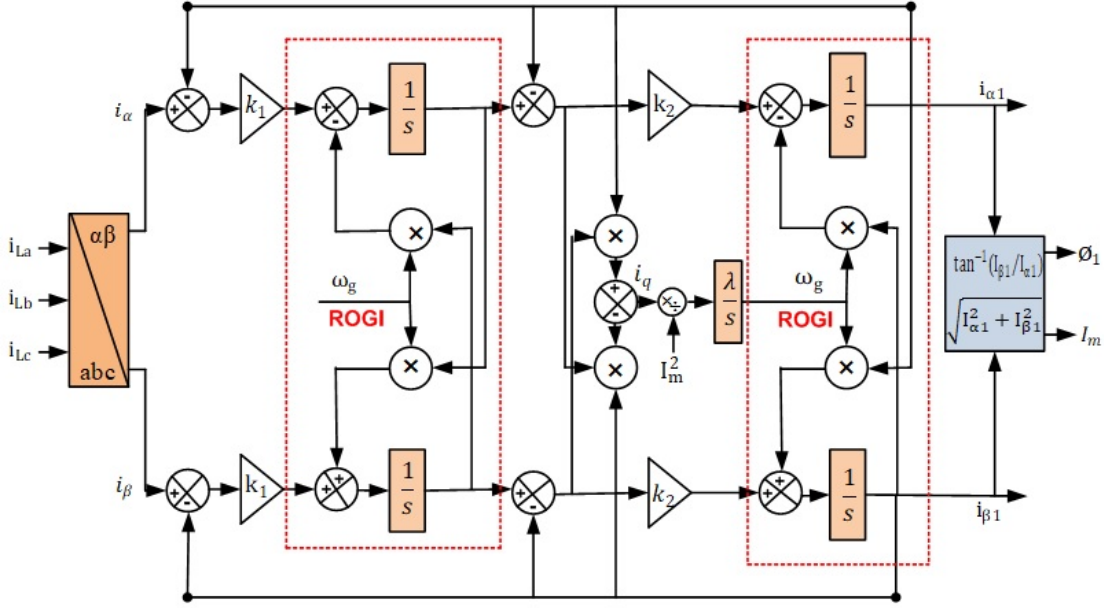
Fig. 4.13 SOSF-FLL based control algorithm

The SOSF-FLL algorithm is controlled by the gain parameters (K and λ). The proposed control algorithm transfer function is depicted as

$$M(s) = \frac{w_n^2}{s^2 + 2\xi w_n s + w_n^2} \tag{4.24}$$

Where ξ and w_n are the damping ratio and undamped natural frequency, respectively. The purposed control approach's open and closed loop transfer functions are provided as

$$T(jw) = \frac{I_m}{i_L} = \frac{k_1 k_2}{(s - jw + k_2)(s - jw)} \tag{4.25}$$

$$T_1(s) = \frac{I_m}{i_L} = \frac{k_1 k_2}{(s - jw' + k_2)(s - jw' + k_1 k_2)} \tag{4.26}$$

The maximum value of the proposed control for closed transfer function is calculated as

$$|T_1(jw)| = \frac{I_m}{i_L} = \frac{k_1 k_2}{\sqrt{\left(k_1 k_2 - (w - w')^2\right)^2 + k_2^2 (w - w')^2}} \tag{4.27}$$

Where k_1 and k_2 are the constant terms of the proposed SOSF-FLL control approach shown in Fig. 4.13. During the dynamic conditions of a microgrid system, the SOSF control produces a rapid response. The variables $\emptyset_1$, ω_g and I_m reflect the evaluated

values of phase, frequency, and amplitude of the fundamental load current component. Two ROGIs are used in the development of the SOSF-based FLL [25].

4.4.1 Computation of Fundamental Load Current Component

The Park transformation allows us to represent three-phase quantities in a two-phase coordinate system. The transformation is depended on the concept of rotating the three-phase currents by a fixed angle to obtain the alpha-beta (i_α, i_β) components.

$$i_\alpha = I_m \cos(\emptyset_1), \text{ and } i_\beta = I_m \sin(\emptyset_1) \qquad (4.28)$$

The fundamental estimated in-phase ($I_{L\alpha1}$) and quadrature current ($I_{L\beta1}$) variables are assessed as

$$I_{L\alpha1} = I_m \cos(\emptyset_1), \text{ and } I_{L\beta1} = I_m \sin(\emptyset_1) \qquad (4.29)$$

Where the phase and amplitude angle of the fundamental load current component are presented as [124]

$$I_m = \sqrt{I_{L\alpha1} + I_{L\beta1}}, \text{ and } \emptyset_1 = \tan^{-1}(I_{L\beta1}/I_{L\alpha1}) \qquad (4.30)$$

4.4.2 Simulation Results

The performance analysis involves simulation studies using MATLAB/Simulink and experimental testing on experimental set-up in laboratory. By comparing the simulated and test results, the study evaluates the dynamic behavior of the controller and assesses its effectiveness in achieving the desired system performance. The SOSF-FLL-based VSC plays a vital role in eliminating harmonics, maintaining voltage & frequency control, providing reactive power support, and enhancing the PQ of the standalone microgrid. It combines advanced control techniques to ensure a stable and high-quality power supply to the microgrid-connected loads.

4.4.2.1 Control Signals of SOSF-FLL Algorithm

In Fig. 4.14(a)-(c), the internal control signals of the SOSF-FLL approach are shown. These control signals are responsible for regulating and controlling various aspects of the microgrid system to ensure stable and optimal operation under nonlinear load conditions. The phase 'a' of the nonlinear load is detached at t=2.8s. Fig. 4.14(a) shows the internal

signal of the control algorithm i_α, i_β, $i_{L\alpha1}$, $i_{L\beta1}$ and ω_g. The variables i_α, i_β and ω_g are the extracted component from load current by abc to alpha-beta clarke transform and ω_g is the centre frequency of SOSF-FLL control algorithm. Fig. 4.14(b) shows the internal signals I_m(extracted fundamental load current component), u_{da} (in-phase unit templates), u_{qa} (quadrature unit templates), i_{smq} (output of AC PI controller) and V_t (voltage amplitude). Fig. 4.14(c) shows the internal control signals i_{Lfd}, i_{Lfq}, i_{pf}, i_{Lp}^*, and i_{Lq}^*, where, i_{Lp}^* and i_{Lq}^* are the extracted active and reactive component of the reference source current. The extracted active/reactive components are combined to generate a sinusoidal reference generator current (i_{gabc}^*). These control signals facilitate the control approach to respond quickly and improve PQ under numerous operating environments.
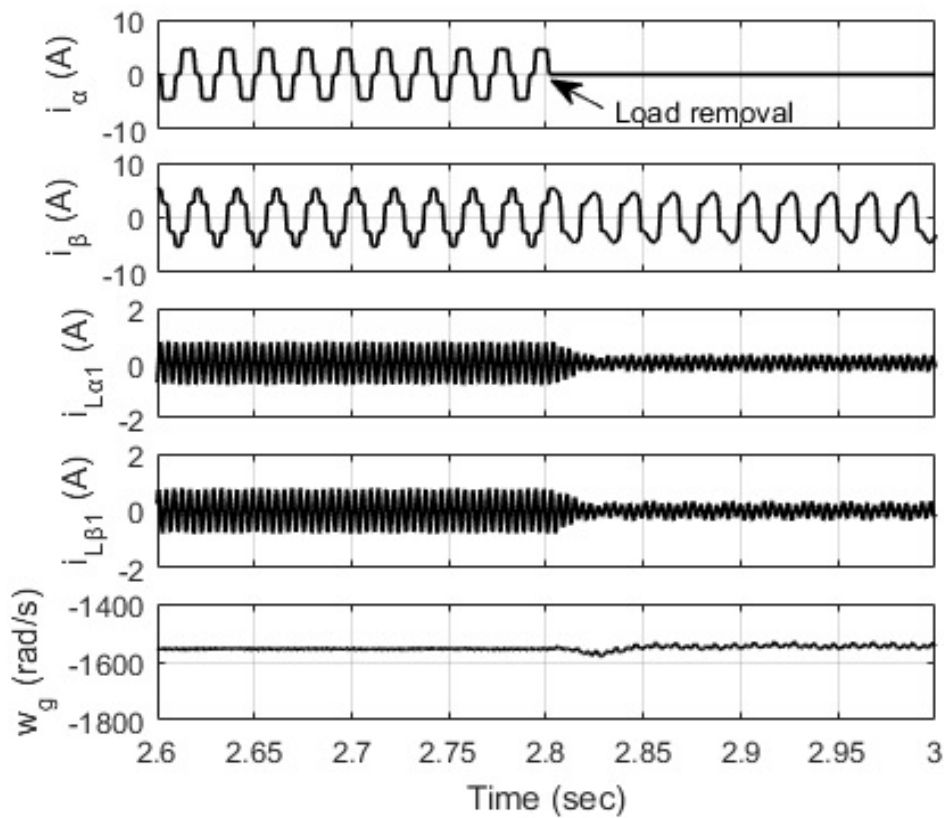
(a)
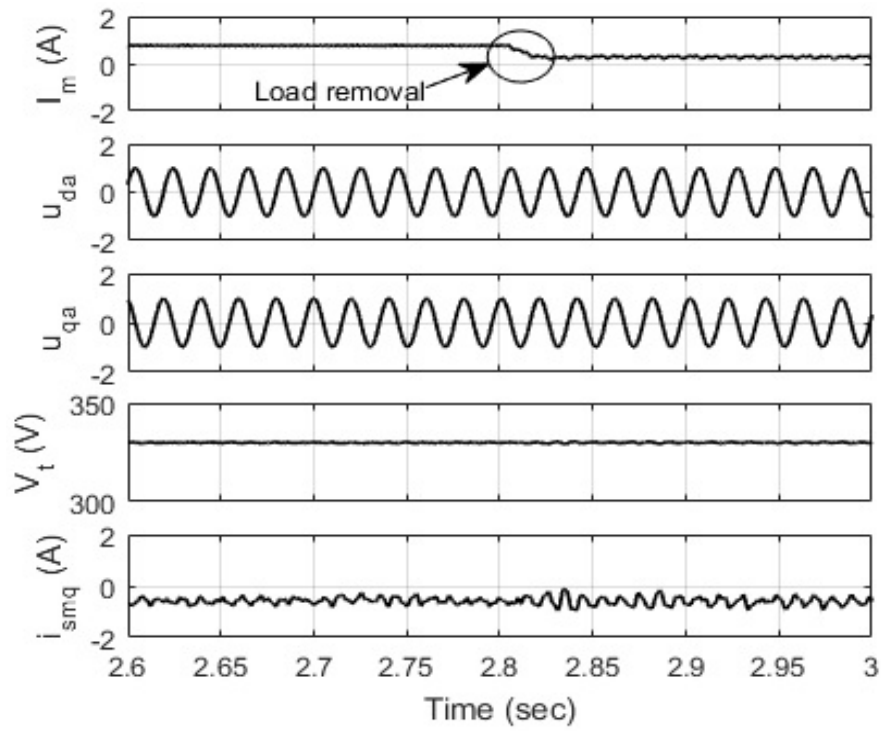
(b)
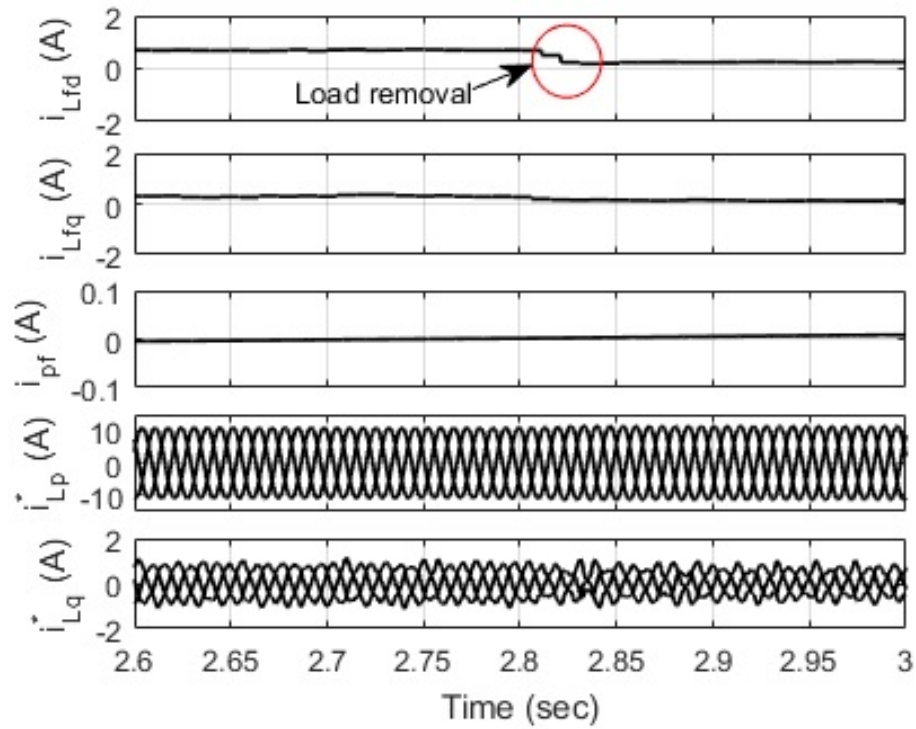
(c)

Fig. 4.14 Estimation of control signal under unbalanced load (a) i_α, i_β, $i_{L\alpha1}$, $i_{L\beta1}$ and ω_g

(b) I_m, u_{da}, u_{qa}, V_t and i_{smq} (c) i_{Lfd}, i_{Lfq}, i_{pf}, i_{Lp}^* and i_{Lq}^*.

4.4.2.2 Dynamic Response of Wind-Solar Microgrid with Fixed Wind Velocity/Varying Solar Insolation Feeding Nonlinear Load

Fig. 4.15(a) and (b) depict the dynamic response of a wind-solar microgrid supplying power to a nonlinear load while keeping the wind velocity constant and varying the solar insolation. In Fig. 4.15(a), the solar insolation is shown to vary from 1000w/m2 to 600w/m2, while the temperature ranges from 35ºC to 25ºC. The wind velocity (V_w) of the wind turbine remains fixed at 13 m/s. The PV current (i_{pv}), PV power (p_{pv}), and duty cycle is diminished as a result of a reduction in solar insolation. Because of changes in solar insolation, the microgrid system's generated power, load power, and PV power are 4.34kW, 3.02kW, and 1.65kW, respectively. At t=2.8s, the battery system switches from charging to discharging mode and provides power support at PCC using VSC to maintain power balance during this irregular solar power circumstance.

In Fig. 4.15(b), it is observed that there is a diminution in solar power at t=2.8s, which leads to a small distortion of 0.02s in the source voltage. However, after this initial disturbance, the controller successfully maintains the voltage profile of the microgrid system. Both the source current and compensator current are decreased due to the reduction in solar power. When there are changes in solar insolation, the BSS reacts quickly to regulate the active power stability in the wind-solar microgrid, particularly in islanded mode. The battery storage plays a crucial role in compensating for the fluctuating power output from the solar panels, ensuring that the microgrid maintains a stable and reliable power supply.
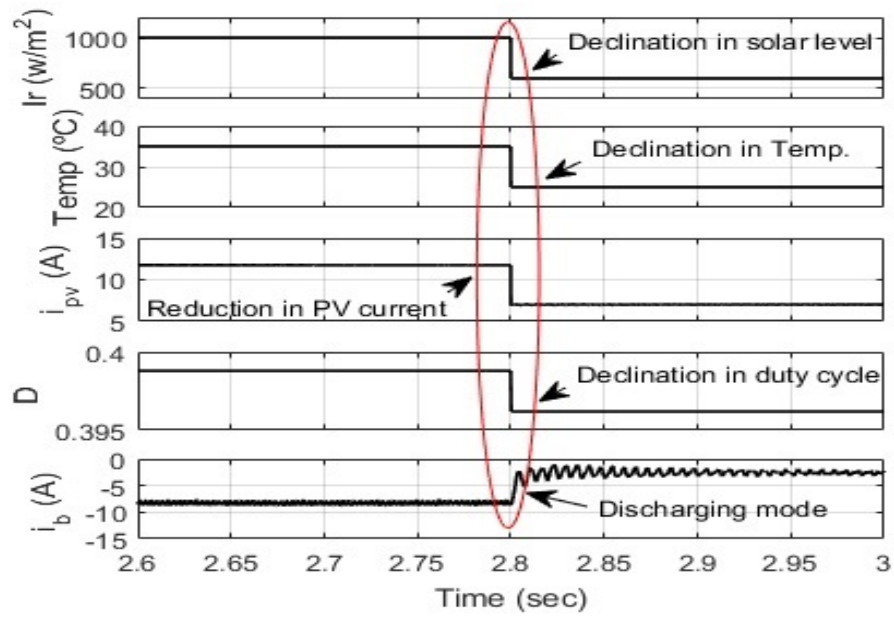
(a)
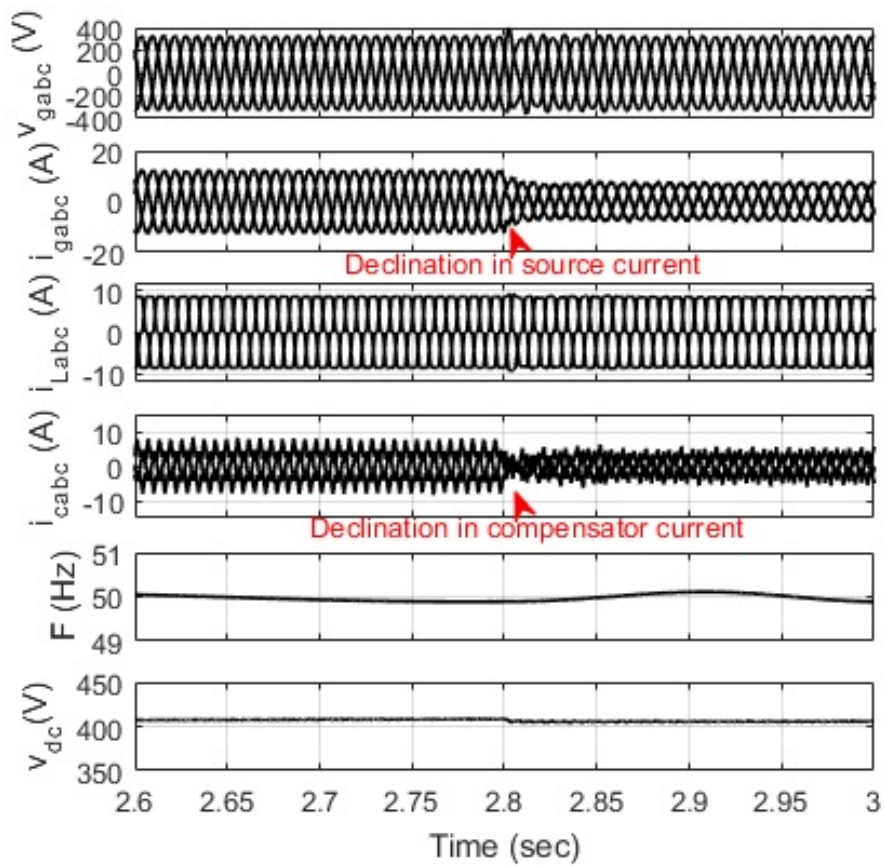
(b)

Fig. 4.15(a) and (b) Dynamic response of wind-solar microgrid with fixed wind velocity/varying solar insolation feeding the nonlinear load

4.4.2.3 Dynamic Response of Wind-Solar Microgrid with Varying Wind Velocity and Fixed Solar Insolation Feeding Nonlinear Load

Fig. 4.16 illustrates the dynamic response of a microgrid supplying power to a nonlinear load while the wind velocity varies and the solar insolation remains fixed. In this case, the solar irradiance is maintained at a constant value of 1000W/m2 with a temperature of 35ºC. The wind velocity (v_w) of the wind turbine, on the other hand, is reduced from 13 m/s to 9 m/s at t=2.8s. During the reduction in wind speed in Fig. 4.16, the generated power decreases to 5.5 kW. As the wind velocity decreases, at t=2.8s, the battery charging current (i_b) also decreases. This reduction in charging current indicates that the battery shifts from charging mode to draining mode. To compensate for the decrease in power generation from the wind turbine, the BDC controller, in conjunction with the VSC, provides active power support at the PCC in the microgrid. This active power support helps to sustain the voltage & current profile of the isolated microgrid system.

Furthermore, the compensator current increases slightly, showing that it contributes to power balancing and system support during the reduced wind speed condition. Other parameters such as frequency and DC link voltage are kept constant throughout the analysis. This indicates that the frequency & voltage of the microgrid system remain stable and are not affected by the change in wind velocity. The results obtained from this analysis demonstrate that the voltage profile and frequency of the microgrid are effectively controlled by the SOSF-FLL based controller, even under varying wind velocities. This controller plays a crucial role in maintaining the stable and reliable operation of the microgrid system, adapting to changes in wind conditions to ensure the desired PQ and isolated system synchronization.
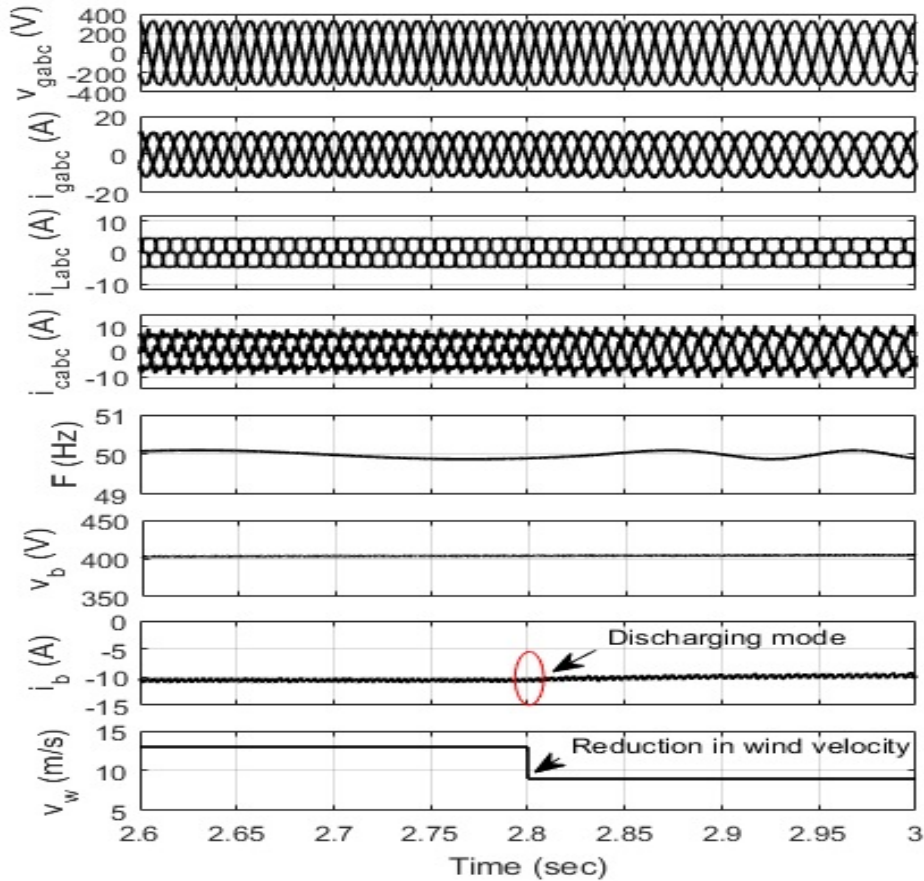
Fig. 4.16 Dynamic response of wind-solar microgrid system with varying wind velocity and fixed solar insolation feeding the nonlinear load

4.4.2.4 Dynamic Response of Wind-Solar Microgrid with Fixed Wind Speed/Solar Insolation Feeding Unbalanced Nonlinear Load

The dynamic response of a wind-solar microgrid with fixed wind velocity/solar insolation feeding varying nonlinear load is shown in Fig. 4.17. From t=2.7s to t=2.9s, phase 'a' of the nonlinear load is kept open. The generated power is increased to 5.89kW during load removal, while the load power is reduced to 1.1kW. The results show that the battery's voltage (v_b) & current (i_b) are increasing, while the load current (i_{Labc}) is decreasing due to the removal of the load. All other parameters remain constant during this period. As the load is increased, the SEIG operates in constant power mode; at t=2.9s, the PCC voltage (v_{gabc}) and current (i_{gabc}) are constant. This system can change the dynamical power sharing among the various RES based on the accessibility of load demand and renewable energy. The battery charging current is increased during one phase of load elimination. Similarly, when the PCC is connected to a load, the charging current

of the battery is reduced while the generated voltage remains sinusoidal. Under varying nonlinear load, the SOSF-FLL-based controller effectively regulates the voltage & frequency of the microgrid.
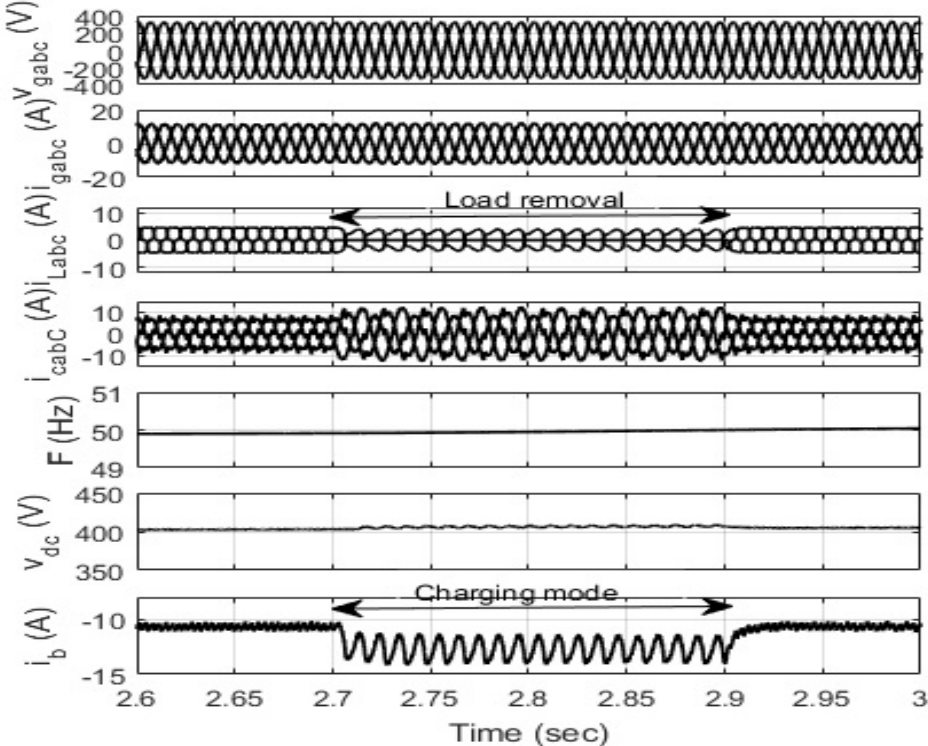
Fig. 4.17 Dynamic response of wind-solar microgrid with fixed wind velocity/solar insolation feeding varying nonlinear

4.4.2.5 Harmonic Distortion in Wind-Solar Microgrid System

Fig. 4.18(a)-(c) represents the harmonic analysis of wind-solar microgrid. The PCC voltage (v_{gabc}), PCC current (i_{gabc}), and load current (i_{Labc}) harmonics are 1.72%, 4.23% and 24.10% respectively. The reported results indicate that the microgrids voltage & current harmonics are within acceptable limits, demonstrating good harmonic performance and ensuring reliable & stable operation of the wind-solar microgrid, even under challenging conditions presented by unbalanced and distorted loads.
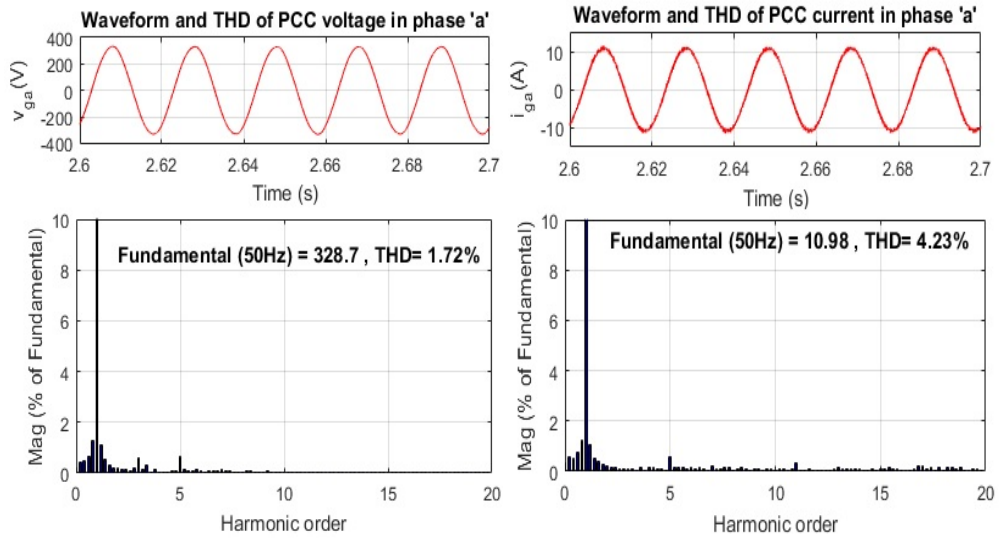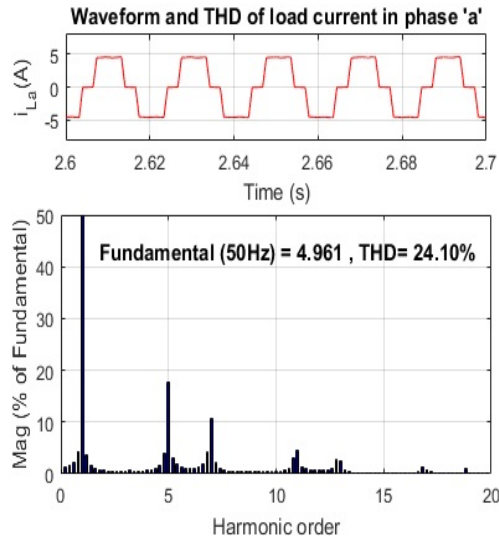
Fig. 4.18(a)-(c) THDs of PCC voltage, PCC current and load current

4.4.3 Experimental Results

The effectiveness of the proposed SOSF-FLL approach has been tested with an experimental prototype developed in the laboratory. The Hall-effect sensors circuit is utilized to measure the voltages and currents of the standalone system. The output of the sensors is fed to the ADC channel of DSP-dSPACE 1104 through appropriate buffer circuitry. The transient response of the proposed system is recorded using KEYSIGHT INFINII VISION DSO-X 2024A and HIOKI PQ3100 power quality analyzer. The

observed experimental results and harmonic indices of the standalone system have been shown in fig. 4.19(a)-(b), 4.20(a)-(b) and 4.21(a)-(b). The dynamic response of SOSF-FLL control approach and a standalone system is expressed as follows.

4.4.3.1 Internal Signals of SOSF-FLL Control Approach

The internal signals of the SOSF-FLL control approach under unbalanced load conditions are depicted in Fig. 4.19(a) & (b). The internal signals of voltage amplitude (V_t), in-phase unit template (u_{da}), quadrature unit template (u_{qa}) and fundamental load current component (I_m) are shown in Fig. 4.20(a). During load elimination, the voltage amplitude remains constant while the amplitude of the fundamental load current component increases. The i_α and i_β are computed using abc to $\alpha\beta$ transformation from the nonlinear load current and $i_{L\alpha 1}$ and $i_{L\beta 1}$ are the extracted component of nonlinear load current depicted in Fig. 4.19(b). During the load elimination period, the extracted component i_α, i_β, $i_{L\alpha 1}$ and $i_{L\beta 1}$ are achieved the zero value.

<center>(a)   (b)</center>
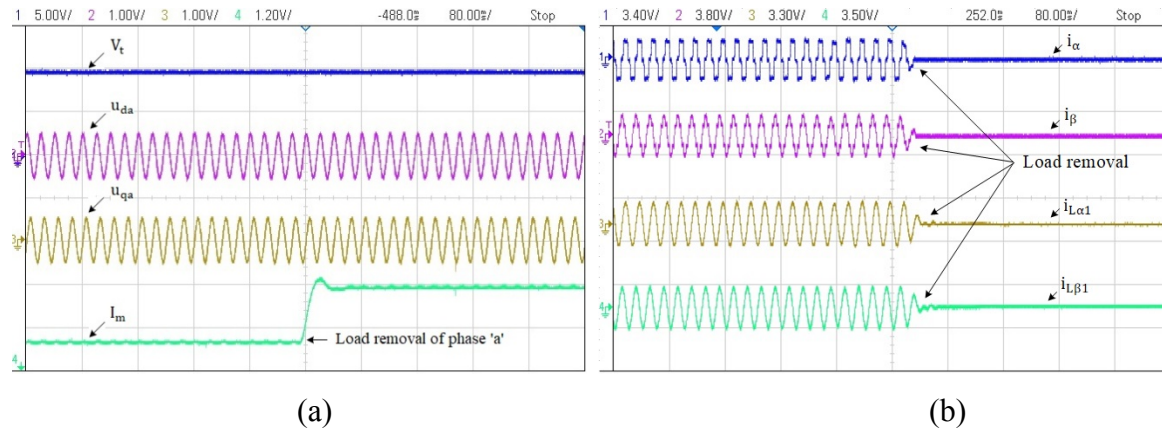
Fig. 4.19 Internal signals of SOSF-FLL control algorithm (a) V_t, u_{da}, u_{qa} and I_m and (b) i_α, i_β, $i_{L\alpha 1}$ and $i_{L\beta 1}$

4.4.3.2 Dynamic Response of Standalone System

The dynamic response of a 3P3W standalone system under load perturbation is depicted in Fig. 4.20(a) & (b). The dynamic response of the DC link voltage, PCC voltage, PCC current, and load current under removal of the phase "a" load is given in Fig. 4.20(a). The PCC current (i_{gabc}) and load current (i_{Labc}) are both decreased as the load is detached, while the dc link voltage is slightly raised. The battery system uses more energy during this operation, and the battery is switched to charging mode.

<center>64</center>

In Fig. 4.20(b), the PCC current (i_{gabc}) and load current (i_{Labc}) are increased during the insertion of load in phase 'a'. BDC regulates the charging and discharging modes of a battery system. Under transient conditions, the battery system is employed to control the dynamics of a standalone system. The SOSF-FLL-based controller successfully maintains the parameters and stabilizes the standalone system's current profile and DC link voltage.

(a)   (b)
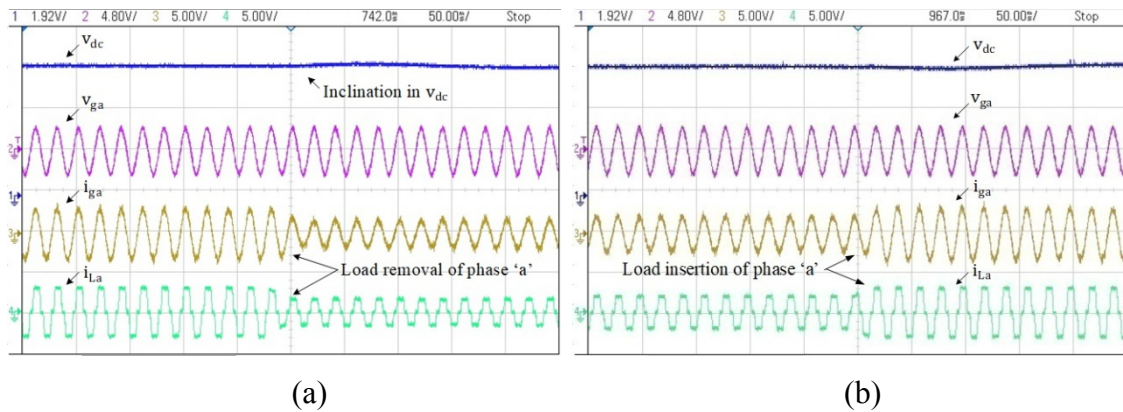
Fig. 4.20(a) and (b) Dynamic response of the standalone system under unbalanced load

4.4.3.3 Harmonic Analysis of Standalone system

The THD of a standalone system PCC voltage (v_{gabc}) & current (i_{gabc}) is always well within the allowable range 5%, while a highly nonlinear load is given to the generator. In SOSF-FLL control approach, the THD's of standalone system PCC voltage & current as represented in Fig. 4.21(a) are 2.0% and 4.07% respectively. These PCC voltage and PCC current THDs at PCC are within the IEEE 519 standard limit. As represented in Fig. 4.21(b), the non-linear load current has a THD of 27.89%. For reactive power support during transient conditions, the converter provides the needed reactive power.

(a)   (b)
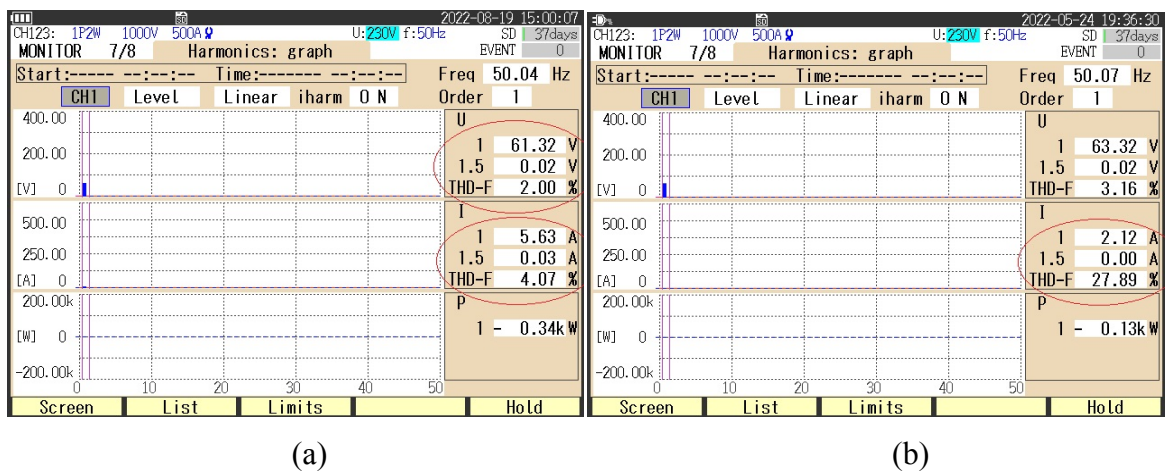
Fig. 4.21(a) THD's of PCC voltage, PCC current and (b) load current

4.5 VGC-IPLL Control Approach

In the described literature, an article introduces an improvement to the conventional Three-Phase-Injection Phase-Locked Loop (3-phIPLL) control algorithm by incorporating adaptive gain adjustment. The conventional control algorithm has a trade-off between steady-state response and tracking response, where choosing a minimum gain results in a good steady-state response but slow tracking, while high gain values lead to quick response but irrational behavior. To address this issue, an adaptive adjustment of the gain factor in the 3-phIPLL is considered. By automatically varying the gain value, the autonomous Microgrid (MG) system achieves improved transient and steady-state performance. The originality of the method lies in the application of the Least Mean Squares (LMS) technique to accomplish adaptive gain variation. Fig 4.22 to illustrates the implementation of the LMS technique for adaptive gain variation. This technique is a widely used adaptive filtering algorithm that adjusts the gain coefficients iteratively based on the error signal to minimize the mean square error between the desired and estimated signals. In the context of the 3-phIPLL, the LMS technique is utilized to update the gain factor dynamically, allowing the control system to adapt and optimize its response based on the prevailing operating conditions. By employing the LMS technique for adaptive gain variation in the 3-phIPLL, the article aims to improve the performance of the control approach, achieving improved transient and steady state behavior in the autonomous Microgrid system.
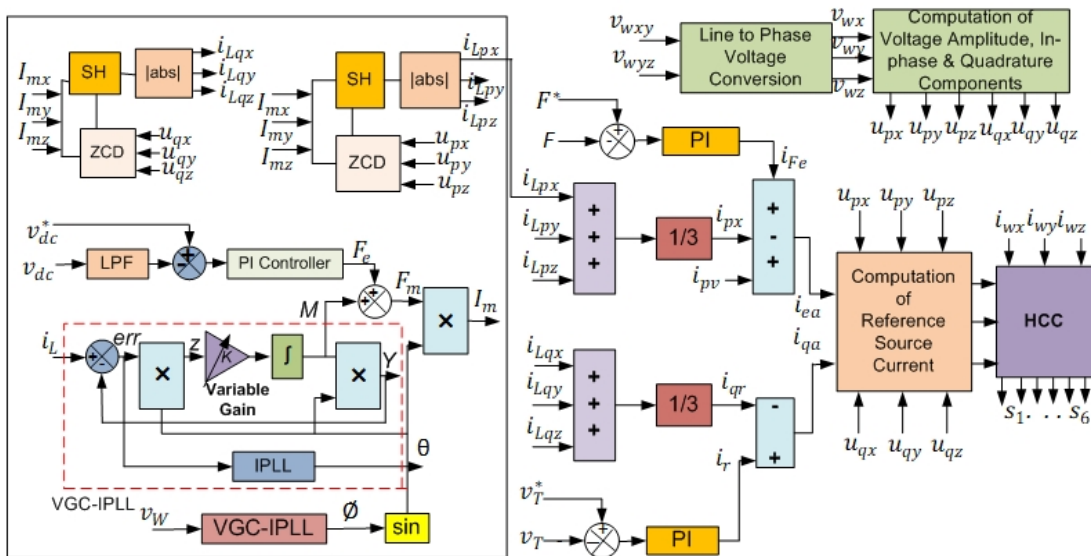
Fig.4.22 Control scheme of proposed topology

The weight K is modified adaptively using the iterative steepest descent technique. Where Q is the objective function, which is evaluated as

$$Q = 0.5 \times err^2 \tag{4.31}$$

Where 'err' is the difference between the estimated and actual quantity, which is used to determine the current for the proposed VGC-based IPLL controller.

$$err = i_L - I \tag{4.32}$$

The weight K is calculated using the LMS approach [34] if the load current is 'i_L' and the estimated fundamental load current is $I = M\sin\emptyset$.

$$Km + 1 = Km + \Delta Km \tag{4.33}$$

$$\Delta K(n) = -\eta \frac{\delta Q}{\delta M} = \eta \times err \times \sin\emptyset \tag{4.34}$$

Where, η is a fixed term that corresponds to the LMS learning rate. The adaptive weight K(m+1), which is based on error (err), LMS learning rate, and sin Ø, substitutes the constant gain K in the 3-phIPLL block. The gain 'K' of a voltage loop is calculated accordingly. Then, in load compensation calculations for reference current generation, the fundamental positive sequence component "M" of the current loop is used. To address the PQ difficulties of autonomous MG, the VGC-IPLL's input signal is used in equation 4.42.

$$i_L = I_m \sin\theta \tag{4.35}$$

Where, load current (i_L), amplitude (I_m) and phase value (θ) are the extracted components. The output equation of the controller is described as

$$Y = M\sin\emptyset \tag{4.36}$$

Where, M and Ø represent the extracted amplitude of load current and phase of Y, which is derived using the voltage loop from Fig. 4.22. Now the error (err) is assessed as

$$err = i_L - Y \tag{4.37}$$

From equations (4.35) and (4.36)

$$err = I_m \sin\theta - M\sin\emptyset \tag{4.38}$$

Fig. 4.22 shows the output 'z' is estimated as

$$z = err \times \sin\emptyset \tag{4.39}$$

From eq. (4.38) & (4.39), z is evaluated as

$$z = (I_m \sin\theta - M\sin\emptyset)\sin\emptyset \tag{4.40}$$

After simplification, the previous equation (4.39) is written as

$$z = \frac{I_m}{2}\cos(\theta - \emptyset) - \frac{M}{2} + \frac{M}{2}\cos(2\emptyset) - \frac{I_m}{2}\cos(\theta + \emptyset) \tag{4.41}$$

When the system approaches a steady state, the third and fourth terms of (4.40) are virtually zero, and (4.41) is rewritten as

$$z = \frac{I_m}{2}\cos(\theta - \emptyset) - \frac{M}{2} \tag{4.42}$$

If 'K' is a constant term, the maximal value of the fundamental component 'M' is determined as

$$M_m = -K\left[\frac{i_M}{2}\sin(\theta - \emptyset_{n-1}) + \int \frac{M_{m-1}}{2}d\emptyset\right] \tag{4.43}$$

$$M_m^* = -K_{n-1}^*\left[\frac{i_M}{2}\sin(\theta - \emptyset_{n-1}) + \int \frac{M_{m-1}^*}{2}d\right] \tag{4.44}$$

The equations (4.43) and (4.44) above are used to calculate the fundamental component and phase angle under various operating circumstances. For improved-PLL with constant weight components (K), equation (4.43) is utilized, whereas equation (4.44) contains variable weight components (K*) [133]. Under the dynamic circumstance of RESs and nonlinear load, the proposed control correctly estimates the components (fundamental peak current and phase angle).

4.5.1   Simulation results

The detailed design and simulation study is carried out for an ESS, SPV and wind driven SEIG generation based autonomous MG in MATLAB/Simulink. The proposed autonomous system is simulated under changes in wind speed/solar intensity while feeding an unbalanced nonlinear load. The simulation results in the form of relevant waveforms such as CPC voltage (v_{wxyz}), CPC current (i_{wxyz}), load current (i_{Lxyz}), compensator current (i_{cxyz}), dc-link voltage (v_{dc}), frequency (F), neutral current (i_{sn}), ESS current

(i_{ess}), SPV voltage (v_{spv}), SPV current (i_{spv}) and duty cycle (μ) are presented under the transient condition of RESs and unbalanced load. Furthermore, the internal signals of the VGC-IPLL control approach are thoroughly investigated.

4.5.1.1 Intermediate Control Signals of Autonomous MG

The intermediate signals of autonomous MG are also determined and discussed in this section. Fig. 4.23(a) and (b) show the intermediate control signals of the VGC-IPLL control scheme. A load of phase 'x' is suddenly removed at t = 2.7s. Fig. 4.23(a) shows the signals u_{px} (in-phase unit template), u_{qx} (quadrature unit templates), v_T (voltage amplitude), i_r (AC PI controller current) and i_{px} (extracted active component). The in-phase/quadrature unit templates are further used to extract the active current component. The voltage amplitude is evaluated from the source voltage and the comparison of voltage amplitude and reference voltage yields voltage error and the error is fed as an input to the PI controller to evaluate the current of the AC PI controller. The PI controller current is utilized to evaluate the quadrature current (i_{qr}). Fig. 4.23(b) shows i_{qr} (extracted quadrature component), i_{Fe} (DC PI controller current), i_{ea} (extracted active current), i_{eq} (extracted quadrature current) and i^*_{wxyz} (extracted reference source current). The DC PI controller current is computed from the comparison of the reference frequency and MG system frequency and the controller output is utilized to evaluate the active component of the current. Moreover, the combination of active/quadrature current components is utilized to generate the reference source current under an unbalanced load. The reference source current drawn is purely sinusoidal during the removal of a load of phase 'x'. The intermediate signals of VGC-IPLL control improve the system performance and enable the autonomous MG to work under dynamic condition of RESs and load perturbation.
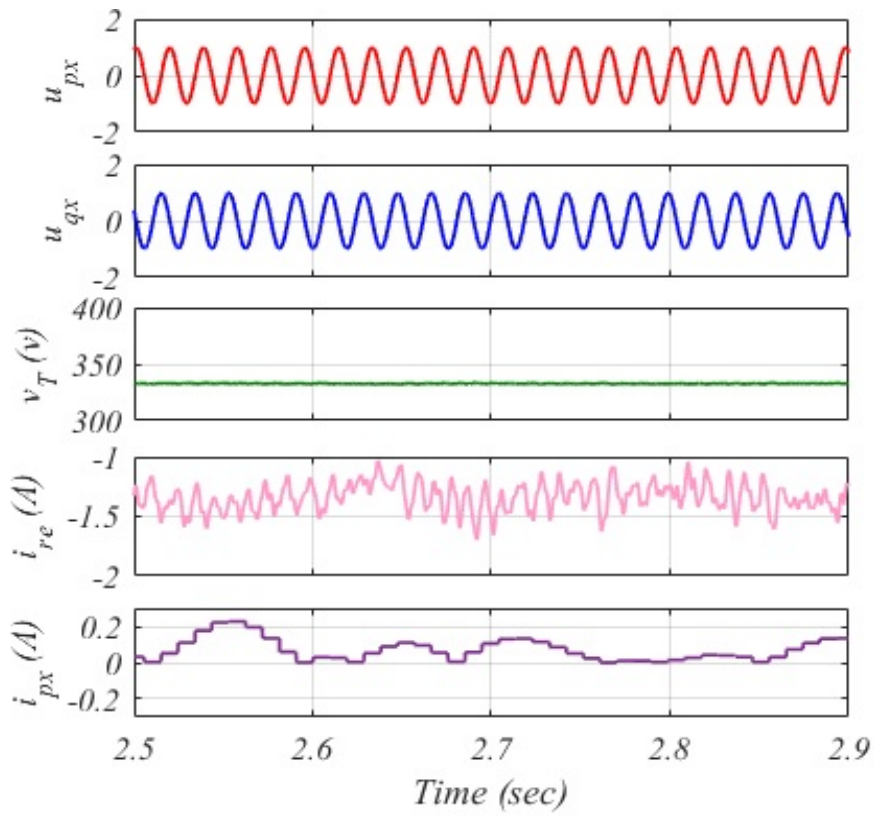
(a)
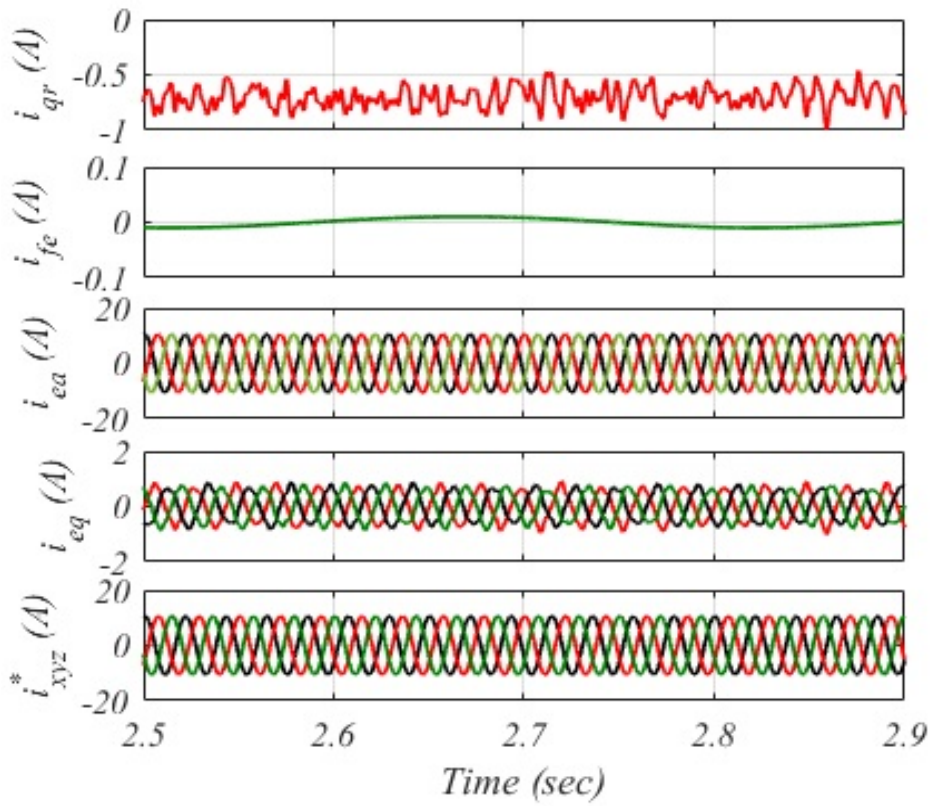
(b)

Fig. 4.23(a) and (b) Intermediate signals of autonomous MG

4.5.1.2 Performance under Variation in Wind Speed

The performance of autonomous MG under fluctuation in wind speed and fixed solar intensity while feeding nonlinear load is represented in Fig. 4.24(a) and (b). Fig. 4.24(a) shows that wind speed is altered from 13m/s to 9m/s at t=2.7s and solar intensity is fixed at 900w/m^2. The VGC-IPLL-based control approach with VSC stabilizes the voltage profile (v_{wxyz}) and current profile (i_{wxyz}). Moreover, the controller also maintains the Dc-link voltage (v_{dc}) and frequency (F) of the autonomous MG under varying wind speeds. Fig. 4.24(b) represents that the compensator current increases during the variation in wind speed and the neutral current are kept to zero with the help of a controller. An ESS supplies power through VSC at CPC to maintain power balance during the changes in wind speed at t=2.7s. A BDC controller determines the charging/discharging mode of an ESS and maintains the power equilibrium at CPC under the dynamic condition of wind.
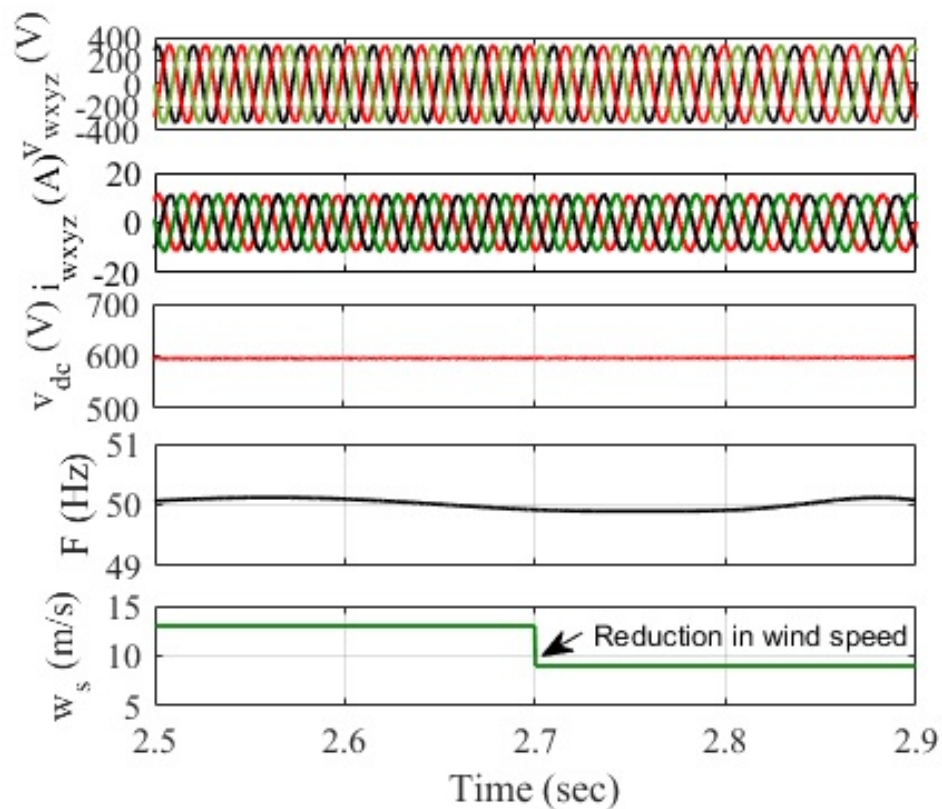
(a)
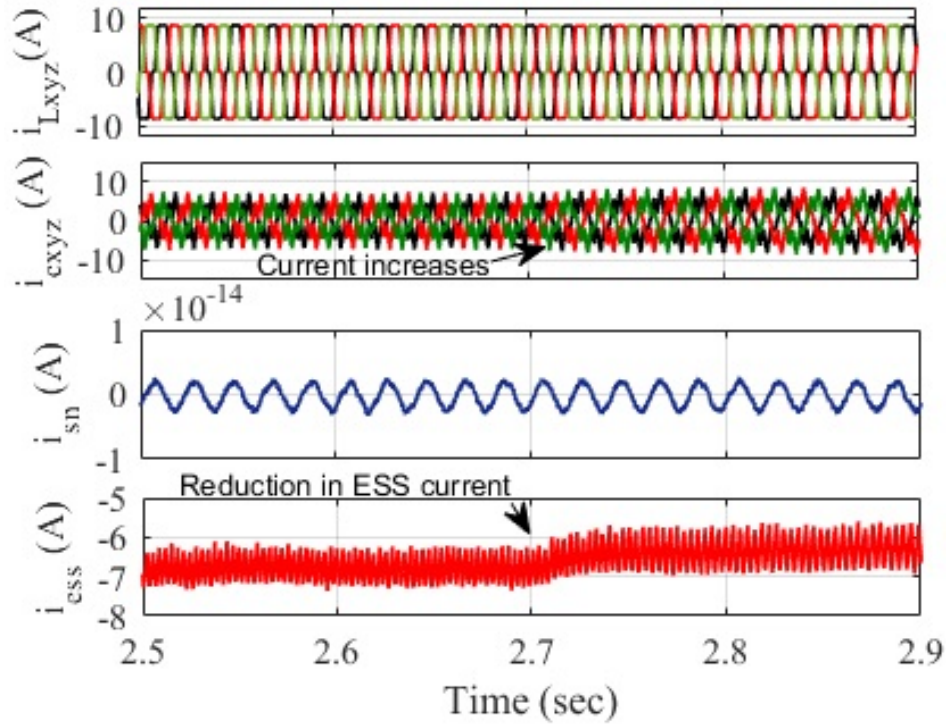
(b)

Fig. 4.24(a) and (b) Performance of autonomous MG under a change in wind speed

4.5.1.3 Performance under Variable Solar intensity

Fig. 4.25(a)-(c) shows the performance of autonomous MG under variation in solar intensity and constant wind speed while feeding a balanced nonlinear load. Fig. 4.25(a) shows that the solar intensity is shifted from 500w/m^2 to 900w/m^2 and temp. from 25°C to 35°C at t=2.7s and the wind speed is fixed at 13m/s. Due to the fluctuations in solar intensity, the PV current and duty cycle are decreased. Fig. 4.25(b) shows that the source voltage of autonomous MG is distorted for 0.008s at t=2.7s due to an alteration in solar intensity. After this, the controller manages the voltage profile of autonomous MG and the source current of the system is also increased from 10A to 15A due to the inclination of solar intensity. The VGC-IPLL-based controller maintains the other parameters of the autonomous microgrid such as DC link voltage and frequency. Fig. 4.25(c) shows that compensator current and ESS current are increased at t=2.7s due to the inclination of solar intensity level. The excess power is supplied to an ESS and ESS is shifted from discharging mode to charging mode. Thus, an ESS maintains the power equilibrium between the autonomous MG and the load.
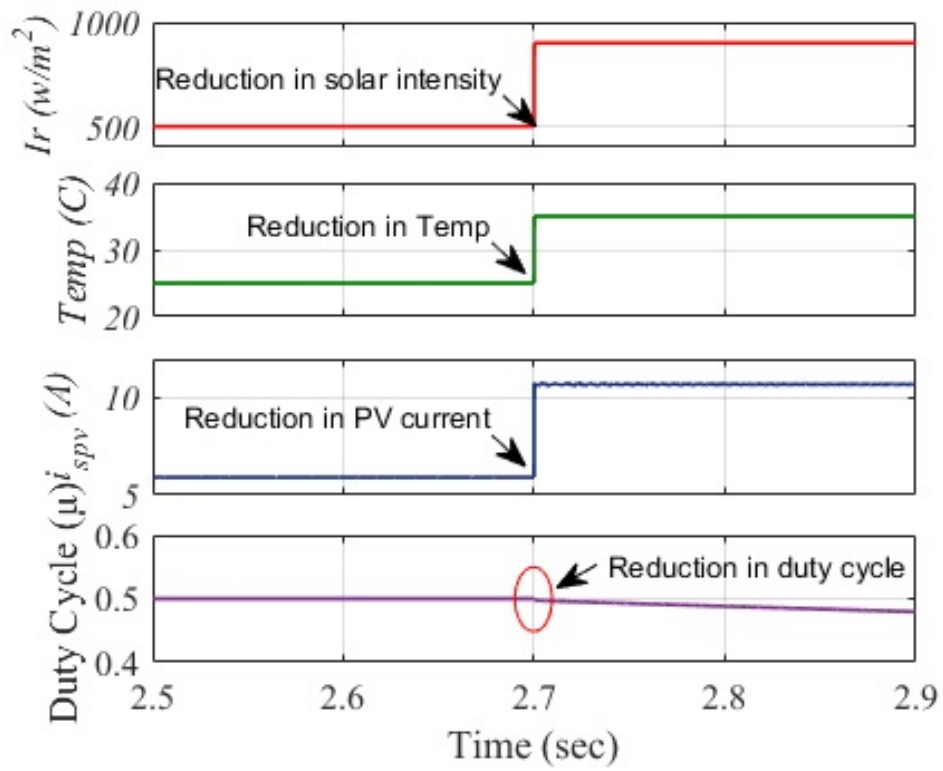
Fig. 4.25(a) Performance of SPV system
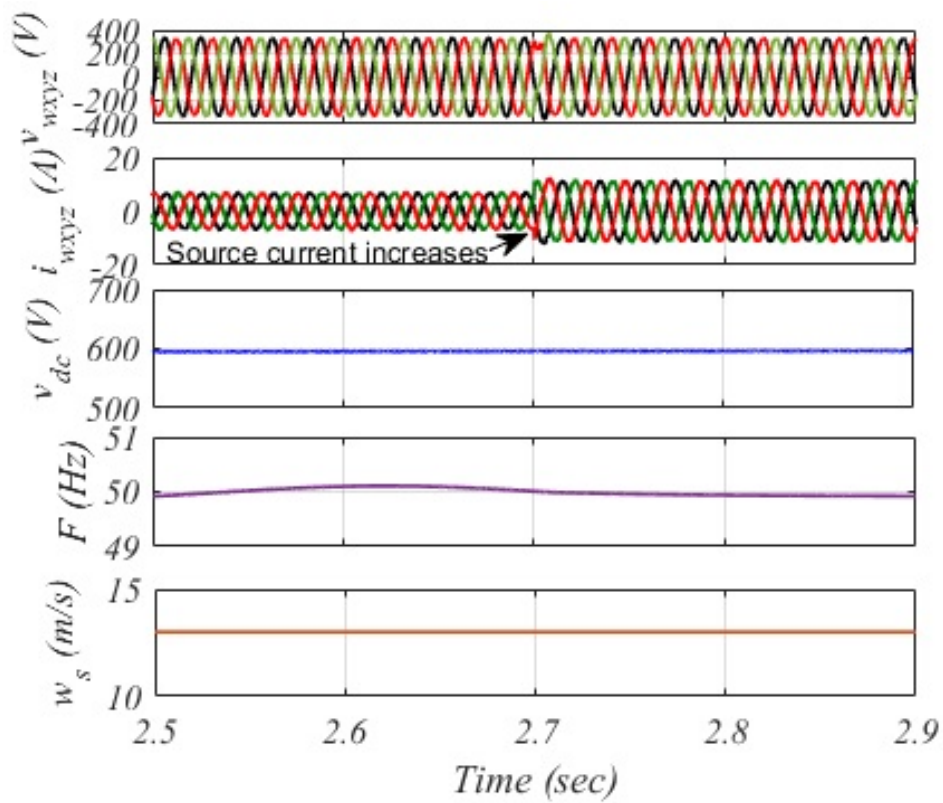
(b)
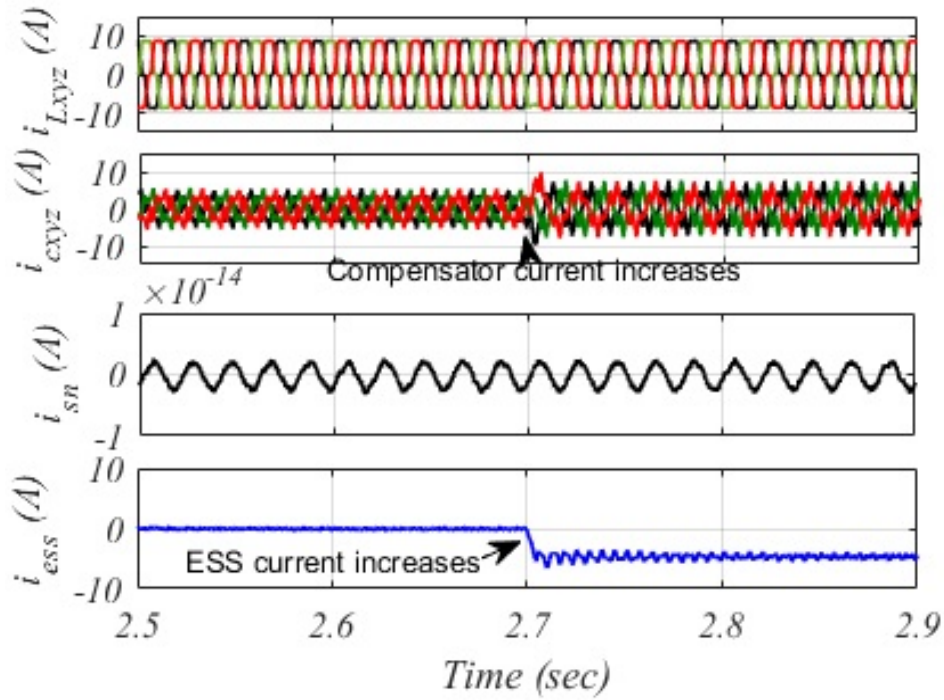
(c)

Fig. 4.25(b) and (c) Performance of autonomous MG under a change in solar intensity

4.5.1.4 Performance under Unbalanced Load

Fig. 4.26(a) and (b) depict the performance of an autonomous MG while feeding an unbalanced nonlinear load with a fixed wind speed/solar intensity. The wind speed and solar intensity are fixed at 13m/s and 900w/m^2 respectively. A load of phase 'x' is removed at t=2.6s to t=2.8s. Fig. 4.26(a) shows the voltage/current profile and frequency maintained by the VGC-IPLL based controller during unbalanced loading. Moreover, a BDC controller manages the ESS power and regulates the dc link voltage during unbalanced loading. Fig. 4.26(b) depicts the load current of the autonomous system is reduced during the elimination of a load of phase 'x'. The ESS charging current is increased during the rejection of load from t=2.6s to t=2.8s. The modes of charging/discharging are successfully controlled by BDC. During load removal duration the generated power and solar power are kept constant.
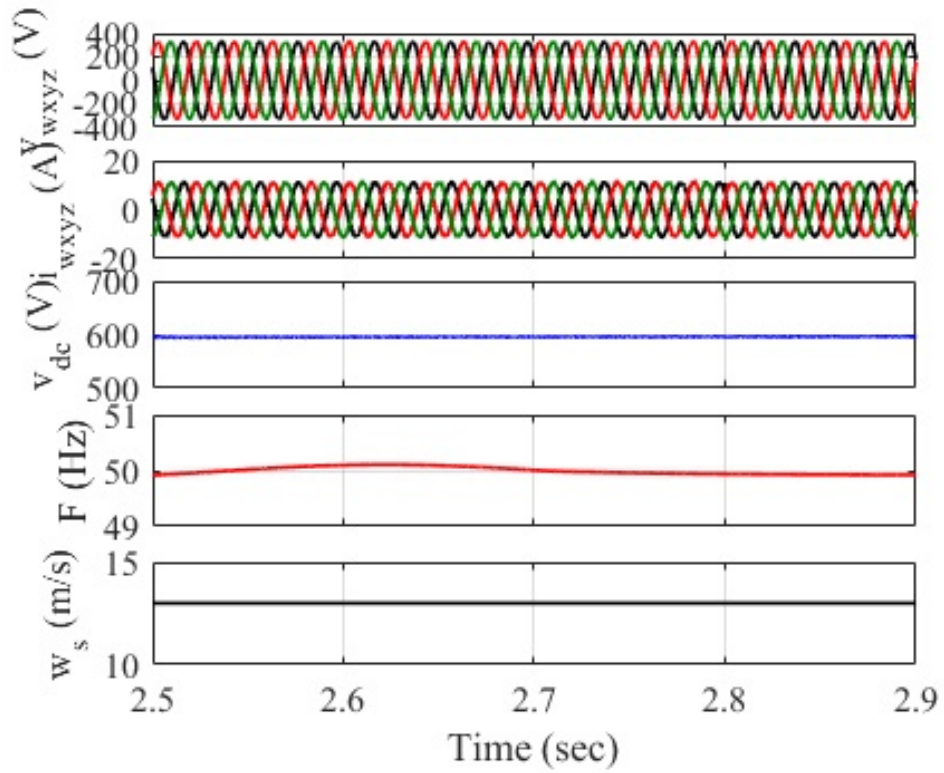
(a)
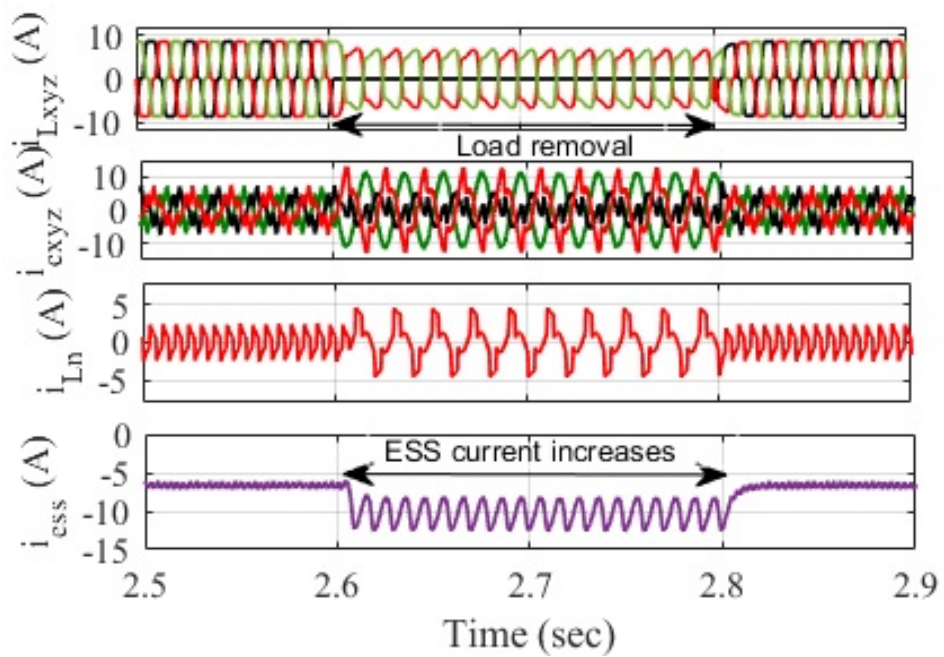
(b)

Fig. 4.26(a) and (b) Performance of autonomous MG feeding unbalanced nonlinear load

4.5.1.5 Analysis of Balance in Power of Autonomous MG

Fig. 4.27(a)-(c) shows power balance of autonomous MG under dynamic operating conditions. Fig. 4.27(a) depicts the generated power, solar power, ESS power and load power under a change in wind speed from 13m/s to 9m/s at t=2.7s and the solar intensity is fixed at 900w/m^2 while feeding a nonlinear load. The generated power declined during the declination in wind speed at t=2.7s. Hence, the total generated power is reduced from 5.5kW to 5.3kW and the ESS power is also reduced. Fig. 4.27(b) represents the generated power, solar power, ESS power and load power under fluctuations in solar intensity from 500w/m^2 to 900w/m^2 and temp. 25°C to 35°C and the wind speed is fixed at 13m/s. Due to the change in solar intensity level, the generated power, and solar power is reduced from 3.18kW to 5.55kW and 0.91kW to 2kW, respectively. During inclination in solar power, the ESS power is increased. Fig. 4.27(c) depicts the generated power, solar power, ESS power and load power under fixed solar intensity/wind speed feeding an unbalanced nonlinear load. A load of phase 'x' is rejected at t=2.6s to t=2.8s. During the rejection of load, the load power is diminished and the ESS power is increased.
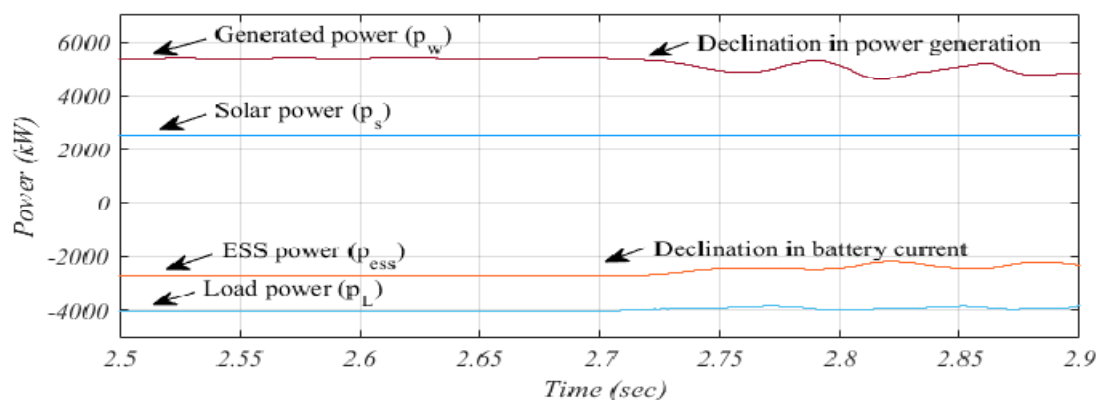
(a)
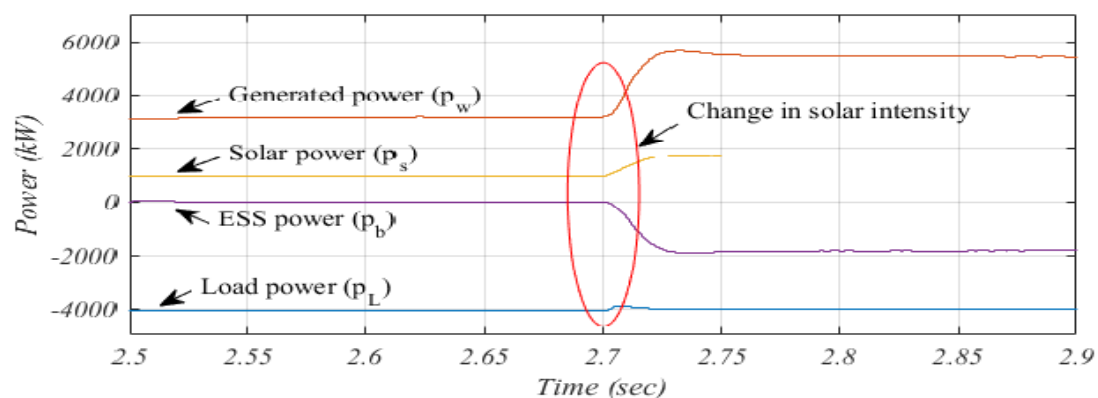
(b)
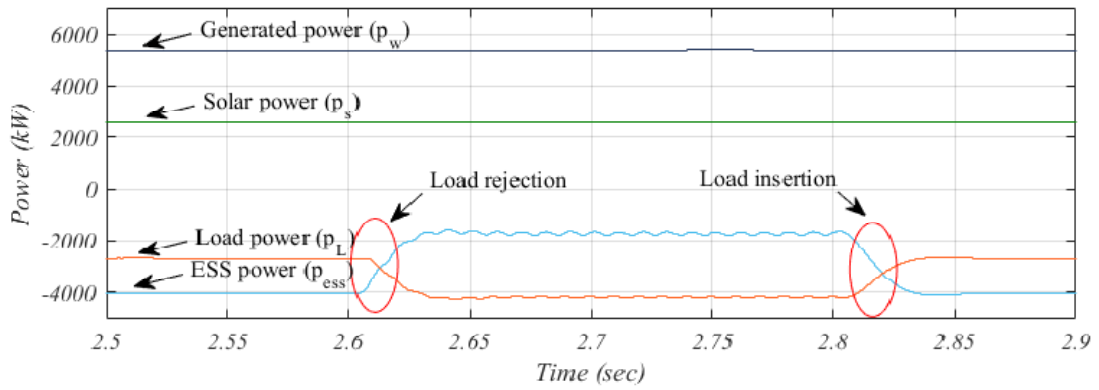
(c)

Fig. 4.27(a)-(c) Power indices of autonomous microgrid (a) change in wind speed, (b) change in the level of solar intensity and (c) unbalanced nonlinear load

4.5.1.6 Steady State Response

The steady-state response of autonomous MG indicates that the CPC voltages and CPC currents are maintained balanced and sinusoidal with minimum harmonics distortion. Fig. 4.28(a)-(c) shows the harmonic spectra of the CPC voltage (v_{wz}), CPC current (i_{wz}) and load current (i_{Lz}) of phase 'z'. In the presence of a distorted load current with a THD of 24.94%, the THDs of CPC currents are determined to be below the permitted limit of 5%, according to the IEEE-519 standard.

(a)   (b)
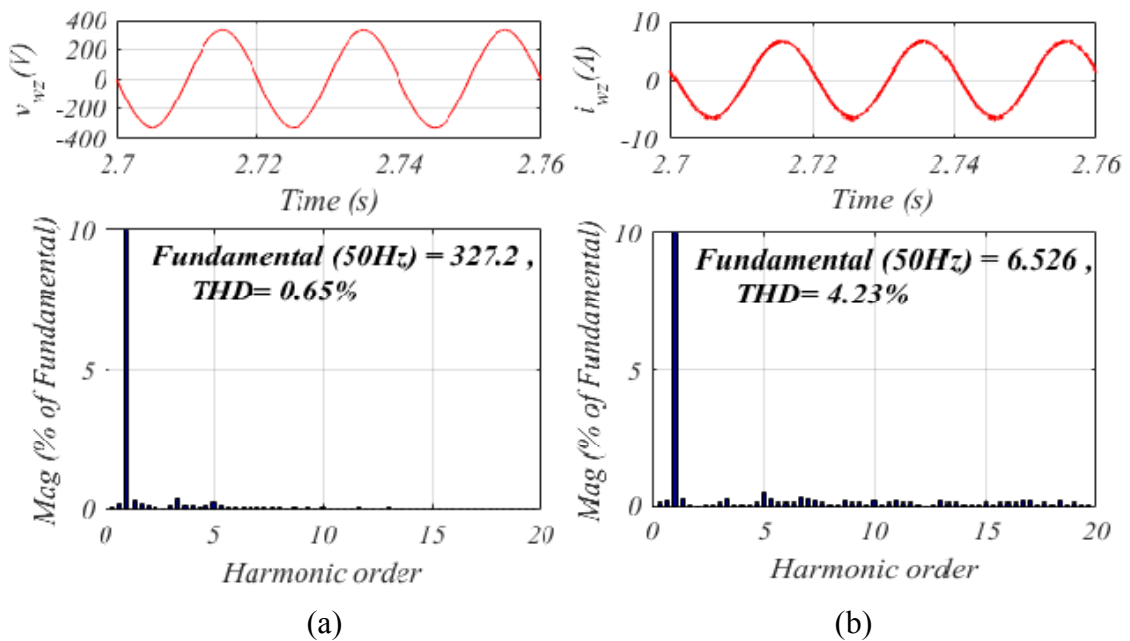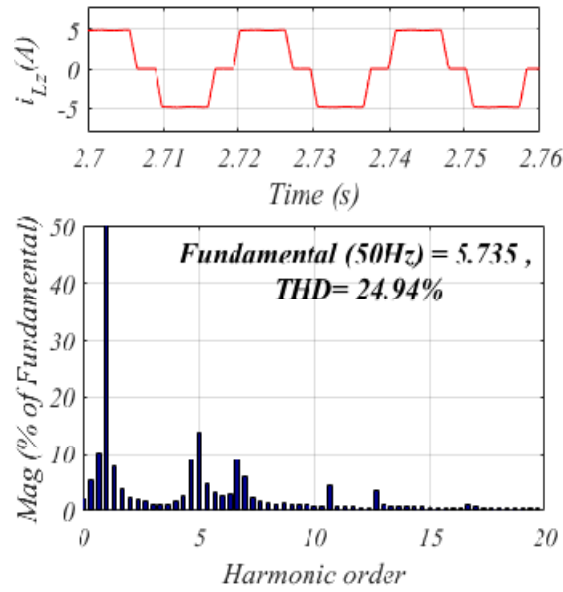
(c)

Fig. 4.28(a)-(c) Harmonic spectrum of phase 'z' (a) CPC voltage (v_{wz}), (b) CPC current (i_{wz}) and (c) Load current (i_{Lz})

4.5.2   Experimental Results

The experimental test results and harmonic indices of the autonomous MG have been shown in Fig. 4.29(a)-(d), 4.30(a) & (b) and 4.31(a) & (b). The transient response of VGC based IPLL control approach and autonomous MG is described as follows.

4.5.2.1 Intermediate Signals of Autonomous System

Fig. 4.29(a)-(d) represents the intermediate signals of the autonomous system under transient circumstances of load. Fig. 4.29(a) shows the nonlinear load current (i_{Lx}) of phase 'x', extracted components using abc to αβ Clarke transformation (i_α and i_β), and amplitude of terminal voltage (v_T) drawn from nonlinear load current. During the insertion of a load of phase 'x', the extracted component (i_α and i_β), and the load current is increased. The terminal voltage is maintained almost constant under fluctuating conditions of load with the help of the proposed control. Fig. 4.29(b) shows the nonlinear load current (i_{Lx}) of phase 'x', extracted component ($i_{L\alpha}$ and $i_{L\beta}$), and amplitude of fundamental current component (I_m) drawn from nonlinear load current. During the insertion of load, the intermediate signals i_{Lx}, $i_{L\alpha}$, $i_{L\beta}$ and I_m are increased is depicted in

Fig. 4.30(b). Fig. 4.29(c) shows the response of load current (i_{Lx}), reference source current (i_{sx}^{*}), in-phase (u_{px}) and quadrature unit templates (u_{qx}) of phase 'x' during dynamic conditions of load. During load removal of phase 'x', the load current is zero and the extracted unit templates are purely sinusoidal. The load current and reference current is increased during the insertion of load as shown in Fig. 4.29(c). The CPC voltage (v_{wx}) of phase 'x' and CPC current (i_{wxyz}) of all phases is depicted in Fig. 4.29(d). The source voltage (v_{wx}) is maintained constant and the source current is increased in all phases (i_{wx}, i_{wy} and i_{wz}) during the injection of load. The observed intermediate parameters are utilized to control the proposed autonomous system under numerous operating conditions.

(a)   (b)

(c)   (d)
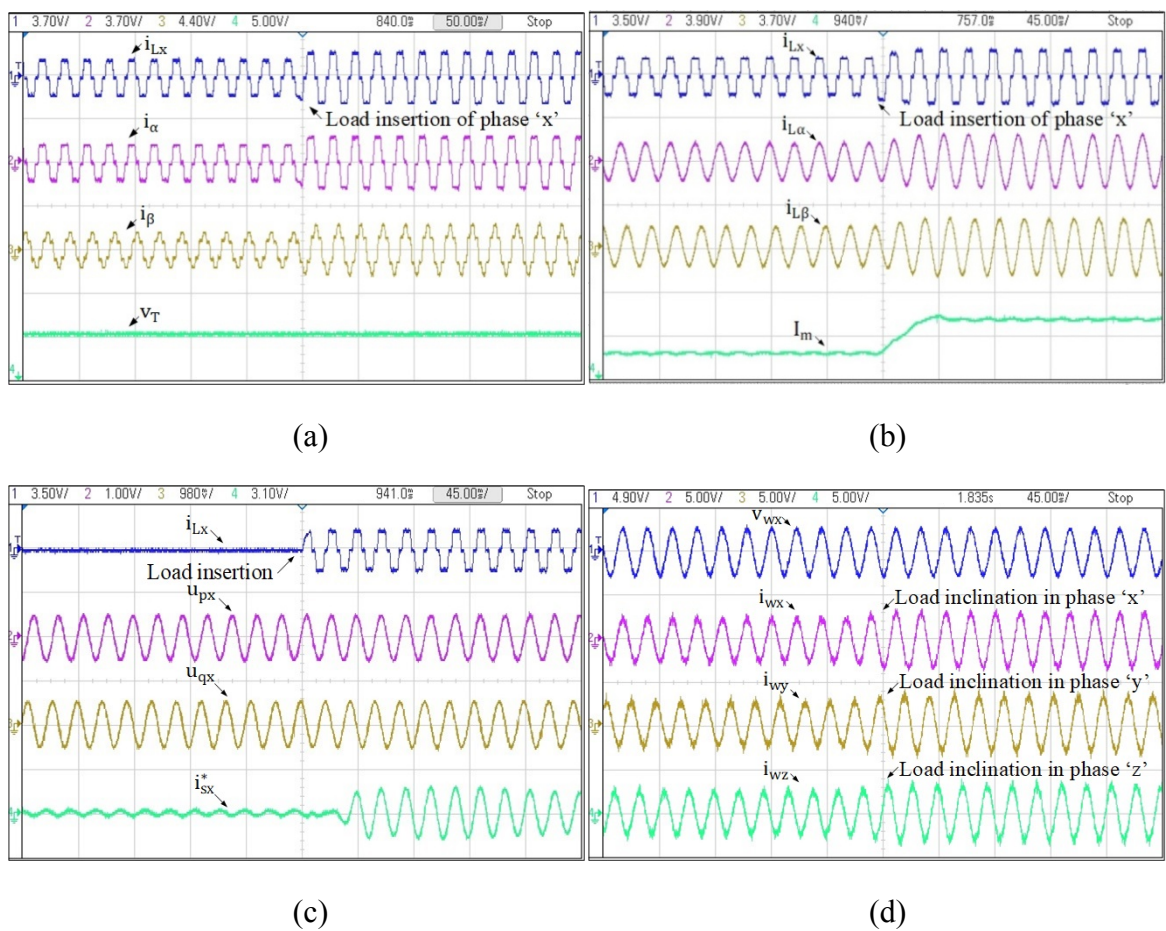
Fig. 4.29(a)-(d) Intermediate signals of (a) Load curent (i_{Lx}), extracted component using Clarke transformation (i_{α} and i_{β}), and amplitude of terminal voltage (v_T), (b) load current (i_{Lx}), extracted component using a variable gain controller from load current ($i_{L\alpha}$ and $i_{L\beta}$) and amplitude of fundamental load current component (I_m), (c) load current (i_{Lx}), refernce source current (i_{sx}^{*}), in − phase (u_{px}) and quadrature unit templates (u_{qx}) (d) CPC voltage of phase 'x'(v_{wx}), CPC current of all phases (i_{wx}, i_{wy} and i_{wz})

4.5.2.2 Transient Response of Autonomous System

Fig. 4.30(a) & (b) represents the transient response of an autonomous system under dynamic load conditions. Fig. 4.30(a) shows the transient response of dc link voltage (v_{dc}), CPC voltage (v_{wx}), CPC current (i_{wx}) and load current under insertion of a load of phase 'x'. During the insertion of load, the CPC current (i_{wxyz}) and load current is increased. On the other side in Fig. 4.30(b), during the insertion of a load of phases 'x' and 'y', the CPC current (i_{wxyz}) and load current is increased. The charging or discharging modes of the ESS system are controlled by BDC. The ESS is utilized to control the dynamics of the autonomous system under dynamic conditions. The VGC based IPLL control successfully maintains the parameters and stablizes the current profile and dc-link voltage of the autonomous system.

(a)   (b)
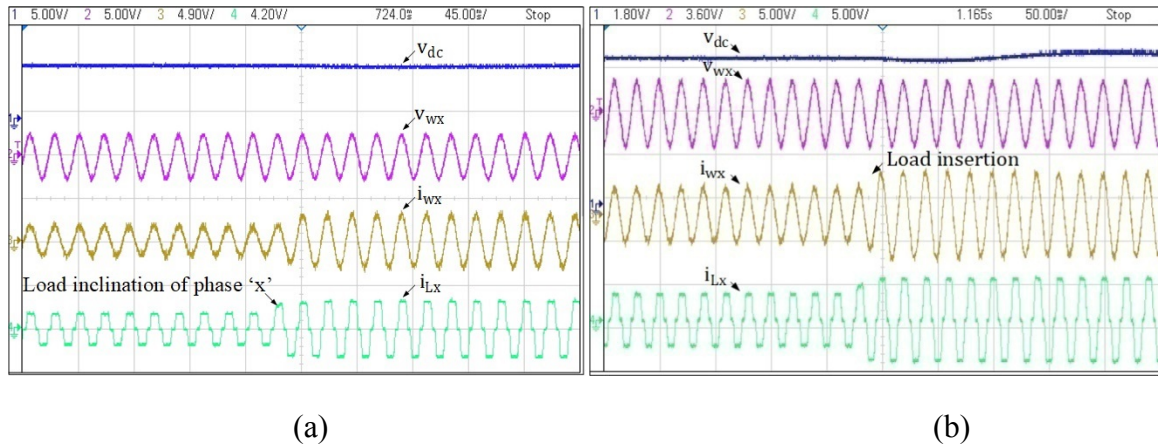
Fig. 4.30(a) and (b) Transient response of dc link voltage (v_{dc}), CPC voltage of phase 'x' (v_{wx}), CPC current of phase 'x' (i_{wx}) and load current (i_{Lx}) at dynamic load conditions

4.5.2.3 Harmonic Indices of Autonomous System

The THD in an autonomous MG system CPC voltage (v_{wxyz}) and CPC current (i_{wxyz}) is always well within the acceptable limit of 5%, while a highly nonlinear load is connected to the generator terminals. In the VGC-IPLL control approach, the THD's of autonomous system CPC voltage and CPC current as shown in Fig. 4.31(a) are 2.71% and 4.73% respectively. These CPC voltage and CPC current THDs at CPC are within the IEEE 519 standard limit. The non-linear load current has a THD of 27.69% as depicted in Fig. 4.31(b).
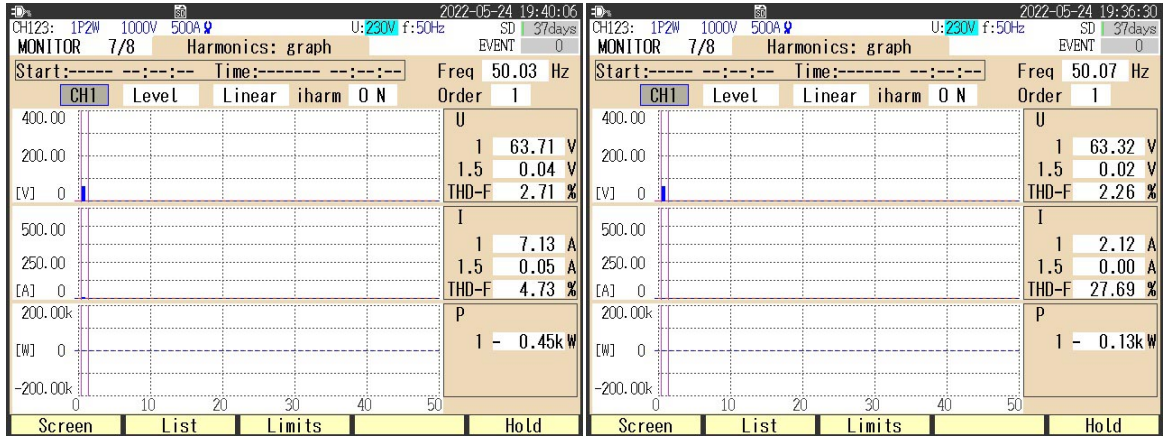
| | (a) | | | (b) |

Fig. 4.31(a) and (b) THDs of CPC voltage, CPC current and load current

4.6 3Ø-APF-PLL Control Approach

The control approach that is employed to maintain voltage profile, frequency and reduce PQ issues is crucial to the proposed SPV-wind-BES-based islanded electrical supply system's ability to operate effectively. The following summarizes the control approach.

4.6.1 Design of 3Ø-APF-PLL

The functional diagram of the 3Ø-APF-PLL approach is given in Fig. 4.32. The proposed control is devised in two sections SRF-PLL and FFPS component detector. The FFPS component detector operates in the stationary frame (αβ) using the theory of instantaneous symmetrical components. According to this theory, the FFPS component of an imbalanced vector in the αβ frame can be retrieved by performing the following transformation [31].

$$\begin{bmatrix} \check{i}_{\alpha 1} \\ \check{i}_{\beta 1} \end{bmatrix} = 0.5 \begin{bmatrix} 1 & -q \\ q & 1 \end{bmatrix} \begin{bmatrix} i_{\alpha}(t) \\ i_{\beta}(t) \end{bmatrix} \tag{4.45}$$

Where, $q = e^{-j\pi/2}$. A first-order APF is utilized to implement the 90° phase-shift operator (q) in the three-phase APF-PLL.

Taking the APF transfer function as

$$G_{APF}(s) = \frac{\omega - s}{\omega + s} \tag{4.46}$$

81

Equation (4.45) can be expressed in space vector notation as follows:

$$[\tilde{\imath}_{\alpha 1}(s) + \tilde{\imath}_{\beta 1}(s)] = \frac{1}{2}\left[1 + j\frac{\omega - s}{\omega + s}\right][i_\alpha(s) + ji_\beta(s)] \quad\quad (4.47)$$

It exhibits unity gain with zero phase at +50 Hz and zero gain at -50 Hz, as expected for an FFPS component detector.
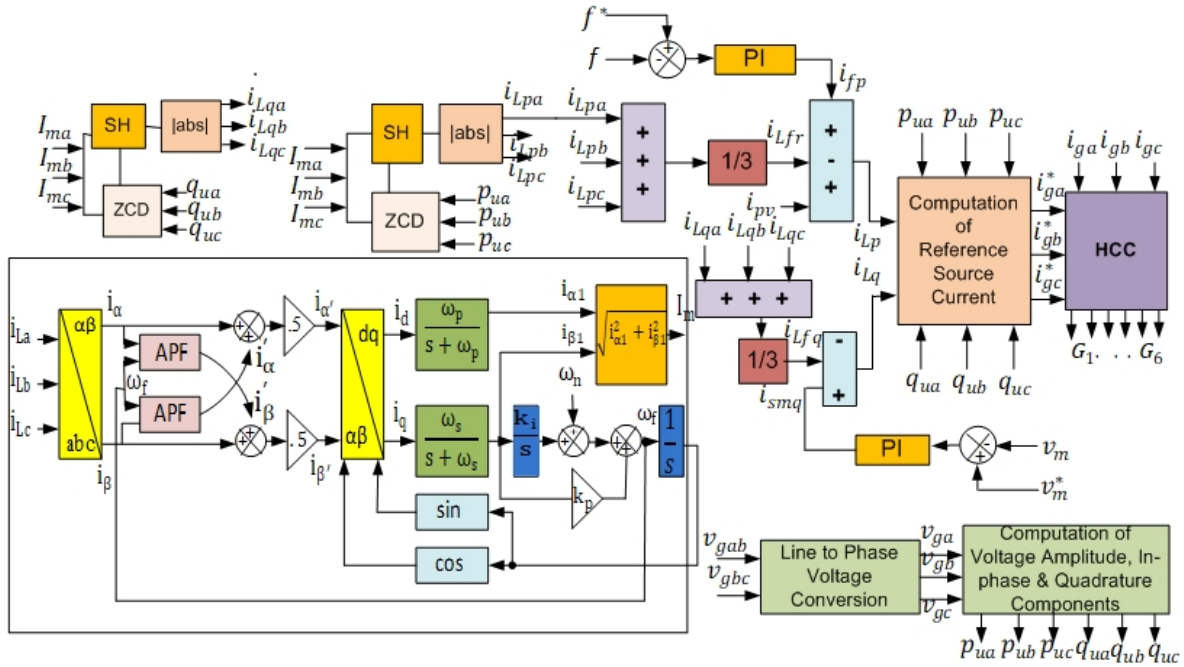
Fig. 4.32 Control scheme of an islanded electrical supply system

4.6.2 Simulation Results

The detailed simulation results using MATLAB for the wind, solar PV, BES, and nonlinear load-based standalone electrical supply system are examined in this section. In this work, the system is simulated with changes in wind speed/solar irradiance, and unbalanced load. In addition, the internal parameters of the designed 3Ø-APF-PLL control strategy are thoroughly examined.

4.6.2.1 Internal Parameters of the 3Ø-APF-PLL Control Approach

Fig. 4.33(a)-(c) represents the internal control parameters of the 3Ø-APF-PLL-based islanded electrical supply system under load perturbation. The load of phase 'a' is detached at t=3.3sec. The control signals i_α, i_β, $i_{L\alpha 1}$, $i_{L\beta 1}$, i_q, and I_m are shown in Fig. 4.33(a). These control signals represent the dynamics of various intermediate variables of

the control scheme under the removal of load. Due to the elimination of load the value of i_α is reaches zero at t=3.3sec. The control signals i_{smq}, p_{uabc}, q_{uabc}, i_{Lfr}, i_{Lfq} and ω_g are shown in Fig. 4.33(b). The control signal shows the extracted maximum value of load current, AC PI controller current, and active/quadrature unit vectors. The control signals i_{pf}, i_{Lp}, i_{Lq}, i_{Lp}^*, i_{Lq}^*, and i_{gabc}^* are shown in Fig. 4.33(c) to represent the extracted reference current is completely sinusoidal during distorted load conditions and the real/reactive reference current, DC PI controller current, and extracted reference current.
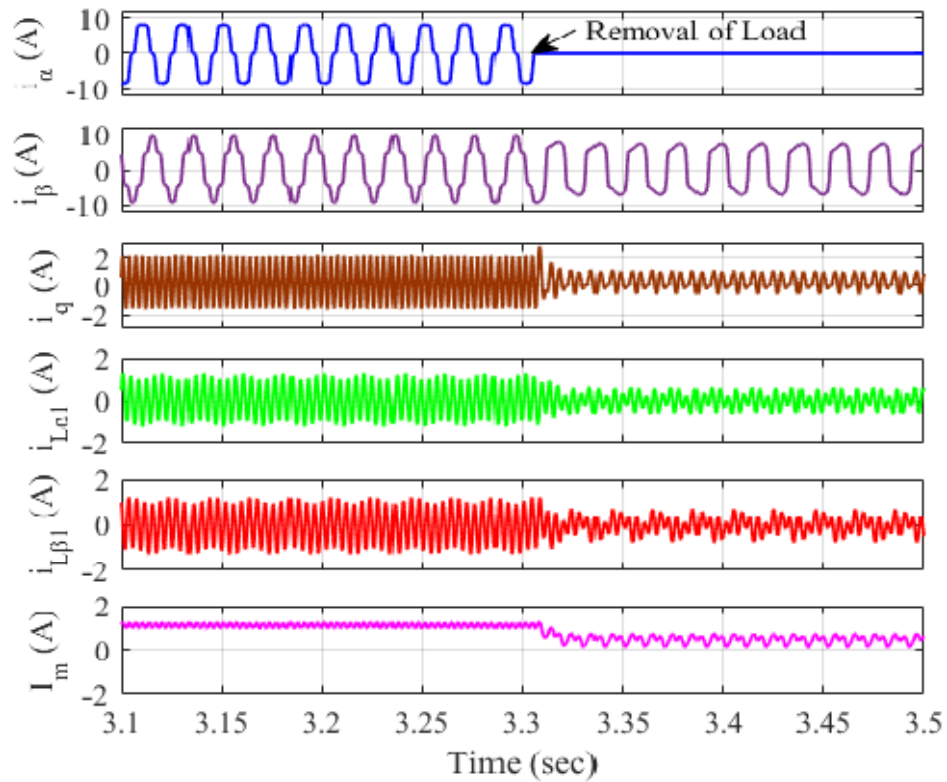
(a)
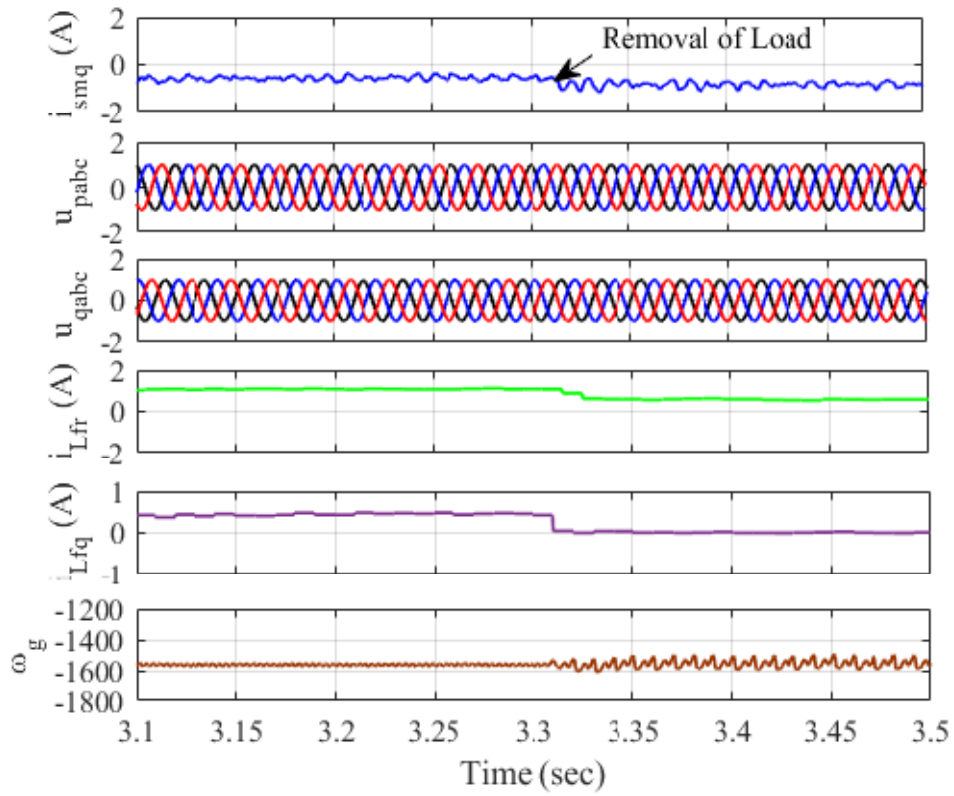
(b)
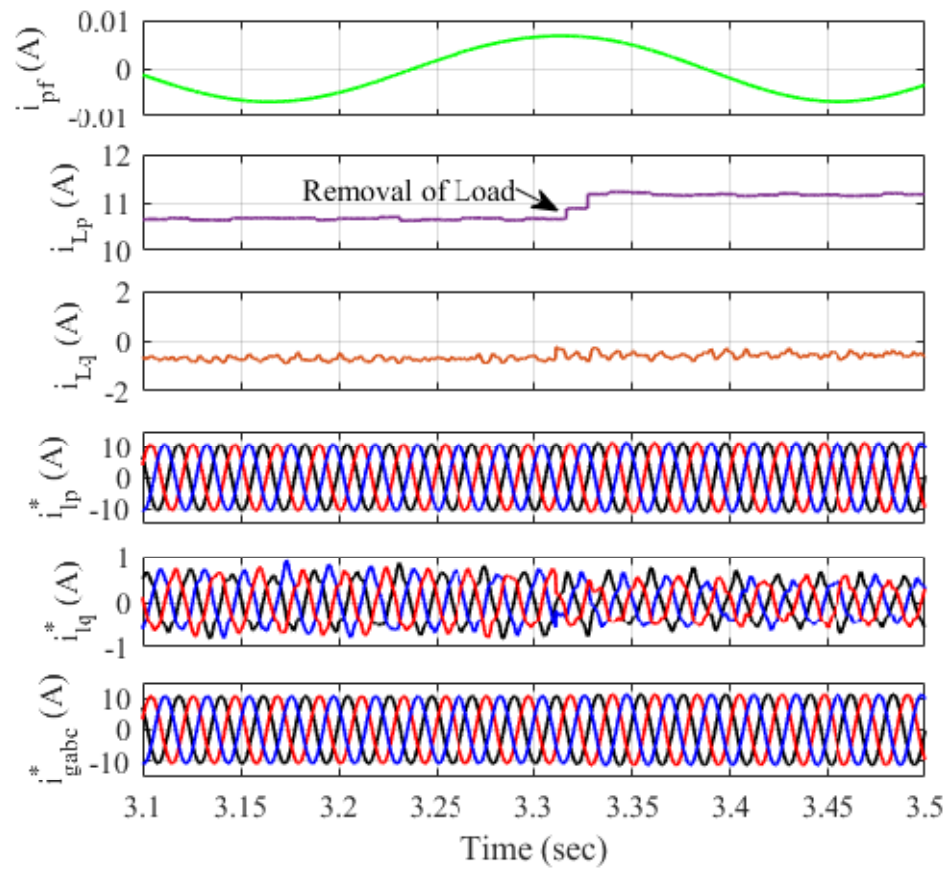
(c)

Fig. 4.33(a)-(c) Estimation of fundamental components of the load current using 3Ø-APF-PLL control algorithm, (b) Estimation of real/reactive unit vectors and AC PI controller current with other intermediate signals using 3Ø-APF-PLL (c) DC PI controller current and reference current generation using 3Ø-APF-PLL.

4.6.2.2 Dynamic Behavior of SolarPV-Wind System during Change in Wind Speed

Fig. 4.34 depicts the dynamic behavior of an islanded electrical supply system with variations in wind speed and constant solar irradiance feeding a linear/nonlinear load. The controller stabilizes the frequency (f) and BES voltage (v_b) or DC-link voltage under the intermittent scenario of wind speed. The wind speed is suddenly shifted from 14m/s to 11m/s at t=3.3sec. results in a decrement in wind power generation and deficit load power which are amplified by the BES through VSC, therefore compensator current is slightly increased and BES charging current is reduced after t=3.3sec. During declination in wind speed, the BES switches from charging to draining mode and maintains the balance of power at PCI. A 3Ø-APF-PLL-based approach with VSC effectively maintains the proposed system voltage & current profile during declination in wind speed.
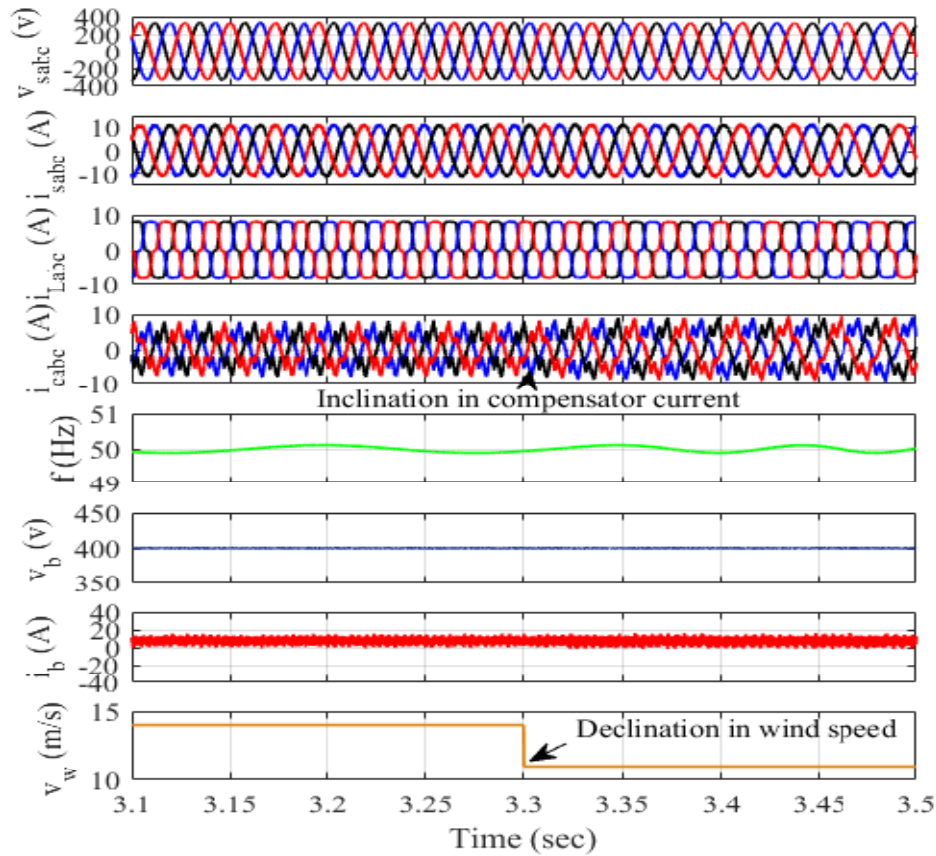
Fig. 4.34 Dynamic behavior of SolarPV-Wind System during Change in Wind Speed

4.6.2.3 Dynamic Behavior of SolarPV-Wind System under the Change in Solar Irradiance

The dynamic behavior of the proposed SPV-wind-BES-based islanded electrical supply system is displayed in Figs. 4.35(a) and (b) with variable solar irradiations 500w/m^2 to 1000w/m^2 and temperature 25ºC to 35ºC, with the wind speed maintained at 14m/s supplying a linear/nonlinear load. Fig. 4.35(a) shows the parameters of the SPV system such as PV current (i_{pv}) and PV power (P) which increases, and decreases in the duty cycle due to changes in solar irradiance at t=3.3sec. During the changing condition of RESs (wind and solar), the BES is employed to maintain the power equilibrium between the applied load and the islanded system. The controller of the islanded electrical supply system monitors the system frequency, voltage, and harmonics, as depicted in Fig. 4.35(b). Due to the inclination of solar power, the BES charging current, PCI current, and compensator current is gradually increased and the controller maintains other parameters

of the islanded system are kept constant. As solar power increases, the BES current shifts from draining to charging mode, and the remaining power is consumed by the BES.
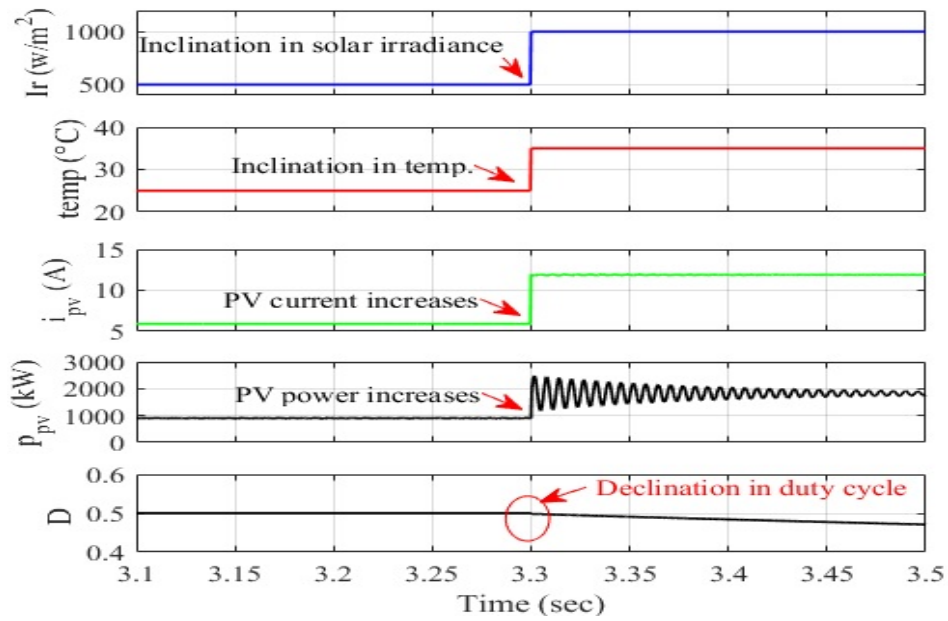
(a)
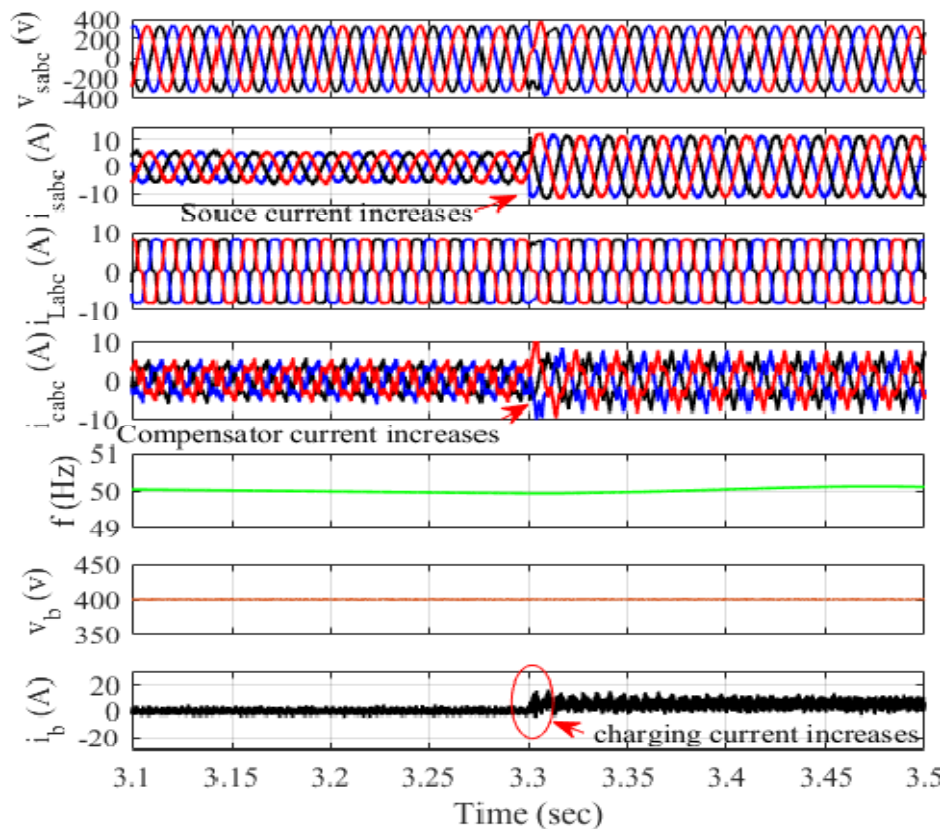
(b)

Fig. 4.35(a) and (b) Dynamic behavior of solarPV-wind System under the change in solar irradiance

4.6.2.4 Dynamic Behavior of SolarPV-Wind System under Unbalanced Load

Fig. 4.36 depicts the dynamic behavior of an SPV-wind-BES-based islanded electrical supply system with a constant wind speed/solar irradiance under load perturbation. The load of phase 'a' is eliminated at t=3.2sec to t=3.4sec. When the load is removed, the BES charging current increases and extra power is given to the BES. The load current is decreased due to disconnection of load at t=3.2sec to t=3.4sec. A 3Ø-APF-PLL-based controller regulates the islanded electrical supply system frequency and stabilizes the voltage profile, current profile, and DC-link voltage or BES voltage during the fluctuations in load. The source current stays sinusoidal and balanced even under dynamic load situations.
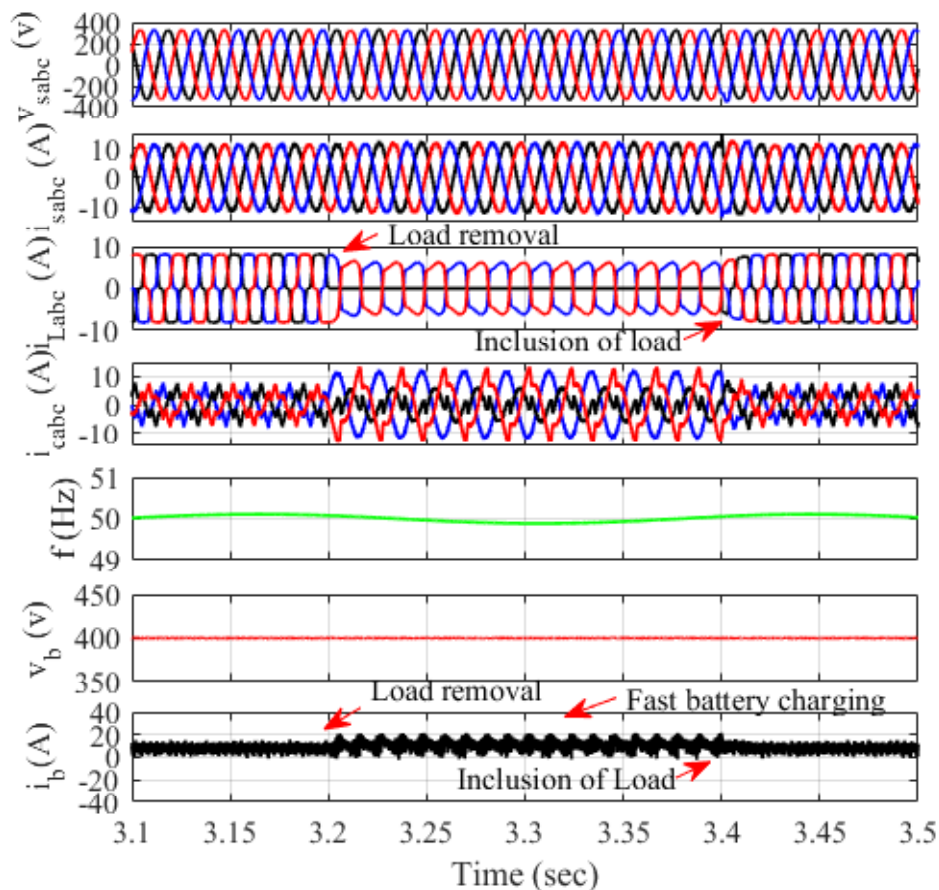
Fig. 4.36 Dynamic behavior of solarPV-wind system under unbalanced load

4.6.2.5 Dynamic Behavior of Solar PV-Wind system under Change in RESs and Load

Fig. 4.37(a) and (b) depict the behavior of the islanded electrical supply system under variations in energy sources feeding an unbalanced load. At t=3.3 sec, the declination in solar irradiance and temperature ranges from $1000w/m^2$ to $500w/m^2$ and 35°C to 25°C. As a result, the PV current, power, and duty cycle are lowered. Fig. 4.37(b) depicts the wind speed declination from 14m/s to 11m/s at t=3.3sec, as well as the imbalanced load (the burden of phase 'a' is abolished from t=3.2sec to t=3.4sec). During the altering condition of RESs and load, a 3Ø-APF-PLL-based controller successfully stabilizes the current & voltage profile of SEIG. Due to the decline in solar irradiance and unbalanced load, the source current of the islanded system is decreased and the load current is also reduced at t=3.2sec to t=3.4sec. The BES current is gradually increasing during load removal which means the remaining power is delivered to the BES for charging. The BES current is reduced during declination in RESs at t=3.3sec i.e. the BES stored power is supplied at PCI to manage the level of power between the RESs and the applied load.
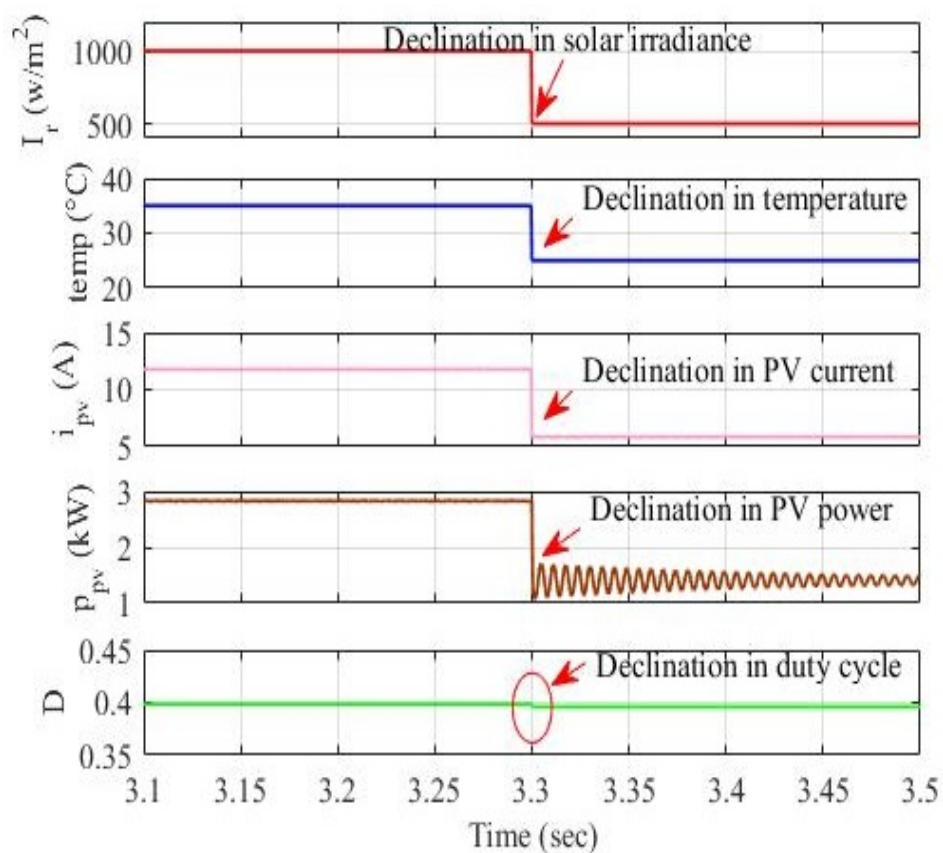
(a)
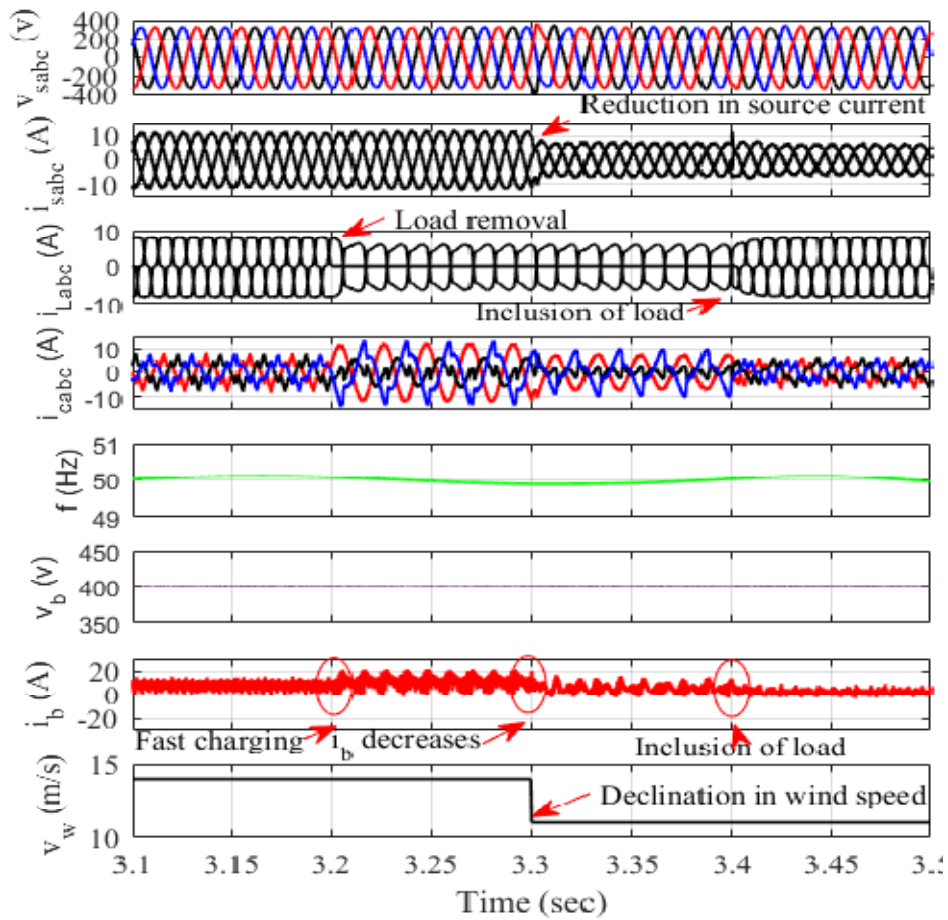
(b)

Fig. 4.37(a) and (b) Dynamic behavior of solarPV-wind system under change in RESs and unbalanced load

4.6.2.6 Harmonics Analysis in Islanded System

Fig. 4.38(a)-(c) shows the harmonics investigation of PCI voltage (v_{gc}), PCI current (i_{gc}) and load current (i_{Lc}) of phase 'c', which are 1.42%, 4.32%, and 25.06%, respectively. When the nonlinear load is applied to the 3Ø-APF-PLL-based islanded electrical supply system, THD of PCI current is less than 5% which satisfies the limit of the IEEE-519 standard.
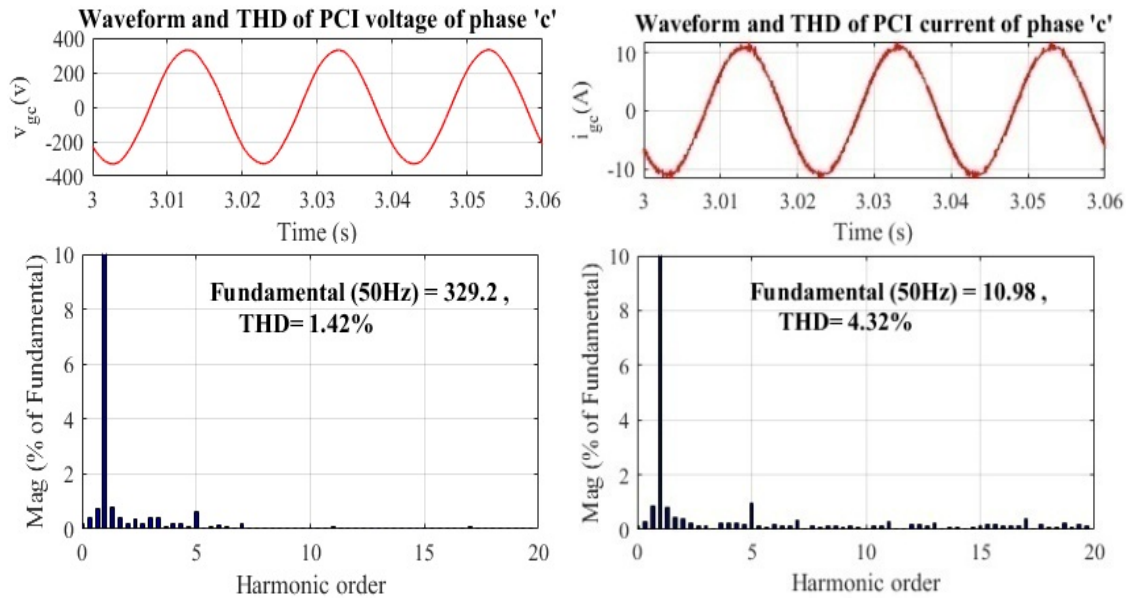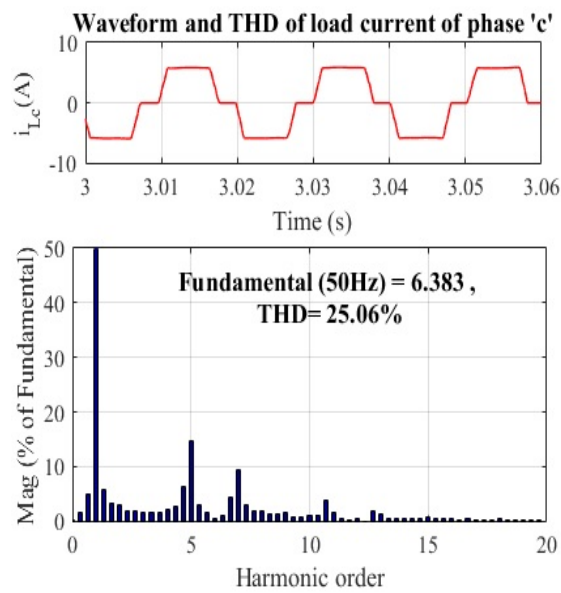
Fig. 4.38(a)-(c) Harmonics analysis in islanded system

4.6.3 Test results

The experimental test results for the wind, solar PV, BES, and nonlinear load-based standalone electrical supply system are analyzed in this section. In this work, the different parameters of the islanded electric supply system with 3Ø-APF-PLL control are examined under numerous operating circumstances.

4.6.3.1 Dynamic Behavior of SPV-Wind-BES Islanded Electrical Supply System

The dynamic behavior of the islanded system is observed using DSO-X 2024A under the unbalanced condition of the load. The observed results are depicted in Fig. 4.39(a)-(f). Fig. 4.39(a) depicts the load current of 3-phases (a, b & c) and DC-link voltage. During the insertion of load phase 'b', the load current of all phases is increased and the DC-link voltage is maintained constant by the proposed controller. Fig. 4.39(b) depicts the DC-link voltage, PCI voltage, PCI current, and load current. Due to the sudden inclination in a load of phase 'a', the PCI current and load current of the islanded system are increased. In Fig. 4.39(c), during an inclination in load, the PCI current and load current are increased. A3Ø-APF-PLL-based controller with VSC maintains the PCI voltage sinusoidal and the DC-link voltage is gradually reduced under inclination in load. Fig. 4.39(d) depicts the load current and PCI current is declined due to the removal of a load of phase 'a'. Fig. 4.39(e) shows a sudden change in load, the DC-link voltage is suddenly increased and the PCI voltage is maintained sinusoidal. Fig. 4.39(f) depicts the parameters of the islanded system; the load of phases 'a' and 'b' is interfaced with the system. Due to the inclination of the two-phase load, the PCI current and load current are increased. During all circumstances, the proposed control has the versatile ability to manage all the parameters of the islanded system. Moreover, the 3Ø-APF-PLL-based control with VSC supplies improved PQ, suppression of harmonics, leveling of load, power compensation, and voltage & frequency stabilization. The BES system stored the unused power and supplies the power through VSC under varying load demands.

(a)   (b)

(c)

(d)

(e)

(f)
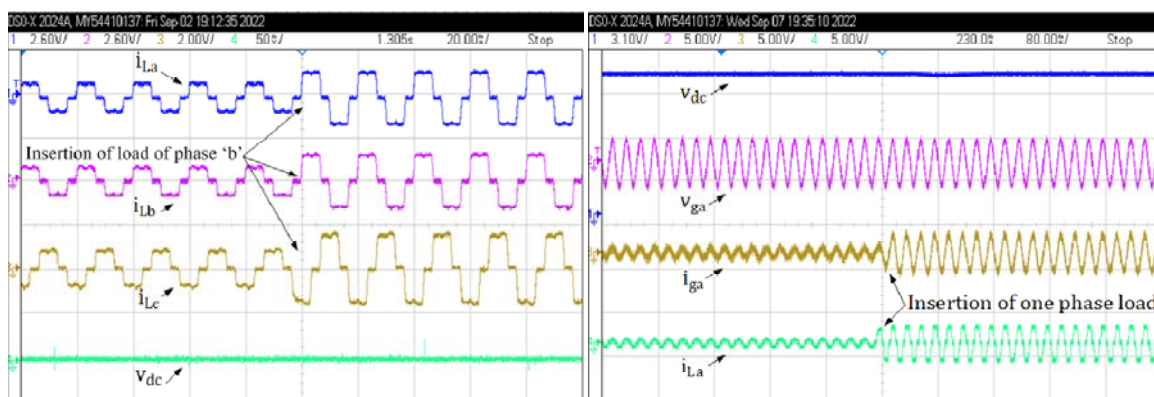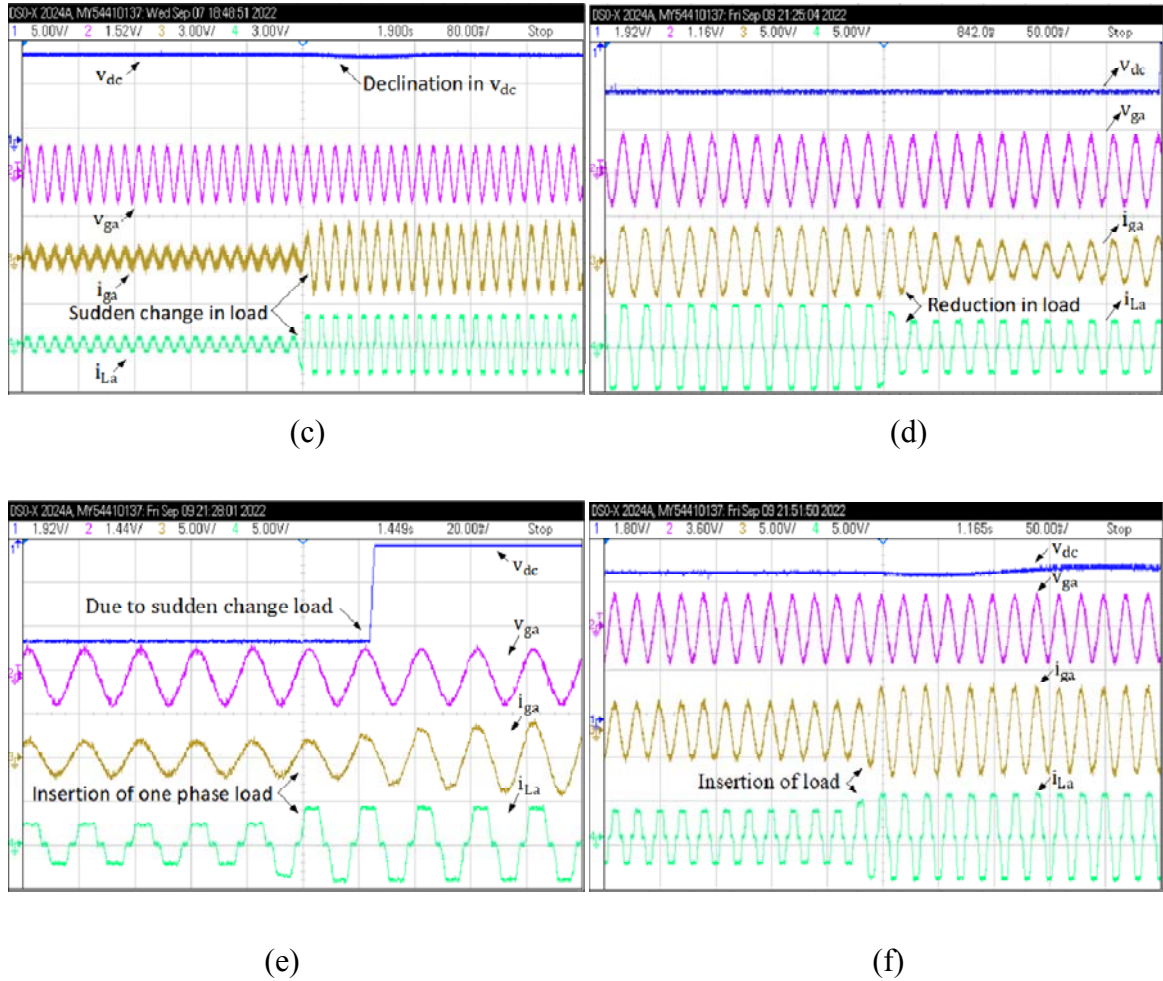
Fig. 4.39(a)-(f) Dynamic behavior of islanded electrical supply system

4.6.3.2 Harmonic spectrum

The harmonic spectrum of islanded system is analyzed using a 3-phase power analyzer. The recorded results show the THD of PCI (voltage & current), and load current are 1.84%, 4.24%, and 25.62% respectively. The THD results are taken under a highly distorted load current. The THD of PCI current is under 5% and fulfills the criteria of the IEEE-519 standard. The 3Ø-APF-PLL-based controller with VSC compensates the harmonics injected by non-sinusoidal load current (25.62%) and maintains the PCI current sinusoidal.
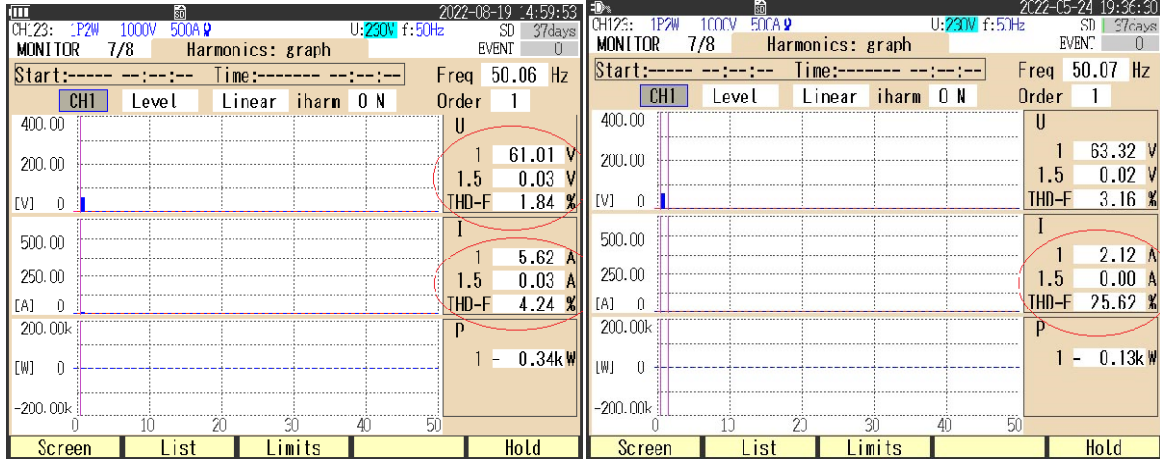
<div align="center">(a)   (b)</div>

<div align="center">Fig. 4.40(a) and (b) Harmonic spectrum</div>

4.7 ICCF-PLL Control Approach

An ICCF-PLL control strategy estimates the magnitude of the preliminary load current component. The proposed controls have effective harmonic filtering capability under varying conditions of RESs and load. The ICCF-PLL contains a pair of complex band-pass (CBP) filters, the Centre frequencies of which are at the fundamental negative and positive order frequencies. These band-pass filters works together to estimate the nonlinear load current's fundamental negative and positive sequence components. The obtained FFPS component is passed into the SRF-PLL, which calculates its peak value, frequency, and phase angle. The calculated frequency is given backward towards the complex filters, which are then adjusted to account for proposed system frequency changes.

4.7.1 Modeling of ICCF-PLL

In the proposed ICCF-PLL, the input signals of the αβ-axis are taken as

$$i_\alpha(s) = i_1^+ \cos(\theta_1^+) \tag{4.48}$$

$$i_\beta(s) = i_1^+ \sin(\theta_1^+) \tag{4.49}$$

Where, (θ_1^+) and (i_1^+) represents the phase angle and is its maximum value of the FFPS component of the nonlinear load current. The evaluated components can be described as

$$i_{\alpha,1}^+ = \hat{\imath}_+^1 \cos(\vec{\theta}_1^+) \tag{4.50}$$

$$i_{\beta,1}^+ = \hat{\imath}_+^1 \sin(\vec{\theta}_1^+) \tag{4.51}$$

Where, $(\hat{\imath}_+^1)$ and $(\vec{\theta}_1^+)$ are ideally equal to (i_1^+) and (θ_1^+), respectively. The phase angle of the obtained FFPS component by the ICCFs can be described using the above assumptions as

$$\hat{\theta}_1^+ = \tan^{-1}\left(\hat{\imath}_{\beta,1}^+ / \hat{\imath}_{\alpha,1}^+\right) \tag{4.52}$$

$$\frac{d\vec{\theta}_1^+}{dt} = \frac{\hat{\imath}_{\alpha,1}^+ \frac{d\hat{\imath}_{\beta,1}^+}{dt} - \hat{\imath}_{\beta,1}^+ \frac{d\hat{\imath}_{\alpha,1}^+}{dt}}{\underbrace{\left(\hat{\imath}_{\alpha,1}^+\right)^2 + \left(\hat{\imath}_{\beta,1}^+\right)^2}_{\left(\hat{\imath}_+^1\right)^2}} \tag{4.53}$$

Where, $\frac{d\hat{\imath}_{\alpha,1}^+}{dt}$ and $\frac{d\hat{\imath}_{\beta,1}^+}{dt}$, according to Fig. 4.41

$$\frac{d\hat{\imath}_{\alpha,1}^+}{dt} = -\hat{\omega}_g \hat{\imath}_{\beta,1}^+ + \omega_p i_\alpha - \omega_p i_{\alpha,1}^+ - \omega_p \hat{\imath}_{\alpha,1}^- \tag{4.54}$$

$$\frac{d\hat{\imath}_{\beta,1}^+}{dt} = -\hat{\omega}_g \hat{\imath}_{\alpha,1}^+ + \omega_p i_\beta - \omega_p i_{\beta,1}^+ - \omega_p \hat{\imath}_{\beta,1}^- \tag{4.55}$$

Substituting (4.54) and (4.55) into (4.53) yields

$$\frac{d\vec{\theta}_1^+}{dt} = \hat{\omega}_g + \frac{\omega_p\left(i_{\alpha,1}^+ i_\beta - i_{\beta,1}^+ i_\alpha\right)}{\left(\hat{\imath}_1^+\right)^2} \tag{4.56}$$

It should be noted that the $\alpha\beta$-axis input signals were assumed to be devoid of any FFNS components. As a result, the obtained FFNS components, $(\hat{\imath}_{\alpha,1}^-)$ and $(\hat{\imath}_{\beta,1}^-)$ are equal to zero in the initial or steady state and have only a minor effect during dynamics.

Substituting (4.48)–(4.51) into (4.56) yields

$$\frac{d\vec{\theta}_1^+}{dt} = \hat{\omega}_g + \frac{\omega_p(\hat{\imath}_{\alpha,1}^+ i_\beta - \hat{\imath}_{\beta,1}^+ i_\alpha)}{\left(\hat{\imath}_+^1\right)^2} \tag{4.57}$$

Assuming that $\theta_1^+ \approx \vec{\theta}_1^+$ and $i_1^+ \approx \hat{\imath}_1^+$ (4.57) can be re-written as

$$\frac{d\vec{\theta}_1^+}{dt} \approx \hat{\omega}_g + \omega_p(\theta_1^+ - \vec{\theta}_1^+) \tag{4.58}$$

The dynamics of the CCF part of the ICCF-PLL are described by Equation (4.58), which is in the form equation of linear differential [23]. The entire model of the ICCF-PLL can be achieved using (4.58) as depicted in Fig. 4.41.
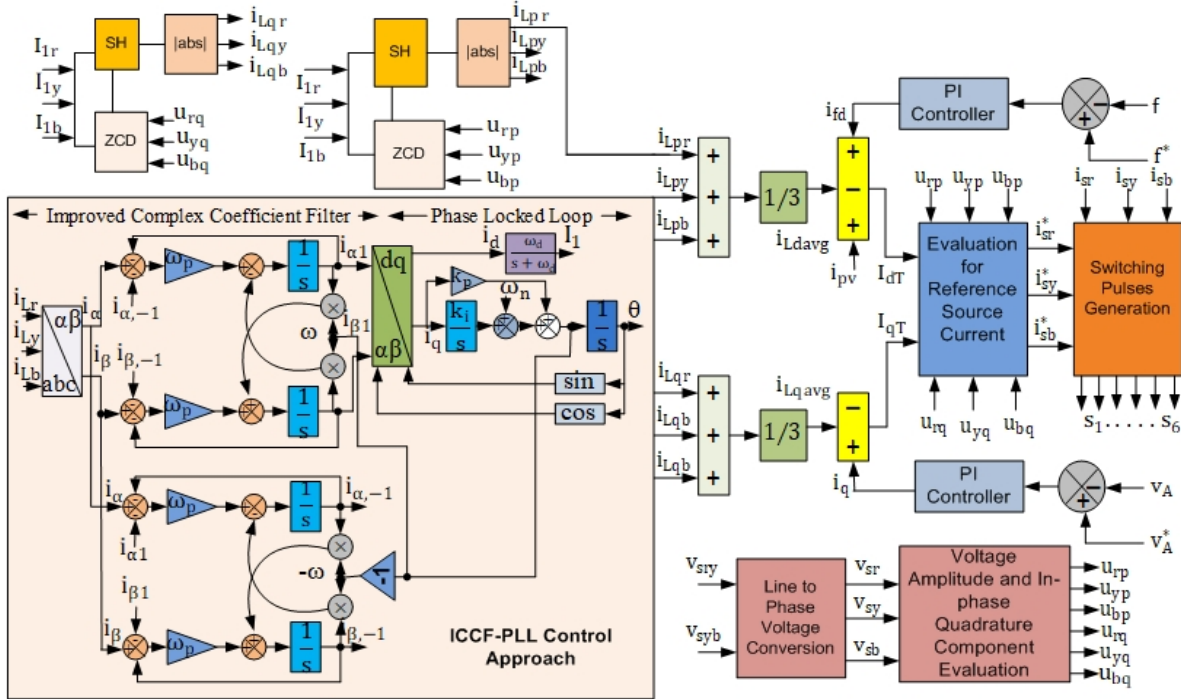
Fig. 4.41 Control scheme of DG system

4.7.2 Simulation Results

The detailed Simulation study and test results of the DG system comprising of WECS, SPV, and BSS generation for ICCF-PLL-based control & standalone applications are carried out using MATLAB and an experimental prototype. The isolated system is designed to compensate for the effects of intermittency conditions in RESs and unbalancing in load. Therefore, the BDC control is utilized to control the charging and discharging of BSS for dynamic power balance. Additionally, intermediate control signals of the used ICCF-PLL control algorithms are also presented for a detailed understanding of the DG system operation.

4.7.2.1 Intermediate Signals of ICCF-PLL Control

Fig. 4.42(a) and (b) show the intermediate control signals of the ICCF-PLL-based algorithm under unbalanced load conditions. The non-linear load is detached at t=2.1s to t=2.3s. Fig. 4.42(a) represents the signals u_{rd} (active unit templates), u_{rq} (quadrature unit

templates), i_q (extracted current from AC PI controller), v_A (voltage amplitude), i_α and i_β (extracted from abc to $\alpha\beta$ transformation). The comparison of a reference voltage and sensed voltage yields an AC PI controller to generate the active current component. During the duration of load removal, the extracted i_α and i_β component are reduced to zero. Fig. 4.42(b) shows the $i_{L\alpha}$, $i_{L\beta}$ (active & reactive load current components), i_{fd} (extracted component from DC PI controller), ω_g (centre frequency), i_{dryb} and i_{qryb} (extracted active and quadrature current components). The comparison of the observed frequency and reference frequency enables the DC PI controller to generate the current component. All the intermediate signals are generated by sensing nonlinear load current (i_{Lryb}). Further, the intermediate signals are employed to control the standalone DG system.
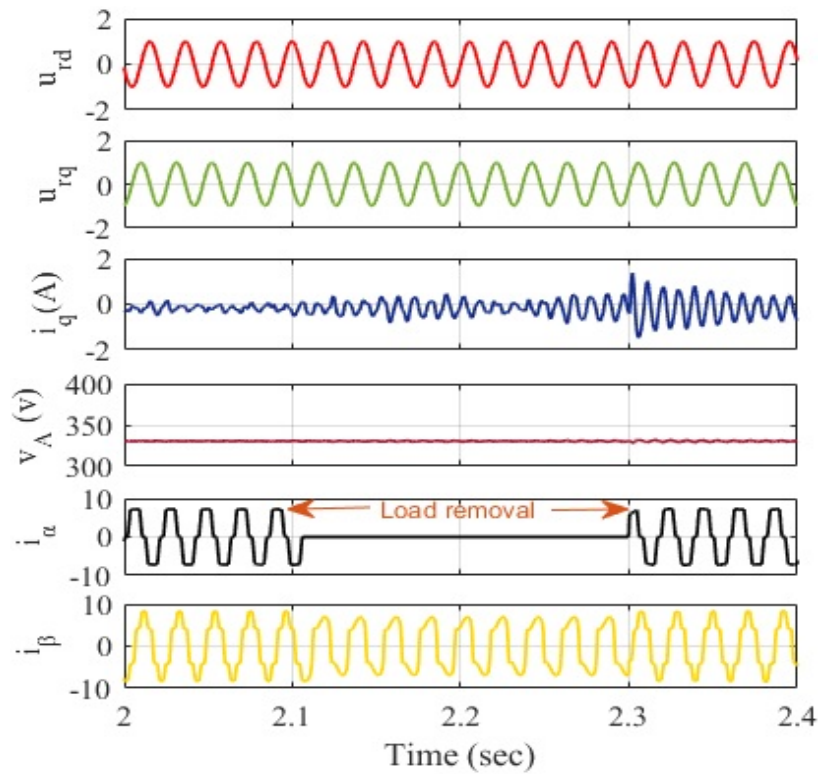
(a)
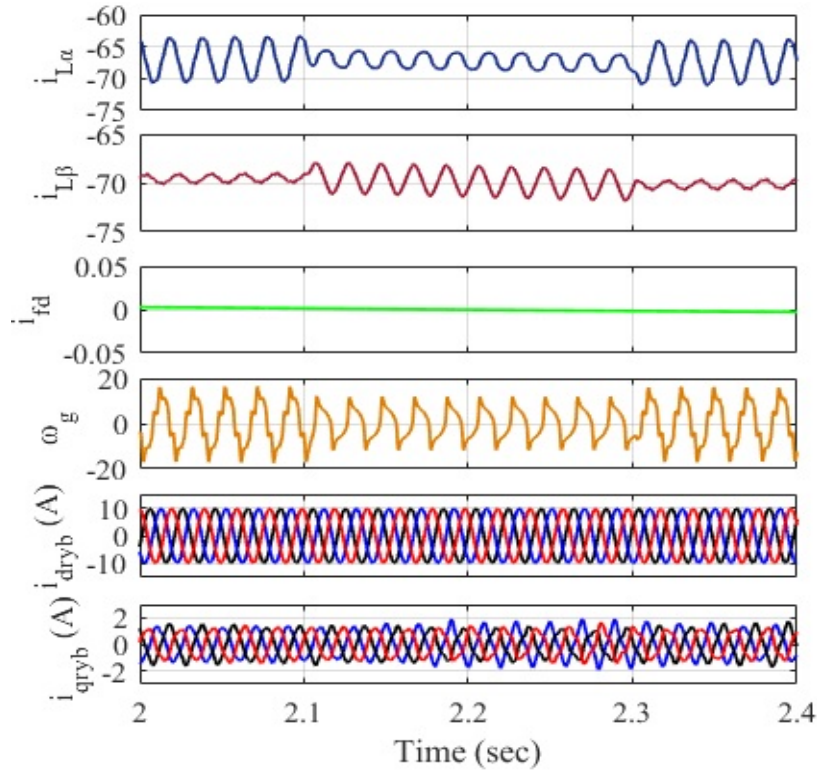
(b)

Fig. 4.42(a) and (b) Intermediate signals of ICCF-PLL control algorithm

4.7.2.2 Dynamic Response of DG System at Differing Wind Speed

Fig. 4.43 represents the dynamic performance of the DG system under changing wind speeds and fixed solar insolation feeding the nonlinear load. The wind speed differed from 12m/s to 9m/s at t=2.2s. An ICCF-PLL-based controller stabilizes the voltage and DG system frequency at the time of the variation in wind speed. The parameters of a standalone system such as frequency and DC-link voltage are almost constant. The compensator current is marginally rising after the removal of load at t=2.2s. The BDC controller manages the process of charging and draining the BSS and controls the DC-link voltage. During the reduction in wind speed, the BSS is shifted to discharging mode and supplies the current at PCI through VSC to manage the frequency stabilization. Further, an ICCF-PLL control with VSC provides abatement of harmonics, power support and improves the overall PQ of the standalone DG system.
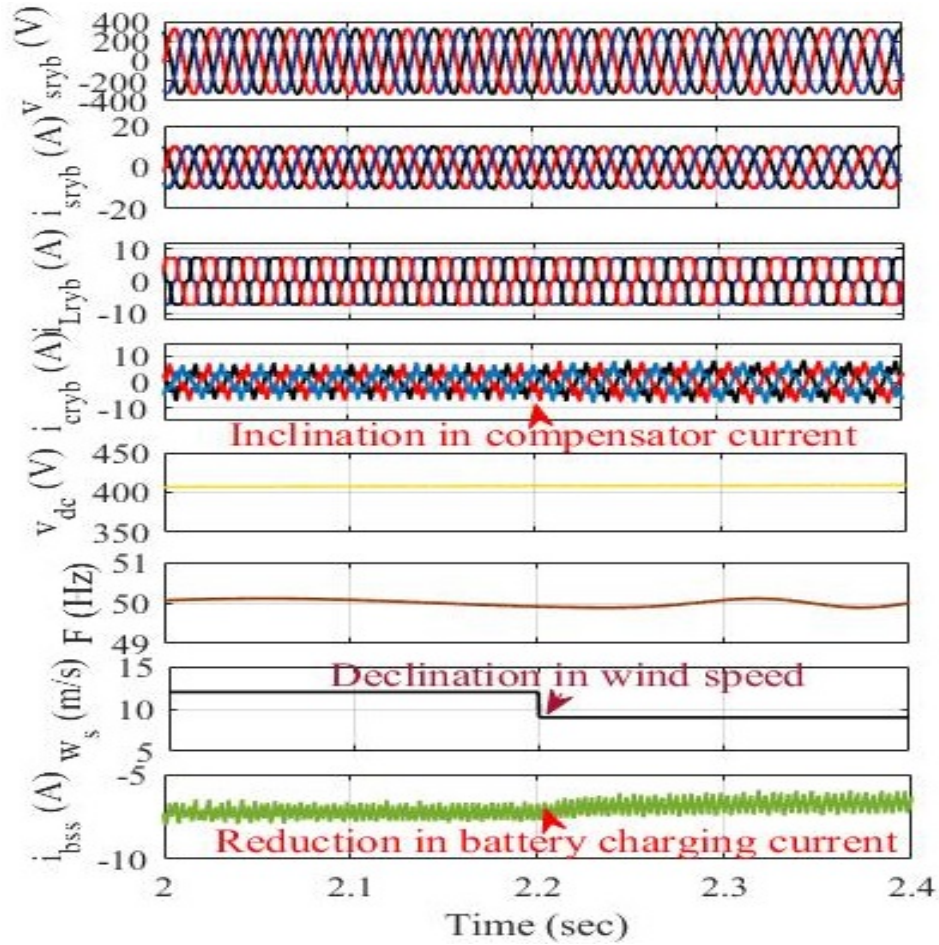
Fig. 4.43 Response at differing wind speed

4.7.2.3 Dynamic Response of DG System under Differing Solar Insolation

Fig 4.44(a) and (b) represent the dynamic performance of isolated microgrid systems at differing solar insolation and fixed wind speed feeding the constant nonlinear load. In this, the solar insolation is shifted from $900w/m^2$ to $500w/m^2$ at t=2.2s and wind speed is fixed at 12m/s with constant load. Fig. 4.44(a) shows due to the reduction in solar insolation, the PV current is reduced from 10.52A to 5.86A, the PV power or solar power is declined from 2.5kW to 1.4kW and the duty cycle is also reduced. Hence, the total power of the isolated system is reduced to 3.48kW from 5.83kW. Fig 4.44(b) shows due to the sudden change in solar insolation at t=2.2s, a small deflection in source voltage of 0.022s is observed after that the proposed controller efficiently controls the source voltage. The source current and the compensator current are reduced according to a change in solar insolation at t=2.2s. An ICCF-PLL-based controller maintains the system frequency

constant during an abrupt change in solar insolation. Therefore, the BDC controller controls the DC-link voltage and shifts the BSS to discharging mode. The stored power in BSS is used to preserve the power balance between the RESs and the nonlinear load. Hence, the controller with the help of VSC contributes voltage and frequency stabilization at PCI, power support, eradication of harmonics, load balancing, and minimizing the PQ problems.
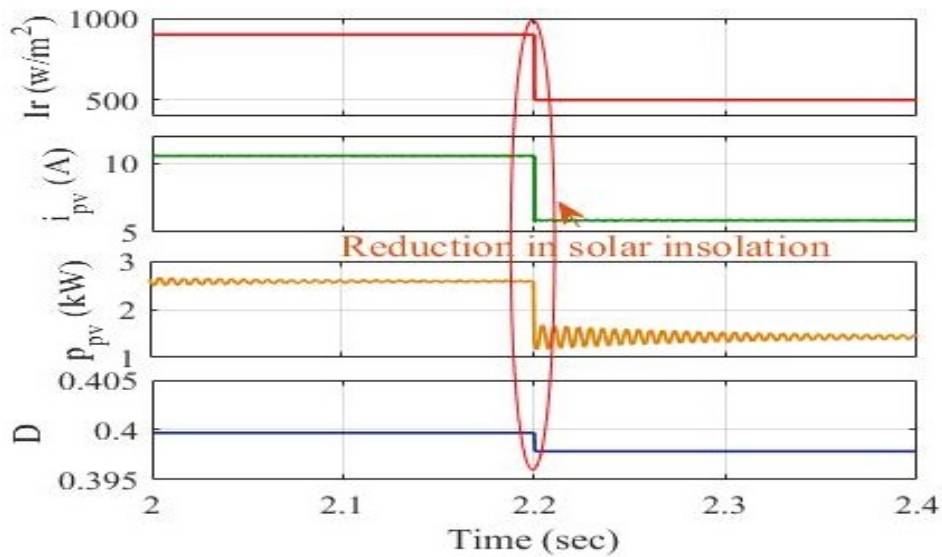
(a)
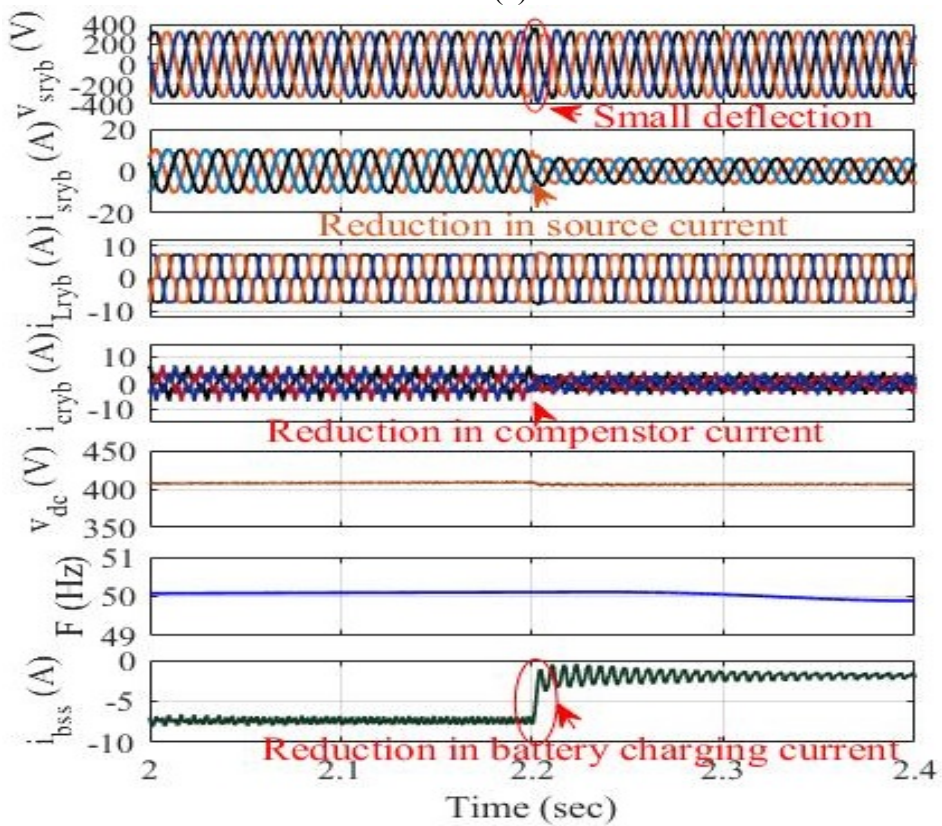
(b)

Fig 4.44(a) and (b) Response at varying solar insolation

4.7.2.4 Dynamic Response of SolarPV-Wind System with ICCF-PLL Control under Unbalanced Load

Fig. 4.45 represents the dynamic response of the standalone DG system under constant wind speed/solar insolation feeding the unbalanced distorted load. A load of phase 'r' is eliminated at t=2.2s to t=2.4s. During the sudden change in load, the load current of the isolated system is reduced and the compensator current is increased. The total generated power of the isolated system is increased to 6.13kW from 5.83kW due to the sudden fall of load. During the sudden variation in load at t=2.2s to t=2.4s, an ICCF-PLL-based controller successfully maintains the DG system frequency and stabilizes the voltage & current profile at PCI. The BSS charging current is suddenly increased during the disconnection of the load of phase 'r' at t=2.2s and during the insertion of load at t=2.4s, the BSS charging current is reduced. Moreover, the BDC controller effectively coordinates the DC-link voltage and manages the charging/discharging modes of BSS. The extra is supplied to BSS during the load rejection process and the stored power of BSS is utilized during the intermittent condition of RESs and load.
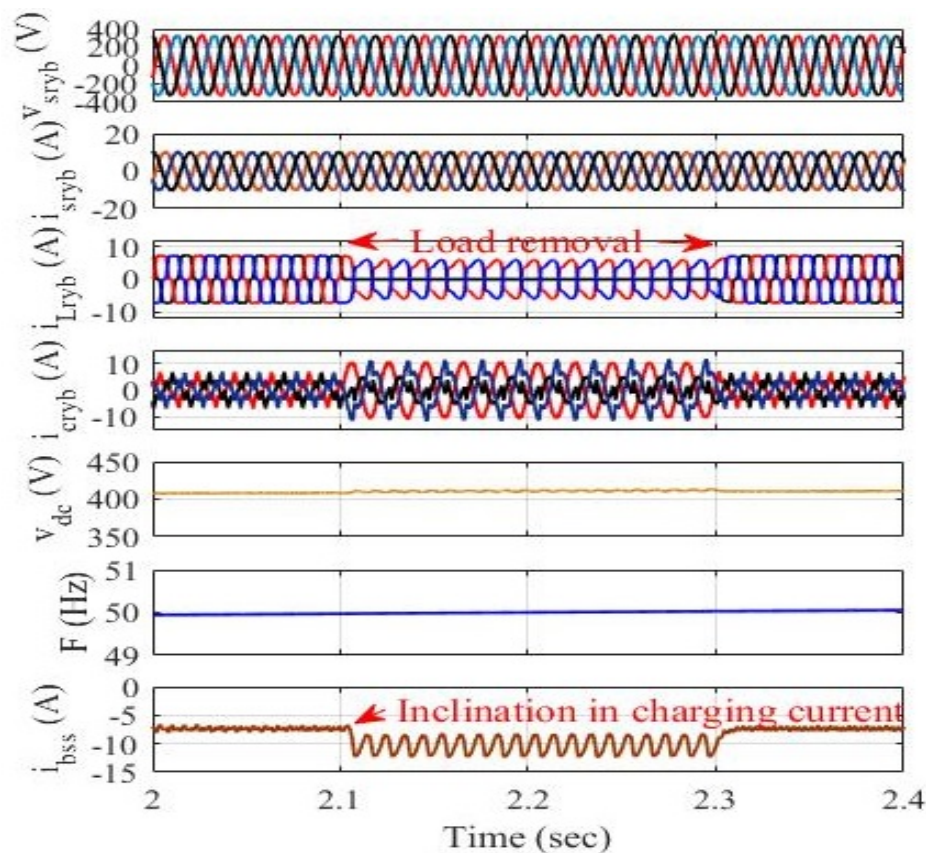
Fig. 4.45 Dynamic Response of SolarPV-Wind System with ICCF-PLL Control under Unbalanced Load

4.7.2.5 Harmonic Spectrum

Fig. 4.46(a)–(c) represents harmonics spectra and waveform of phase 'r' of the standalone DG system. An ICCF-PLL control-based DG system is used for standalone applications. The THD of the PCI (voltage & current), and load current are found 1.29%, 4.6%, and 25.07% respectively. At steady-state, the PCI currents are sinusoidal with minimum harmonic distortion. The harmonic spectrum of the PCI (voltage & current), and load current of phase 'r' in polluted load condition with a THD of 25.07% is shown in Fig. 4.46(a)-(c), Also, the THDs of the PCI currents are well suited within the required range of 5% due to VSC control.

(a)   (b)

(c)
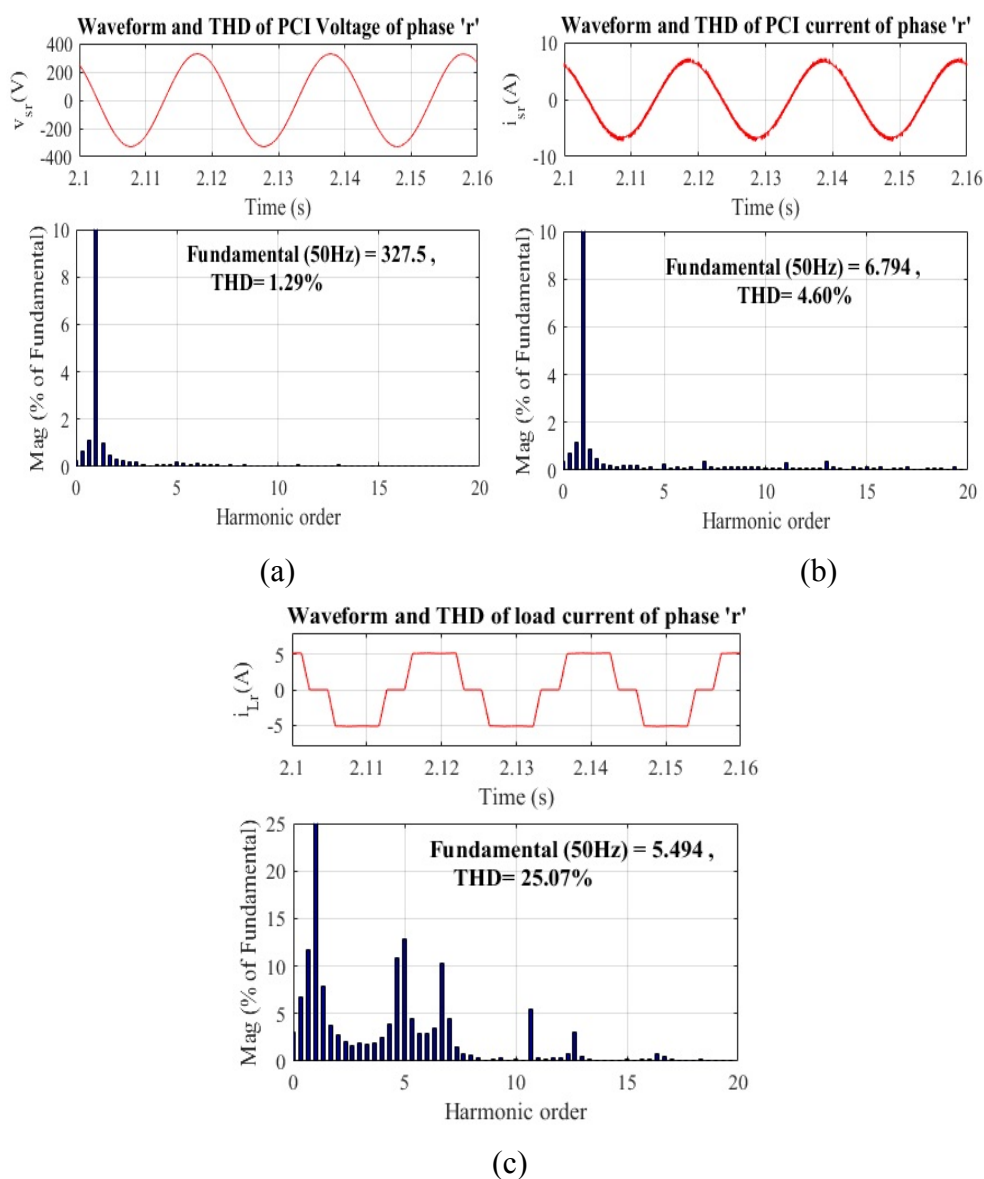
Fig. 4.46(a)-(c) Harmonic spectrum

4.7.3 Experimental Test Results

The experimental test results for standalone applications of DG system are analyzed in this section. The isolated system is designed to compensate for the effects of intermittency conditions in RESs and unbalancing in load. Therefore, the BDC control is utilized to control the charging & draining of BSS for dynamic power balance. A VSC, interface and filtering inductors, an optocoupler, connecting cables, and nonlinear loads are included in the proposed hardware setup. The LEM LA-25-based sensors are used to detect PCI current and load side current in standalone DG system phases 'r' and 'y.' The sensor output is forwarded to the DSP-dSPACE 1104's ADC channel through the use of appropriate buffer circuitry.

4.7.3.1 Intermediate Signals of Proposed ICCF-PLL Control Approach

Fig. 4.47(a)-(d) reveals the intermediate signals of the ICCF-PLL control approach during load dynamics. Fig. 4.47(a) and (b) reveal load current (i_{Lr}), in-phase unit templates (u_{rd}), quadrature unit templates (u_{rq}) and reference current (i_{sr}^*) of phase 'r' after introducing load dynamics. The load current and reference current reach zero during the load removal and the unit templates are maintained sinusoidal by the proposed control during the load dynamics. Fig. 4.47(c) and (d) represent the load current (i_{Lr}), extracted component (i_α and i_β) and voltage amplitude (v_A). The extracted component (i_β) is 90° phase from (i_α). The load current and extracted components are increased or decreased during the dynamic condition of the load and the voltage amplitude is maintained constant during load dynamics by the proposed control approach. The proposed ICCF-PLL control algorithm helps to maintain all internal parameters and regulates the system frequency and voltage of the proposed isolated DG system under all operating conditions.

(a)

(b)

(c)

(d)
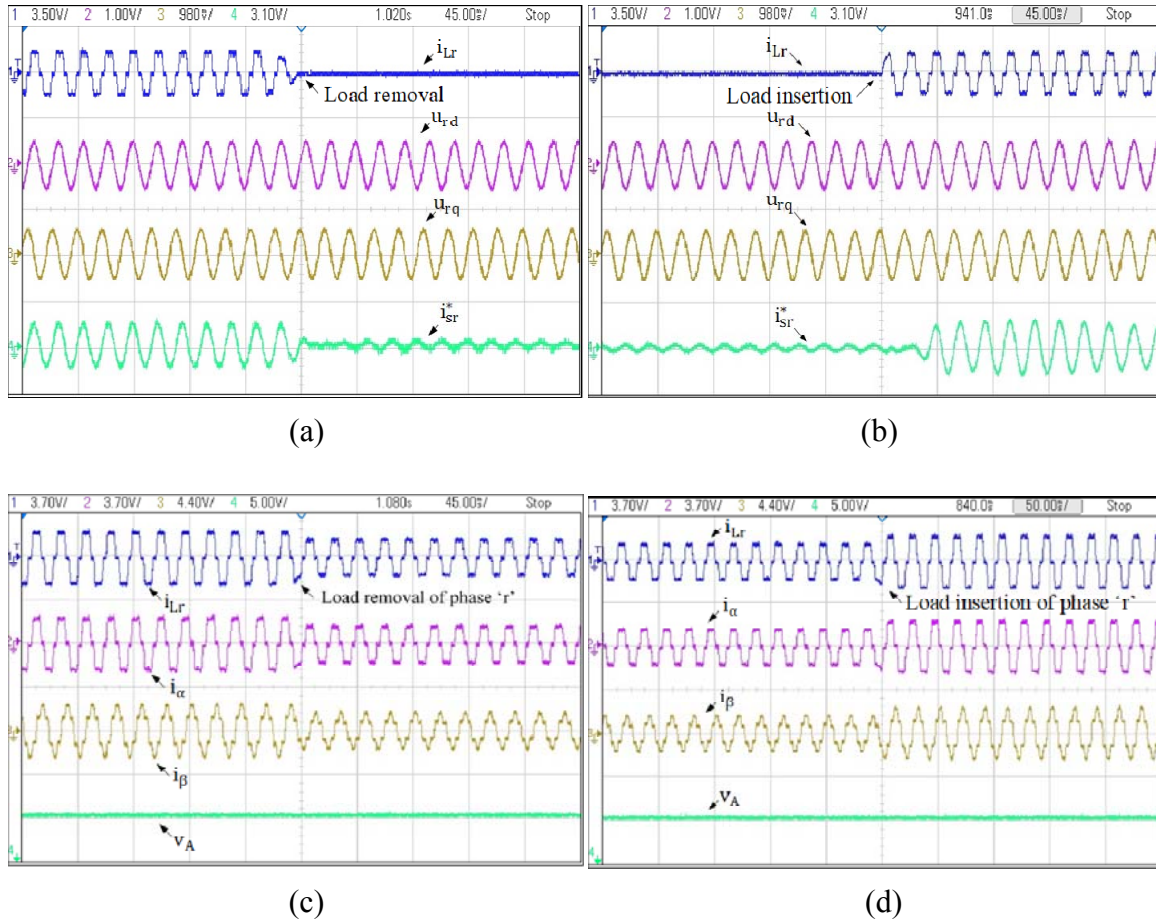
Fig. 4.47(a)-(d) Intermediate signals of (a) & (b) i_{Lr}, u_{rd}, u_{rq} and i_{sr}^*, and (c) & (d) i_{Lr}, i_α, i_β and v_A

4.7.3.2 Dynamic Performance of Isolated DG System

The dynamic response of the proposed DG system during dynamic load conditions is depicted in Fig. 4.48(a)-(f). During load removal, the load current of phase 'r' and the CPI current of all phases are depicted in Fig. 4.48(a). The load current and source current is decreased during loading reduction. On the other hand in Fig. 4.48(b), the load current and source current of all phases is increased during the process of load insertion. The observed test results reveal that the generated current is balanced and sinusoidal even when the load is nonlinear and dynamic. The parameters of the experimental prototype are taken as line voltage (V_{LL}) = 110V, Freq. (f) = 50Hz, and DC-link voltage = 200V. During the declination in load, the load current of phase 'r' is reduced to 4.2A from 5.3A, and after load insertion, the load current is increased from 4.2A to 5.3A, and the PCI current of all the phases is also reduced to 4.2A from 5.3A during load declination and increased from

4.2A to 5.3A after load insertion as shown in Fig. 4.48(a) & (b). Fig. 4.48(c) & (d) show the response of the PCI voltage of phase 'r' and the CPI current of all the phases under the transient condition of the load. During the load removal and insertion, the control algorithm stabilizes both CPI voltage & current. Fig. 4.48(e) & (f) represent the DC-link voltage is settled at 200V, the PCI current is changed from 5.2A to 3.2A during the disconnection of load of two phases and the CPI current is increased from 3.2A to 5.2A during the insertion of load. The CPI current and load current are changed with the variation in load. The extra power is supplied to the battery under reduced load demand. The recorded result shows that the PCI voltage & current are maintained sinusoidal by the proposed ICCF-PLL control during unbalanced load conditions. Moreover, the proposed control with VSC provides harmonics abatement, power support, load balancing, and voltage stabilization with reduced overall PQ problems.
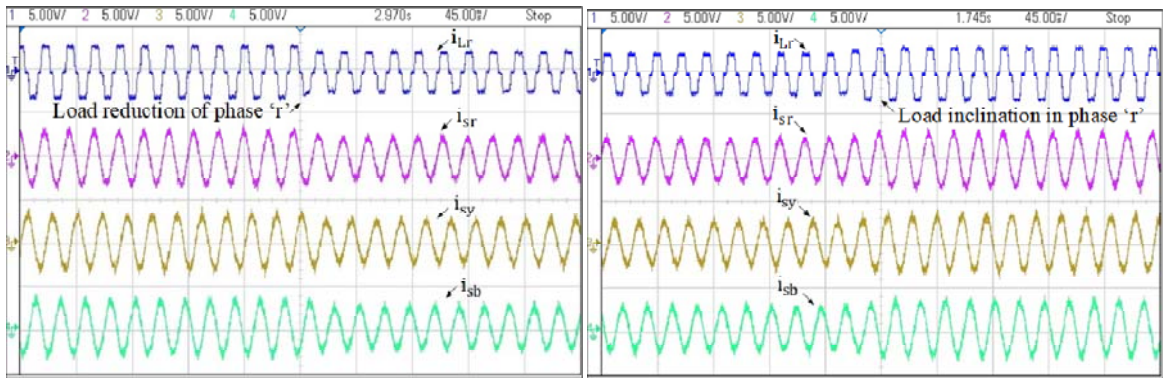
(a)

(b)
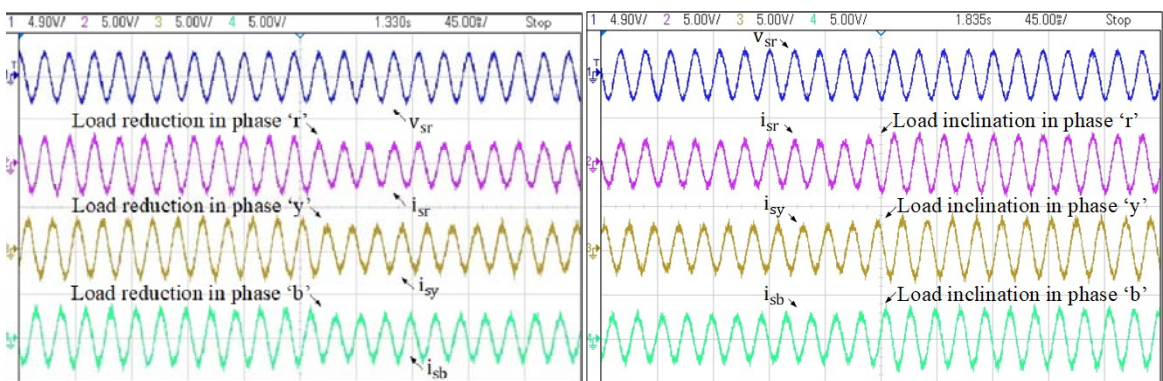
(c)

(d)
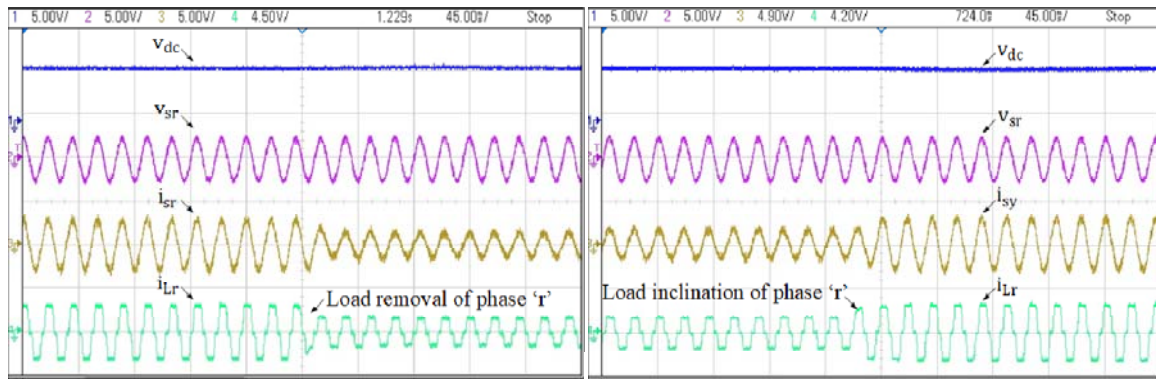
(e)   (f)

Fig. 4.48(a)-(f) Dynamic response at unbalanced load (a)-(b) i_{Lr}, i_{sr}, i_{sy} and i_{sb}, (c)-(d) v_{sr}, i_{sr}, i_{sy} and i_{sb}, (e)-(f) v_{dc}, v_{sr}, i_{sr} and i_{Lr}

4.7.3.3 Harmonic Spectra of DG System

The harmonics spectrum with waveforms of the proposed standalone DG system is analyzed in detail. The test results validate that THD of the PCI current (i_{sr}), is 4.17%, and is within the standard limit of the IEEE 519 when connected to a nonlinear load with a current of 27.35% THD. The required power support is provided by the battery system through VSC during dynamic conditions of load and wind speed. The proposed control with VSC maintains the power equilibrium and synchronization between the load and RESs.
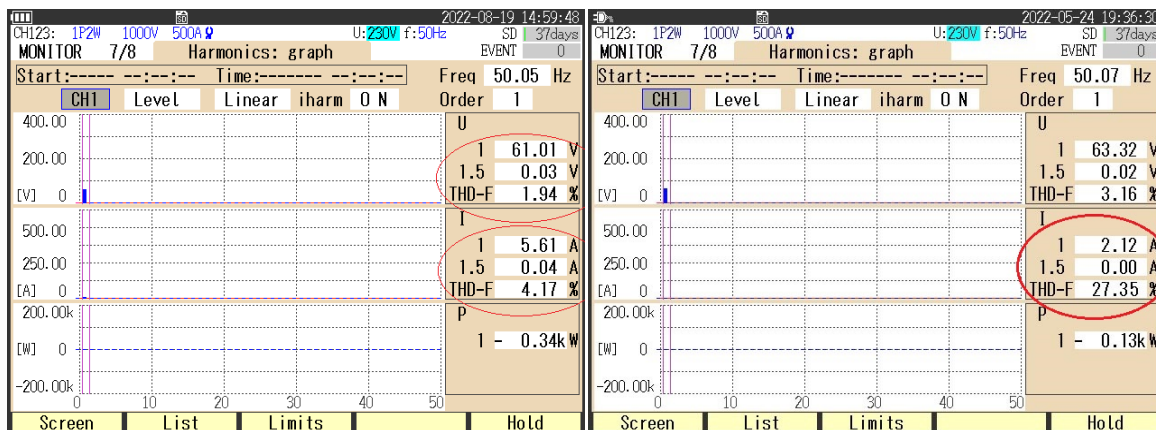
(a)   (b)

Fig. 4.49(a) and (b) Harmonic Spectra of DG System (a) PCI current (i_{sr}) and (b) load current (i_{Lr})

4.8   Summary

In this chapter, unit template estimation, DSC-FLL, SOSF-FLL, VGC-IPL, 3Ø-APF-PLL and ICCF-PLL-based control algorithms have been designed and applied for the 3P3W wind-solar-BSS-based islanded hybrid system. The performance of all the above-said algorithms is carried out in MATLAB/Simulink. SOSF-FLL and VGC-IPL perform consistently in 3P3W hybrid system for standalone applications under the intermittent condition of wind/solar and load perturbation. The experimental performance of SOSF-FLL and VGC-IPL has also been added in this section for the islanded system. The performance approves the VGC-IPLL control algorithms with VSC and provides power compensation, harmonics abatement, load leveling and voltage & frequency stabilization of the islanded system. The PQ has been improved under intermittency circumstances of wind & solar and nonlinear load. Further, the MPPT techniques (P&O and IC) give their better performance during the intermittent condition of solar power. The BSS successfully consumes the extra power during light demand and supplies the power during high load demand and provides active/reactive power compensation through VSC.

Chapter 5

Control Techniques for Three-Phase Four-Wire (3P4W) Islanded Wind-Solar-BES-based Hybrid System

5.1 General

Three phase four wire (3P4W) electric power distribution networks are widely used in low power distribution system. VSC based compensation are used to improve PQ in 3P4W system. A precise estimation of phase and frequency is mandatory for the control and synchronization of the islanded hybrid system. Out of several synchronization techniques discussed in literature PLLs and FLLs are popular. Some conventional and advanced control techniques for three-phase PLLs & FLLs are employed in this chapter for the computation of phase, frequency, amplitude and the synchronizing signals under uncertain conditions of RESs and unbalanced load. The designed PLLs & FLLs are further applied for the PQ improvement and compensation of reactive power in a 3P4W islanded hybrid system.

Various three-phase control techniques are implemented in this section to analyze the performance of the islanded hybrid system under different operating circumstances. These include DSOGI-PLL, DROGI-FLL, DTOGI-PLL, and ADF-FLL. Their individual control technique performance is examined under operating scenarios.

5.2 DROGI-FLL based Control Approach of 3P4W Wind-Solar-BES Hybrid System

A DROGI-FLL control algorithm is designed to evaluate the components such as phase angle, frequency and fundamental load current. A ROGI-based signal decomposition technique employs two parallel ROGIs centred at the fundamental positive frequency and a μ-order disturbance frequency, as well as a FLL for changing their centre frequencies to frequency variations. By employing the DROGI-FLL control algorithm with parallel ROGIs and a FLL, the input signal can be accurately decomposed into its

fundamental and interference components. This allows for precise evaluation of parameters such as phase angle, frequency, and fundamental load current, enabling effective control and regulation of the system.
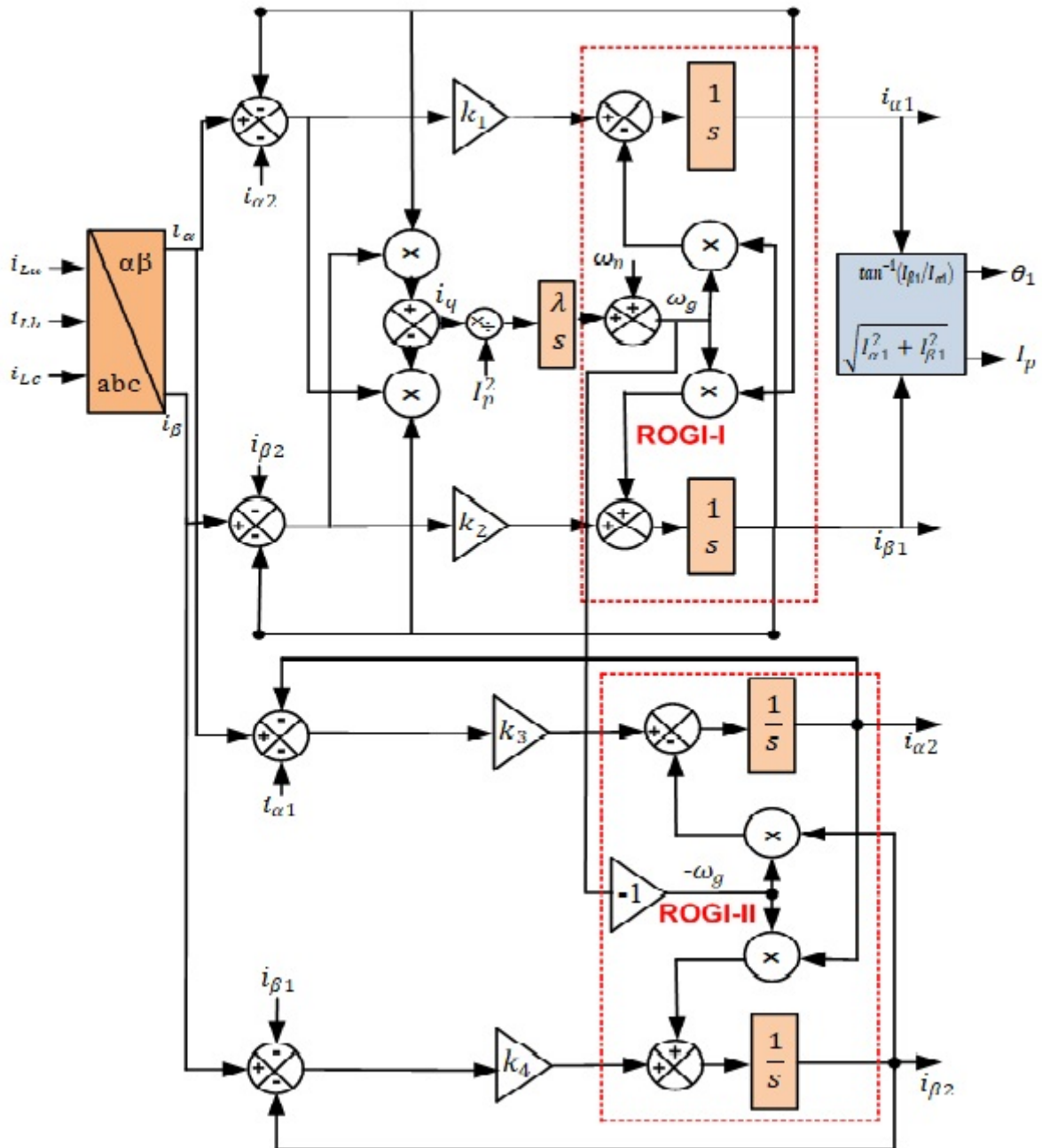
Fig. 5.1 DROGI-FLL based control approach for 3P4W Solar-Wind Hybrid System

The ROGI is transfer function is given by

$$G_{ROGI}(s) = \frac{1}{s - j\omega_g}$$

(5.1)

Where, ω_g denotes the centre frequency of the ROGIs. Fig. 5.1 shows the block diagram DROGI-FLL control algorithm. Where k_1, k_2, k_3, k_4 and λ are the gain parameters $i_{\alpha 1}$ and $i_{\beta 1}$ ($i_{\alpha 2}$ and $i_{\beta 2}$) are evaluations of the FFPS (μ-order frequency) component of the load current in the $\alpha\beta$ frame. θ_1 and I_p are the evaluated of the phase angle and the maximum value of the FFNS (μ-order frequency) component of the load current. ω_g is an evaluation of the fundamental angular frequency of the load current. $\mu = -1$ represents extracting the fundamental negative sequence component of the DROGI-FLL control algorithm [108].

5.2.1 Simulation Results

The simulation results represent the dynamic response of the 3P4W wind-solar hybrid system for isolated locations. The behavior of the proposed standalone hybrid system is studied and analyzed under fixed/varying wind speed/solar intensity/linear/nonlinear load. To analyze the dynamic response of the hybrid system, simulation results accommodate significant signals. The internal signals of the DROGI-FLL control algorithms that have been implemented are also deeply analyzed.

5.2.1.1 Internal Signals of DROGI-FLL Algorithm

Fig. 5.2(a)-(c) shows the all internal control signals of the 3P4W standalone wind-solar hybrid system. The control signals of the standalone hybrid system are designed under the phase 'a' of linear/nonlinear load disconnected at t=2.7 sec. Fig. 5.2(a) Shows the control signals of DROGI-FLL control algorithm $i_{a1}, i_{b1}, \omega_g, i_{a2}, i_{b2}, i_p, V_t$ and u_{pa}. Where, $i_{a1}, i_{a2}, i_{b1}, i_{b2}, \omega_g, i_p, V_t$ and u_{pa} are the fundamental estimated in-phase current of ROGI-I & ROGI-II, fundamental estimated quadrature current of ROGI-I & ROGI-II, centre frequency, maximum value of the extracted component of load current, the amplitude of generator voltage and in-phase unit vector of phase 'a'. Fig. 5.2(b) Shows the internal control signals are such as $u_{qa}, i_{sh1}, i_{sh2}, i_q, i_{Lfa}, i_{Lfq}, i_{pv}$ and i_{pa}. Where, the signals are the estimated quadrature unit vector, sample and hold circuit current, AC PI controller current, extracted active/quadrature load current component, solar PV current, and DC PI controller current. Fig. 5.2(c) represents the internal control signal of the control algorithm are $i_{Ld}, i_{Lq}, i^*_{Ld}, i^*_{Lq}$ and i^*_{gabc}. Where, the control signals represent the extracted active component of load current and quadrature current, extracted reference source current. The

control signal gives a rapid dynamic response, fast convergence speed to the DROGI-FLL control algorithm and remove the disturbing harmonic component under the worst load condition. The simulation results represent the dynamic response of 3P4W hybrid system for isolated locations. The behavior of the proposed standalone system is studied and analyzed under fixed/varying wind speed/solar intensity/linear/nonlinear load. To analyze dynamic response of the hybrid system, simulation results accommodate significant signals.
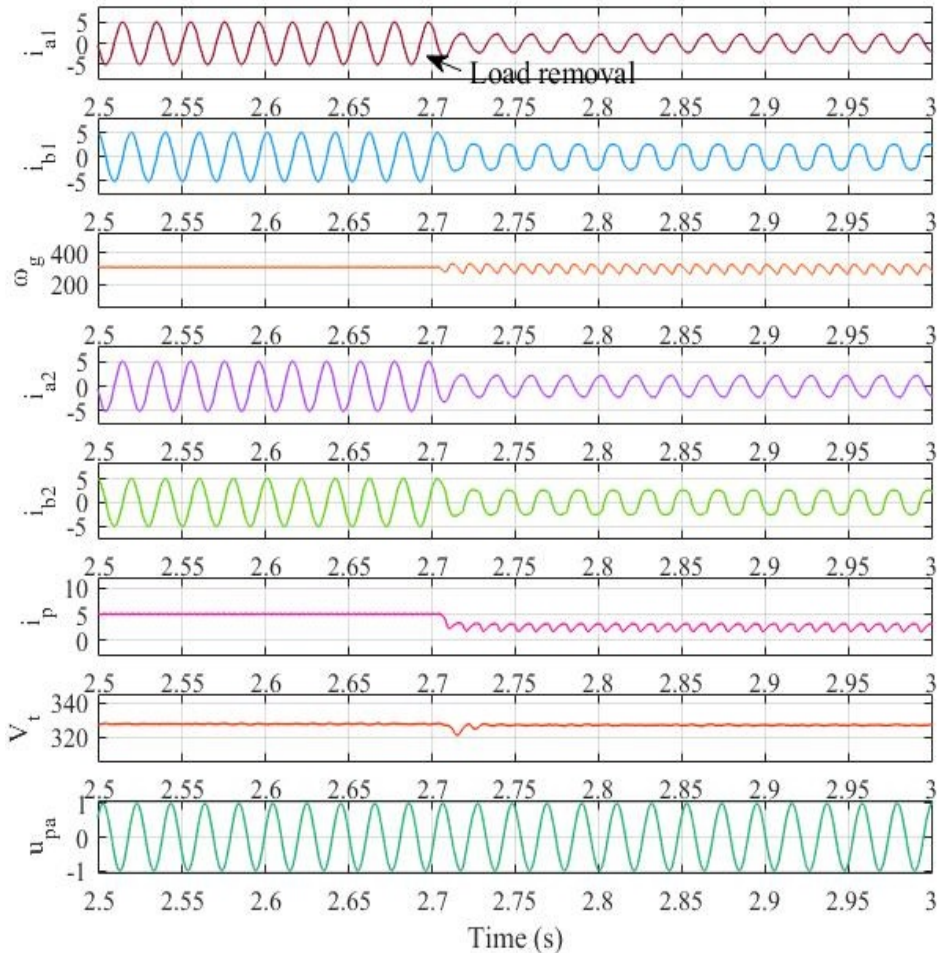
(a)
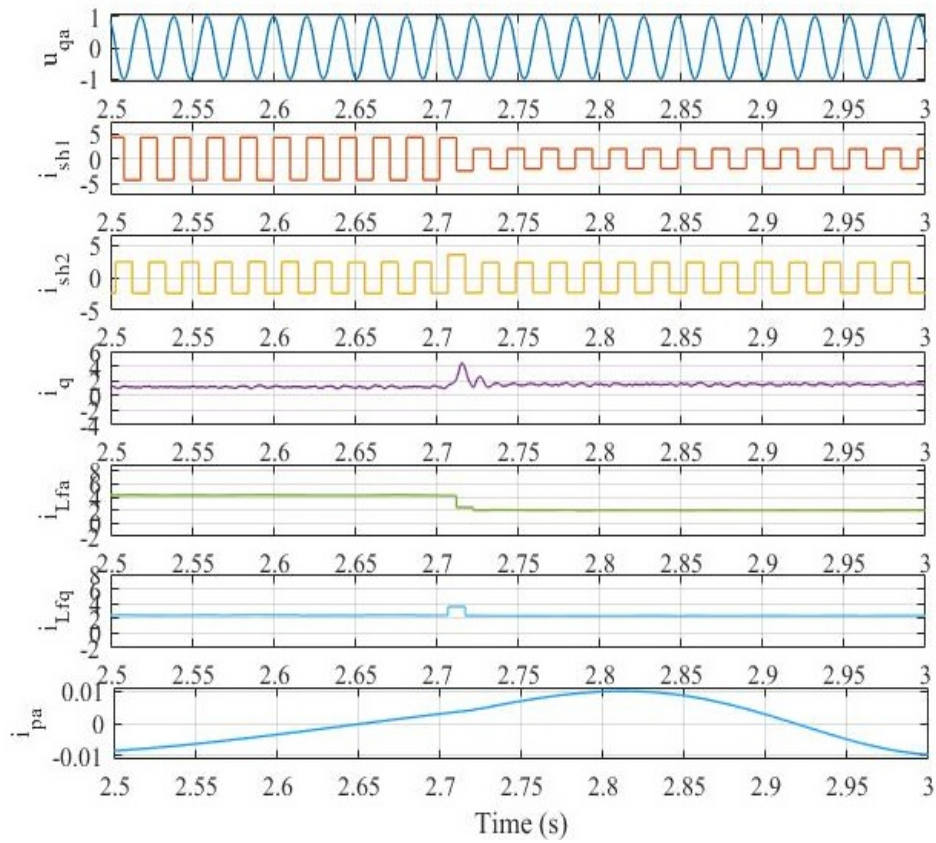
(b)
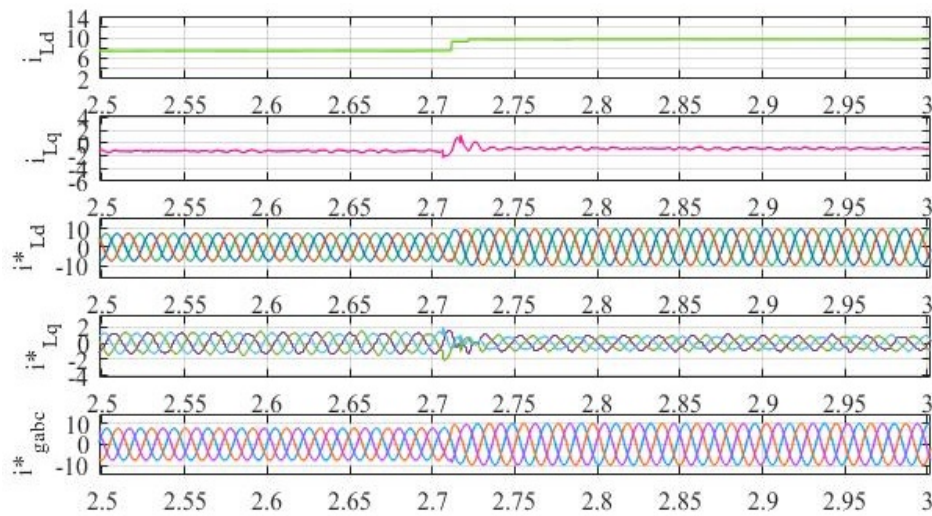
(c)

Fig. 5.2(a)-(c) Internal control signal of DROGI-FLL control algorithm (a) Active/reactive load current component of ROGI-I&II, center freq., amplitude of PCC voltage (b) Active/reactive load current component, DC PI controller current, PV current (c) Extracted active/reactive component, extracted reference source current

5.2.1.2 Dynamic Performance of Hybrid System under Varying Wind Speed/Fixed Solar Intensity Feeding Linear/Nonlinear Load

The performance of a 3P4W standalone hybrid system under varying wind speed and fixed solar intensity feeding linear/nonlinear load is shown in Fig 5.3. The wind speed varies from 18 m/s to 14 m/s at t=2.7 sec and solar intensity and temperature are fixed at 900 w/m² and 25° C. Due to a decline in wind speed, the generated power is reduced then the battery system is to support real power to the system and the compensator current is slightly increasing at t=2.7 sec. As a result, the battery charging current is reduced to meet load requirements while maintaining active power. The excess generated power transfers to the battery for power leveling. The controller maintains the generated voltage, generator current, load current, and system frequency are constant. Fig. 5.3 shows the solar intensity level changes, and so does the output power of the SPV. When the generator power is kept constant while the solar intensity increases, the extra power is fed to the battery, and the battery enters the charging mode. Similarly, as solar intensity decreases, the battery discharges to supply the required load. As a result, the controller maintains the power balance even when the solar intensity changes dynamically.
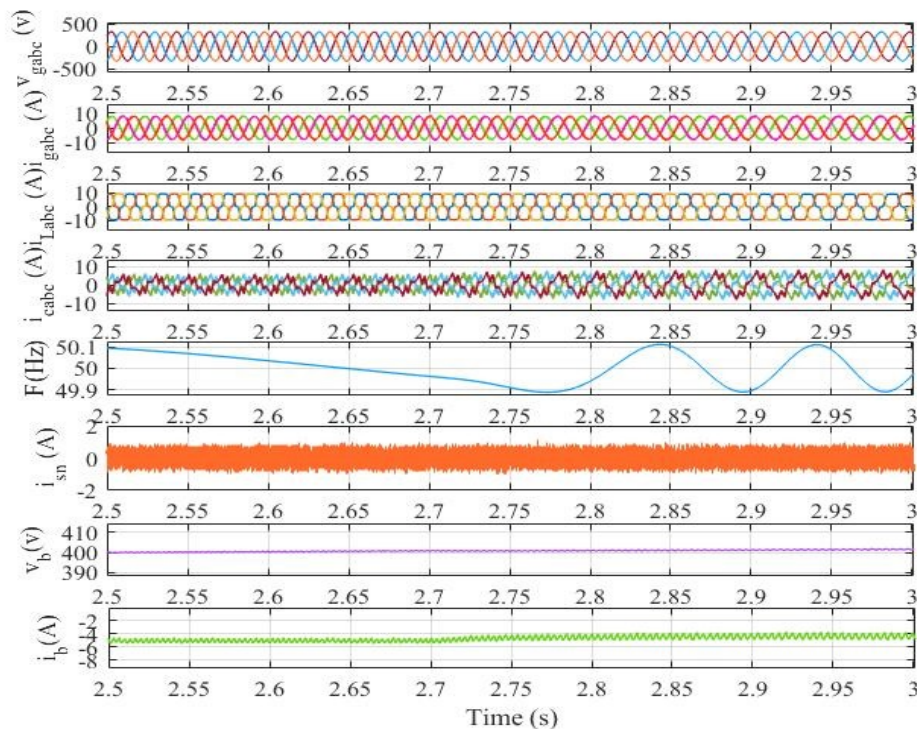
Fig. 5.3 Dynamic performance of a 3P4W standalone system under varying wind speed and fixed solar intensity feeding linear/nonlinear load

5.2.1.3 Dynamic Performance of Hybrid System under Varying Solar Intensity/Fixed Wind Speed Feeding Linear/Nonlinear Load

The dynamic performance of a standalone wind-solar hybrid system under varying solar intensity and fixed wind speed feeding linear/nonlinear load is shown in Fig 5.4(a) and (b). The wind speed is fixed at 18 m/s and the solar intensity and temperature vary from 900 w/m^2 to 600 w/m^2 and 25° C to 20° C. Due to the reduction in solar intensity, the generator current, battery voltage and battery current are slightly reduced and compensator current is slightly increased. The DROGI-FLL based VSC controller maintains the generated voltage, load current and frequency are constant. Fig. 5.4(b) Shows due to change in solar intensity at t=2.7 sec, the PV current, solar PV power, and duty cycle are reduced. If the solar intensity is reduced, the PV current is also reduced as the solar intensity decreases, resulting in a reduction in total generated power. The load, on the other hand, is fixed, so the battery is used to provide the necessary power. As a result, the battery current decreases, and the battery switches from charging to draining mode. When the connected linear/nonlinear load is fixed, the generated solar power drops instantly; as a result, the battery current discharges (changes from charging to draining mode) to maintain the required power balance between source and load.
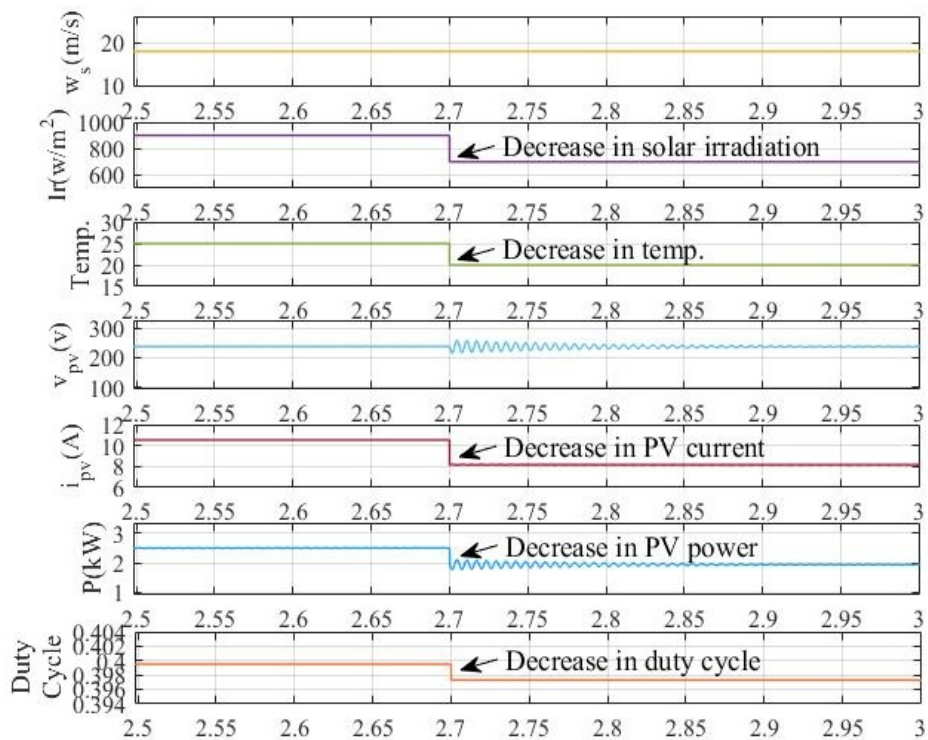
(a)
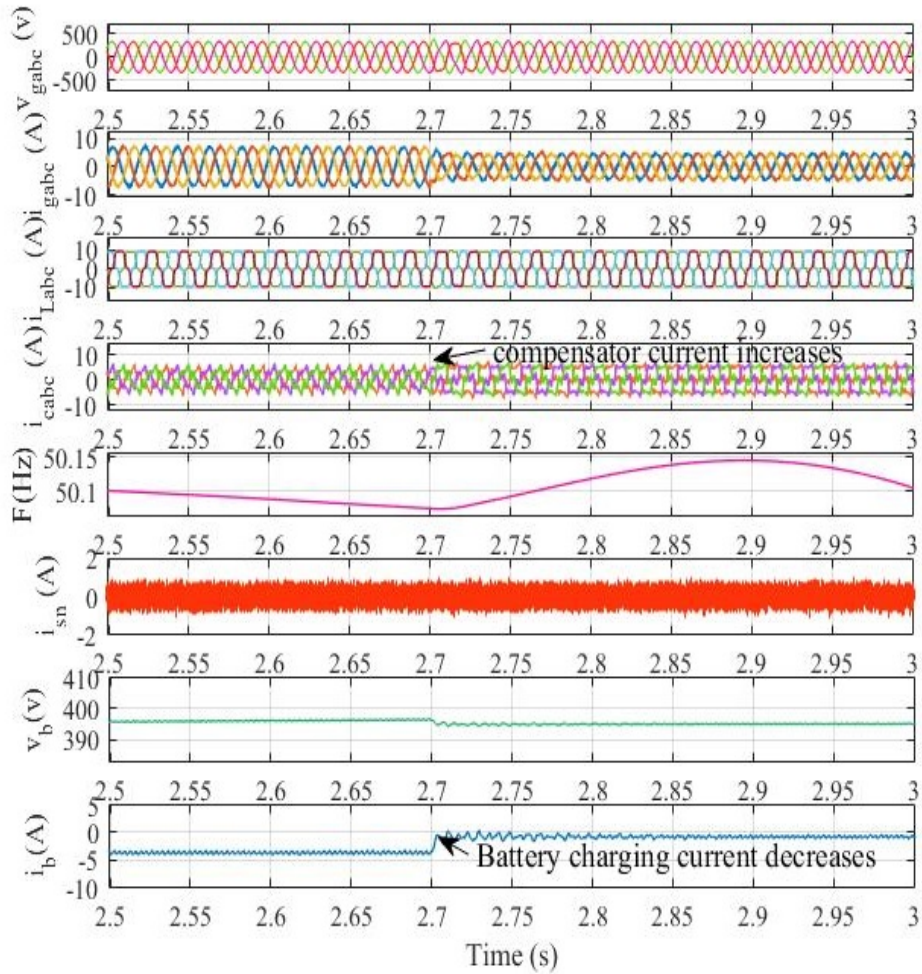
(b)

Fig. 5.4(a) and (b) Dynamic response of wind-solar hybrid system under varying solar intensity and fixed wind speed feeding linear/nonlinear load

5.2.1.4 Dynamic Performance of Hybrid System under Fixed Wind Speed/Solar Intensity Feeding Varying Linear/Nonlinear Load

Fig. 5.5 depicts the dynamic performance of a standalone hybrid system with varying linear/nonlinear load and fixed wind speed/solar intensity. The phase 'a' of linear/nonlinear load is disconnected at t=2.65 sec to t=2.85 sec., then the generator current is remain sinusoidal and balanced. During this duration, the compensator current, and battery current is increasing and load current is decreasing. The generated voltage, neutral current, and frequency are all kept constant by the controller. As results of the removals of load one phase 'a,' the load requirement is reduced, and the excess power that

was previously supplied to the load is now fed to the battery. Hence, the battery current is (+ ve direction) increases.
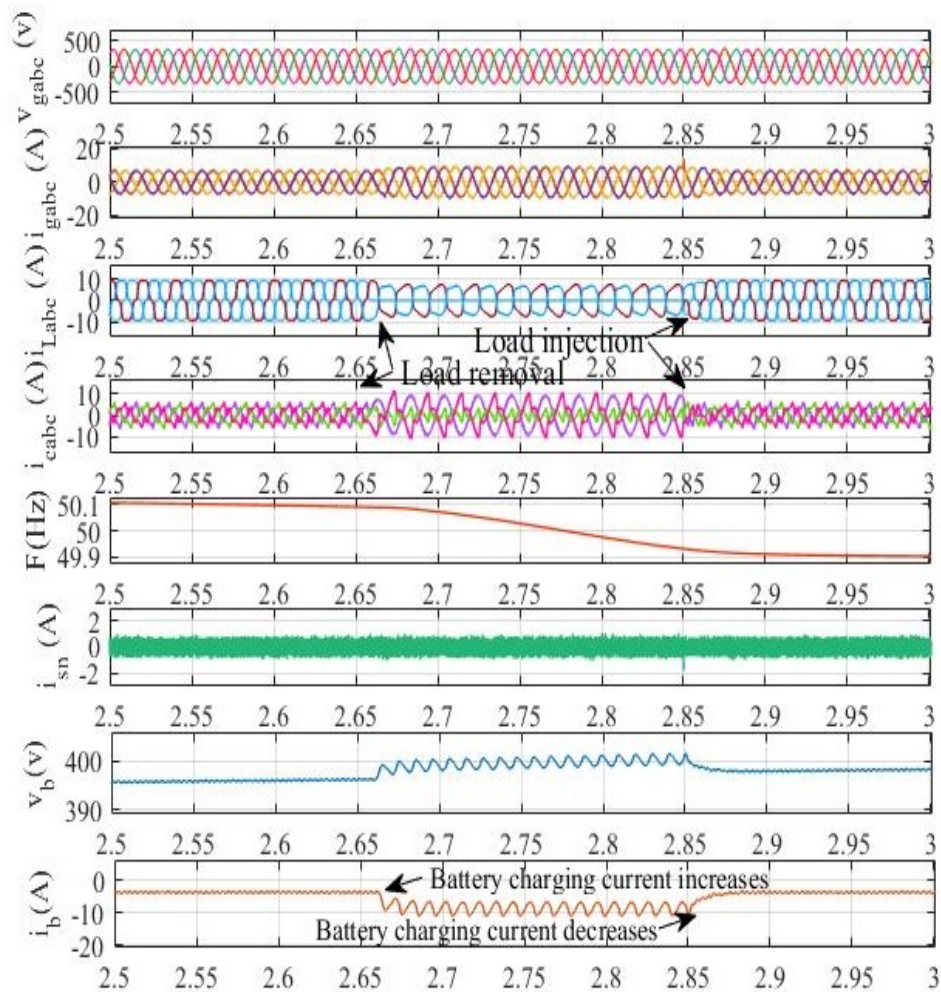
Fig. 5.5 Dynamic response of hybrid system under fixed wind speed/solar intensity feeding varying linear/nonlinear load

5.2.1.5 Power Balance Analysis of Standalone Hybrid System

Fig 5.6(a)-(d) shows the simulation result of the power balance analysis of a standalone hybrid system under different operating circumstances. Fig. 5.6(a) shows the generated power, load power and solarPV power under fixed wind speed/solar intensity feeding linear/nonlinear load. Fig. 5.6(b) shows the effect of declination in wind speed, the controller maintains the system frequency/voltage and the balance power is provided by the battery system. Fig. 5.6(c) Shows the reduction in generated power due to declination in solar intensity at t=2.7 sec. under constant load power condition. Fig. 5.6(d) Shows the rise in generated power and reduction in load power at t=2.65 sec to t=2.85 sec due to

disconnection of load of phase 'a'. During sudden disconnection of load og phase 'a', the unused power supply is delivered for battery charging. The DROGI-FLL-based controller maintains the power under varying load conditions/solar intensity/wind speed. The battery system with VSC is employed to provide active/reactive power support and consume the extra power during less load demand.
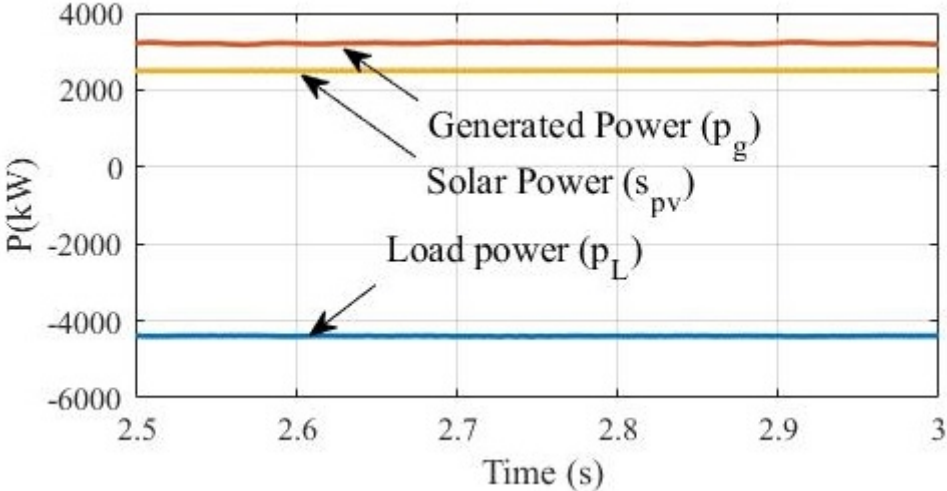
(a)
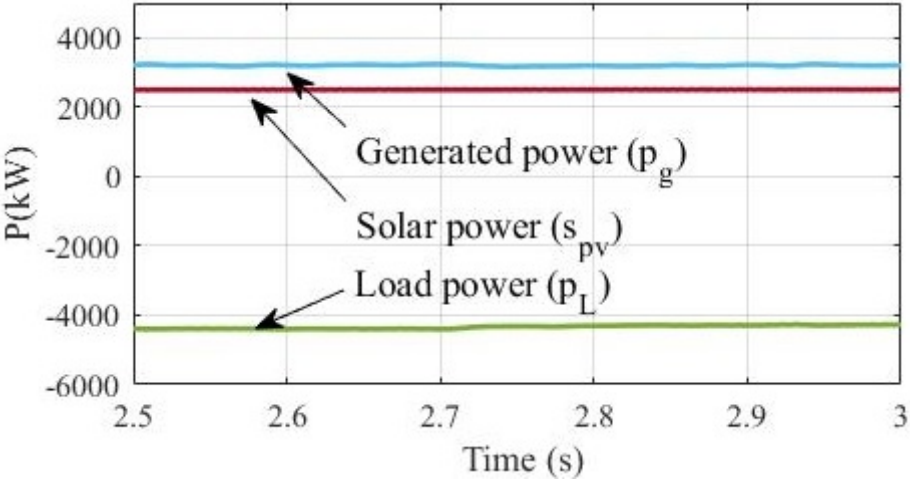
(b)
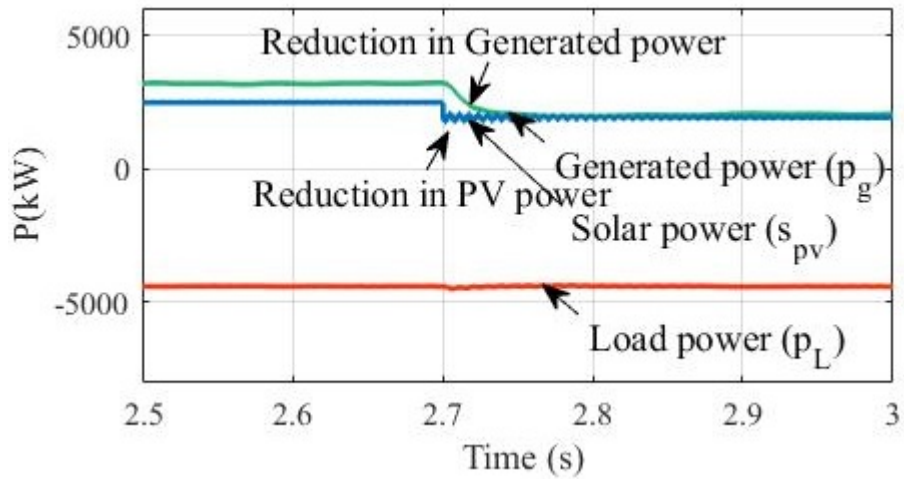
(c)
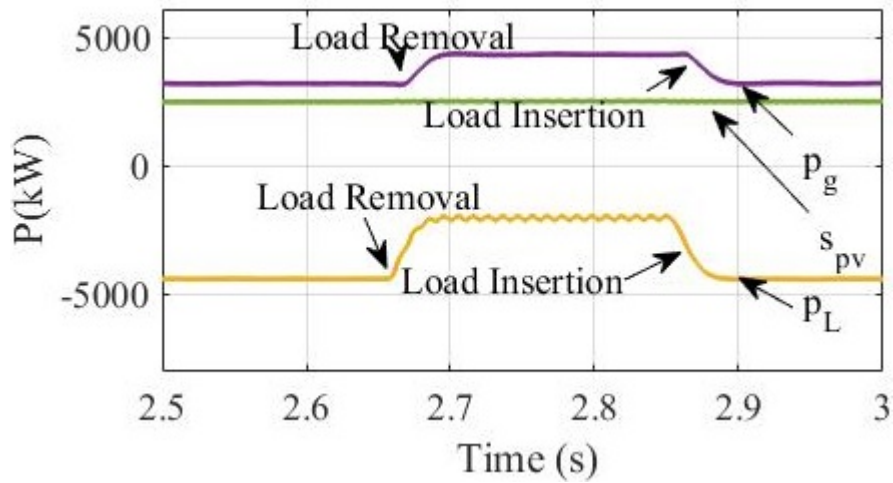
(d)

Fig. 5.6(a)-(d) Power balance analysis of standalone hybrid system (a) Fixed wind speed/solar intensity feeding linear/nonlinear load (b) Varying wind speed and fixed solar intensity feeding linear/nonlinear load (c) Varying solar intensity and fixed wind speed feeding linear/nonlinear load (d) Fixed wind speed/solar intensity feeding linear/nonlinear load

Table 5.1 Generated power, Load power, and PV power under different operating conditions of standalone hybrid system

S.No.	Parameters	Generated Power (p$_g$)	Load power (p$_L$)	PV power (p$_{pv}$)
1	Fixed wind speed/solar intensity feeding linear/nonlinear load	3.2 kW	4.4 kW	2.5 kW
2	Decline wind speed and fixed solar intensity feeding linear/nonlinear load	3.2 kW	4.27 kW	2.5 kW
3	Fixed wind speed and decline solar intensity feeding linear/nonlinear load	2.06 kW	4.4 kW	1.93 kW
4	Fixed wind speed/solar intensity, when load is disconnected of phase 'a' at t=2.65 sec to t=2.85 sec	4.34 kW	1.98 kW	2.5 kW

Table 5.1 represents the power balance of a standalone hybrid system under different operating conditions.

5.2.1.6 Waveform and Harmonic Analysis of Standalone Hybrid System

Fig. 5.7(a)-(c) shows the harmonic spectrum of a standalone hybrid system feeding nonlinear load. The 3P4W standalone hybrid system gives a good response under nonlinear load even in one or two-phase load is disconnected. The THD of the generated voltage, generator current and load current are 0.64%, 4.17% and 26.45% respectively. The THD of the generator current becomes below than 5% which is underneath an IEEE-519 standard.
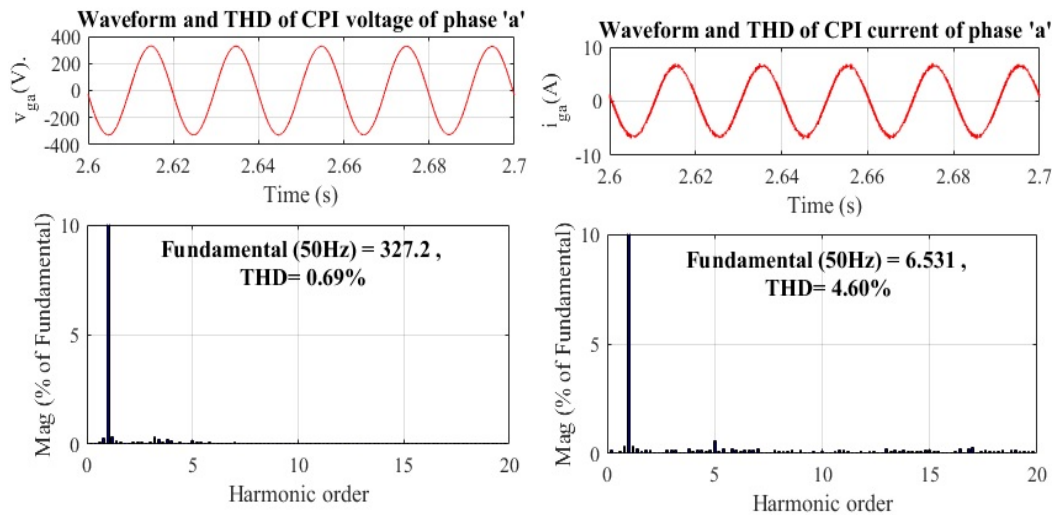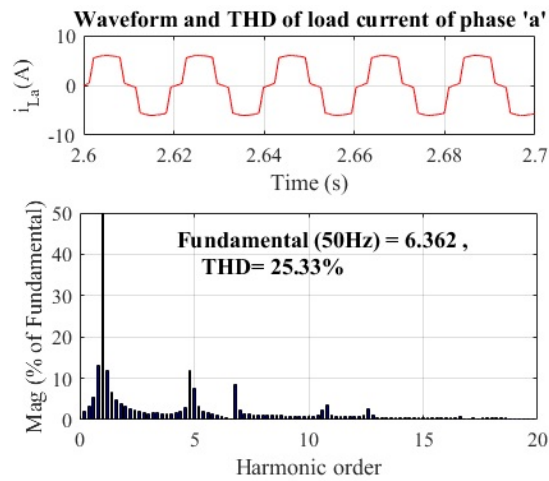
Fig. 5.7 Waveform and Harmonic analysis of (a) Generated voltage (b) Generator current (c) Load current

Table 5.2 Harmonic analysis of all the phases from simulation

S. No.	Phase	Values of THD		
		v_g, %	i_g, %	i_L, %
1	A	0.64	4.17	26.45
2	B	0.67	4.20	26.85
3	C	0.67	4.22	27.01

Table 5.2 represents the THD analysis of generated voltage, generator current and load current per phase under nonlinear load of the standalone hybrid system.

5.3 DTOGI-PLL Control Approach

The DTOGI-PLL control is depicted in Fig. 5.8. The DTOGI-PLL employs a TOGI-based adaptive filter for each i_α and i_β current component in the pre-filtering stage of PLL. The component of currents i_α and i_β (i'_α and i'_β) and their quadrature current components (qi'_α and qi'_β) are extracted using DTOGI-PLL. The transfer function of TOGI control is evaluated as

$$R(s) = \frac{i'_{\alpha,\beta}}{i_{\alpha,\beta}} = \frac{k_1\omega^2 s}{s^3 + k_2\omega s^2 + (k_1+1)\omega^2 s + k_2\omega^3} \tag{5.2}$$

$$Q(s) = \frac{qi'_{\alpha,\beta}}{i_{\alpha,\beta}} = \frac{\omega}{s} R(s) = \frac{k_1\omega^3}{s^3 + k_2\omega s^2 + (k_1+1)\omega^2 s + k_2\omega^3} \tag{5.3}$$
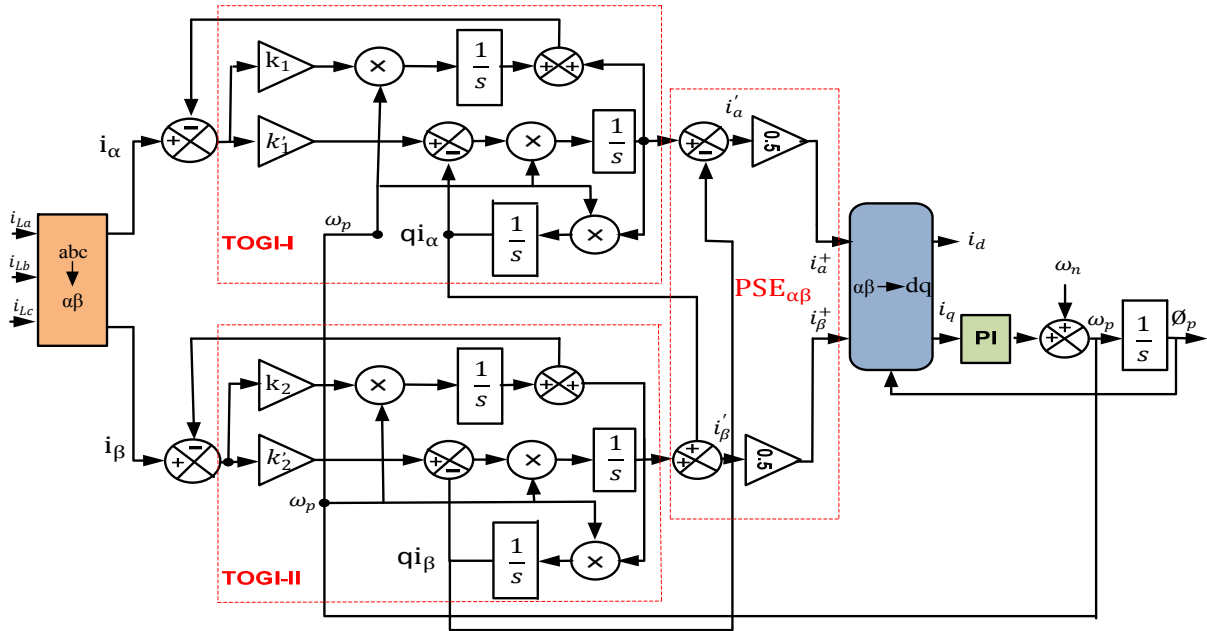
Fig 5.8 DTOGI-PLL control approach

Where, ω_p represents the estimated frequency of autonomous microgrids and k_1 and k_2 are the gain controllers of DTOGI-PLL. The gain controllers k_1 and k_2 finalize the bandwidth of the filter and affects the response time of the filter. The sinusoidal quantities (i'_α, i'_β, qi'_α and qi'_β) from the TOGI control filters are entered into the positive sequence evaluator (PSE) to draw the FFPS components (i_α^+ and i_β^+). The instantaneous symmetrical components (ISC) control method in the stationary reference frame is utilized to evaluate the (i_α^+ and i_β^+) current components.

$$i_\alpha^+ = 0.5(i_\alpha^+ - qi_\beta^+) \tag{5.4}$$

$$i_\beta^+ = 0.5(qi_\alpha^+ + i_\beta^+) \tag{5.5}$$

Then, the extracted FFPS parameters are passed through the SRF-PLL to calculate the microgrid components like as phase angle and current amplitude in MG. The evaluated frequency is fed back to the DTOGI-FLL-based control to make the control frequency adaptive [126], [185].

5.3.1 ADF-FLL Control Approach

The ADF-FLL control approach is depicted in Fig. 5.9. The load currents (i_{La}, i_{Lb} and i_{Lc}) are transformed to generate (i_α and i_β) current components. The complex gain parameters are utilized between α-β axis to enhance the performance of the ADF-FLL. The fundamental current in-phase and quadrature components are computed as

$$i_{a1} = I_a \cos(\emptyset_p) \tag{5.6}$$

$$i_{\beta1} = I_a \sin(\emptyset_p) \tag{5.7}$$

The amplitude of current component (I_a) and phase angle ($\emptyset_p$) in ADF-FLL is estimated as

$$I_a = \sqrt{i_{a1}^2 + i_{\beta1}^2} \tag{5.8}$$

$$\emptyset_p = \tan^{-1}(i_{\beta1}/i_{\alpha1}) \tag{5.9}$$

Where, k_1' and k_2' are the gain parameters and give an additional degree of freedom in this control algorithm and λ, k_1 and k_2 are the complex gain constants. ω_p is the evaluated angular frequency of ADF-FLL [25].
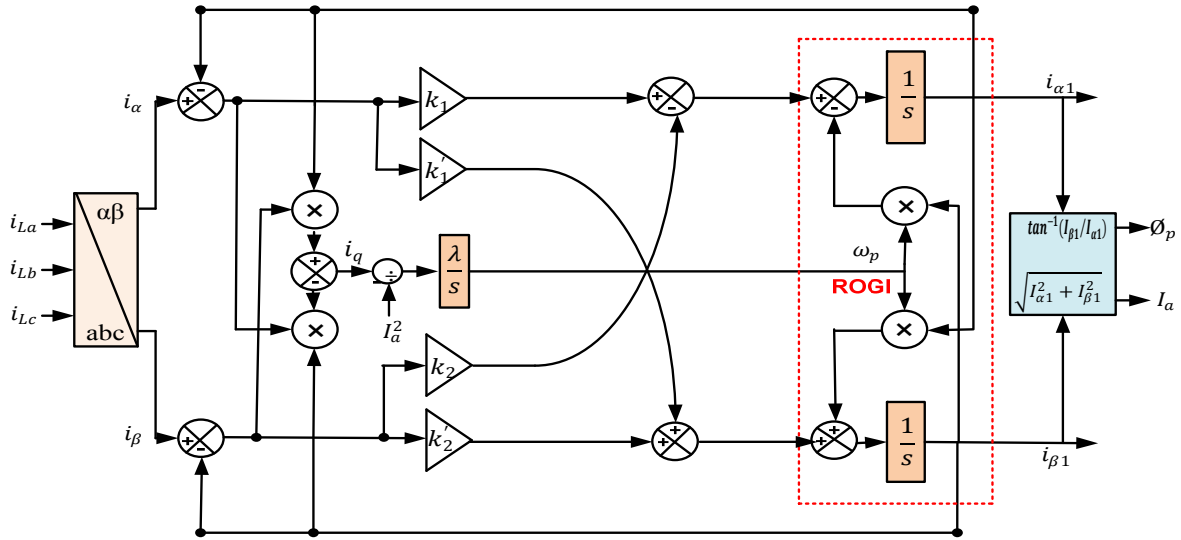
Fig. 5.9 ADF-FLL control algorithm

5.3.2 Simulation Results

The proposed DTOGI-PLL and ADF-FLL control scheme is analyzed through simulation & experimental study of the integrated system under intermittent conditions of an isolated microgrid.

5.3.2.1 Intermediate Parameters of Control Approaches

The intermediate signals of the DTOGI-PLL and ADF-FLL control approach under an unbalanced load are shown in Fig. 5.10(a)-(d). Fig. 5.10(a) shows the internal signals i_α, i_β, qi_α, qi_β, i_q (Extracted current components) and w_p (angular frequency) under unbalanced load. The load on phase 'a' is detached at t=2.8s. The i_α, i_β, qi_α and qi_β are the active & reactive extracted components of the load current. During the removal of the load the extracted signals i_α and qi_α have become zero. Fig. 5.10(b) represents the internal signals v_T (amplitude voltage), u_{aa} (in-phase template), u_{ra}(reactive or quadrature template), i_{fp} (output of DC PI controller), i_A (output of AC PI controller) and $\emptyset_p$ (phase angle) of isolated microgrid under unbalanced load. All internal signals are extracted from sensed nonlinear load current. Fig. 5.10(c) shows the internal signals i_α, i_β, $i_{L\alpha}$, $i_{L\beta}$, w_p and i_{Lpa}. Since, i_α becomes zero and extracted active current (i_{Lpa}) is decreased due to the disconnection of the load of phase 'a' at t=2.8s. The other parameters in Fig. 5.10(d) are also changed due to load disconnection. Fig. 5.10(d) displays the voltage amplitude (v_T),

u_{aa} (in-phase unit template), u_{ra} (quadrature unit template), i_{fp} (DC PI controller), i_A (AC PI controller) and $\emptyset_p$ (phase angle). The extracted parameters are utilized to control and manage the isolated system during load perturbation and dynamic conditions of RESs.
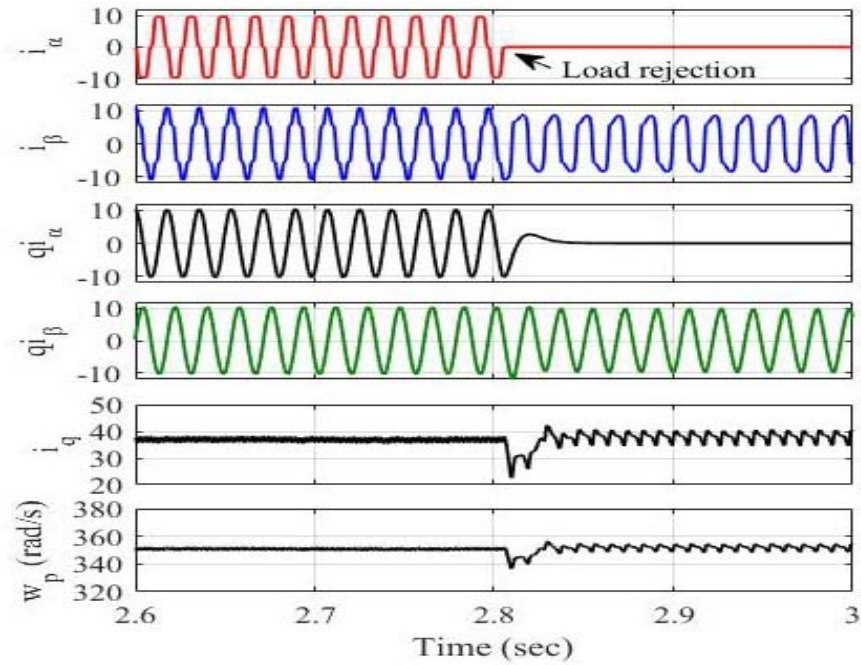
(a)
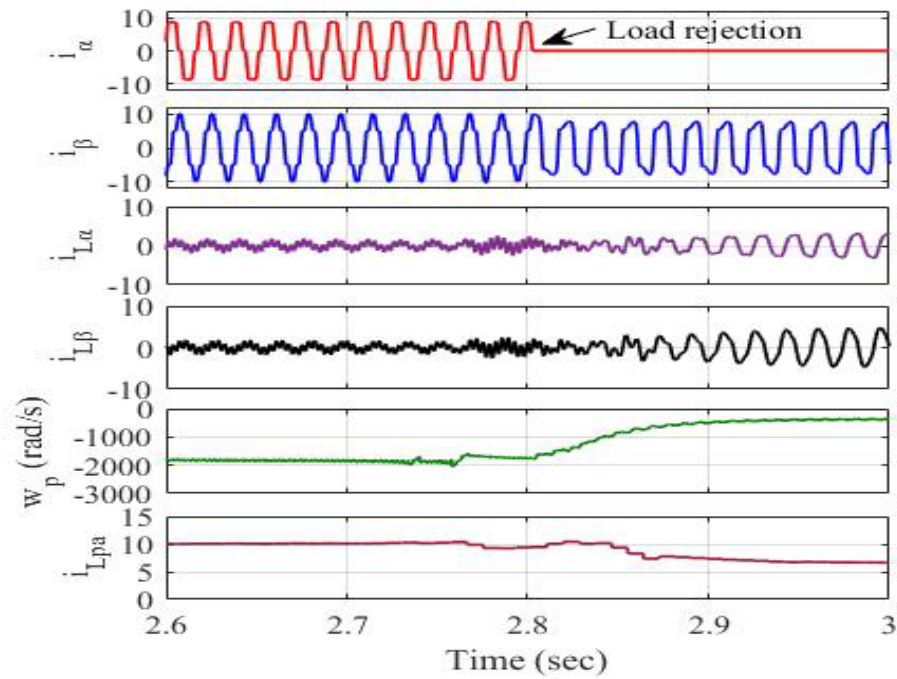
(b)
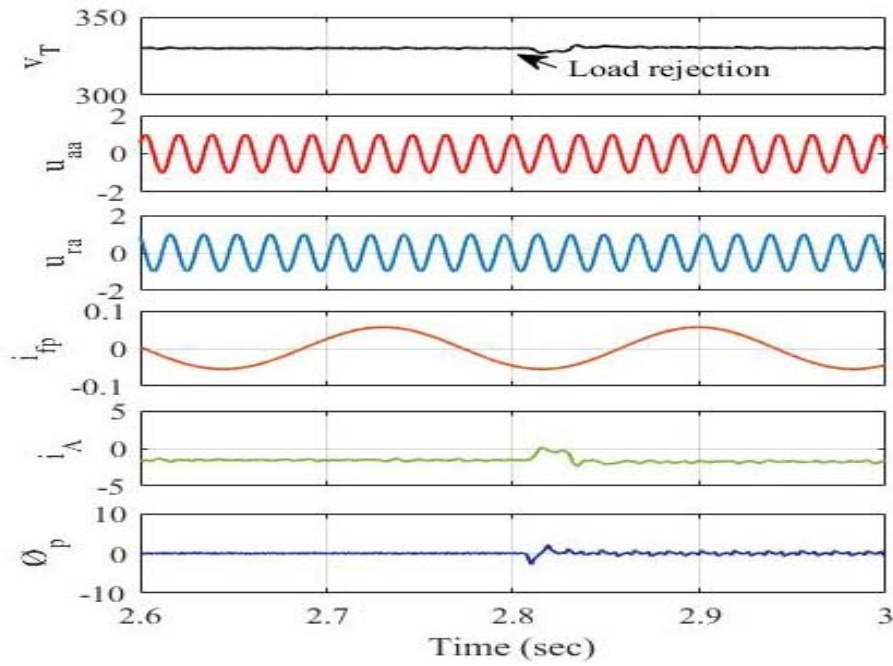
(c)
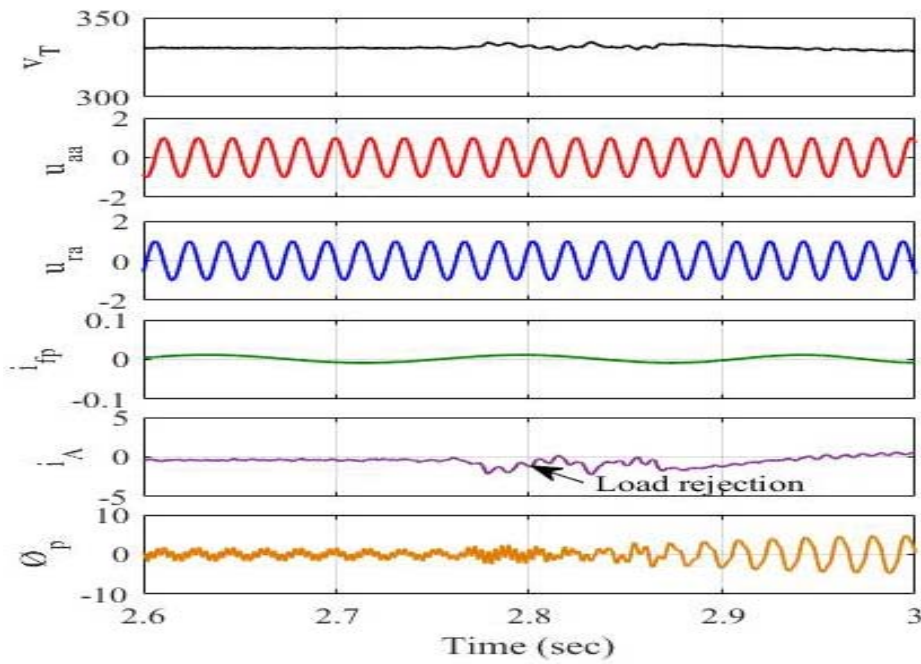
(d)

Fig. 5.10(a)-(d) Internal signals (a) i_α, i_β, qi_α, qi_β, i_q and w_p internal signal under one phase load removal (b) i_α, i_β, qi_α, qi_β, i_q and w_p at unbalanced load (c) v_T, u_{aa}, u_{ra}, i_{fp}, i_A and $\emptyset_p$ internal signals under one phase load removal (d) v_T, u_{aa}, u_{ra}, i_{fp}, i_A and $\emptyset_p$ at unbalanced load.

125

5.3.2.2 Dynamic Performance during Variations in Wind Velocity

Fig. 5.11(a) represents the simulation results of the isolated microgrid system under an abrupt change in wind velocity. The isolated system is in steady-state before t=2.8s, where wind velocity is 12m/s and CPI voltage (v_{gabc}) and CPI current (i_{gabc}) are sinusoidal. The wind velocity is decreased from 12m/s to 9m/s at t=2.8s. However, the DTOGI-PLL-based controller stabilizes the voltage and current of an isolated microgrid. The generated power declined from 5.4kW to 5.3kW due to a reduction in wind velocity. However, the load is balanced and the power demanded by the load is fed from the ESS. The solar radiations and temperature are fixed at 900w/m^2 and 35°C respectively. Fig. 5.11(b) represents the behavior of an isolated system under the variation in wind velocity and unbalanced nonlinear load. The wind velocity (w_v) is changed from 12m/s to 9m/s and the load of phase 'a' is detached at t=2.7s to t=2.9s depicted in Fig. 5.11(b). The generated voltage & current are sinusoidal during the variation in wind velocity and load. During the inclusion of load at t=2.9s, the compensator current and generated current is slightly decreased for 0.02s, after this, the controller maintains these parameters. During the removal of one phase load, the load current is declined and the unused power during this duration is supplied to the ESS. Moreover, with the inclusion of load at t=2.9s, an ESS changes its mode from charging to discharging mode. The DC-link voltage and other parameters of the microgrid are maintained constant with the help of ADF-FLL-based controller.
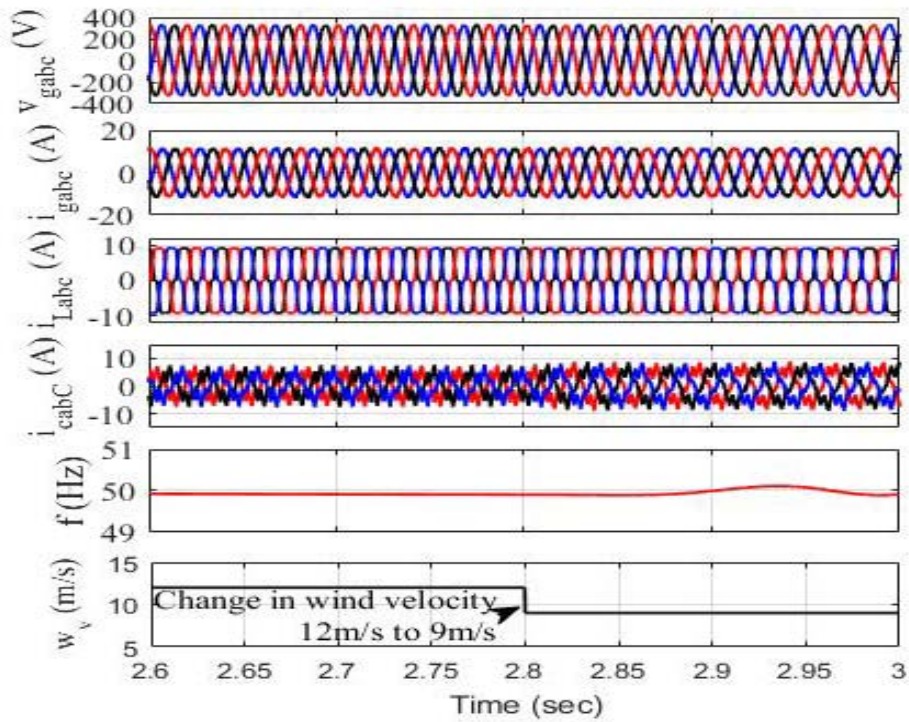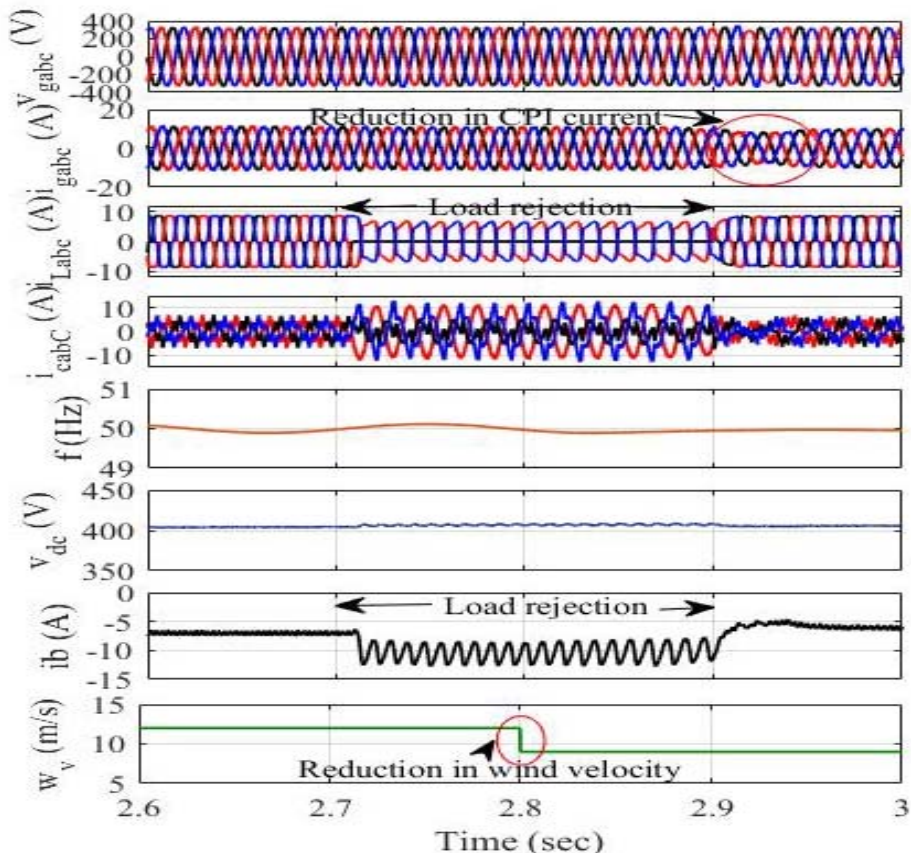
Fig. 5.11(a) and (b) Dynamic performance of isolated microgrid (a) Variations in wind velocity, and (b) Change in wind velocity and unbalanced load

127

5.3.2.3 Dynamic Performance during Variations in Solar Intensity and Unbalanced Load

The performance of isolated microgrid is studied under variations in solar radiations and unbalanced loading conditions. Fig. 5.12(a) shows the microgrid in a steady state before t=2.8s, when the solar radiations and temperature is fixed at 900w/m^2 and 35°C. If the solar radiations and temperature are changed to 600w/m^2 from 900w/m^2 and 35°C to 25°C, then PV current is reduced due to solar radiation level declination and thus decreasing the generated power, PV power and duty cycle. Fig. 5.12(c) shows the response of islanded microgrid under variations in solar radiations and unbalanced load conditions. The load of phase 'a' is removed from t=2.7s to t=2.9s. During the disconnection of one phase load, there is a declination in load demand, and the extra power is absorbed by ESS. Thus, the ESS maintains the power equilibrium between the source and the load. If the solar radiations and the unbalanced load condition occur simultaneously in the microgrid as shown in Fig. 5.12(c) the microgrid frequency remains fixed but the generated current and load current is slightly reduced.

On the other hand, Fig. 5.12(b) and (d) depicts the dynamic response of isolated microgrid under a change in solar radiations. The wind velocity is fixed at 12 m/s. Fig. 5.12(b) shows solar radiations level and temperature which are increased from 600w/m^2 to 900w/m^2 and 25°C to 35°C respectively. Due to change in solar radiation level the PV current (i_{PV}) increases from 7.09A to 11.7A, PV power (p_s) increases from 1.1kW to 1.7kW. Fig 5.12(d) shows the performance of ADF-FLL-based controller which maintains the voltage profile, current profile and frequency under variations in solar radiations and nonlinear load. The generated current and compensator current increases at t=2.8s due to an inclination in solar radiation. The ESS charging current is reduced, when the solar radiations are reduced to 600w/m^2 as shown in Fig. 5.12(d). At t=2.8s, the solar radiations are increased from 600w/m^2 to 900w/m^2, and the ESS charging current is also increased accordingly. Hence, the ESS maintains the power balance under the abrupt circumstances of solar power.
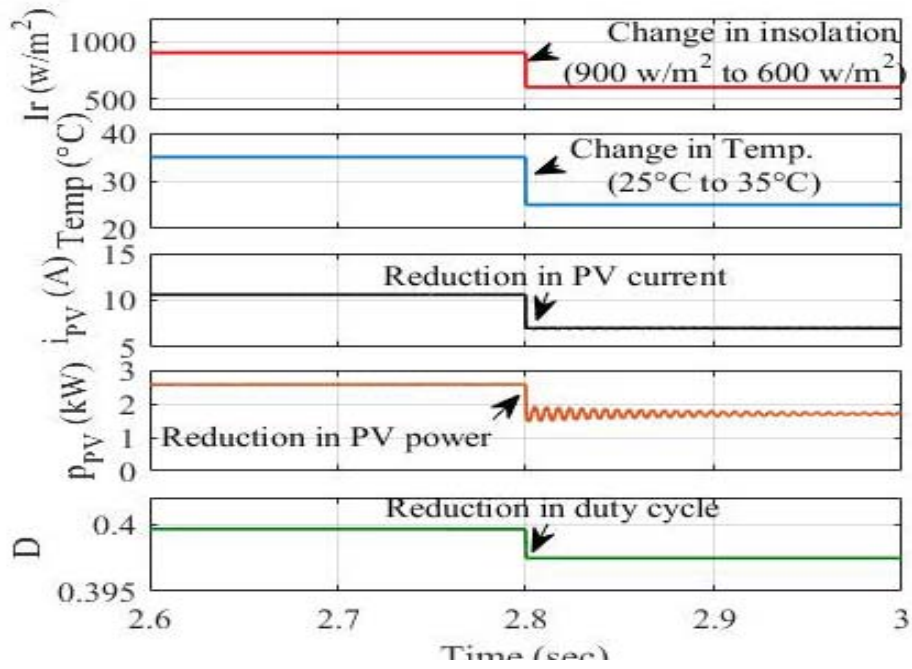
(a)
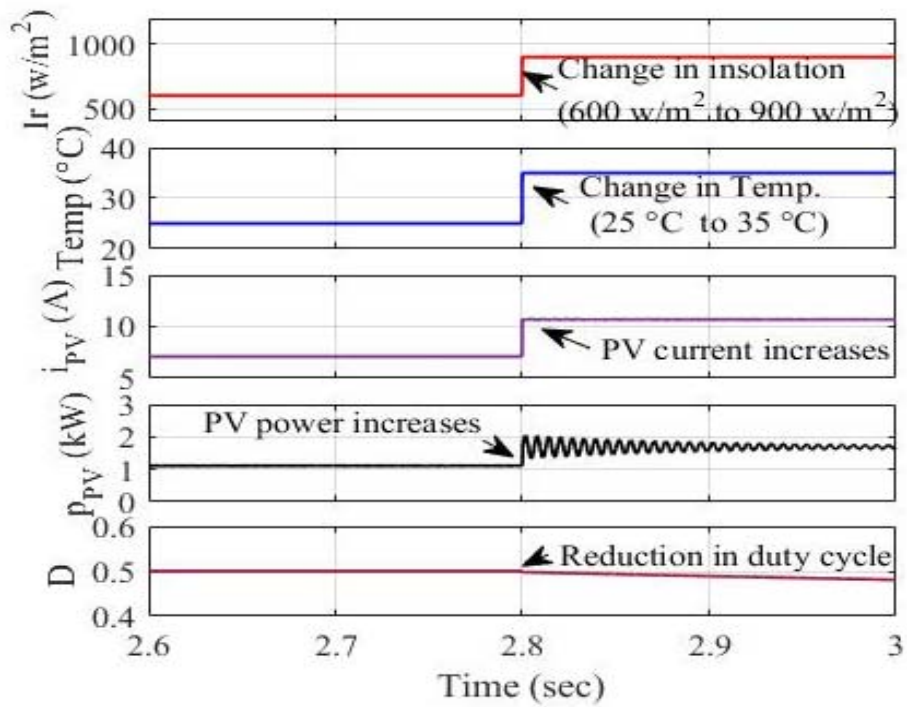
(b)
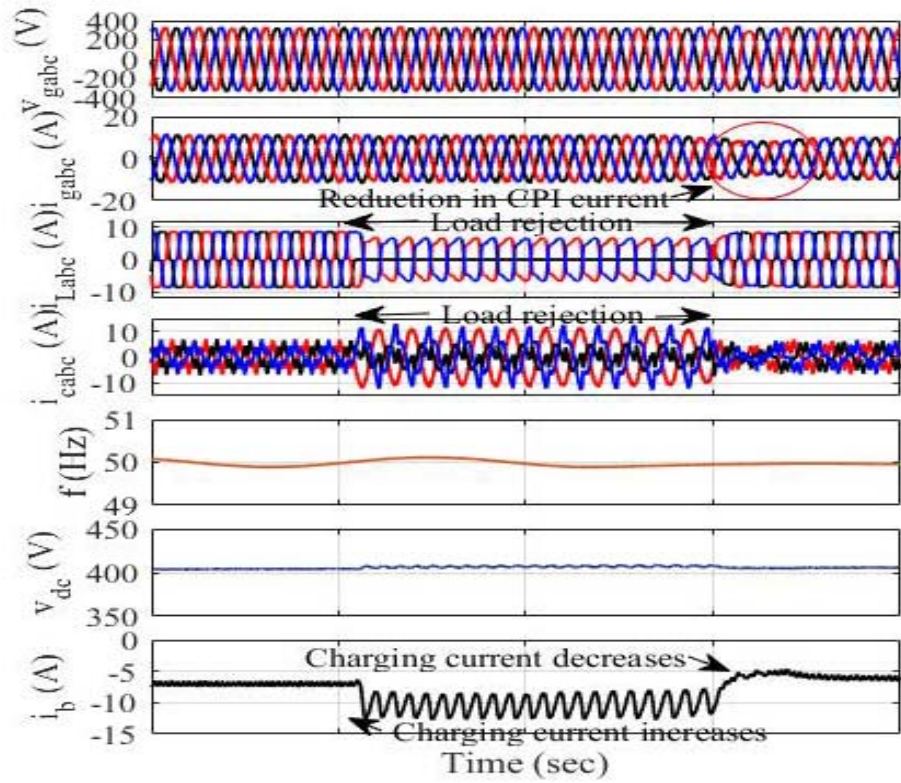
(c)
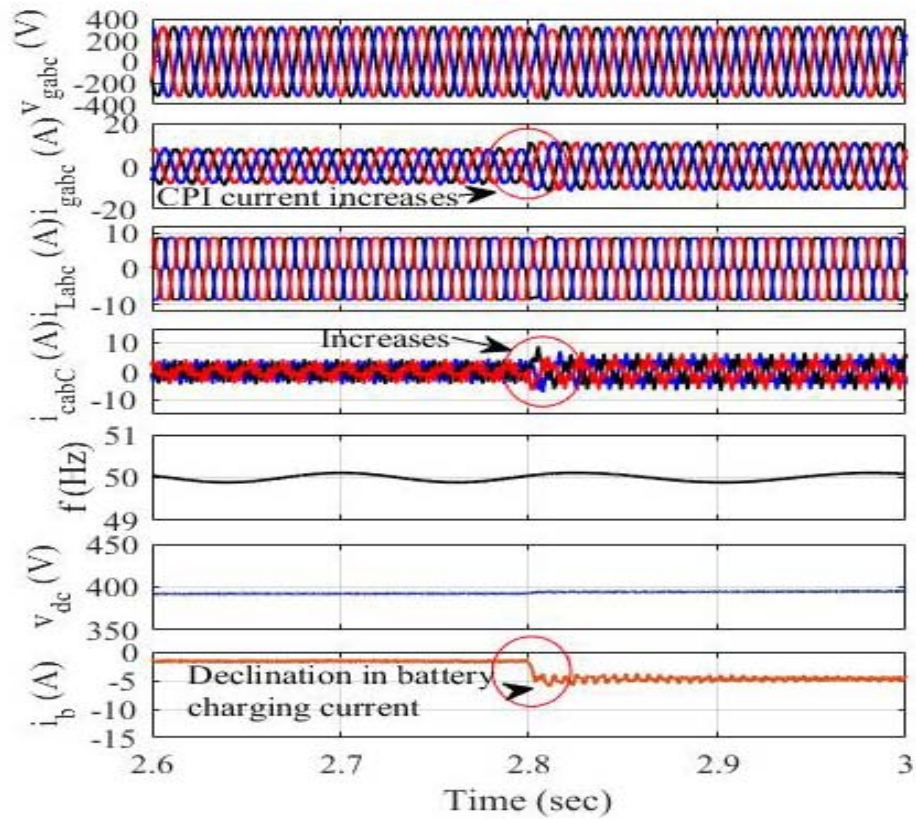
(d)

Fig. 5.12 Dynamic performance of isolated microgrid (a)-(b) Variation in solar intensity level, and (c)-(d) Unbalanced load using DTOGI-PLL and ADF-FLL control algorithms

5.3.2.4 Harmonics analysis

The harmonic analysis of voltage and current in an isolated microgrid based on DTOGI-PLL and ADF-FLL adaptive control approach are plotted in Figs. 5.13(a)-(f). The Total Harmonic Distortions (THDs) of CPI (voltage & current) and load current of phase 'a' are 0.69%, 4.14% and 25.33% respectively using DTOGI-PLL control depicted in Fig. 5.13(a)-(c) and the THDs are 0.87%, 4.60% and 26.45% respectively using ADF-FLL control approach depicted in Fig 5.13(d)-(f) of the isolated microgrid system. These THDs of voltages/currents of isolated microgrid based on DTOGI-PLL and ADF-FLL control algorithms are determined under nonlinear load conditions. It is examined that the Total Harmonic Distortions (THDs) of CPI voltage & current, and load current are as per the IEEE-519 standard.
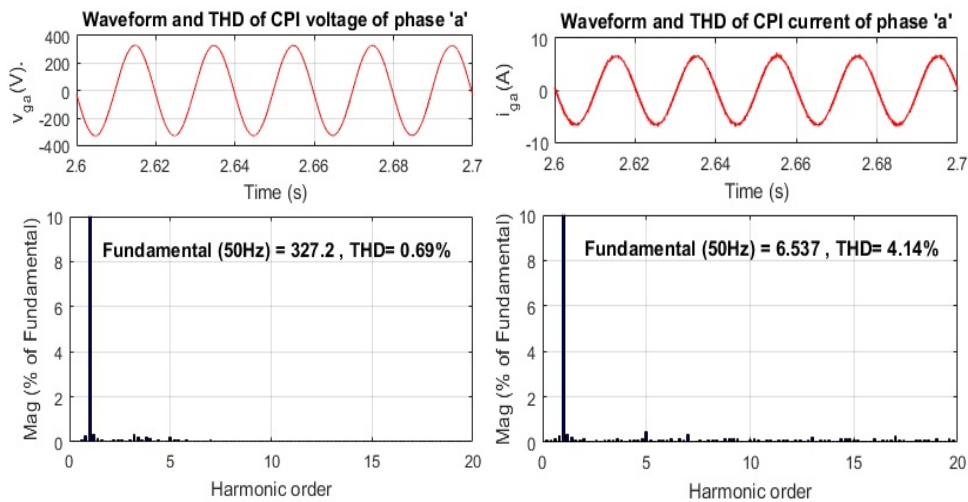
(a)   (b)
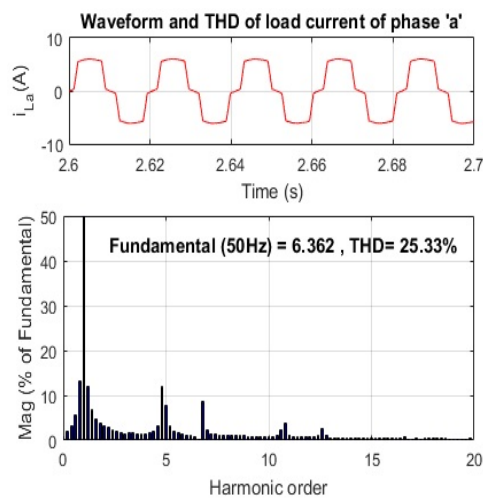
(c)
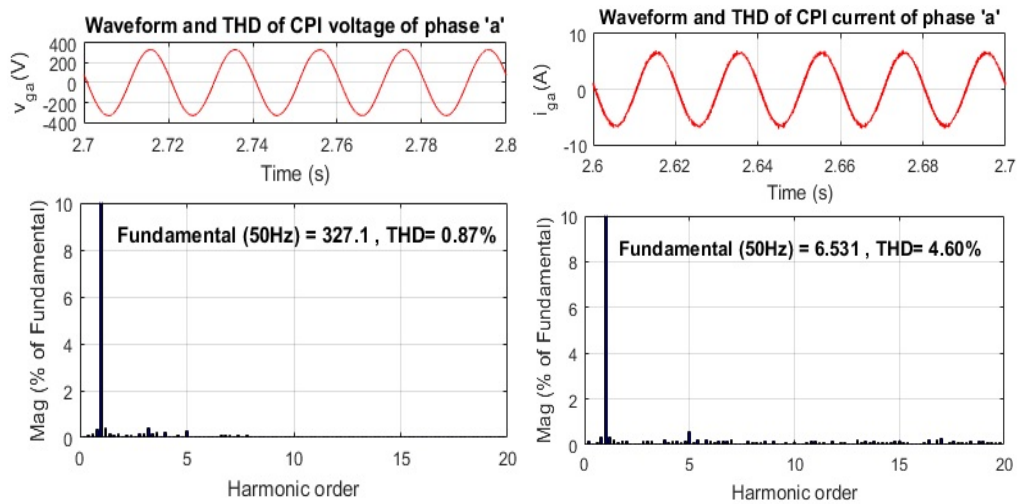
(d)   (e)
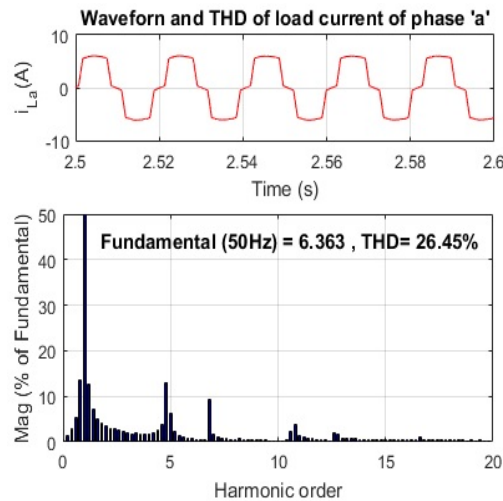
(f)

Fig. 5.13 Harmonic analysis of DTOGI-PLL and ADF-FLL control-based isolated microgrid

5.3.3 Test Results

A prototype is developed that validates the findings of the standalone system's tests under various conditions. A prime mover, SEIG, capacitor bank, BDC, opto-coupler, VSC, and ESS are included in the prototype. The wind-powered SEIG is interfaced to a delta-connected capacitor bank, which supplies the reactive power needed for power generation.

5.3.3.1 Dynamic Response of an Islanded System

Fig. 5.14(a)-(f) shows the dynamic response of islanded system after introducing load harmonics. Fig. 5.14(a) depicts the intermediate signals of isolated system under the removal of load. The load current (i_{La}) and extracted source current (i_{ga}^*) are reduced to zero during load disconnection. The active (u_{aa}) & (u_{ra}) quadrature unit templates are sinusoidal during nonlinear and unbalanced loads. Fig. 5.14(b) depicts v_{dc}, v_{ga}, i_{ga}, and i_{La} under insertion of one phase load. During the insertion of the load, the i_{ga} and i_{La} are increased. Fig. 5.14(c) and (d) show the v_{ga}, and i_{gabc} of all phases is sinusoidal during unbalanced and nonlinear load conditions. Fig. 5.14(e) and (f) depict the response of the isolated system under load insertion of 2-phases & 3-phases. The dynamic results present an effective performance of a standalone system. During the load declination, the extra power is supplied to the ESS for charging. The proposed DTOGI-PLL effectively controls all the parameters under different circumstances.
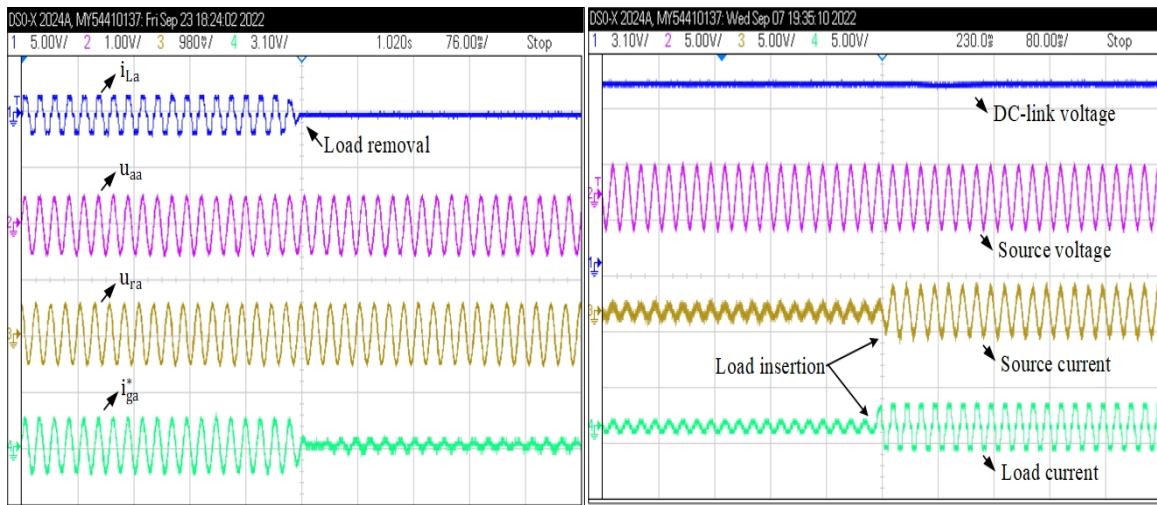
(a)   (b)
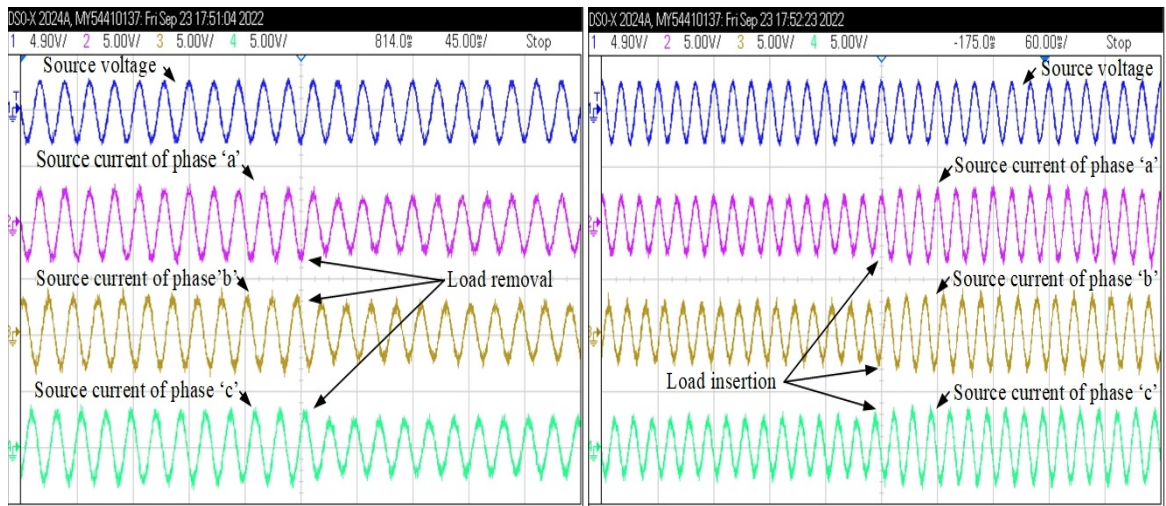
(c)

(d)
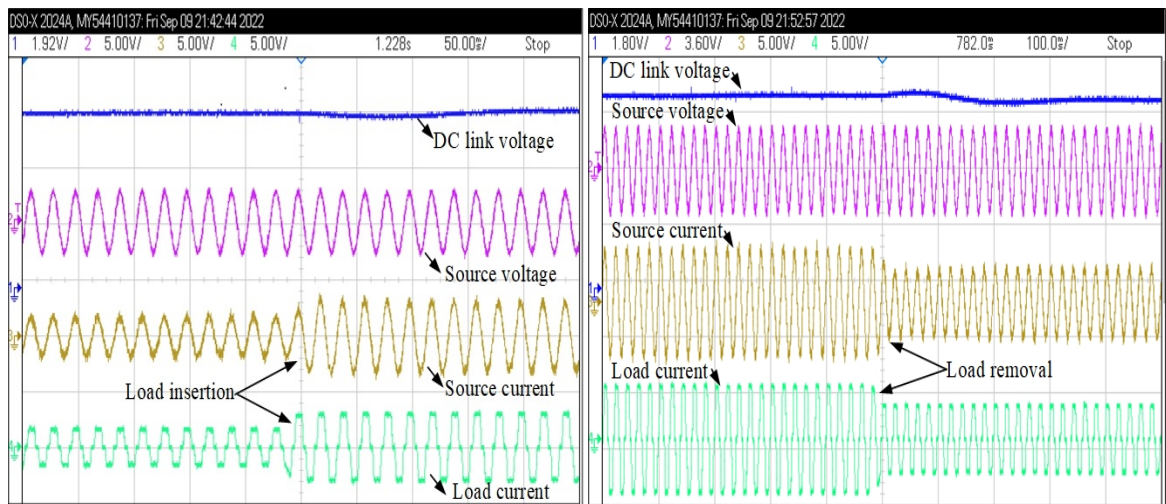
(e)

(f)

Fig. 5.14(a)-(f) Dynamic response of an islanded system

5.3.3.2 Harmonic analysis

The harmonics results of the isolated system have been recorded under nonlinear load conditions. The THD of the CPI voltage & current is below 5%, which satisfies the limit of IEEE-519 standard. Fig 5.15(a) and (b) depict the THD of CPI voltage, CPI current, & load current are 2.03%, 4.21%, and 27.71 respectively. The proposed DTOGI-PLL control effectively managed all the parameters and maintains CPI current sinusoidal after applying nonlinear load to the standalone system.
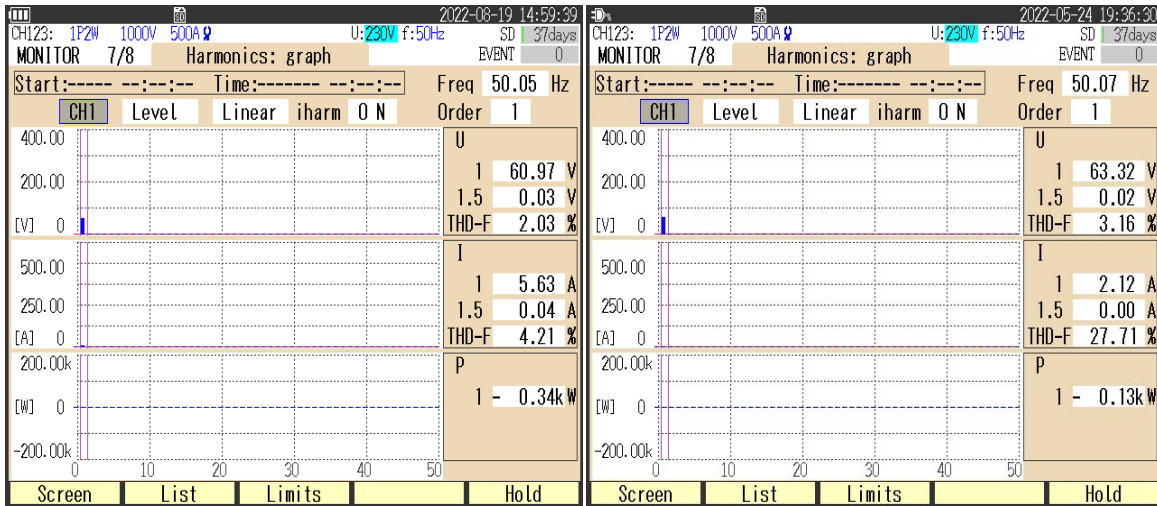
(a)　　　　　　　　　　　　　　　　　　　(b)

Fig. 5.15(a) and (b) Harmonic analysis of isolated system

5.4　DSOGI-PLL Control Approach

The control algorithm for VSC is capable of ensuring sinusoidal source currents and mitigating the effects of nonlinear loads at CPI. A DSOGI-PLL approach is employed to estimate the fundamental component as shown in Fig 5.16. The dual SOGI is designed using two in-loop filter-based SOGIs. The implemented SOGI generates two 90° phase shifted signals. Each SOGI & QSG is utilized to produce two quadrature voltages with the transfer help of function.
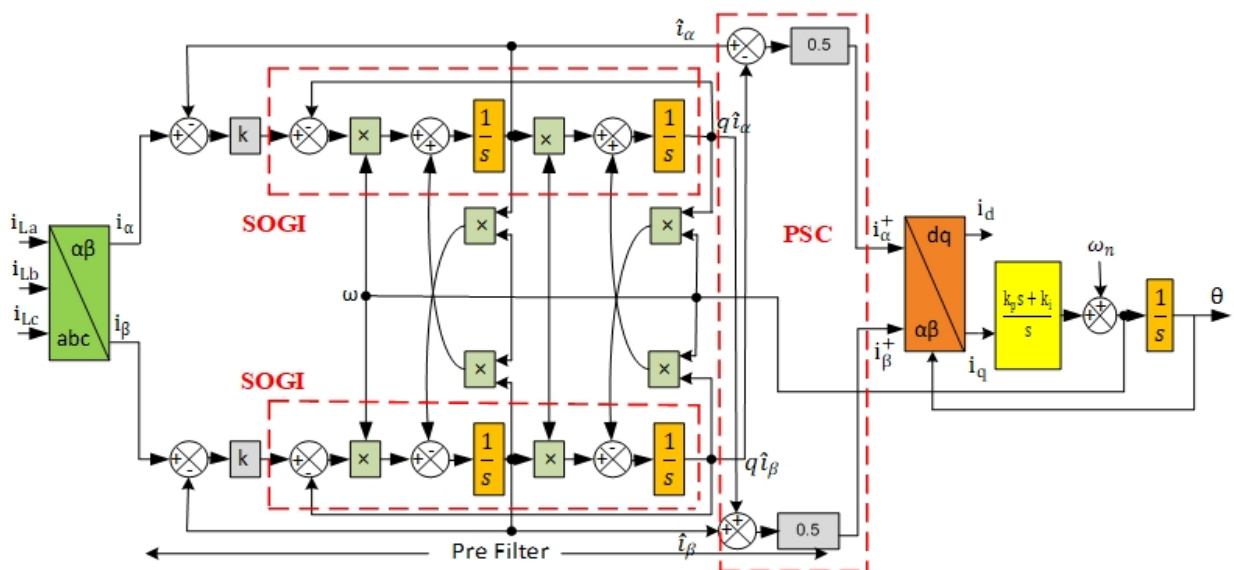
Fig. 5.16 DSOGI-PLL control approach

$$D_\rho(q) = \frac{i'_\rho}{i_\rho} = \frac{k\omega s}{s^2 + k\omega s + \omega^2} \tag{5.10}$$

$$Q_\rho(q) = \frac{qi'_\rho}{i_\rho} = \frac{k\omega^2}{s^2 + k\omega s + \omega^2} \tag{5.11}$$

Where $\rho \in (\alpha, \beta)$ denotes the two extracted reactive components. For their respective reactive component, the two reactive components have filtering qualities such as low-pass and band-pass. As a consequence, the low-order current harmonics of the detected current can be reduced. The DSOGI output is supplied into the positive sequence extractor (PSE) to exclude double frequency phase oscillations in the currents of-q reference frame. The combined DSOGI & PSE transfer function is stated as,

$$\begin{pmatrix} i_\alpha^+ \\ i_\beta^+ \end{pmatrix} = \frac{1}{2} \frac{k\omega}{s^2 + k\omega s + \omega^2} \begin{pmatrix} s & -\omega \\ \omega & s \end{pmatrix} \begin{pmatrix} i_\alpha(s) \\ i_\beta(s) \end{pmatrix} \tag{5.12}$$

The double frequency and imbalanced voltage components are eliminated by a low-pass filter. In a synchronously rotating reference frame, these positive sequence currents are now utilized to determine the d & q-axis currents as below [24]

$$\begin{pmatrix} i_d \\ i_q \end{pmatrix} = \begin{pmatrix} \cos(\theta) & \sin(\theta) \\ -\sin(\theta) & \cos(\theta) \end{pmatrix} \begin{pmatrix} i_\alpha^+ \\ i_\beta^+ \end{pmatrix} \tag{5.13}$$

The extracted fundamental load current component (I_f) and phase angle from the distorted load current is calculated [186]

$$I_f = \sqrt{i_d^2 + i_q^2}, \text{ and } \theta = \tan^{-1}\left(\frac{i_q}{i_d}\right) \tag{5.14}$$

5.4.1 Simulation Results

The result of the proposed 3P4W standalone system is analyzed under intermittency in solar irradiance, wind speed and consumer load. During variations in load demand and variation in solar PV insolation, the reliability of the proposed DSOGI-PLL approach is validated through a simulation study. The simulation results of CPI voltage (v_{sabc}), CPI current (i_{sabc}), load current (i_{Labc}), compensator current (i_{cabc}), dc-link voltage (v_{dc}), frequency (F), neutral load current (i_{Ln}), PV current (i_{pv}), duty cycle (α) and PV power (P) are taken under various operating circumstances.

5.4.1.1 Dynamic Response of Wind and SPV System during Unbalanced Load

Fig. 5.17 represents the dynamic response of the proposed wind & SPV system during constant wind speed/solar irradiance feeding an unbalanced load. The wind speed and solar irradiance are fixed at 15m/s and 900w/m^2, respectively. A load of phase 'b' is detached at t=2.7s to t=2.9s. During the exclusion of load in phase 'b', the load current is declined and the controller manages the CPI voltage, CPI current, frequency, and dc-link voltage of the proposed DG system. The total generation of the standalone system is increased from 5.2kW to 5.8kW during the disconnection of a load of phase 'b'. Further, the compensator current and neutral load current is increased during load detached. The DSOGI-PLL control with VSI provides multi-functions like voltage/frequency control, neutral current compensation, harmonics eradication, power support, and enhances overall PQ of the standalone system.
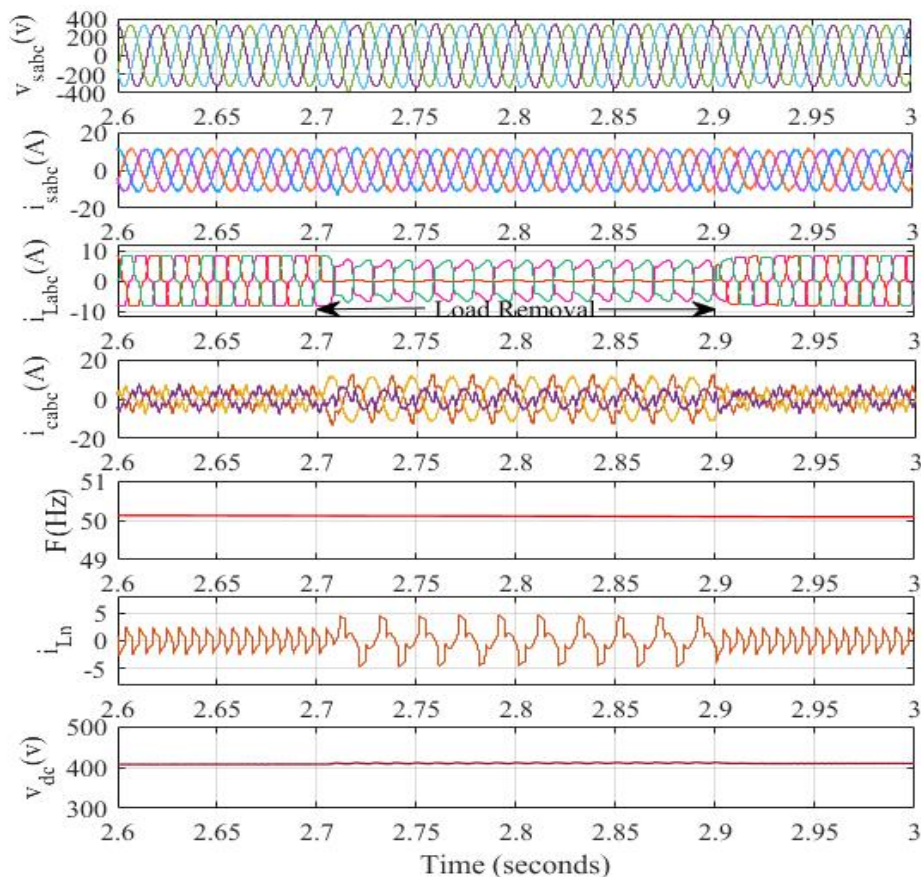
Fig.5.17 Dynamic response of wind and SPV system during unbalanced load

5.4.1.2 Dynamic Response under Intermittency

The dynamic performance of the standalone wind & SPV system during wind variation feeding balanced nonlinear load is observed and depicted in Figs. 5.18(a) and (b). Fig. 5.18(a) represents the wind speed is altered from 15m/s to 12m/s at t=2.8s and the solar irradiance is shifted 500w/m^2 to 900w/m^2 at t=2.7s. Due to inflation in solar irradiance, the PV current and the PV power of the proposed standalone system are increased from 5.9A to 11.77A and 1.8kW to 2.8kW respectively and the duty cycle is decreased. Further, the total power generation is reduced from 5.8kW to 4.4kW due to a decrease in wind speed from 15m/s to 12m/s. Fig. 5.18(b) depicts that during the variation in solar irradiance at t=2.7s, the CPI voltage shows a slight deflection of 0.01s, and then the controller manages the CPI voltage. The CPI current and compensator current are increased during the intermittency of wind speed and solar radiation. Further, the VSI continuously provides power support during the change in wind/solar irradiance with the help of a dc-link connected BSS. Moreover, the controller manages the frequency and dc-link voltage of the renewable energy based system.
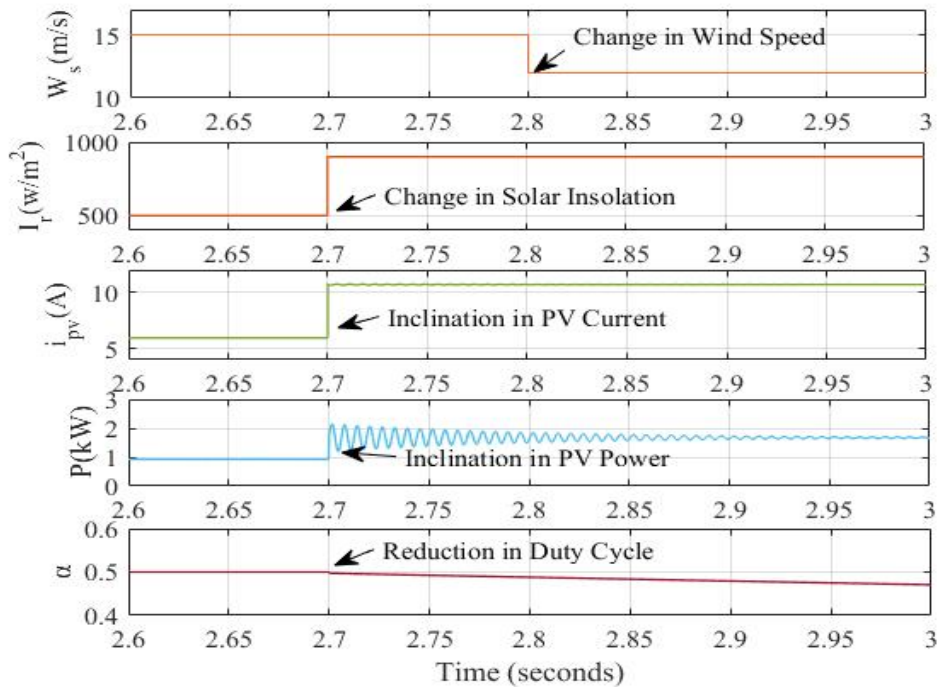
(a)
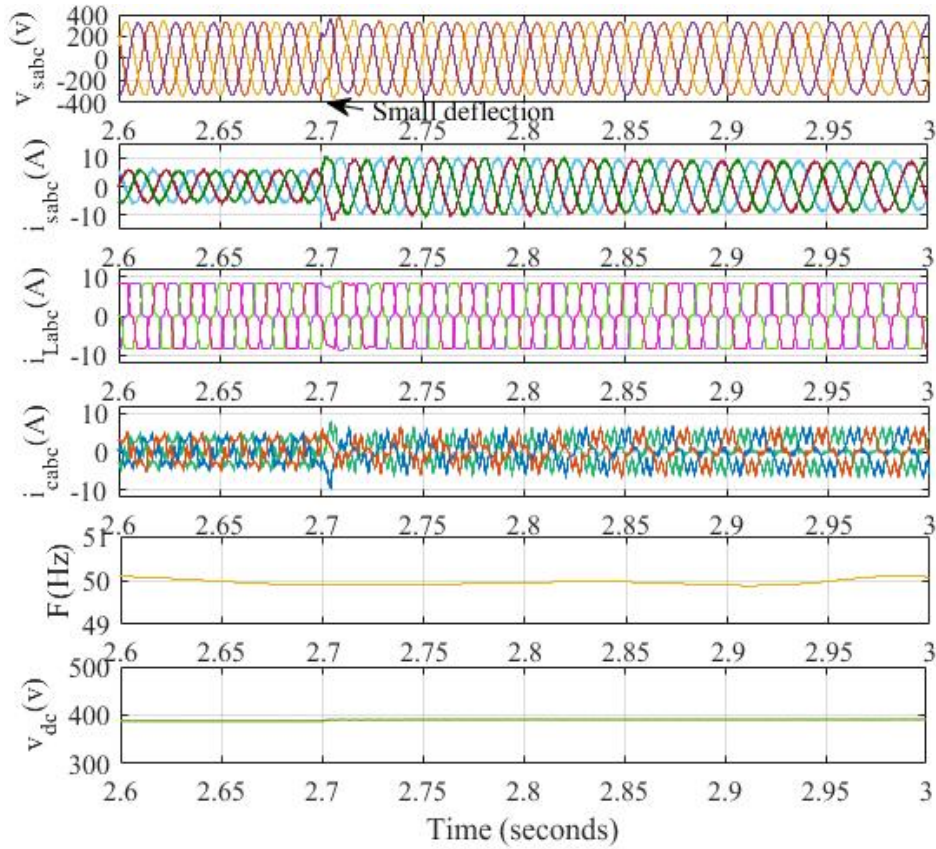
(b)

Fig. 5.18(a) and (b) Dynamic response of renewable energy based system under intermittency

5.4.1.3 BSS Response during Intermittency

The transient response of BSS under various operating conditions is depicted in Fig. 5.19. The BSS response is analyzed (i) Fixed solar irradiance/wind speed feeding balanced nonlinear load (ii) Solar irradiance/constant wind speed under uncertain conditions of nonlinear load (iii) Change in wind speed and fixed solar irradiance feeding balanced load (iv) Change in solar irradiance and constant wind speed feeding balanced load. During the elimination of a load of phase 'b', the excess power is transferred to the BSS. The BSS is shifted to the charging mode and the BSS current is improved due to the removal of load. During the abrupt change in wind speed 15m/s to 12m/s, the BSS charging current is reduced. Also, during the reduction in solar irradiance 900w/m^2 to 500w/m^2 at t=2.8s, The BSS is switched to draining mode and delivers power to CPI through VSI. The designed controller successfully balances all standalone system parameters under all operating situations.
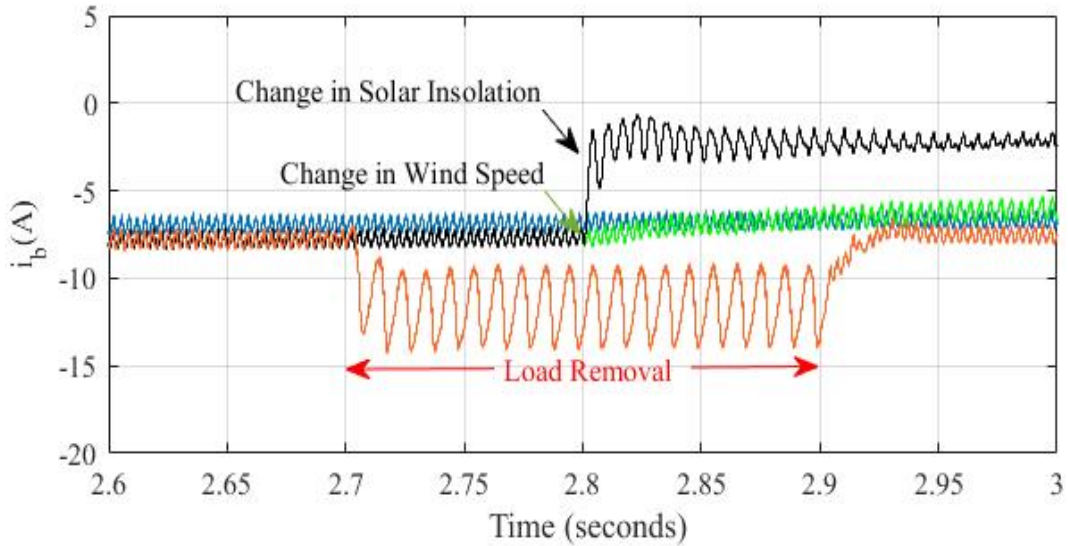
Fig. 5.19 BSS response during intermittency

5.4.1.4 Harmonic Profiles of Standalone System

Fig. 5.20(a) and (b) represents harmonic profiles of the source current and load current of the proposed renewable based standalone system. The THD's of source current and load current of phase 'a' is 4.54% and 26.01%, respectively. The harmonic analysis of the 3P4W standalone system is analyzed under uncertain load conditions. The THD's of the standalone system is found in limit and follow the IEEE-514-2014 standard.

(a)   (b)
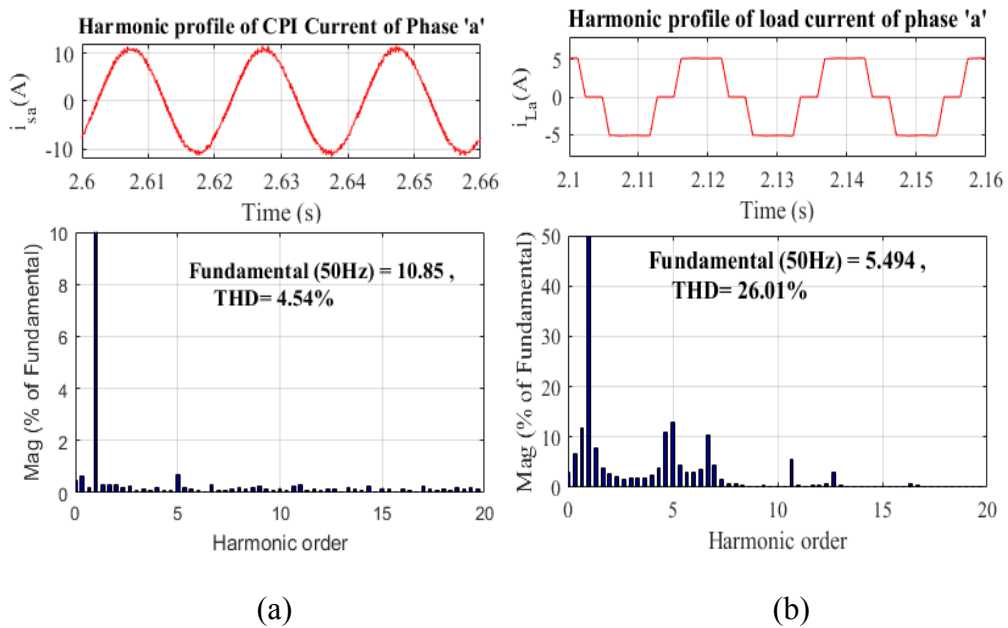
Fig. 5.20(a) and (b) Harmonic profiles of a standalone system

5.5 Summary

In this chapter, DROGI-FLL, DTOGI-PLL, ADF-FLL, DSOGI-PLL-based control algorithms have been designed and applied for operation and control of the 3P4W wind-solar-BSS-based islanded hybrid system. The performance of all the above-said algorithms is carried out in Simulink/MATLAB. The above-said control approaches successfully extract the fundamental component from nonlinear and unbalanced load current and give a fast dynamic response with reduced oscillations compared with other conventional algorithms. The experimental performance of DTOGI-PLL has also been added in this section. The performance approves the proposed control algorithms with VSC provides power compensation (active/reactive), harmonics abatement, load leveling, voltage & frequency stabilization, and improves overall PQ of the islanded system under load perturbation and dynamic environments of wind & solar. The MPPT control-based PV system with BSS is integrated at the DC-link of VSC and effectively provides power compensation through VSC during dynamic load demand and perturbation in wind & solar power.

Chapter 6

Comparative Performance Analysis of Different Control Algorithms of Wind-Solar-BES-Islanded Hybrid System

6.1 General

In this chapter, the comparative performance of the wind-solar-BES-based islanded hybrid system under various operational circumstances such as variation in wind speed, change in solar insolation, and varying load is discussed. In the proposed work different types of new control algorithms such as SOSF-FLL, VGC-IPLL, DTOGI-PLL, 3Ø-APF-PLL and ICCF-PLL have been implemented and their response is examined to that of conventional control algorithms. The comparative performances are devised in five categories is follows:

6.2 Case-I: Performance Comparison of SOSF-FLL Control with Existing Control Algorithms

The response of the proposed SOSF-FLL control versus conventional control algorithms under an unbalanced load is displayed in Fig. 6.1(a) and (b). Fig. 6.1(a) shows the load of phase 'a' is removed at t=2.7s. The proposed control in comparison of MLMS and SOGI-FLL control yields fast dynamic response and less dynamic oscillations with the reduced error of fundamental load current component (I_m) under load elimination. Fig. 6.1(b) depicts that during the insertion of load at t=2.9s, the proposed control yields a fast dynamic response and less steady oscillations under load perturbation.
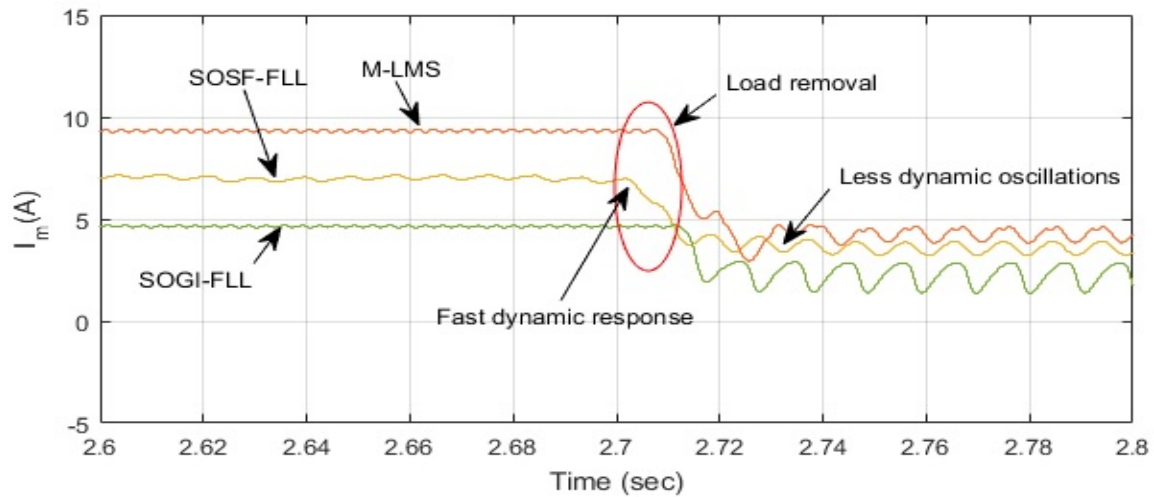
(a)
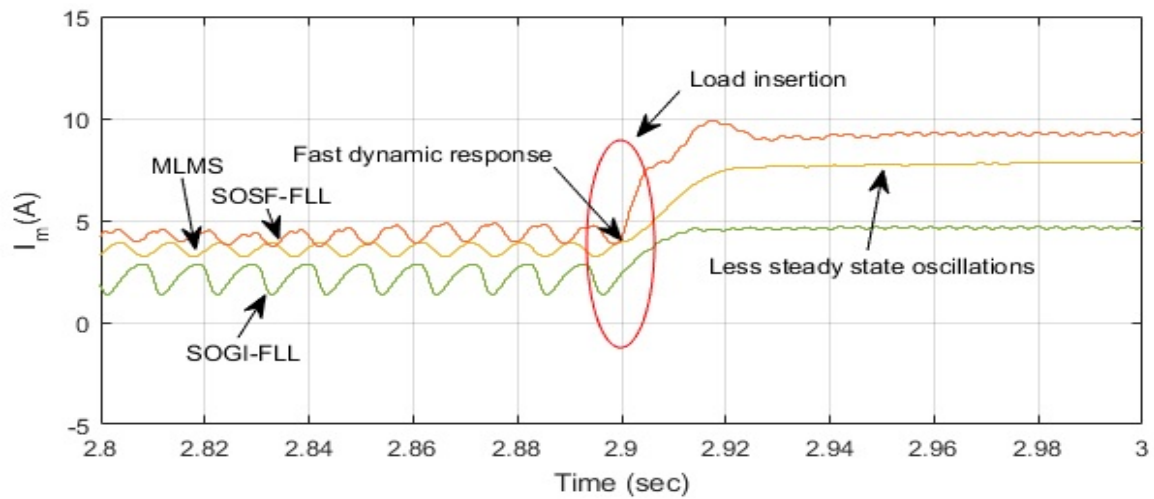
(b)

Fig. 6.1(a) and (b) Performance comparison of SOSF-FLL control with existing control
approaches under load perturbation

6.3 Case-II: Comparative Performance of VGC-IPLL Control with DSOGI-FLL and ILMS Control Approach

The comparative response of VGC-IPLL control over the conventional controls such as DSOGI-FLL, improved least mean square (ILMS) control is shown in Fig. 6.2. A fundamental current component (I_m) is extracted under load removal condition from t=2.6s to t=2.8s and variation in solar intensity level from 900w/m^2 to 500w/m^2 at t=2.7s. Under unbalanced load and changes in solar intensity, the proposed control provides a

quick dynamic response with low steady-state error. When the system is operated using the proposed VGC-IPLL control, the weight oscillation associated with the system is very less when compared to other existing controls. Table 6.1 compares the effectiveness of the VGC-IPLL control technique to conventional controls.
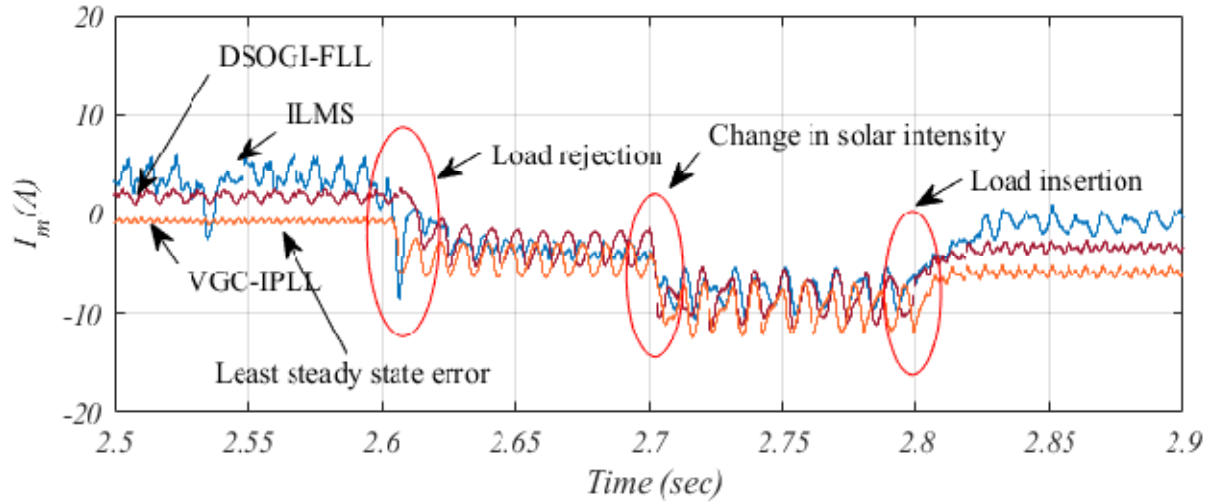
Fig. 6.2 Comparative performance

Table 6.1 performance comparison of VGC-IPLL control with DSOGI-FLL and ILMS control algorithm

S.No.	Operation		DSOGI-PLL	ILMS	VGC-IPLL
1	Stability		Better	Better	Best
2	Convergence rate		Medium	Medium	Fast
3	Static error		Medium	Large	Least
4	Oscillations		Medium	Medium	Least
	THD%	CPC Voltage	2.1%	2.4%	0.65%
		CPC Current	4.9%	5.1%	4.23%
		Load Current	29.94%	33.12%	24.94%

6.4 Case-III: Comparative Performance of 3Ø-APF-PLL, SOGI-FLL and LMS Control Algorithms

Fig. 6.3(a) and (b) compare the response of 3Ø-APF-PLL, SOGI-FLL, and LMS under an unbalanced load. The proposed method has the benefit of quick convergence, fast dynamic response, and fast BES charging response under varying load demands. Fig. 6.3(a) depicts the comparative simulation study of the extracted fundamental load current component. Under dynamic load circumstances, the 3Ø-APF-PLL control exhibits reduced

steady-state oscillations, quicker convergence, and dynamic responsiveness. The computation time of the 3Ø-APF-PLL-based control is one cycle under dynamic conditions. Fig. 6.3(b) compares the response of BES charging current for 3Ø-APF-PLL, SOGI-FLL, and LMS when the load of one phase is detached from t=3.2sec to t=3.4sec. During the removal of load, the 3Ø-APF-PLL control technique provides fast dynamic response and convergence. Table 6.2 given comparison of response of the 3Ø-APF-PLL, SOGI-FLL, and LMS control algorithms.
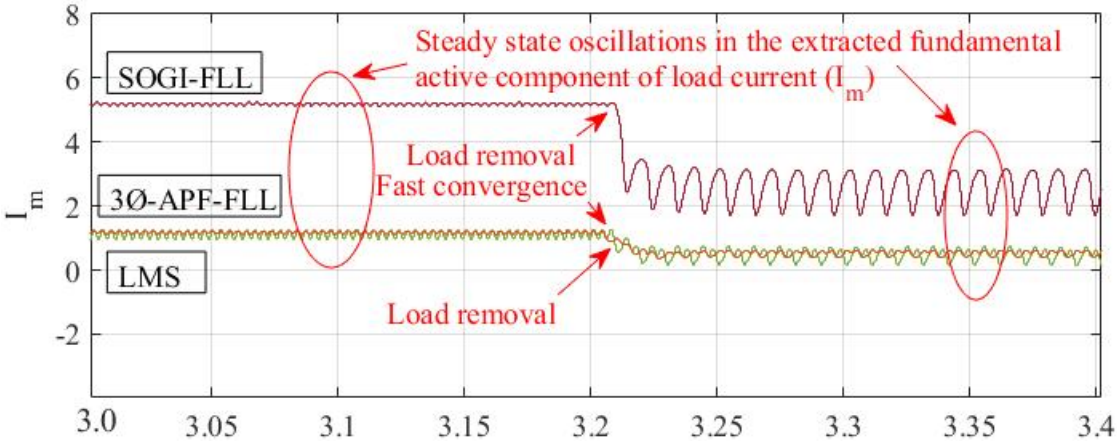
(a)
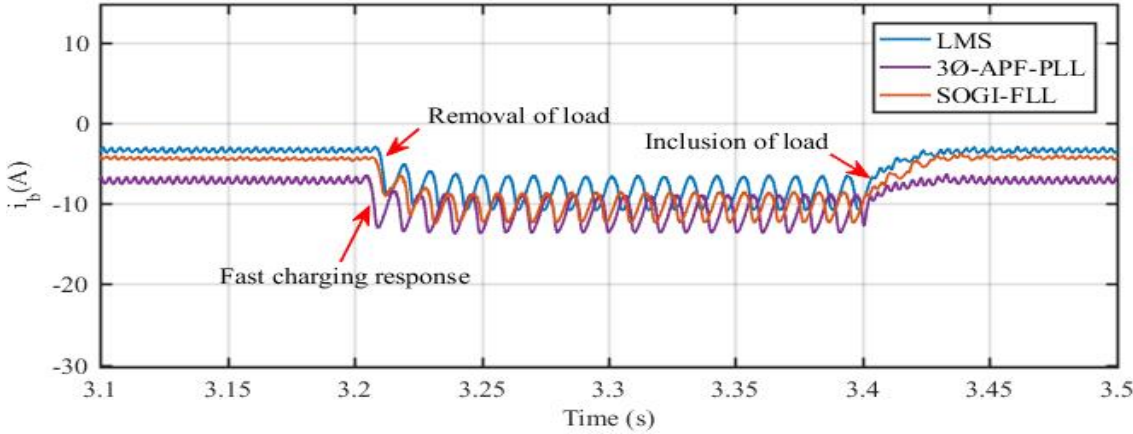
(b)

6.3(a) and (b) Comparison in the response of fundamental load current component (I_m) and (b) BES charging response for 3Ø-APF-PLL, SOGI-FLL and LMS under disconnection of a load of phase 'a'

Table 6.2 Comparative performances of 3Ø-APF-PLL, SOGI-FLL and LMS control algorithms

S.no	Parameters		3Ø-APF-PLL	SOGI-FLL	LMS
1	Computation time for fundamental extraction of load current component		One cycle	Three cycle	Three cycle
2	Steady-state oscillations		Less	Medium	High
3	Stability		Best	Good	Bad
4	Response		Fast	Medium	Medium
5	THD Obtained	PCI voltage	1.42%	2.85%	3.73%
		PCI current	4.32%	4.89%	5.19%
		Load current	25.06%	26.18%	24.79%

6.5   Case-IV: Comparative Assessment of ICCF-PLL Control with Existing Control Algorithms

The proposed ICCF-PLL control provides a fast dynamic response with reduced oscillations under the fitful condition of RESs and load dynamics. Fig. 6.4 depicts the load being rejected of phase 'r' at t=2.1s and injected at t=2.3s. When one phase of a partial load is temporally detached and applied, i.e., the extracted fundamental component must first acquire its appropriate value in comparison to the existing control. A frequency-adaptive ICCF-PLL control technique, on the other hand, gives an accurate computation of the fundamental component during dynamic situations. The TOGI-PLL and ILMS have substantial oscillations during load rejection and the dynamic response is excessively slow, while the reaction time is 0.02s longer in both cases (Load removal and injection). But, the ICCF-PLL response time is quite high and provides a fundamental load current component with less oscillation. Whereas, the ICCF-PLL-based control provides a fast dynamic response and the least steady error with reduced oscillations and extracts the fundamental load current component under different operating conditions.
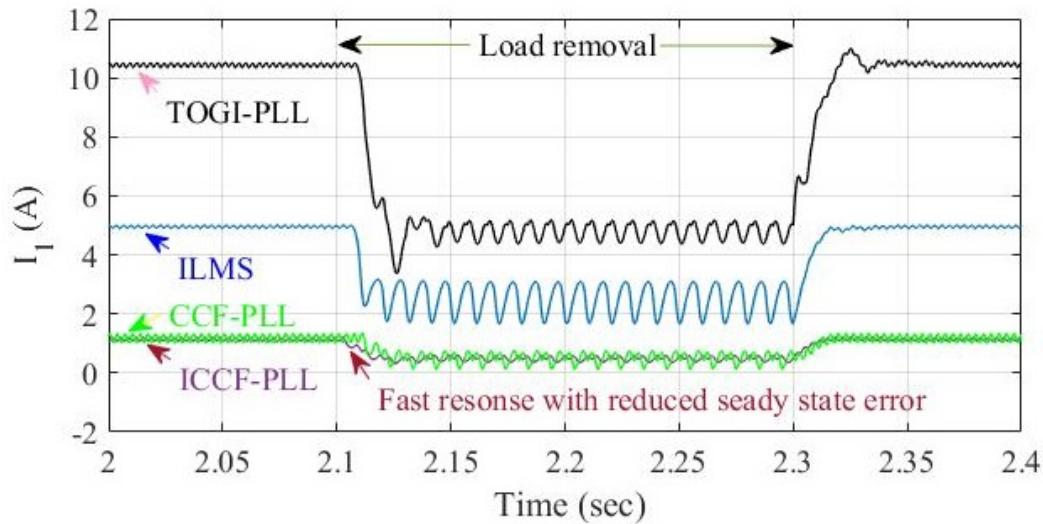
Fig. 6.4 Comparative assessment of ICCF-PLL control with conventional control algorithms

Table 6.3 Comparative performance of control algorithms

S.no.	Parameters	ICCF-PLL	CCF-PLL	ILMS	TOGI-PLL
1	Settling time	0.02	0.02	0.03	0.04
2	THD	4.17	4.6	4.66	4.8
3	obtained				
4	Stability	Best	Better	Good	Good
5	Static error	Very less	Less	Large	Medium
	Oscillations	Very less	Less	Large	Medium

Table 6.3 and Fig. 6.4 show the performance of the ICCF-PLL control approach with CCF-PLL, ILMS, and TOGI-PLL algorithms while extracting the maximum value of the fundamental component. The settling and rise time of the ICCF-PLL approach is less than one cycle after introducing load dynamics. Moreover, the proposed control has fewer oscillations with minimal error, the least harmonics, and the best stability while feeding the dynamic nonlinear load.

6.6 Case-V: Comparative Analysis of DTOGI-PLL, ADF-FLL, TOGI-FLL and LMS Control

Fig. 6.5 shows the simulation response of the microgrid for DTOGI-PLL, ADF-FLL, TOGI-PLL and LMS adaptive control approaches after introducing load dynamics. A load of

one phase is detached at t=2.7s to t=2.9s and the comparison of the fundamental current component (I_a) are presented. Moreover, it is observed that the DTOGI-PLL and ADF-FLL have the least oscillations with reduced steady-state error in comparison to traditional control approaches. The comparison also shows the DTOGI-PLL has a rapid response and the least settling time. The comparative analysis of DTOGI-PLL and ADF-FLL with the conventional existing control method TOGI-PLL and LMS control algorithm is illustrated in Table 6.4.

Table-6.4 Comparison analysis of DTOGI-PLL, ADF-FLL, TOGI-FLL and LMS under unbalanced nonlinear load

S.no.	Operation	DTOGI-PLL	ADF-FLL	TOGI-PLL	LMS
1	Convergence rate	Fast	Medium	Medium	Slow
2	Stability	Best	Better	Better	Worst
3	Static error	Less	Large	Large	Largest
4	THD (CPI Voltage)	0.69%	087%	1.20%	2.20%
	CPI current	4.14%	4.60%	4.90%	5.10%
	Load current	25.33%	26.45%	28.55%	31.40%
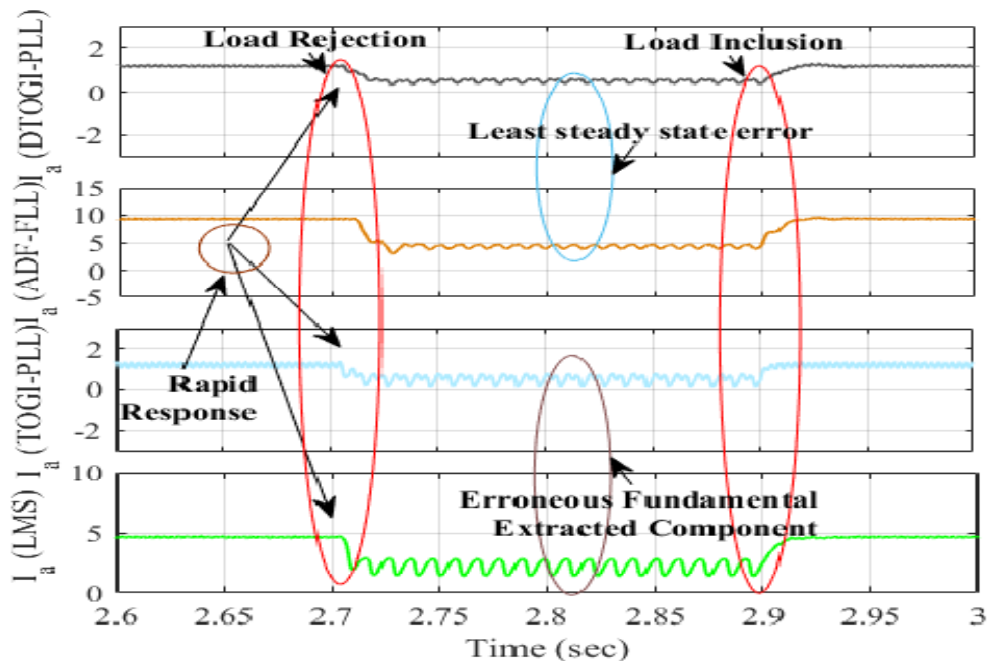
Fig. 6.5 Comparative performance of microgrid using DTOGI-PLL, ADF-FLL, TOGI-FLL and LMS algorithms after introducing load dynamics

6.7 Comparative Performance Analysis of Implemented Control Algorithms for 3P3W & 3P4W Wind-Solar-BES based Islanded Hybrid System

Table 6.5 shows the comparative performance analysis of implemented control algorithms for 3P3W & 3P4W wind-solar-BES based islanded hybrid system. The control algorithms have been examined under various operating circumstances such as variation in wind speed, solar irradiance and load perturbation. During the variation in wind speed and solar irradiance, the SOSF-FLL shows the best performance for both amplitude and frequency evaluation. The fundamental load current component estimated by VGC-IPLL shows the least steady-state error and faster convergence. During the unbalanced and nonlinear load condition, DSC-FLL, DTOGI-PLL and VGC-IPLL show the best performance as they filter out harmonic effectively. A DTOGI-PLL and ICCF-PLL shows the best performance as it has a faster response during dynamic conditions and least error during steady-state conditions.

Table-6.5 Comparative performance analysis of implemented control algorithms for 3P3W & 3P4W wind-solar-BES based islanded hybrid system

S. No.	Operation	DSC-FLL	SOSF-FLL	VGC-IPLL	3Ø-APF-PLL	ICCF-PLL	DROGI-FLL	DTOGI-PLL	ADF-FLL	DSOGI-PLL
1	Stability	Better	Better	Best	Best	Best	Better	Best	Best	Better
2	Convergence rate	Medium	Fast	Fast	Medium	Fast	Medium	Fast	Fast	Medium
3	Static-state error	Medium	Medium	Least	Least	Least	Medium	Least	Medium	Least
4	Oscillations	Medium	Medium	Least	Medium	Least	Medium	Least	Medium	Least
5	Source current THD%	4%	4.23%	4.23%	4.32%	4.60%	4.60%	4.14%	4.60%	4.54%

6.8 Summary

In this chapter, comparative performance of control techniques has been presented for both 3P3W and 3P4W wind-solar-BES-based microgrid system for standalone applications. The control techniques have been examined under different operational circumstances such as changes in wind speed, solar irradiance and unbalanced nonlinear load. During the change in wind speed and solar irradiance, the SOSF-FLL shows the best performance for both amplitude and frequency estimation. The frequency estimated by SOSF-FLL shows the least error and faster convergence. SOSF-FLL has an inherent frequency-locked loop hence it estimates frequency precisely. During the unbalanced and nonlinear load condition, DTOGI-PLL and ICCF-PLL show the best performance as they filter out harmonic effectively. A 3Ø-APF-PLL shows the best performance as it has a faster response during dynamic conditions and minimal error during steady-state conditions.

Chapter 7

Main Conclusions and Future Scope of Work

7.1 Main Conclusions

The primary goal of this thesis work is to provide voltage & frequency regulation, harmonics abatement, load leveling, power compensation, and improvement in PQ of islanded wind-solar-BES based hybrid system feeding non-linear loads. These goals are achieved by designing the wind-solar-BES energy supported with VSC, operating with proposed control algorithms.

- The control algorithms require synchronization techniques, and to compute fundamental component from the distorted load current under dynamic conditions of wind, solar and nonlinear load.
- An MPPT technique-based PV system with BES is integrated at the DC-link of the VSC to support the standalone system.
- A BDC controller is utilized to manage the charging & draining of the BES.
- A comparative performance analysis is also carried out between the advanced control algorithms used in the present work & conventional control techniques of PQ improvements.
- The developed experimental test set-up and simulation results show the effectiveness of control approaches and islanded hybrid system under various operational circumstances.

7.2 Future Scope of Work

The development, control and analysis of the wind-solar-BES-based isolated system have been demonstrated in this work. Some conventional and new synchronization algorithm has been designed to work in adverse operating conditions. More work is still required to develop

new synchronization techniques, especially under dynamic conditions of renewable energy sources. Mathematical stability analysis could also be done for the stable operation of the synchronization techniques under dynamic conditions of load and renewable energy sources.

Conventional IC and P&O MPPT methods has been employed to achieve maximal power from the SPV in the islanded system for the fixed or changing irradiance conditions. New techniques should be developed for varying irradiance and partial shading conditions. These days PV is widely used for electricity generation. In this thesis work DC-offset component of load current has not been analyzed and if such component available should be mitigated. The operation of solar-wind-BES based renewable energy system can be examined for electrical vehicle battery charging in remote areas for standalone applications.

Appendix

Appendix: Rating of Machines and Parameters of Solar-Wind-BES Hybrid System

S.No.	Quantity	Parameters
1	SEIG and filtering inductors	3-Phase, 400 V, 3.7 kW, 4-Poles, 50 Hz and star connected. R_s =1.405 Ω, L_s =0.0078 H, R_r =1.39, L_r = 0.0078 H, Inertia = 0.138, Friction factor = 0, Pole Pairs = 2 and L_f = 5mH.
2	PV system	$V_{pv} = 2.9kW, V_{pv} = 252.32V, i_{pv} = 11.69A$
3	Battery Energy Storage	400V, 7.5Ah
4	Nonlinear load	R=22Ω and L=200µH with 3-phase diode rectifier
5	Hardware parameters	$V_{LL} = 110V$, 50Hz, $V_{dc} = 200V$, $k_p = 0.2, k_i = 0.01$, Nonlinear load: R=4KΩ and L=100mH with 3-phase diode rectifier

List of Publications

Details of Publications in SCI/SCIE Journals

1) Sombir Kundu, Madhusudan Singh & Ashutosh K. Giri, "Control Algorithm for Coordinated Operation of Wind-Solar Microgrid Standalone Generation System", 2022, Taylor & Francis, Energy Sources, Part A: Recovery, Utilization, and Environmental Effects, 44:4, 1002410044, DOI: 10.1080/15567036.2022.2143943.

2) Sombir Kundu, Madhusudan Singh & Ashutosh K. Giri , "Implementation of Variable Gain Controller based Improved Phase Locked Loop Approach to Enhance Power Quality in Autonomous Microgrid", 2022, John Wiley & Sons Ltd., ISSN: 1099-1204, doi: 10.1002/JNM3082.

3) Sombir Kundu, Madhusudan Singh, and Ashutosh K Giri, "Adaptive Control Approach based Isolated Microgrid System with Alleviating Power Quality Problems",2023, Taylor & Francis, Electric Power Components and Systems, 0(0); 1-16, ISSN: 1532-5008, doi: 10.1080/15325008.2023.2239222.

4) Sombir Kundu, Madhusudan Singh, and Ashutosh K Giri, "SPV-Wind-BES based Islanded Electrical Supply System for Remote Applications with Power Quality Enhancement" Electrical Engineering, Springer, doi: 10.1007/s00202-023-01979-0.

5) Sombir Kundu, Madhusudan Singh, Ashutosh K. Giri, "Synchronization and control of WECS-SPV-BSS-based distributed generation system using ICCF-PLL control approach", Electric Power Systems Research, Volume 226, 2024, 109919, ISSN 0378-7796, https://doi.org/10.1016/j.epsr.2023.109919.

Details of Communicated Papers in SCI/SCIE/ESCI Journals

1) Sombir Kundu, Madhusudan Singh, Ashutosh K Giri, Sunil Kadiyan, Prakash Chittora and Divyansh Shailly, "Robust and Fast Control Approach for Islanded Microgrid System and EV Charging Station Applications" Electrical Engineering, Springer (***Under minor revision***).

2) Sombir Kundu, Madhusudan Singh and Ashutosh K Giri, "Adaptive Control of Standalone Renewable Energy Based Generation System with Intermittency" International Journal of Ambient Energy *(Under review).*

3) Sombir Kundu, Madhusudan Singh, and Ashutosh K Giri, "Experimental Investigation of an Adaptive Generalized Maximum Versoria Criterion Control Approach for a Three-Phase Standalone Wind-SolarPV-ESS-based Microgrid System", IEEE Transaction on Power Electronics (*Under review*).

Details of Publications in International Conferences

1) S. Sombir and M. Singh, "Voltage and Frequency Control of Self Excited Induction Generator Integrated with PV System," IECON 2020 The 46th Annual Conference of the IEEE Industrial Electronics Society, 2020, pp. 4306-4311, doi: 10.1109/IECON43393.2020.9254608.

2) Kundu, S., Singh, M., Giri, A.K., "Design and Control of a Standalone Wind–Solar System with SEIG Feeding Linear/Nonlinear Loads" In: Mohapatro, S., Kimball, J. (eds) Proceedings of Symposium on Power Electronic and Renewable Energy Systems Control. Lecture Notes in Electrical Engineering, 2021, vol 616. Springer, Singapore. https://doi.org/10.1007/978-981-16-1978-6_28.

3) Sombir, M. Singh and A. K. Giri, "Implementation of In-loop Filter based DSC-FLL Control Approach for Power Quality Improvement in Isolated Microgrid," 2022 IEEE 31st International Symposium on Industrial Electronics (ISIE), 2022, pp. 516-521, doi: 10.1109/ISIE51582.2022.9831712.

Details of Publications in Book Chapter

1) Sombir, Madhusudan Singh, Ashutosh K Giri, Sabha Raj Arya, "DROGI-FLL-Based Control Algorithm for Coordinated Operation of 3P4W Wind/Solar Hybrid System" Distributed Energy Systems: Design, Modeling, and Control (1st ed.). CRC Press. (2022), DOI: 10.1201/9781003229124.

References

[1] M. A. Mat Daut, M. Y. Hassan, H. Abdullah, H. A. Rahman, M. P. Abdullah, and F. Hussin, "Building electrical energy consumption forecasting analysis using conventional and artificial intelligence methods: A review," *Renew. Sustain. Energy Rev.*, vol. 70, no. September, pp. 1108–1118, 2017, doi: 10.1016/j.rser.2016.12.015.

[2] R. E. H. Sims, H. H. Rogner, and K. Gregory, "Carbon emission and mitigation cost comparisons between fossil fuel, nuclear and renewable energy resources for electricity generation," *Energy Policy*, vol. 31, no. 13, pp. 1315–1326, 2003, doi: 10.1016/S0301-4215(02)00192-1.

[3] F. H. Jufri, D. R. Aryani, I. Garniwa, and B. Sudiarto, "Optimal battery energy storage dispatch strategy for small scale isolated hybrid renewable energy system with different load profile patterns," *Energies*, vol. 14, no. 11, 2021, doi: 10.3390/en14113139.

[4] F. Sorgulu and I. Dincer, "A renewable source based hydrogen energy system for residential applications," *Int. J. Hydrogen Energy*, vol. 43, no. 11, pp. 5842–5851, 2018, doi: 10.1016/j.ijhydene.2017.10.101.

[5] A. K. Giri, S. R. Arya, and R. Maurya, "Compensation of Power Quality Problems in Wind-Based Renewable Energy System for Small Consumer as Isolated Loads," *IEEE Trans. Ind. Electron.*, vol. 66, no. 11, pp. 9023–9031, Nov. 2019, doi: 10.1109/TIE.2018.2873515.

[6] G. K. Singh, "Self-excited induction generator research - A survey," *Electr. Power Syst. Res.*, vol. 69, no. 2–3, pp. 107–114, 2004, doi: 10.1016/j.epsr.2003.08.004.

[7] S. K. Tiwari, B. Singh, and P. K. Goel, "Design and Control of Autonomous Wind-Solar System with DFIG Feeding 3-Phase 4-Wire Loads," *IEEE Trans. Ind. Appl.*, vol. 54, no. 2, pp. 1119–1127, 2018, doi: 10.1109/TIA.2017.2780168.

[8] R. E. Raj, C. Kamalakannan, and R. Karthigaivel, "Genetic algorithm-based analysis of wind-driven parallel operated self-excited induction generators supplying isolated loads," *IET Renew. Power Gener.*, vol. 12, no. 4, pp. 472–483, 2018, doi: 10.1049/iet-rpg.2017.0449.

[9]   A. Parida and D. Chatterjee, "Model-based loss minimisation scheme for wind solar hybrid generation system using (grid-connected) doubly fed induction generator," *IET Electr. Power Appl.*, vol. 10, no. 6, pp. 548–559, 2016, doi: 10.1049/iet-epa.2016.0040.

[10]   S. Kewat and B. Singh, "Grid Synchronization of WEC-PV-BES Based," vol. 56, no. 6, pp. 7088–7098, 2020.

[11]   R. W. Mosobi, T. Chichi, and S. Gao, "Power quality analysis of hybrid renewable energy system," *Cogent Eng.*, vol. 2, no. 1, pp. 1–15, 2015, doi: 10.1080/23311916.2015.1005000.

[12]   A. Tuan, V. V. Pham, and X. Phuong, "Integrating renewable sources into energy system for smart city as a sagacious strategy towards clean and sustainable process," *J. Clean. Prod.*, vol. 305, p. 127161, 2021, doi: 10.1016/j.jclepro.2021.127161.

[13]   P. A. Owusu and S. Asumadu-Sarkodie, "A review of renewable energy sources, sustainability issues and climate change mitigation," *Cogent Eng.*, vol. 3, no. 1, pp. 1–14, 2016, doi: 10.1080/23311916.2016.1167990.

[14]   S. Kewat, B. Singh, and I. Hussain, "Power management in PV-battery-hydro based standalone microgrid," *IET Renew. Power Gener.*, vol. 12, no. 4, pp. 391–398, 2018, doi: 10.1049/iet-rpg.2017.0566.

[15]   R. S. Sreeleksmi, A. Ashok, and M. G. Nair, "A fuzzy logic controller for energy management in a PV-Battery based microgrid system," *Proc. 2017 IEEE Int. Conf. Technol. Adv. Power Energy Explor. Energy Solut. an Intell. Power Grid, TAP Energy 2017*, pp. 1–6, 2018, doi: 10.1109/TAPENERGY.2017.8397282.

[16]   N. Karami, N. Moubayed, and R. Outbib, "General review and classification of different MPPT Techniques," *Renew. Sustain. Energy Rev.*, vol. 68, no. July 2015, pp. 1–18, 2017, doi: 10.1016/j.rser.2016.09.132.

[17]   S. K. Kollimalla and M. K. Mishra, "Variable perturbation size adaptive P&O MPPT algorithm for sudden changes in irradiance," *IEEE Trans. Sustain. Energy*, vol. 5, no. 3, pp. 718–728, 2014, doi: 10.1109/TSTE.2014.2300162.

[18]   K. S. Rajesh, S. S. Dash, R. Rajagopal, and R. Sridhar, "A review on control of ac microgrid," *Renew. Sustain. Energy Rev.*, vol. 71, no. December, pp. 814–819, 2017, doi: 10.1016/j.rser.2016.12.106.

[19]   A. Nicastri and A. Nagliero, "Comparison and evaluation of the PLL techniques for the

design of the grid-connected inverter systems," *IEEE Int. Symp. Ind. Electron.*, pp. 3865–3870, 2010, doi: 10.1109/ISIE.2010.5637778.

[20] K. R. Patil and H. H. Patel, "Modified dual second-order generalised integrator FLL for synchronization of a distributed generator to a weak grid," *EEEIC 2016 - Int. Conf. Environ. Electr. Eng.*, 2016, doi: 10.1109/EEEIC.2016.7555824.

[21] F. Chishti, S. Murshid, and B. Singh, "Development of Wind and Solar Based AC Microgrid with Power Quality Improvement for Local Nonlinear Load Using MLMS," *IEEE Trans. Ind. Appl.*, vol. 55, no. 6, pp. 7134–7145, 2019, doi: 10.1109/TIA.2019.2923575.

[22] C. Pazhanimuthu, I. Baranilingesan, and A. Karthick, "An improved control algorithm for Series Hybrid Active Power Filter based on SOGI-PLL under dynamic load conditions," *Solid State Commun.*, vol. 333, no. March, p. 114357, 2021, doi: 10.1016/j.ssc.2021.114357.

[23] M. Ramezani, S. Golestan, S. Li, and J. M. Guerrero, "A Simple Approach to Enhance the Performance of Complex-Coefficient Filter-Based PLL in Grid-Connected Applications," *IEEE Trans. Ind. Electron.*, vol. 65, no. 6, pp. 5081–5085, 2018, doi: 10.1109/TIE.2017.2772164.

[24] A. Ranjan, S. Kewat, and B. Singh, "DSOGI-PLL with In-Loop Filter Based Solar Grid Interfaced System for Alleviating Power Quality Problems," *IEEE Trans. Ind. Appl.*, vol. 57, no. 1, pp. 730–740, 2021, doi: 10.1109/TIA.2020.3029125.

[25] S. Golestan, "A Study On Three-Phase FLLs," Transactions on Power Electronics vol. 8993, no. c, 2018, doi: 10.1109/TPEL.2018.2826068.

[26] S. Golestan, J. M. Guerrero, and J. C. Vasquez, "Single-phase PLLs: A review of recent advances," *IEEE Trans. Power Electron.*, vol. 32, no. 12, pp. 9013–9030, 2017, doi: 10.1109/TPEL.2017.2653861.

[27] J. Philip, "Control and Implementation of a Standalone Solar Photovoltaic Hybrid System," *IEEE Trans. Ind. Appl.*, vol. 52, no. 4, pp. 3472–3479, 2016, doi: 10.1109/TIA.2016.2553639.

[28] B. Singh, A. Adya, A. P. Mittal, and J. R. P. Gupta, "Modeling and control of DSTATCOM for three-phase, four-wire distribution systems," *Conf. Rec. - IAS Annu. Meet. (IEEE Ind. Appl. Soc.*, vol. 4, pp. 2428–2434, 2005, doi:

10.1109/IAS.2005.1518801.

[29] B. Singh, D. T. Shahani, and A. K. Verma, "Power balance theory based control of grid interfaced solar photovoltaic power generating system with improved power quality," *PEDES 2012 - IEEE Int. Conf. Power Electron. Drives Energy Syst.*, 2012, doi: 10.1109/PEDES.2012.6484359.

[30] L. Zhang, R. Norman, and W. Shepherd, "Long-range predictive control of current regulated PWM for induction motor drives using the synchronous reference frame," *IEEE Trans. Control Syst. Technol.*, vol. 5, no. 1, pp. 119–126, 1997, doi: 10.1109/87.553670.

[31] J. Yu, W. Shi, J. Li, L. Deng, and M. Pei, "A Discrete-Time Non-Adaptive SOGI-Based Frequency-Locked Loop," *IEEE Trans. Power Syst.*, vol. 35, no. 6, pp. 4912–4915, 2020, doi: 10.1109/TPWRS.2020.3018625.

[32] B. Singh, S. Member, and J. Solanki, "A Comparison of Control Algorithms for DSTATCOM," vol. 56, no. 7, pp. 2738–2745, 2009.

[33] A. Parida and B. Subudhi, "Modified leaky LMS-based control strategy for reliable operation of single-stage three-phase grid-tied PV system," *IET Renew. Power Gener.*, vol. 14, no. 9, pp. 1453–1462, 2020, doi: 10.1049/iet-rpg.2019.0776.

[34] S. Kewat and B. Singh, "Modified amplitude adaptive control algorithm for power quality improvement in multiple distributed generation system," *IET Power Electron.*, vol. 12, no. 9, pp. 2321–2329, 2019, doi: 10.1049/iet-pel.2018.5936.

[35] S. Pradhan, B. Singh, B. K. Panigrahi, and S. Murshid, "A composite sliding mode controller for wind power extraction in remotely located solar PV-wind hybrid system," *IEEE Trans. Ind. Electron.*, vol. 66, no. 7, pp. 5321–5331, 2019, doi: 10.1109/TIE.2018.2868009.

[36] S. A. Mohamed, M. Abd, and E. Sattar, "A comparative study of P & O and INC maximum power point tracking techniques for grid connected PV systems," *SN Appl. Sci.*, vol. 1, no. 2, pp. 1–13, 2019, doi: 10.1007/s42452-018-0134-4.

[37] E. Masero, M. Francisco, J. M. Maestre, S. Revollar, and P. Vega, "Hierarchical distributed model predictive control based on fuzzy negotiation," *Expert Syst. Appl.*, vol. 176, no. February 2020, 2021, doi: 10.1016/j.eswa.2021.114836.

[38] G. Pathak, B. Singh, and B. K. Panigrahi, "Wind-hydro microgrid and its control for

rural energy system," *IEEE Trans. Ind. Appl.*, vol. 55, no. 3, pp. 3037–3045, 2019, doi: 10.1109/TIA.2019.2897659.

[39] F. Chishti, S. Murshid, and B. Singh, "LMMN-Based Adaptive Control for Power Quality Improvement of Grid Intertie Wind–PV System," *IEEE Trans. Ind. Informatics*, vol. 15, no. 9, pp. 4900–4912, 2019, doi: 10.1109/tii.2019.2897165.

[40] R. C. Bansal, "Three-phase self-excited induction generators: An overview," *IEEE Trans. Energy Convers.*, vol. 20, no. 2, pp. 292–299, 2005, doi: 10.1109/TEC.2004.842395.

[41] S. S. Murthy, G. Bhuvaneswari, S. Gao, and R. K. Ahuja, "Self excited induction generator for renewable energy applications to supply single-phase loads in remote locations," *2010 IEEE Int. Conf. Sustain. Energy Technol. ICSET 2010*, 2010, doi: 10.1109/ICSET.2010.5684947.

[42] G. Raina and O. P. Malik, "Wind energy conversion using a self-excited induction generator," *IEEE Trans. Power Appar. Syst.*, vol. PAS-102, no. 12, pp. 3933–3936, 1983, doi: 10.1109/TPAS.1983.317933.

[43] N. H. Malik and A. A. Mazi, "Capacitance Requirements for Isolated Self Excited Induction Generators.," *IEEE Trans. Energy Convers.*, vol. EC-2, no. 1, pp. 62–69, 1987, doi: 10.1109/TEC.1987.4765805.

[44] D. Joshi, K. S. Sandhu, and R. C. Bansal, "Steady-state analysis of self-excited induction generators using genetic algorithm approach under different operating modes," *Int. J. Sustain. Energy*, vol. 32, no. 4, pp. 244–258, 2013, doi: 10.1080/14786451.2011.622763.

[45] K. Arthishri, K. Anusha, N. Kumaresan, and S. Senthil Kumar, "Simplified methods for the analysis of self-excited induction generators," *IET Electr. Power Appl.*, vol. 11, no. 9, pp. 1636–1644, 2017, doi: 10.1049/iet-epa.2017.0282.

[46] T. S. I. Generator, a K. Tandon, and S. Member, "Transient Performance of Series-Compensated Feeding Dynamic Loads," *IEEE Trans. Ind. Appl.*, vol. 46, no. 4, pp. 1271–1280, 2010.

[47] Y. K. Chauhan, S. K. Jain, and B. Singh, "A prospective on voltage regulation of self-excited induction generators for industry applications," *IEEE Trans. Ind. Appl.*, vol. 46, no. 2, pp. 720–730, 2010, doi: 10.1109/TIA.2009.2039984.

[48] M. Benghanem, A. M. Bouzid, M. Bouhamida, and A. Draou, "Voltage control of an isolated self-excited induction generator using static synchronous compensator," *J. Renew. Sustain. Energy*, vol. 5, no. 4, 2013, doi: 10.1063/1.4816494.

[49] B. Singh, S. S. Murthy, and S. Gupta, "An Improved Electronic Load Controller for Self-Excited Induction Generator in Micro-Hydel Applications," *IECON Proc. (Industrial Electron. Conf.*, vol. 3, pp. 2741–2746, 2003, doi: 10.1109/IECON.2003.1280681.

[50] E. Muljadi, J. Sallan, M. Sanz, and C. P. Butterfield, "Investigation of self-excited induction generators for wind turbine applications," *Conf. Rec. - IAS Annu. Meet. (IEEE Ind. Appl. Soc.*, vol. 1, pp. 509–515, 1999, doi: 10.1109/ias.1999.800001.

[51] S. A. Deraz and F. E. Abdel Kader, "A new control strategy for a stand-alone self-excited induction generator driven by a variable speed wind turbine," *Renew. Energy*, vol. 51, pp. 263–273, 2013, doi: 10.1016/j.renene.2012.09.010.

[52] B. Singh, S. S. Murthy, and S. Gupta, "Transient analysis of self-excited induction generator with electronic load controller (ELC) supplying static and dynamic loads," *Proc. Int. Conf. Power Electron. Drive Syst.*, vol. 1, no. 5, pp. 771–776, 2003, doi: 10.1109/PEDS.2003.1283000.

[53] B. Sawetsakulanond and V. Kinnares, "Investigation on the Behavior and Harmonic Voltage Distortion of Terminal Voltage Regulation by Static Var Compensators for a Three Phase Self-Exited Induction Generator," pp. 483–488, 2008.

[54] L. A. C. Lopes and R. G. Almeida, "Wind-driven self-excited induction generator with voltage and frequency regulated by a reduced-rating voltage source inverter," *IEEE Trans. Energy Convers.*, vol. 21, no. 2, pp. 297–304, 2006, doi: 10.1109/TEC.2006.874244.

[55] S. C. Tripathy, M. Kalantar, and N. D. Rao, "Wind turbine driven self-excited induction generator," *Energy Convers. Manag.*, vol. 34, no. 8, pp. 641–648, 1993, doi: 10.1016/0196-8904(93)90098-U.

[56] L. Wang and J. Y. Su, "Dynamic performances of an isolated self-excited induction generator under various loading conditions," *IEEE Power Eng. Rev.*, vol. 17, no. 12, p. 56, 1997.

[57] L. Wang and S. C. Kuo, "Steady state performance of a self-excited induction

generator under unbalanced load," *Proc. IEEE Power Eng. Soc. Transm. Distrib. Conf.*, vol. 1, no. 1, pp. 408–412, 2002, doi: 10.1109/pesw.2002.985032.

[58] R. Chaturvedi, "Use of Conventioncil Induction Motor Cis Ci Wind Driven Self," pp. 2051–2055, 1989.

[59] H. Geng, D. Xu, B. Wu, and W. Huang, "Direct voltage control for a stand-alone wind-driven self-excited induction generator with improved power quality," *IEEE Trans. Power Electron.*, vol. 26, no. 8, pp. 2358–2368, 2011, doi: 10.1109/TPEL.2010.2104329.

[60] L. Wang and C. H. Lee, "Long-shunt and short-shunt connections on dynamic performance of a SEIG feeding an induction motor load," *IEEE Trans. Energy Convers.*, vol. 15, no. 1, pp. 1–7, 2000, doi: 10.1109/60.849108.

[61] S. S. Murthy, B. Singh, S. Gupta, and B. M. Gulati, "General steady-state analysis of three-phase self-excited induction generator feeding three-phase unbalanced load/single-phase load for stand-alone applications," *IEE Proc. Gener. Transm. Distrib.*, vol. 150, no. 1, pp. 49–55, 2003, doi: 10.1049/ip-gtd:20030072.

[62] T. R. Ayodele, A. S. O. Ogunjuyigbe, and B. B. Adetokun, "Optimal capacitance selection for a wind-driven self-excited reluctance generator under varying wind speed and load conditions," *Appl. Energy*, vol. 190, pp. 339–353, 2017, doi: 10.1016/j.apenergy.2016.12.137.

[63] J. DALEI and K. B. MOHANTY, "Performance improvement of three-phase self-excited induction generator feeding induction motor load," *Turkish J. Electr. Eng. Comput. Sci.*, vol. 23, pp. 1660–1672, 2015, doi: 10.3906/elk-1404-191.

[64] T. M. Masaud and P. K. Sen, "Modeling and analysis of self-excited induction generator for wind energy conversion," *2015 IEEE Power Energy Soc. Innov. Smart Grid Technol. Conf. ISGT 2015*, pp. 1–5, 2015, doi: 10.1109/ISGT.2015.7131901.

[65] B. Abdelhamid, M. Taoufik, and S. Lassad, "Shunt and short shunt compensation for induction machine generator," pp. 392–396, 2016.

[66] L. Wang and C. H. Lee, "Dynamic analyses of parallel operated self-excited induction generators feeding an induction motor load," *IEEE Trans. Energy Convers.*, vol. 14, no. 3, pp. 479–485, 1999, doi: 10.1109/60.790900.

[67] K. Natarajan, A. M. Sharaf, S. Sivakumar, and S. Naganathan, "Modeling and control

design for wind energy power conversion scheme using self-excited induction generator," *IEEE Trans. Energy Convers.*, vol. EC-2, no. 3, pp. 506–512, 1987, doi: 10.1109/TEC.1987.4765879.

[68] C. C. Yeh *et al.*, "Design of Special Protection System for an Offshore Island with High-PV Penetration," *IEEE Trans. Ind. Appl.*, vol. 53, no. 2, pp. 947–953, 2017, doi: 10.1109/TIA.2016.2627518.

[69] M. Jedari Zare Zadeh and S. H. Fathi, "A New Approach for Photovoltaic Arrays Modeling and Maximum Power Point Estimation in Real Operating Conditions," *IEEE Trans. Ind. Electron.*, vol. 64, no. 12, pp. 9334–9343, 2017, doi: 10.1109/TIE.2017.2711571.

[70] A. Dolara, S. Leva, and G. Manzolini, "Comparison of different physical models for PV power output prediction," *Sol. Energy*, vol. 119, pp. 83–99, 2015, doi: 10.1016/j.solener.2015.06.017.

[71] A. A. Desai and S. Mikkili, "Modelling and analysis of PV configurations (alternate TCT-BL, total cross tied, series, series parallel, bridge linked and honey comb) to extract maximum power under partial shading conditions," *CSEE J. Power Energy Syst.*, vol. PP, no. 99, pp. 1670–1683, 2019, doi: 10.17775/CSEEJPES.2020.00900.

[72] S. R. Pendem and S. Mikkili, "Modeling, simulation and performance analysis of solar PV array configurations (Series, Series–Parallel and Honey-Comb) to extract maximum power under Partial Shading Conditions," *Energy Reports*, vol. 4, pp. 274–287, 2018, doi: 10.1016/j.egyr.2018.03.003.

[73] S. N. Deshkar, S. B. Dhale, J. S. Mukherjee, T. S. Babu, and N. Rajasekar, "Solar PV array reconfiguration under partial shading conditions for maximum power extraction using genetic algorithm," *Renew. Sustain. Energy Rev.*, vol. 43, no. 2015, pp. 102–110, 2015, doi: 10.1016/j.rser.2014.10.098.

[74] M. A. Hasan and S. K. Parida, "An overview of solar photovoltaic panel modeling based on analytical and experimental viewpoint," *Renew. Sustain. Energy Rev.*, vol. 60, pp. 75–83, 2016, doi: 10.1016/j.rser.2016.01.087.

[75] R. Ahmad, A. F. Murtaza, and H. A. Sher, "Power tracking techniques for efficient operation of photovoltaic array in solar applications – A review," *Renew. Sustain. Energy Rev.*, vol. 101, no. November 2017, pp. 82–102, 2019, doi:

10.1016/j.rser.2018.10.015.

[76] K. Sundareswaran, V. Vigneshkumar, P. Sankar, S. P. Simon, P. Srinivasa Rao Nayak, and S. Palani, "Development of an Improved P&O Algorithm Assisted Through a Colony of Foraging Ants for MPPT in PV System," *IEEE Trans. Ind. Informatics*, vol. 12, no. 1, pp. 187–200, 2016, doi: 10.1109/TII.2015.2502428.

[77] B. N. Alajmi, K. H. Ahmed, S. J. Finney, and B. W. Williams, "Fuzzy-logic-control approach of a modified hill-climbing method for maximum power point in microgrid standalone photovoltaic system," *IEEE Trans. Power Electron.*, vol. 26, no. 4, pp. 1022–1030, 2011, doi: 10.1109/TPEL.2010.2090903.

[78] R. I. Putri, S. Wibowo, and M. Rifa, "Maximum power point tracking for photovoltaic using incremental conductance method," *Energy Procedia*, vol. 68, pp. 22–30, 2015, doi: 10.1016/j.egypro.2015.03.228.

[79] M. Seyedmahmoudian, "State of the art artificial intelligence-based MPPT techniques for mitigating partial shading effects on PV systems – A review," *Renew. Sustain. Energy Rev.*, vol. 64, pp. 435–455, 2016, doi: 10.1016/j.rser.2016.06.053.

[80] A. K. Pandey, V. V. Tyagi, J. A. Selvaraj, N. A. Rahim, and S. K. Tyagi, "Recent advances in solar photovoltaic systems for emerging trends and advanced applications," *Renew. Sustain. Energy Rev.*, vol. 53, pp. 859–884, 2016, doi: 10.1016/j.rser.2015.09.043.

[81] N. Beniwal, S. Member, I. Hussain, and B. Singh, "Implementation of DSTATCOM with i-PNLMS Based Control Algorithm under Abnormal Grid Conditions," *IEEE Trans. Ind. Appl.*, vol. PP, no. c, p. 1, 2018, doi: 10.1109/TIA.2018.2846739.

[82] S. Pati, S. kumar Kar, K. B. Mohanty, and D. Panda, "Voltage and Frequency Stabilization of a Micro Hydro –PV Based Hybrid Micro Grid using STATCOM Equipped with Battery Energy Storage System.," *IEEE Int. Conf. Power Electron. Drives Energy Syst. PEDES 2016*, vol. 2016-Janua, pp. 1–5, 2017, doi: 10.1109/PEDES.2016.7914481.

[83] A. Verma and B. Singh, "Energy Management Strategy of Solar PV-Battery and Diesel Generator Based Electric Vehicle Charging Station," *2018 IEEE Energy Convers. Congr. Expo. ECCE 2018*, pp. 1043–1050, 2018, doi: 10.1109/ECCE.2018.8557669.

[84] M. J. H. Moghaddam, "Improved voltage unbalance and harmonics compensation

control strategy for an isolated microgrid," *Energies*, vol. 11, no. 10, 2018, doi: 10.3390/en11102688.

[85] M. Abdul and K. Aziz, "Enhancement of Power Quality in Distribution System using D-Statcom," pp. 2093–2098, 2016.

[86] S. R. Arya, S. Member, B. Singh, and R. Niwas, "Power Quality Enhancement Using DSTATCOM in Distributed Power Generation System," pp. 1–10, 2016, doi: 10.1109/TIA.2016.2600644.

[87] V. Kavitha and K. Subramanian, "Investigation of power quality issues and its solution for distributed power system," *Proc. IEEE Int. Conf. Circuit, Power Comput. Technol. ICCPCT 2017*, 2017, doi: 10.1109/ICCPCT.2017.8074372.

[88] T. I. M. Slangen, "Grid Impact of Electric Vehicle Fast Charging Stations : Trends , Standards , Issues and Mitigation Measures - An Overview," vol. 2, no. November 2020, 2021, doi: 10.1109/OJPEL.2021.3054601.

[89] I. S. Association, *Ieee Standard 1159 - 1995*. 1995.

[90] IEEE Std 1159, *Monitoring Electric Power Quality Developed by the Transmission and Distribution Committee IEEE Power and Energy Society*, vol. 2019. 2019.

[91] R. G. Suryavanshi, "A review on power quality issues due to high penetration level of solar generated power on the grid," pp. 464–467, 2019.

[92] D. Committee, I. Power, and E. Society, "IEEE Std 519^{TM}-2014," *IEEE Std 519-2014 (Revision IEEE Std 519-1992)*, vol. 2014, 2014.

[93] IEEE, "IEEE 1547 - 2003 Standards," *1547 TM IEEE Stand. Interconnecting Distrib. Resour. with Electr. Power Syst. Stand.*, no. July, 2003.

[94] IEEE Std 1547, *IEEE Standard for Interconnection and Interoperability of Distributed Energy Resources with Associated Electric Power Systems Interfaces*. 2018.

[95] S. Rahmani, A. Hamadi, S. Member, K. Al-haddad, and L. A. Dessaint, "A Combination of Shunt Hybrid Power Filter and Thyristor-Controlled Reactor for Power Quality," vol. 61, no. 5, pp. 2152–2164, 2014.

[96] A. Kumar, "Design , Modeling and Performance of Static Synchronous Series Compensator Regulated Self- excited induction generator," pp. 519–525, 2019.

[97] S. V. Compensator, R. K. Varma, S. Auddy, and S. Member, "Mitigation of Subsynchronous Oscillations in a Series Compensated Wind Farm with," pp. 1–7,

2006.

[98] B. Singh and F. Ieee, "DVR Based Voltage Regulator for Isolated Asynchronous Generators Feeding Three Phase Load," pp. 1–6.

[99] F. Dstatcom, B. Singh, P. Jayaprakash, S. Kumar, and D. P. Kothari, "Implementation of Neural-Network-Controlled Three-Leg VSC and a Transformer as Three-Phase," vol. 47, no. 4, pp. 1892–1901, 2011.

[100] B. Jena and A. Choudhury, "Voltage and frequency stabilisation in a micro-hydro-PV based hybrid microgrid using FLC based STATCOM equipped with BESS," *Proc. IEEE Int. Conf. Circuit, Power Comput. Technol. ICCPCT 2017*, 2017, doi: 10.1109/ICCPCT.2017.8074291.

[101] K. F. Krommydas and A. T. Alexandridis, "Modular Control Design and Stability Analysis of Isolated PV-Source/Battery-Storage Distributed Generation Systems," *IEEE J. Emerg. Sel. Top. Circuits Syst.*, vol. 5, no. 3, pp. 372–382, 2015, doi: 10.1109/JETCAS.2015.2462172.

[102] R. R. Chilipi, B. Singh, S. S. Murthy, and L. Fellow, "Performance of a Self-Excited Induction Generator With DSTATCOM-DTC Drive-Based Voltage and Frequency Controller," vol. 29, no. 3, pp. 545–557, 2014.

[103] M. Abdul, A. Yahiya, M. Abdul, and R. Uzair, "Performance Analysis of DVR , DSTATCOM and UPQC For Improving The Power Quality With Various Control Strategies," 2016.

[104] S. Kaur and B. Dwivedi, "Power quality issues and their mitigation techniques in microgrid system- A review," *India Int. Conf. Power Electron. IICPE*, vol. 2016-Novem, 2016, doi: 10.1109/IICPE.2016.8079543.

[105] B. Singh, R. Sharma, and S. Kewat, "Robust Control Strategies for SyRG-PV and Wind-Based Islanded Microgrid," *IEEE Trans. Ind. Electron.*, vol. 68, no. 4, pp. 3137–3147, 2021, doi: 10.1109/TIE.2020.2978723.

[106] M. Bajaj, M. Pushkarna, and A. S. Rana, "An Improved SRF based Control Algorithm for D-STATCOM under Abnormal Source Voltage," pp. 1–6, 2015.

[107] E. Engineering and E. S. Engineering, "EPLL based Controller for Voltage Harmonic Mitigation in Grid Connected Wind Systems," no. 2, pp. 1157–1161, 2017.

[108] S. Jiao, R. R. Krishna, and K. Rajashekara, "A Novel Phase-Locked Loop based Four-

leg Converter Control for Unbalanced Load Compensation under Distorted and Unbalanced Grid Condition," *ECCE 2020 - IEEE Energy Convers. Congr. Expo.*, pp. 4749–4754, 2020, doi: 10.1109/ECCE44975.2020.9236389.

[109] A. J. Wang, B. Y. Ma, and C. X. Meng, "A frequency-locked loop technology of three-phase grid-connected inverter based on improved reduced order generalized integrator," *Proc. 2015 10th IEEE Conf. Ind. Electron. Appl. ICIEA 2015*, no. 1, pp. 730–735, 2015, doi: 10.1109/ICIEA.2015.7334204.

[110] A. Kumar, S. Kewat, B. Singh, and R. Jain, "CC-ROGI-FLL based control for grid-tied photovoltaic system at abnormal grid conditions," 2020, doi: 10.1049/iet-gtd.2019.0765.

[111] F. Wu and X. Li, "Multiple DSC Filter-Based Three-Phase EPLL for Nonideal Grid Synchronization," *IEEE J. Emerg. Sel. Top. Power Electron.*, vol. 5, no. 3, pp. 1396–1403, 2017, doi: 10.1109/JESTPE.2017.2701498.

[112] R. Sebastián and A. Nevado, "Study and simulation of awind hydro isolated microgrid," *Energies*, vol. 13, no. 22, pp. 1–15, 2020, doi: 10.3390/en13225937.

[113] G. Pathak, B. Singh, and B. K. Panigrahi, "Control of Wind-Diesel Microgrid Using Affine Projection-Like Algorithm," *IEEE Trans. Ind. Informatics*, vol. 12, no. 2, pp. 524–531, 2016, doi: 10.1109/TII.2016.2518643.

[114] M. Qasim, P. Kanjiya, and V. Khadkikar, "Artificial-neural-network-based phase-locking scheme for active power filters," *IEEE Trans. Ind. Electron.*, vol. 61, no. 8, pp. 3857–3866, 2014, doi: 10.1109/TIE.2013.2284132.

[115] M. Izadbakhsh, A. Rezvani, and M. Gandomkar, "Dynamic response improvement of hybrid system by implementing ANN-GA for fast variation of photovoltaic irradiation and FLC for wind turbine," *Arch. Electr. Eng.*, vol. 64, no. 2, pp. 291–314, 2015, doi: 10.1515/aee-2015-0024.

[116] T. S. Babu, J. P. Ram, T. Dragičević, M. Miyatake, F. Blaabjerg, and N. Rajasekar, "Particle swarm optimization based solar PV array reconfiguration of the maximum power extraction under partial shading conditions," *IEEE Trans. Sustain. Energy*, vol. 9, no. 1, pp. 74–85, 2018, doi: 10.1109/TSTE.2017.2714905.

[117] Z. Ding, H. Hou, G. Yu, E. Hu, L. Duan, and J. Zhao, "Performance analysis of a wind-solar hybrid power generation system," *Energy Convers. Manag.*, vol. 181, no.

November 2018, pp. 223–234, 2019, doi: 10.1016/j.enconman.2018.11.080.

[118] M. Abdolrasol, R. Mohamed, M. Hannan, A. Al-Shetwi, M. Mansor, and F. Blaabjerg, "Artificial Neural Network Based Particle Swarm Optimization for Microgrid Optimal Energy Scheduling," *IEEE Trans. Power Electron.*, vol. 36, no. 11, pp. 12151–12157, 2021, doi: 10.1109/TPEL.2021.3074964.

[119] A. Kumar, R. Garg, and P. Mahajan, "Performance Analysis of Grid Integrated PV System using SRF and IRPT Control," *2019 1st Int. Conf. Signal Process. VLSI Commun. Eng. ICSPVCE 2019*, 2019, doi: 10.1109/ICSPVCE46182.2019.9092869.

[120] B. Singh, D. T. Shahani, and A. K. Verma, "IRPT based control of a 50 kw grid interfaced solar photovoltaic power generating system with power quality improvement," *2013 4th IEEE Int. Symp. Power Electron. Distrib. Gener. Syst. PEDG 2013 - Conf. Proc.*, pp. 1–8, 2013, doi: 10.1109/PEDG.2013.6785601.

[121] L. A. Pittorino, A. Horn, and J. H. R. Enslin, "Power theory evaluation for the control of an active power filter," *IEEE AFRICON Conf.*, vol. 2, pp. 676–681, 1996, doi: 10.1109/afrcon.1996.562970.

[122] Sujono, I. Sudiharto, and O. A. Qudsi, "Application of D-STATCOM to reduce unbalanced load using synchronous reference frame theory," *EECCIS 2020 - 2020 10th Electr. Power, Electron. Commun. Control. Informatics Semin.*, no. 3, pp. 65–70, 2020, doi: 10.1109/EECCIS49483.2020.9263476.

[123] R. N. Tripathi and A. Singh, "SRF theory based grid interconnected Solar Photovoltaic (SPV) system with improved power quality," *Proc. - 2013 Int. Conf. Emerg. Trends Commun. Control. Signal Process. Comput. Appl. IEEE-C2SPCA 2013*, 2013, doi: 10.1109/C2SPCA.2013.6749390.

[124] A. Kumar, Seema, B. Singh, and R. Jain, "ROGI with FsLMS Based Control Technique for Solar PV System under Weak Grid," *Proc. - 2019 IEEE Int. Conf. Environ. Electr. Eng. 2019 IEEE Ind. Commer. Power Syst. Eur. EEEIC/I CPS Eur. 2019*, 2019, doi: 10.1109/EEEIC.2019.8783710.

[125] B. Sahoo, S. K. Routray, and P. K. Rout, "A modified least mean square technique for harmonic elimination," *1st Odisha Int. Conf. Electr. Power Eng. Commun. Comput. Technol. ODICON 2021*, 2021, doi: 10.1109/ODICON50556.2021.9428970.

[126] A. Kherbachi, A. Chouder, A. Bendib, K. Kara, and S. Barkat, "Enhanced structure of

second-order generalized integrator frequency-locked loop suitable for DC-offset rejection in single-phase systems," *Electr. Power Syst. Res.*, vol. 170, no. December 2018, pp. 348–357, 2019, doi: 10.1016/j.epsr.2019.01.029.

[127] S. Golestan, J. M. Guerrero, M. J. H. Rawa, A. M. Abusorrah, and Y. Al-Turki, "Frequency-Locked Loops in Electrical Power and Energy Systems: Equivalent or Different to Phase-Locked Loops?," *IEEE Ind. Electron. Mag.*, vol. 15, no. 4, pp. 54–64, 2021, doi: 10.1109/MIE.2021.3054580.

[128] A. K. Giri, S. R. Arya, R. Maurya, and B. Chitti Babu, "VCO-less PLL control-based voltage-source converter for power quality improvement in distributed generation system," *IET Electr. Power Appl.*, vol. 13, no. 8, pp. 1114–1124, Aug. 2019, doi: 10.1049/iet-epa.2018.5827.

[129] D. G. A. Krishna and A. Karthikeyan, "Design and analysis of frequency adaptive CDSC-PLL for Dynamic Voltage Restorer during adverse grid conditions," *2020 IEEE Int. Conf. Power Electron. Smart Grid Renew. Energy, PESGRE 2020*, no. 1, pp. 5–9, 2020, doi: 10.1109/PESGRE45664.2020.9070625.

[130] A. Jain, R. Saravanakumar, and S. Shankar, "Moving Average Filter-PLL-Based Voltage and Frequency Control of Standalone WECS," *IETE J. Res.*, vol. 68, no. 5, pp. 3628–3637, 2022, doi: 10.1080/03772063.2020.1772128.

[131] S. Golestan, J. M. Guerrero, and J. C. Vasquez, "Three-Phase PLLs: A Review of Recent Advances," *IEEE Trans. Power Electron.*, vol. 32, no. 3, pp. 1894–1907, 2017, doi: 10.1109/TPEL.2016.2565642.

[132] S. Golestan, J. M. Guerrero, and J. C. Vasquez, "Is Using A Complex Control Gain in Three-Phase FLLs Reasonable?," *IEEE Trans. Ind. Electron.*, vol. 67, no. 3, pp. 2480–2484, 2020, doi: 10.1109/TIE.2019.2903748.

[133] P. Chittora, A. Singh, and M. Singh, "Adaptive EPLL for improving power quality in three-phase three-wire grid-connected photovoltaic system," *IET Renew. Power Gener.*, vol. 13, no. 9, pp. 1595–1602, 2019, doi: 10.1049/iet-rpg.2018.5261.

[134] V. Khare, S. Nema, and P. Baredar, "Solar-wind hybrid renewable energy system: A review," *Renew. Sustain. Energy Rev.*, vol. 58, pp. 23–33, 2016, doi: 10.1016/j.rser.2015.12.223.

[135] S. Inoue and H. Akagi, "A Bi-directional DC/DC converter for an energy storage

system," *Conf. Proc. - IEEE Appl. Power Electron. Conf. Expo. - APEC*, pp. 761–767, 2007, doi: 10.1109/APEX.2007.357601.

[136] F. Xue, R. Yu, W. Yu, A. Q. Huang, and Y. Du, "A novel bi-directional DC-DC converter for distributed energy storage device," *Conf. Proc. - IEEE Appl. Power Electron. Conf. Expo. - APEC*, vol. 2015-May, no. May, pp. 1126–1130, 2015, doi: 10.1109/APEC.2015.7104489.

[137] Seema and B. Singh, "Analysis and control of a standalone PV-BESS-DG based microgrid," *India Int. Conf. Power Electron. IICPE*, vol. 2016-Novem, pp. 1–6, 2016, doi: 10.1109/IICPE.2016.8079483.

[138] H. Mahmood and J. Jiang, "Autonomous coordination of multiple PV/Battery hybrid units in islanded microgrids," *IEEE Trans. Smart Grid*, vol. 9, no. 6, pp. 6359–6368, 2018, doi: 10.1109/TSG.2017.2709550.

[139] T. T. Ku and C. S. Li, "Implementation of Battery Energy Storage System for an Island Microgrid with High PV Penetration," *IEEE Trans. Ind. Appl.*, vol. 57, no. 4, pp. 3416–3424, 2021, doi: 10.1109/TIA.2021.3075655.

[140] Y. Wang, K. T. Tan, and P. L. So, "Coordinated control of battery energy storage system in a microgrid," *Asia-Pacific Power Energy Eng. Conf. APPEEC*, 2013, doi: 10.1109/APPEEC.2013.6837211.

[141] D. Segaran, B. P. McGrath, and D. G. Holmes, "Adaptive dynamic control of a bi-directional DCDC converter," *2010 IEEE Energy Convers. Congr. Expo. ECCE 2010 - Proc.*, pp. 1442–1449, 2010, doi: 10.1109/ECCE.2010.5618258.

[142] B. Housseini, A. F. Okou, and R. Beguenane, "Robust nonlinear controller design for on-grid/off-grid wind energy battery-storage system," *IEEE Trans. Smart Grid*, vol. 9, no. 6, pp. 5588–5598, 2018, doi: 10.1109/TSG.2017.2691707.

[143] C. Xiang, Y. Wang, S. Hu, and W. Wang, "A new topology and control strategy for a hybrid battery-ultracapacitor energy storage system," *Energies*, vol. 7, no. 5, pp. 2874–2896, 2014, doi: 10.3390/en7052874.

[144] C. Jamroen, A. Pannawan, and S. Sirisukprasert, "Battery Energy Storage System Control for Voltage Regulation in Microgrid with High Penetration of PV Generation," *Proc. - 2018 53rd Int. Univ. Power Eng. Conf. UPEC 2018*, pp. 1–6, 2018, doi: 10.1109/UPEC.2018.8541888.

[145] P. S. Kumar, R. P. S. Chandrasena, V. Ramu, G. N. Srinivas, and K. V. S. M. Babu, "Energy Management System for Small Scale Hybrid Wind Solar Battery Based Microgrid," *IEEE Access*, vol. 8, pp. 8336–8345, 2020, doi: 10.1109/ACCESS.2020.2964052.

[146] S. Kumar Tiwari, B. Singh, and P. K. Goel, "Design and Control of Microgrid Fed by Renewable Energy Generating Sources," *IEEE Trans. Ind. Appl.*, vol. 54, no. 3, pp. 2041–2050, 2018, doi: 10.1109/TIA.2018.2793213.

[147] R. Al Badwawi, M. Abusara, and T. Mallick, "A Review of Hybrid Solar PV and Wind Energy System," *Smart Sci.*, vol. 3, no. 3, pp. 127–138, 2015, doi: 10.1080/23080477.2015.11665647.

[148] E. Espina, J. Llanos, C. Burgos-Mellado, R. Cárdenas-Dobson, M. Martínez-Gómez, and D. Sáez, "Distributed control strategies for microgrids: An overview," *IEEE Access*, vol. 8, pp. 193412–193448, 2020, doi: 10.1109/ACCESS.2020.3032378.

[149] R. Sharma, S. Kewat, and B. Singh, "Robust 3IMPL control algorithm for power management of SyRG/PV/BES-Based distributed islanded microgrid," *IEEE Trans. Ind. Electron.*, vol. 66, no. 10, pp. 7765–7777, 2019, doi: 10.1109/TIE.2018.2880673.

[150] S. Mahesar *et al.*, "Power management of a stand-alone hybrid (wind/solar/battery) energy system: An experimental investigation," *Int. J. Adv. Comput. Sci. Appl.*, vol. 9, no. 6, pp. 216–221, 2018, doi: 10.14569/IJACSA.2018.090631.

[151] R. G. Wandhare and V. Agarwal, "Novel integration of a PV-wind energy system with enhanced efficiency," *IEEE Trans. Power Electron.*, vol. 30, no. 7, pp. 3638–3649, 2015, doi: 10.1109/TPEL.2014.2345766.

[152] D. A. Pedroso, C. A. De Souza, L. G. Scherer, and R. F. De Camargo, "Development and Control of a Hydro-PV Power Generation System with BESS and ELC," *2019 IEEE PES Conf. Innov. Smart Grid Technol. ISGT Lat. Am. 2019*, pp. 1–6, 2019, doi: 10.1109/ISGT-LA.2019.8895340.

[153] T. Hirose and H. Matsuo, "Standalone hybrid wind-solar power generation system applying dump power control without dump load," *IEEE Trans. Ind. Electron.*, vol. 59, no. 2, pp. 988–997, 2012, doi: 10.1109/TIE.2011.2159692.

[154] Seema and B. Singh, "PV-Hydro-Battery Based Standalone Microgrid for Rural Electrification," *2018 5th IEEE Uttar Pradesh Sect. Int. Conf. Electr. Electron.*

Comput. Eng. UPCON 2018, pp. 1–6, 2018, doi: 10.1109/UPCON.2018.8597005.

[155] A. K. Pandey, "Variable Wind Speed," *2018 5th IEEE Uttar Pradesh Sect. Int. Conf. Electr. Electron. Comput. Eng.*, no. Mv, pp. 1–6, 2018.

[156] A. S. Sánchez, E. A. Torres, and R. A. Kalid, "Renewable energy generation for the rural electrification of isolated communities in the Amazon Region," *Renew. Sustain. Energy Rev.*, vol. 49, pp. 278–290, 2015, doi: 10.1016/j.rser.2015.04.075.

[157] Q. Shafiee, J. M. Guerrero, and J. C. Vasquez, "Distributed secondary control for islanded microgrids-a novel approach," *IEEE Trans. Power Electron.*, vol. 29, no. 2, pp. 1018–1031, 2014, doi: 10.1109/TPEL.2013.2259506.

[158] R. Sharma, S. Kewat, and B. Singh, "Robust MMSOGI-FLL control algorithm for power quality improvement of solar PV-SyRG pico hydro-BES based islanded microgrid with dynamic load," *IET Power Electron.*, vol. 13, no. 13, pp. 2874–2884, 2020, doi: 10.1049/iet-pel.2019.1002.

[159] R. J. Harrington and F. M. M. Bassiouny, "New approach to determine the critical capacitance for self-excited induction generators," *IEEE Trans. Energy Convers.*, vol. 13, no. 3, pp. 244–249, 1998, doi: 10.1109/60.707603.

[160] T. F. Chan, "Analysis of self-excited induction generators using an iterative method," *IEEE Trans. Energy Convers.*, vol. 10, no. 3, pp. 502–507, 1995, doi: 10.1109/60.464874.

[161] S. N. Mahato, S. P. Singh, and M. P. Sharma, "Excitation capacitance required for self excited single phase induction generator using three phase machine," *Energy Convers. Manag.*, vol. 49, no. 5, pp. 1126–1133, 2008, doi: 10.1016/j.enconman.2007.09.007.

[162] B. Singh, S. S. Murthy, and S. Gupta, "Analysis and design of electronic load controller for self-excited induction generators," *IEEE Trans. Energy Convers.*, vol. 21, no. 1, pp. 285–293, 2006, doi: 10.1109/TEC.2005.847950.

[163] K. Arthishri, N. Kumaresan, and N. A. Gounden, "Analysis and Application of Three-Phase SEIG with Power Converters for Supplying Single-Phase Grid from Wind Energy," *IEEE Syst. J.*, vol. 13, no. 2, pp. 1813–1822, 2019, doi: 10.1109/JSYST.2018.2875761.

[164] M. Taoufik, B. Abdelhamid, and S. Lassad, "Stand-alone self-excited induction generator driven by a wind turbine," *Alexandria Eng. J.*, vol. 57, no. 2, pp. 781–786,

2018, doi: 10.1016/j.aej.2017.01.009.

[165] M. I. Mosaad, "Model reference adaptive control of STATCOM for grid integration of wind energy systems," *IET Electr. Power Appl.*, vol. 12, no. 5, pp. 605–613, 2018, doi: 10.1049/iet-epa.2017.0662.

[166] H. Mahmood, D. Michaelson, and J. Jiang, "A power management strategy for PV/battery hybrid systems in Islanded microgrids," *IEEE J. Emerg. Sel. Top. Power Electron.*, vol. 2, no. 4, pp. 870–882, 2014, doi: 10.1109/JESTPE.2014.2334051.

[167] M. M. Neam, F. F. M. El-Sousy, M. A. Ghazy, and M. A. Abo-Adma, "The dynamic performance of an isolated self-excited induction generator driven by a variable-speed wind turbine," *Proc. 11th Int. Middle East Power Syst. Conf. MEPCON'2006*, vol. 1, pp. 167–174, 2006.

[168] Z. Salam, K. Ishaque, and H. Taheri, "An improved two-diode photovoltaic (PV) model for PV system," *2010 Jt. Int. Conf. Power Electron. Drives Energy Syst. PEDES 2010 2010 Power India*, vol. 1, no. 4, pp. 1–5, 2010, doi: 10.1109/PEDES.2010.5712374.

[169] K. Ishaque, Z. Salam, H. Taheri, and Syafaruddin, "Modeling and simulation of photovoltaic (PV) system during partial shading based on a two-diode model," *Simul. Model. Pract. Theory*, vol. 19, no. 7, pp. 1613–1626, 2011, doi: 10.1016/j.simpat.2011.04.005.

[170] H. Saxena, A. Singh, and J. N. Rai, "Design and analysis of different PLLs as load compensation techniques in 1-∅ grid-tied PV system," *Int. J. Electron.*, vol. 106, no. 11, pp. 1632–1659, 2019, doi: 10.1080/00207217.2019.1600745.

[171] D. Jena and V. V. Ramana, "Modeling of photovoltaic system for uniform and non-uniform irradiance: A critical review," *Renew. Sustain. Energy Rev.*, vol. 52, pp. 400–417, 2015, doi: 10.1016/j.rser.2015.07.079.

[172] Y. T. Tan, D. S. Kirschen, and N. Jenkins, "A model of PV generation suitable for stability analysis," *IEEE Trans. Energy Convers.*, vol. 19, no. 4, pp. 748–755, 2004, doi: 10.1109/TEC.2004.827707.

[173] S. Motahhir, A. El Ghzizal, S. Sebti, and A. Derouich, "Modeling of Photovoltaic System with Modified Incremental Conductance Algorithm for Fast Changes of Irradiance," *Int. J. Photoenergy*, vol. 2018, 2018, doi: 10.1155/2018/3286479.

[174] J. Philip, B. Singh, and S. Mishra, "Design and operation for a standalone DG-SPV-BES microgrid system," *Proc. 6th IEEE Power India Int. Conf. PIICON 2014*, 2014, doi: 10.1109/34084POWERI.2014.7117727.

[175] T. Halder, "Charge controller of solar photo-voltaic panel fed (SPV) battery," *India Int. Conf. Power Electron. IICPE 2010*, pp. 4–7, 2011, doi: 10.1109/IICPE.2011.5728056.

[176] Z. Tao and L. Li, "Control loop design and bidirectional control strategy of a bidirectional DC/DC converter," *Proc. IECON 2017 - 43rd Annu. Conf. IEEE Ind. Electron. Soc.*, vol. 2017-Janua, pp. 5720–5725, 2017, doi: 10.1109/IECON.2017.8216992.

[177] K. Bin Liu, C. Y. Liu, Y. H. Liu, Y. C. Chien, B. S. Wang, and Y. S. Wong, "Analysis and controller design of a universal bidirectional DC-DC converter," *Energies*, vol. 9, no. 7, 2016, doi: 10.3390/en9070501.

[178] Y. X. Wang, F. F. Qin, and Y. B. Kim, "Bidirectional DC-DC converter design and implementation for lithium-ion battery application," *Asia-Pacific Power Energy Eng. Conf. APPEEC*, vol. 2015-March, no. March, pp. 0–4, 2014, doi: 10.1109/APPEEC.2014.7066140.

[179] J. A. Mane and A. M. Jain, "Design, modelling and control of bidirectional DC-DC converter (for EV)," *2015 Int. Conf. Emerg. Res. Electron. Comput. Sci. Technol. ICERECT 2015*, pp. 294–297, 2016, doi: 10.1109/ERECT.2015.7499029.

[180] J. Park and S. Choi, "Design and control of a bidirectional resonant dc-dc converter for automotive engine/battery hybrid power generators," *IEEE Trans. Power Electron.*, vol. 29, no. 7, pp. 3748–3757, 2014, doi: 10.1109/TPEL.2013.2281826.

[181] H. Saxena, A. Singh, and J. N. Rai, "Design and performance analysis of improved Adaline technique for synchronization and load compensation of grid-tied photovoltaic system," *Int. Trans. Electr. Energy Syst.*, vol. 30, no. 6, pp. 1–18, 2020, doi: 10.1002/2050-7038.12388.

[182] P. Chittora, A. Singh, and M. Singh, "Simple and efficient control of DSTATCOM in three-phase four-wire polluted grid system using MCCF-SOGI based controller," *IET Gener. Transm. Distrib.*, vol. 12, no. 5, pp. 1213–1222, 2018, doi: 10.1049/iet-gtd.2017.0901.

[183] B. Singh, S. S. Murthy, and S. Gupta, "A stand-alone generating system using self-

excited induction generators in the extraction of petroleum products," *IEEE Trans. Ind. Appl.*, vol. 46, no. 1, pp. 94–101, 2010, doi: 10.1109/TIA.2009.2036519.

[184] B. Singh, G. K. Kasal, A. Chandra, and Kamal-Al-Haddad, "An independent active and reactive power control of an isolated asynchronous generator in 3-phase 4-wire applications," *PESC Rec. - IEEE Annu. Power Electron. Spec. Conf.*, pp. 2057–2063, 2008, doi: 10.1109/PESC.2008.4592246.

[185] S. Golestan, E. Ebrahimzadeh, B. Wen, J. M. Guerrero, and J. C. Vasquez, "Dq-Frame Impedance Modeling of Three-Phase Grid-Tied Voltage Source Converters Equipped with Advanced PLLs," *IEEE Trans. Power Electron.*, vol. 36, no. 3, pp. 3524–3539, 2021, doi: 10.1109/TPEL.2020.3017387.

[186] A. Singh, M. Badoni, and B. Singh, "Application of least means square algorithm to shunt compensator: An experimental investigation," *2014 IEEE Int. Conf. Power Electron. Drives Energy Syst. PEDES 2014*, 2014, doi: 10.1109/PEDES.2014.7042044.